



## Durham E-Theses

---

### *Muons in extensive air showers of size $10(^4)$ to $10(^7)$ particles*

Hawkes, R. C.

#### How to cite:

---

Hawkes, R. C. (1977) *Muons in extensive air showers of size  $10(^4)$  to  $10(^7)$  particles*, Durham theses, Durham University. Available at Durham E-Theses Online: <http://etheses.dur.ac.uk/8322/>

#### Use policy

---

The full-text may be used and/or reproduced, and given to third parties in any format or medium, without prior permission or charge, for personal research or study, educational, or not-for-profit purposes provided that:

- a full bibliographic reference is made to the original source
- a [link](#) is made to the metadata record in Durham E-Theses
- the full-text is not changed in any way

The full-text must not be sold in any format or medium without the formal permission of the copyright holders.

Please consult the [full Durham E-Theses policy](#) for further details.

**MUONS IN EXTENSIVE AIR SHOWERS OF SIZE**

**$10^4$  TO  $10^7$  PARTICLES**

by

**R.C. HAWKES, B.Sc.**

The copyright of this thesis rests with the author  
No quotation from it should be published without  
his prior written consent and information derived  
from it should be acknowledged

**A Thesis submitted to the University of Durham**

**for the Degree of Doctor of Philosophy**

**June, 1977**



To my Mother and Father.

ABSTRACT

Using the Durham spectrograph and Small Extensive Air Shower Array situated 40 m. above sea level, the rate of single muons and muon pairs of momentum in the range 20 GeV/c to 1000 GeV/c in air showers of size  $10^4$  to  $10^7$  particles have been measured. The rate of unassociated muon pairs has also been recorded.

The large solid iron spectrograph (MARS) is of toroidal design having two distinct halves, which both have a maximum detectable momentum of about 3000 GeV/c, and an acceptance of  $487 \text{ cm}^2 \text{ sr}$  for single air shower accompanied muons. Both halves are triggered by scintillation counters, whilst muon track location is achieved by digitised neon flash tubes on the Eastern half, and by photography of the flash tubes on the Western half. The air shower array (SARA) has 14 plastic scintillation counters having areas varying from  $0.26 \text{ m}^2$  to  $2.0 \text{ m}^2$  and placed in an hexagonal geometry around the spectrograph. The array has a characteristic radius of 60 m. and is sensitive to showers of size  $10^5$  to  $3 \times 10^6$  particles.

The measured rates of single and double muons accompanied by air showers are compared to the predictions of semi-empirical electron and muon structure functions. Broad support is found for the structure of muons for small radial distances ( $\lesssim 100 \text{ m.}$ ) as predicted by the expression introduced by Greisen (1960) including an extrapolation to muons of momentum above 1000 GeV/c. A comparison is also made with the predictions of both the CKP, and Feynman scaling model of high energy particle interactions as applied to extensive air showers by Goned (1975) and Fishbane, et al., (1974). Evidence is found to support the suggestion (Gaisser and Maurer (1972) Fishbane, et al., (1974), Wdowczyk and Wolfendale (1973)) that the combination

of a scaling particle interaction model and an assumed primary spectrum dominated by protons predicts too low a ratio of muons to electrons in air showers at sea level. In contrast the predictions of the CKP model largely coincide with the experimental data.

Some evidence is also found for coincident muon pairs at sea level unaccompanied by shower particles.

PREFACE

This thesis contains an account of the work carried out in the period 1973-1976 while the author was a research student under the supervision of Dr. M. G. Thompson in the Cosmic Ray Group of the Physics Department of the University of Durham.

When the author joined the group, the MARS spectrograph was essentially complete but only one arm of the instrument was being used for the muon momentum spectrum measurements up to 5000 GeV/c. The author was responsible for the assembly of the second arm of the instrument which incorporates trays of neon-filled flash tubes which are used as trajectory defining elements. He was responsible for the design and running of the photographic recording system for that arm and also helped with adjustments to the electronics of the composite equipment, and with the running of all the experiments performed with the spectrograph.

The analysis of the data reported here has been carried out by the author using the techniques developed by Wells (1972), Daniel (private communication) and Smith (1976). The author is also responsible for the interpretation of the results with regard to the predictions of other workers.

The essential results of this work have been presented to the XVth International Cosmic Ray Conference in Plovdiv, Bulgaria. (Hawkes, et al., 1977).

ACKNOWLEDGEMENTS

I wish to thank Professor A.W.Wolfendale, F.R.S., for the provision of the facilities for this study, and for his encouragement at all stages of the experiment. The Science Research Council is acknowledged for providing a Research Studentship and funding the experiment.

I am deeply indebted to my supervisor, Dr.M.G.Thompson, for his constant advice and guidance throughout this work.

All members of the MARS group are thanked for their help with the construction and the running of the apparatus. I would especially like to thank Dr. A.C.Smith for many interesting and extremely helpful discussions, and express my gratitude to Dr. M.R.Whalley, Mr. T.R.Stewart, Mr. W.S.Rada, Mr. R. Thornley and Mr. J.M.Baxendale for help and suggestions of both a theoretical and practical nature.

Mr. K. Tindale is thanked for his skilled assistance in the laboratory and in particular for his help with the photographic system and for developing over half a mile of 35 mm. film. I am most grateful to Dr. B.J.Daniel and Mrs.S.E.Davidson for their painstaking efforts in transferring and accessing the experimental data through the computing systems.

I would like to thank Dr. B.A. Khrenov, Dr. A. Goned and Dr.J.Wdowczyk for valuable suggestions and help at various stages of this work.

Finally, I wish to extend special thanks to Mrs. A. Gregory for her excellent drawing of the diagrams, and to Mrs. S.Mellanby for transforming this thesis through her precise and rapid typing.

CONTENTS

	Page
Abstract	i
Preface	iii
Acknowledgements	iv
Contents	v
CHAPTER 1 : INTRODUCTION	
1.1 The Historical Background of Cosmic Ray Studies	1
1.2 The Intensity and Origin of Primary Cosmic Rays	3
1.3 Extensive Air Showers	6
1.4 Scope of the Present Work in Relation to Some Current Physical Problems	8
CHAPTER 2 : THE SPECTROGRAPH AND AIR SHOWER ARRAY	
2.1 Introduction	13
2.2 General Description of M.A.R.S. (Magnetic Automated Research Spectrograph)	13
2.2.1 The Magnetic Field	15
2.2.2 The Scintillation Counters	16
2.2.3 Flash Tube Techniques	16
2.2.4 The Blue Side Momentum Selector Trays and Associated Logic	17
2.2.5 The Blue Side Measuring Trays	18
2.2.6 The Red Side Measuring Trays	19
2.2.7 Flash Tube Tray Alignment Using Geiger Tray Information	21
2.2.8 The Acceptance and The Maximum Detectable Momentum of the Spectrograph	22
2.3 General Description of S.A.R.A. (Shower Automated Research Array)	23
2.3.1 The Detecting Elements	24
2.3.2 Density Measurements	25
2.3.3 Fast-Timing Measurements	25

	Page
2.3.4 The Data Handling Electronics	25
2.3.5 Digitisation of the Detectors Signal	25
2.3.6 The Storage of the Shower Data	26
2.3.7 The Interrogation Technique	27
2.4 The Daily Running of the Spectrograph and Array	27
2.5 The Experimental Description	28
2.5.1 The Rate of High Energy Muons in Air Showers	28
2.5.2 Air Shower Array Interrogation	28
2.5.3 Muon Pair Experiment	28
2.6 The Role of the Author	29
CHAPTER 3 : GENERAL ANALYSIS OF THE DATA	
3.1 Introduction	30
3.2 The Analysis of the Muon Data	31
3.2.1 Muon Momentum Determination	31
3.2.2 Trajectory Fitting by Computer Programme	32
3.2.3 Air Shower Accompanied Muons	34
3.2.4 The Analysis Procedure	37
3.3 The Analysis of the Air Shower Array Data	38
3.3.1 Introduction	38
3.3.2 The Analysis Procedure	39
3.3.3 The Minimisation of the Array Data	40
3.3.4 Accuracy of the Array Analysis	40
3.4 The Determination of Shower Particle Density From the Top Measuring Tray of the Spectrograph	41
3.4.1 Introduction	41
3.4.2 The Density of Shower Particles from Flash Tube Data	42
3.4.3 The Validity of the Muon Data	47
CHAPTER 4 : THE RATE OF MUONS IN AIR SHOWERS	
4.1 Introduction	49
4.2 The Experimental Results	49
4.3 The Charge Ratio of Muons in Air Showers	51
4.4 The Nature of the Muon Events Accompanied by Particles	51

	Page
4.5 The Probability of the Spectrograph Being Triggered	52
4.6 The Rate of Events Determined from the Sea Level Shower Size Spectrum	56
4.7 The Predictions of the C.K.P. and Scaling Models	61
4.7.1 Introduction	61
4.7.2 The Muon Component Determined from Nuclear Interaction Models	62
4.7.3 The Scaling Model	63
4.7.4 The C.K.P. Model	66
4.7.5 The Method of Calculation	67
4.7.6 Application to the Present Experiment	67
4.7.7 The Electron Component	68
4.7.8 The Mean Shower Size Predicted by the C.K.P. Model	70
4.7.9 The Mean Shower Size Predicted by the Scaling Model	71
4.7.10 The Primary Cosmic Ray Composition	75
4.7.11 The Trial Models and Primary Spectra	78
4.7.12 The Predicted Rate of Events Using the C.K.P. and Scaling Models	80
CHAPTER 5 : THE COINCIDENT MUON PAIR EXPERIMENT	
5.1 Introduction	83
5.2 The Acceptance of the Spectrograph for Muon Pairs	84
5.2.1 The Acceptance for Two Muons Traversing the Blue Side	84
5.2.2 One Muon Traversing Each Side of the Spectrograph	86
5.3 General Data of the Muon Pair Experiment	88
5.3.1 Introduction	88
5.3.2 The Experimental Data	88
5.3.3 Angular Separation of Muons	89
5.3.4 Spacial Separation of the Muon Pair	90
5.3.5 Angular Deviation of Muon Pair From Shower Axis Direction	91

	Page
5.4 The Predicted Rate of Coincident Muon Pairs Accompanied by An Air Shower	93
5.4.1 Introduction	93
5.4.2 The Conversion of the Rate of Events Into the Intensity of Muon Pairs	93
5.4.3 The Muon Pair Intensity Predicted From the Shower Size Spectrum	95
5.4.4 The Intensity of Muon Pairs Predicted by the Interaction Models	98
5.5 Muon Pair Production	99
 CHAPTER 6 : THE INTERPRETATION OF THE RESULTS	
6.1 Introduction	104
6.2 The Lateral Structure of Electrons	105
6.3 The Energy Threshold for Electron Detection	108
6.4 The Lateral Structure of Muons	110
6.5 The Dependence of the Predictions of the C.K.P. and Scaling Models on the Primary Spectrum	113
6.6 The Effect of the Rising Proton-Air Cross Section and the Effect of a Nuclear Projectile and Target	114
6.7 The Effect of Representing a Distribution of Shower Sizes by a Mean Shower Size	118
6.8 Comparison of the Measured and Predicted Rates	120
 CHAPTER 7 : CONCLUSION AND FUTURE WORK	122
 APPENDICES :	
'A' - The Monte Carlo Technique	125
'B' - Monte Carlo Determination of Acceptance	128
'C' - The Spectrograph Acceptance for Shower Associated Muons	131
'D' - The Effective Area and Solid Angle of the Blue Side of the Spectrograph for Air Shower Accompanied Muons	132
'E' - The Acceptance of the Spectrograph for Two Coincident Muons	137
'F' - The Effect of Detector Area on the Density of Particles Determined from the Lateral Distribution	140
'G' - The Relation of the Sea Level Shower Size Spectrum to the Primary Spectrum for Different Model Predictions	143
'H' - The Scintillation Counter Efficiencies	145
 REFERENCES :	146

CHAPTER 1

INTRODUCTION

1.1 THE HISTORICAL BACKGROUND OF COSMIC RAY STUDIES

Over the past 60 years the study of cosmic radiation has led to major advances in our understanding of the fundamental processes of nature. The enormous energy carried by individual particles has enabled some insight of both the smallest and largest parts of the universe. Indeed the ultimate resolution of the constituents of matter (possibly quarks) may require the energy available in cosmic rays, and one of the most intriguing physical problems is the mechanism by which particles can be accelerated to the highest energies seen in the cosmic radiation, of greater than  $10^{20}$  eV in a single particle.

At the turn of the century the first indications of a penetrating extraterrestrial radiation came from studies of the residual conductivity of enclosed and shielded samples of air. Elster, (1900) and Geitel, (1900) noticed that despite attempts to remove ions from a sample of air a significant residual conductivity remained, and Wilson, (1900) and (1901) in studies with an ionization chamber suspected the presence of ionizing radiation that could pass through thick layers of earth, and he speculated a possible extraterrestrial source for this radiation. It fell to Hess, (1912) to demonstrate in a balloon flight that after an initial reduction with altitude in ionization in a pressurised ionization chamber, ultimately an increase in ionization occurred that continued up to the greatest height that he reached, of about 5 km. The initial assumption that the radiation was  $\gamma$ -rays was due to its highly penetrating power. However, with the introduction of more sophisticated techniques involving cloud chambers and Geiger-Muller tubes, the latitude and East-West effects were seen which could not be explained in terms of  $\gamma$ -rays. The latitude effect indicated a lower intensity of cosmic rays near the equator where the horizontal component of the earth's geomagnetic field is stronger, and hence Clay, (1927) concluded that the



primary cosmic rays must be charged. The East-West effect of more particles arriving from the west than the east, led Johnson and Street, (1933) to the conclusion that the majority of primary cosmic rays were positively charged. It became clear that the primary cosmic radiation interacted with the earth's atmosphere to produce further radiation and experiments continued to determine the nature of the primary and secondary radiation and speculation arose about the origin of the primary rays.

One of the first major successes of cosmic ray studies was the discovery by Anderson, (1932) of the positron which had been predicted by Dirac. The electron positron pair created by a photon was a vital indication of relativistic physics involving energy and momentum and the transmutation from energy to matter. Secondary cosmic rays were classified into the soft (absorbed) component, and the hard component that could penetrate 15 cm. of lead. Unfortunately, the hard component particles were mistakenly thought to be the mediator of the strong force that holds nucleons together that had been predicted by Yukawa, (1935). This was largely because of its closeness in mass, about 200 times the mass of the electron, to the particle introduced by Yukawa, called the meson. The direct observation of the so called  $\pi$ -meson by Lattes et al., (1947) finally resolved the mystery of the lack of interaction of the penetrating particle, the muon, which is now known to be a lepton and as such is not subject to the strong interaction force. Particle discoveries continued when Rochester and Butler, (1947) identified in a cloud chamber a neutral particle, the  $\Lambda^0$ , by its decay into a positive and negative particle, which made necessary the introduction of the quantum number of strangeness.

The study of cosmic rays has divided naturally into two parts; the study of the actual primary radiation, and the study of the secondary radiation produced when the primary particles interact with the atmosphere. The main effort in the 1930's and up to the 1950's was the attempt to understand the elementary particles produced by cosmic rays and their interactions at high

energies, but with the advent of particle accelerators the interest switched to include more geophysical and astrophysical aspects of the primary rays. However, more recently many new effects have been seen at incident particle energies below  $2 \cdot 10^3$  GeV using present day accelerators which has returned interest to the still higher cosmic ray energies. In particular, the suggestions of Feynman, (1969) and Benecke, et al., (1969) which are designed to describe the processes of energy distribution and multiplicity of particle production in interactions below  $2 \cdot 10^3$  GeV, can be extrapolated from this energy region to a further test at the higher energies present in cosmic rays.

## 1.2 THE INTENSITY AND ORIGIN OF PRIMARY COSMIC RAYS

The primary cosmic rays that impinge on the earth's atmosphere have an intensity that ranges from about  $10^{-6} \text{ m}^{-2} \text{ s}^{-1} \text{ sr}^{-1} \text{ ev}^{-1}$  at an energy of about  $10^7$  eV per nucleon to about  $10^{-38} \text{ m}^{-2} \text{ s}^{-1} \text{ sr}^{-1} \text{ ev}^{-1}$  at an energy of about  $10^{20}$  eV per nucleus. In the region below about  $10^9$  eV the interplanetary magnetic field reduces the primary intensity below its value far from the sun and at the highest energies, Greisen, (1966) has suggested a possible cut in the spectrum due to energy loss by high energy primary protons by photo-pion production. This may occur at a proton energy of just above  $5 \cdot 10^{19}$  eV in interactions with the isotropic microwave background radiation corresponding to a black-body temperature of about  $2.7^{\circ}$  K (Roll and Wilkinson, 1966). Hillas, (1975) points out that nuclei may suffer photo-disintegration on starlight above about  $10^{17}$  eV, but concludes from air shower measurements that the cosmic ray spectrum seems uninterrupted to  $\sim 2 \cdot 10^{20}$  eV.

It is becoming customary to consider gamma rays as part of the cosmic radiation if for no other reason because gamma ray astronomy measures directly the presence and effects of energetic charged cosmic ray particles. The galaxy is extremely transparent to gamma rays and hence they can bring information largely unchanged from the point of their creation. The gamma ray intensity observed involves clearly established gamma ray sources super-

imposed on a general diffuse radiation background. The longitudinal and latitudinal distribution along the galactic plane of the intensity of gamma rays appears generally correlated with galactic structural features, and particularly with spiral arm segments. Distinct sources appear to be the regions of the galaxy associated with the Crab Nebula,  $V\alpha 10$  and the Orion clouds.

The proportion of different nuclei making up the cosmic ray spectrum have been measured directly by many different balloon and satellite experiments up to about  $10^{12}$  eV per nucleon, but beyond this energy the situation is unclear. Figure 1.1 shows the abundance distribution of the elements present as cosmic rays in the range from a few hundred MeV per nucleon to about one GeV per nucleon for hydrogen up to iron as given by Mayer et al., (1974). For comparison the solar system abundances are also shown in Figure 1.1. The presence in cosmic rays of the light nuclei elements (Li, Be and B) in quantities considerably in relative excess over the solar system abundances can be understood if the majority of these nuclei are fragmentation products which originate in the collisions of heavier nuclei with the matter between the source and the earth. Nuclei heavier than iron have been found to be present in cosmic rays, see Fowler, (1973) but with intensities lower by a factor of about  $10^5$  than that of iron. In Figure 1.2 is shown the primary particle flux as compiled by Hillas, (1975). The highest energy at which direct measurements have been made are reported by Grigorov et al., (1970) but have not received universal acceptance mainly because of the significantly lower flux of protons detected by their PROTON satellite compared to the spectrum suggested by less direct means. However, Hillas, (1975) points out that some recent determinations of the spectrum suggest intensities closer, than earlier values, to the 'Grigorov' spectrum. The least certain part of the primary spectrum is the region around  $10^{15}$  eV per nucleus where the flux deduced from air shower measurements is higher than either the flux suggested by Grigorov or from indirect muon studies. The underground multiple muon studies by the Utah group (Elbert et al., (1975)) have

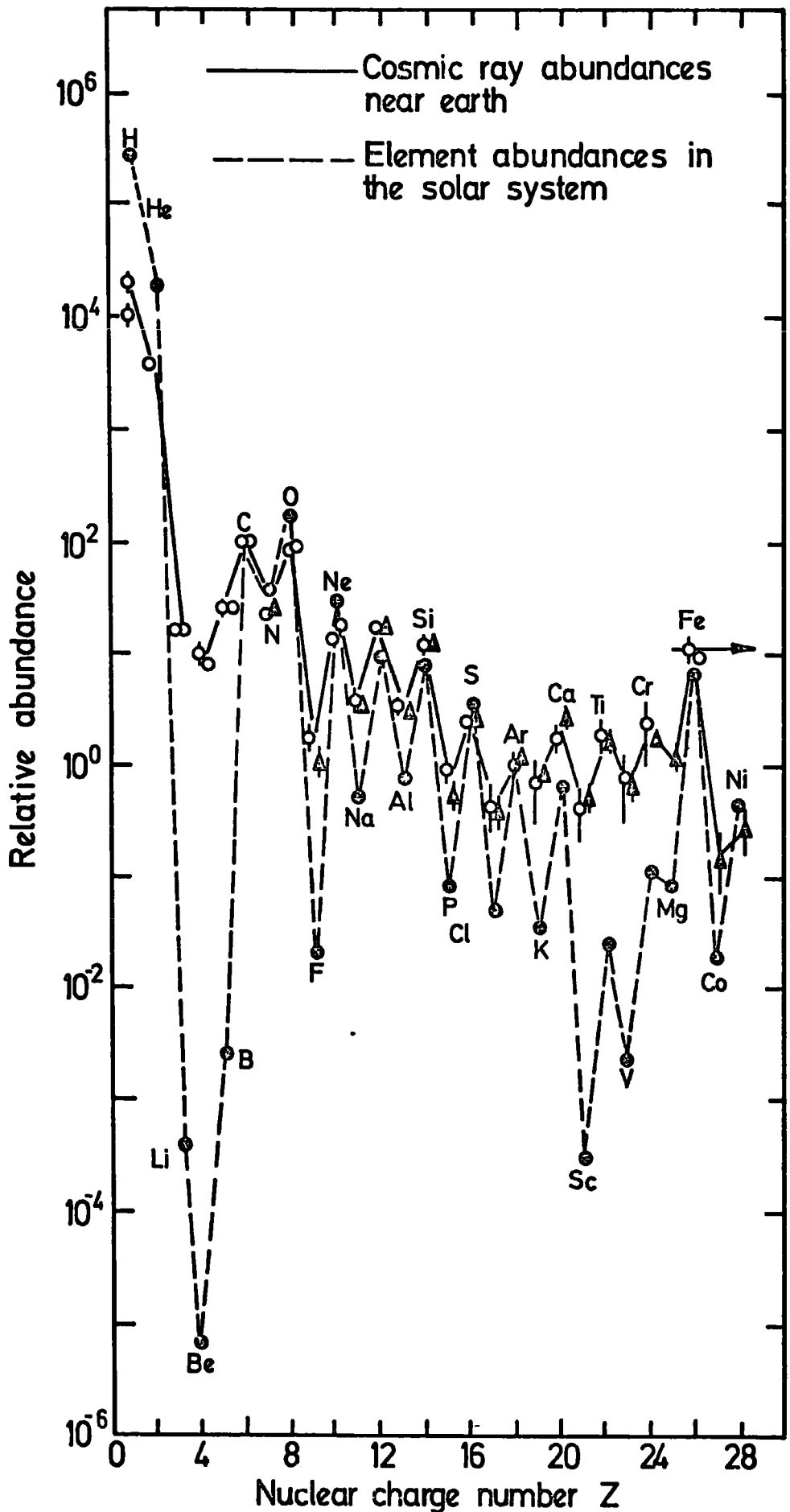


Figure 1.1. Relative abundance of the elements from hydrogen to the iron group normalized to that of carbon (C=100) (After Meyer et al., 1974)

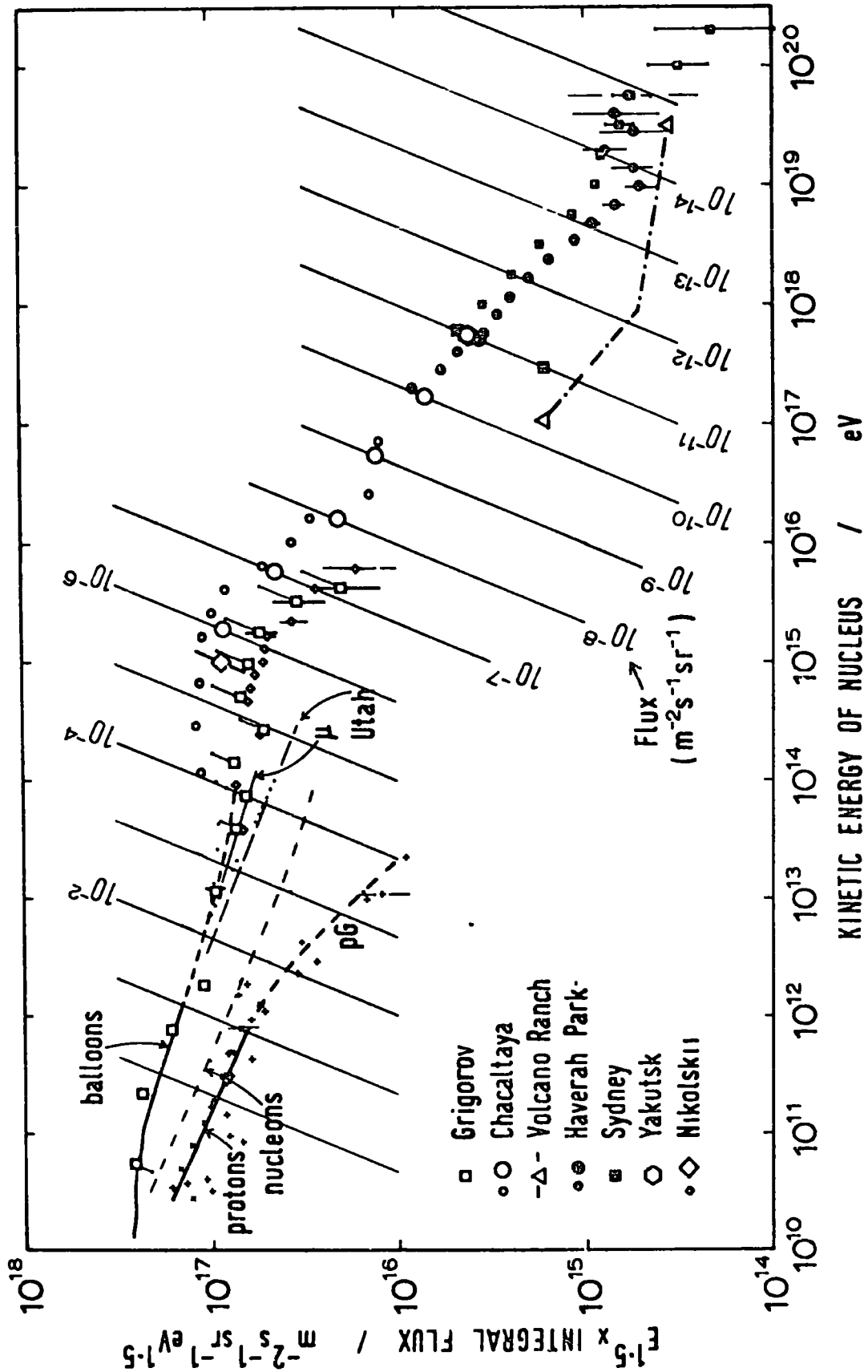


Figure 1.2 The integral energy spectrum of primary particles.  
(After Hillas, 1975)

led these workers to suggest that primary nuclei of energies up to  $10^{14}$  eV per nucleon are responsible for the muons they detect. Some latter calculations, as reported by Hillas, (1975) suggest that nuclei heavier than protons produce the muons, thus at  $10^{14}$  eV per nucleon the proton flux is somewhat reduced, but the helium and heavier nuclei are considerably increased relative to an extrapolation from  $10^{11}$  eV per nucleon. The line marked  $\mu$  in Figure 1.2 is drawn to continue the primary spectrum with a slope of  $\gamma = 2.7$  beyond  $10^{12}$  eV. This is concluded from a summary of many muon spectrometer experiments, (Ng et al., 1973) as reported by Hillas, (1975) and does not indicate a steepening of the proton spectrum up to about  $4 \times 10^{13}$  eV. Bell, (1976) suggests that the latest primary spectrum determined from measurements of the largest showers detected by the Sydney array agree well with the steepest spectra quoted by the Haverah Park and Chacaltaya groups and has a differential slope of  $-3.35 \pm 0.15$ .

The origin of cosmic rays remains uncertain but the bulk of the particles are not of solar origin, and the effects of propagation from the source or sources, have proved difficult to unravel. In a conservative model the energy spectrum has been interpreted such that 3 regions of the spectrum, from particles of energy  $10^{11}$  to  $10^{20}$  eV are considered as the summation of 3 distinct processes. Below (at smaller energies)  $10^{15}$  eV the cosmic rays essentially diffuse through the spiral arms from galactic sources, and above the 'knee', which occurs at about  $3 \times 10^{15}$  eV, a reduction occurs because particles have started to escape from the galaxy as their orbits in the galactic magnetic fields become too large for containment. Beyond  $10^{18}$  eV a reduction in the spectral slope is seen as the eventual domination of a uniform background of universal cosmic rays. Recent reports of two groups who detect large air showers (Haverah Park; see Edge et al. (1973) and Sydney; see Bell, et al., (1974)) no longer indicate a flattening of the spectrum beyond  $10^{18}$  eV, but uncertainties must still exist about the conversion from density measurements to shower size and the subsequent estimation of the primary

energy. For the actual sites at which the cosmic ray particles are accelerated and receive their energy, Colgate, (1966) suggests that supernovae could provide an acceleration mechanism to give an abundance of elements, up to iron, similar to that observed in cosmic rays. Ostriker and Gunn, (1969) suggest that if pulsars are rapidly rotating neutron stars then they may provide an adequate acceleration mechanism for very high energy cosmic rays. Kempa, et al., (1974) suggest the possible existence of a definite 'bump' in the primary spectrum in the range of  $10^{13}$  to  $10^{16}$  eV per nucleon. Karakula, et al., (1974) suggest that this may be due to cosmic rays from galactic pulsars superimposed on a normal background. However, Elbert et al., (1975) make use of a model incorporating Feynman scaling for the secondaries produced by cosmic rays and suggest that a bump of the prominence proposed is inconsistent with multiple muon rates measured underground.

### 1.3 EXTENSIVE AIR SHOWERS

The primary cosmic rays that enter the atmosphere interact strongly with the components of an air nucleus, and a large number of secondary particles are produced in the process of multiple production. At an incident proton energy of  $10^3$  GeV an average of about 20 secondaries are produced. These are mainly mesons of which the majority are pions produced in equal numbers of both charges ( $\pi^+$ ) and neutrals ( $\pi^0$ ). For high energy primary particles the secondary particles are energetic enough to interact with further air nuclei lower in the atmosphere and an extensive shower of particles is produced. If the primary energy is greater than about  $10^{13}$  eV the effect of this multiplication of the cosmic ray 'signal', can be detected at sea level where the particles observed are some thirteen generations removed from the primary. The  $\pi^0$ 's produced in the initial and secondary interactions decay promptly in about  $10^{-15}$  s to two gamma-rays which produce electron positron pairs by pair production. These relativistic electrons produce

further  $\gamma$ -rays by bremsstrahlung. These  $\gamma$ -rays then produce further electrons, and the shower of particles resulting is known as an electromagnetic cascade. This is constantly rejuvenated by  $\pi^0$ 's from the hadronic core of the air shower. The majority of particles in air showers are these cascade electrons which spread out over large areas, deviated mainly by coulomb scattering. Air showers are usually referred to and studied according to the electron 'size', which is the number of electrons above some threshold energy at the depth of detection in the atmosphere. The number of electrons at sea level from any given energy of primary will depend upon statistical fluctuations mainly due to the height (or depth into the atmosphere) of the first interaction, and will also depend upon the mass (and therefore the extent of fragmentation) of the primary. At shower maximum an approximate relation of

$$E_{\text{primary}} = 2 \cdot 10^9 N_{\text{max}} \text{ GeV} \quad (1.1)$$

holds, where  $E_{\text{primary}}$  is the energy of the primary particle and  $N_{\text{max}}$  is the number of particles at shower maximum (Clark et al., (1958)). However, for practical measurements at sea level, the total number of electrons in an air shower is determined by measurements of the density of electrons at different points in the shower, and then evaluation by reference to a structure function. The lateral structure determined empirically and theoretically appears to be a characteristic of air showers largely independent of the size of the shower. Good agreement is found with experiment (Greisen, 1960) with the form of the radial density ( $\rho$ ) for a pure electromagnetic cascade (Nishimura and Kamata, (1950), (1951), (1952),

$$\rho = \frac{N}{r_1^2} f(s, r/r_1) \quad (1.2)$$

where  $N$  is the size,  $r$  the perpendicular distance from the shower centre,

which is characterised by a high density of electrons and a high concentration of nuclear-active particles, and  $s$  is the age parameter, and  $r_1$  the Moliere unit.

The charged pions produced in air showers either interact to continue the nuclear-active cascade or decay to muons. High in the atmosphere even high energy pions (greater than about 10 GeV) that are time dilated have a finite chance of decay to muons because of the relatively low density. Lower in the atmosphere the probability of interaction with an air nucleus increases considerably. Once produced, the muon component largely survives to sea level, because not only do muons have a longer lifetime of about  $2 \mu s$ , which is considerably dilated because of the relativistic energies involved, but they do not interact strongly. The effects of coulomb scattering and geomagnetic deflection on the muon trajectories are relatively small; so that the muon component on the whole retains far more information about the region of the production of the parent pions than the electron-photon component. The competition between decay and interaction of the pion is influenced by the angle of incidence of the particle. This is because the density per unit path length decreases at large angles and hence the decay probability is effectively increased and more pions (and kaons) decay to muons. Thus a ' $\sec \theta$ ',  $\theta$  = zenith angle, enhancement occurs at large angles. As the energy of the muon increases the cross-section for nuclear interaction increases and at low muon energies the probability of decay to an electron increases.

#### 1.4 SCOPE OF THE PRESENT WORK IN RELATION TO SOME CURRENT PHYSICAL PROBLEMS

It has been emphasised through the study of cosmic rays and the use of particle accelerators that to physically probe smaller distances, higher energies must be employed; if an energy smaller than the binding energy is transferred to a composite system it will recoil elastically and remain as

as a whole. Attempts to resolve the structure of the proton have involved the highest energy particles that have been accelerated by machines, and the even higher energy particles available in the cosmic radiation. Much current theoretical and experimental effort has followed the suggestions of Gell-Mann,(1962) and Ne'eman,(1961) that all hadrons may be composed of 3 fundamental constituents, which Gell-Mann,(1964) called quarks. This model assumes that the observable hadron properties are due to the added contributions of the individual quarks, such as charge, where the proposed non-integral charge of the quarks always must add up to give the observed integral charge of hadrons. This constituent quark model succeeds in supplying a good description of hadron spectroscopy, and attempts to explain the electromagnetic and weak currents as a coupling to individual quarks, where the coupling to hadrons is the sum of the contributions of the individual quark couplings. However, even though the free quark has remained unobserved (see for instance Ashton and Saleh, 1975) the deep inelastic collisions of leptons on protons (electron experiments at the Stanford linear accelerator, SLAC) and neutrino proton experiments (at the European Organization for Nuclear Research, CERN) suggest that to a first approximation the electric and weak charges of the nucleon are concentrated on three small 'centres'. (See G. Altarelli,(1974) and Lipkin,(1973) for reviews). These centres, which can possibly be identified with the postulated quark, appear to have an energy distribution such that the mean is about 1/6 of the nucleon energy. Thus one half of the total nucleon energy may be neutral (that is without electric or weak charge) and associated with the very strong field which binds these centres together inside the nucleon. In this constituent-quark description baryons are composed of three quarks and mesons are single quark-antiquark pairs.

In some contrast the parton model of the hadron, due to Feynman,(1969) (1969a) describes the hadron as consisting of a very large number of point-like constituents, and a possible interpretation is that the parton is the so-called current quark. The current quark model is used with an extreme

relativistic approximation in the frame where the hadron is moving with infinite momentum and like the parton model describes the hadron as consisting of a very large number of point-like constituents, (quark-anti quark pairs) as well as three current quarks and some neutral "glue". Feynman postulates a specific spectrum of soft or "wee" partons in the form of a distribution. He defines wee as typically a momentum of 1 GeV or a fraction  $f$  ( $f \sim 1 \text{ GeV}/c / P$ ) of the nucleon momentum ( $P$ ) and suggests they are responsible for the hadronic cross-section, whilst the "hard" partons are seen in the deep inelastic processes. Feynman's scaling hypothesis is that when expressed in terms of the transverse momentum ( $p_t$ ) in absolute scale, and the longitudinal momentum in relative scale,  $x = \frac{p_L}{P_{Lmax}}$ , the inclusive distribution of fragments produced in an interaction has a definite limit as the longitudinal energy producing those fragments goes to infinity. This is based on the parton model of the hadron and if demonstrated to be true in high energy collisions will have consequences for successful descriptions of the hadronic state of matter.

The current situation is that partial confirmation of scaling has come from the intersecting storage rings which collide protons at a centre of mass energy of up to about 62 GeV. The violation of scaling, near  $x = 0$  only, at this energy may reflect some fundamental violation of scaling or that the asymptotic region has not been reached. Information from higher energies is required to resolve this problem and to test the continuation of scaling for  $x > 0$ . Attempts to predict the distribution and energy spectra of the components of extensive air showers, have met with some success when the CKP model of secondaries produced in high energy collisions is used. (See for a current review Grieder, (1976)). This model was originally based (see de Beer, et al., (1966)) on the suggestions of Cocconi, Koester and Perkins, (1961) who studied the characteristics of the secondaries from high-energy interactions of protons with light nuclei. (For a more up-to-date version, see Cocconi, (1971)). However, the two fireball approach of this model is ruled out by

the ISR data because although the predicted separation of forward and backward centre-of-mass fireballs of produced pions is seen, there is also a central production of pions that is not predicted. The continued use of this model is, however, possibly justified as it represents models that predict a higher multiplicity of secondaries in interactions than the scaling model.

The present work relates to the muon component of air showers and coincident muon pairs both associated with and without an air shower. The range of shower sizes involved is from about  $5 \cdot 10^3$  to over  $10^7$  particles and muons are detected above a threshold momentum of about 6 GeV/c up to a maximum detectable momentum of over 3000 GeV/c. The data has been collected and analysed in an attempt to compare the results with the predictions of the scaling and CKP models in relation to very high energy muons in small air showers.

The existence of the muon and the role it plays in the structure of matter has remained a mystery for over 30 years. It is identical to the electron in all ways except that it is about 200 times as massive, and decays. However, 'muon number', possessed by the muon and its neutrino only, is conserved, and radiative decay of the muon into the electron has not been seen to occur.

Thus



However the muon's properties render it a suitable conveyor of information from high energy interactions of cosmic rays high in the earth's atmosphere.

The acquisition of the data related to both the muon and electron component of air showers and the unassociated muon pairs has taken place

alongside and as secondary experiments to the determination of the unassociated muon momentum spectrum by the spectrograph and the determination of the shower size spectrum by the air shower array. In this context this thesis is an account of the collection and analysis of data, and its interpretation, in the light of biases necessarily present in the apparatus during its collection.

## CHAPTER 2

### THE SPECTROGRAPH AND AIR SHOWER ARRAY

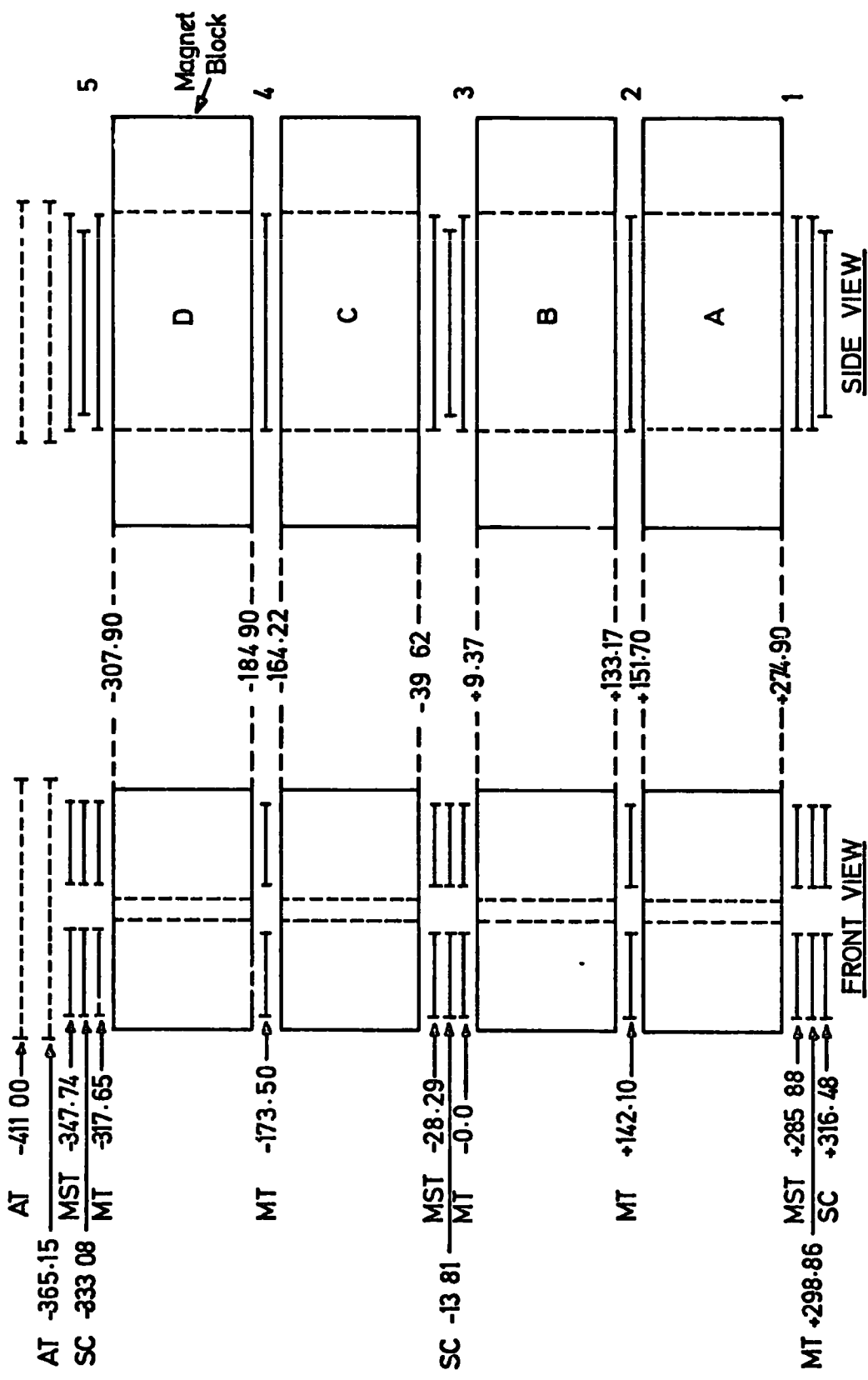
#### 2.1 INTRODUCTION

In this chapter an overall view of the M.A.R.S. spectrograph and S.A.R.A. air shower array will be given and attention will be paid to the details of the apparatus that are relevant to the present work. Construction of the spectrograph began in 1968, and since then experiments to study many aspects of cosmic ray muons have been performed. (The muon interaction asymmetry, Hamdan, 1972, Grupen et al., 1972 ; the absolute rate of energy loss by muons in Iron, Wells, 1972, Ayre et al., 1971 (a) ; the Muon momentum spectrum to 800 GeV/c, Whalley, 1974, Ayre et al., 1975 ; the Muon charge ratio, Hume, 1975, Baxendale et al., 1975 ; Muon burst spectra in iron, Hansen, 1975, 1975 (a), 1976, and the momentum spectrum above 300 GeV/c, Piggott, 1976, Baxendale et al., 1975).

Work on the air shower array was started in 1973 and measurements of the shower size spectrum and rates of high energy muons in air showers are taking place. For a complete description of the spectrograph see Ayre et al., 1971, 1972 (a), 1972 (b), and Thompson and Wells, 1972, and of the array, see Smith 1976 and Rada et al., 1977, and Smith and Thompson, 1977.

#### 2.2 GENERAL DESCRIPTION OF M.A.R.S. (Magnetic Automated Research Spectrograph)

Figure 2.1 shows the front and side view of the spectrograph. The muon spectrograph is over 7 m tall and consists of four 71 ton solid iron electromagnets of toroidal design interleaved with particle detectors. The magnets deflect the muon's trajectory as it passes down through the spectrograph and the detectors locate its position at the different levels. Each magnet block, being a toroid, has the field in opposite sense in each



All dimensions are given in cm and are accurate to 0.1cm.

MST Momentum Selector Tray  
 MT Measuring Tray  
 SC Scintillation Counter

Figure 2.1. The MARS Spectrograph.

half and hence the spectrograph is divided into two symmetrical arms. The arms or halves are referred to as the blue (Eastern) side and red (Western) side. In both arms the particle detectors are of two basic types : scintillation counters and neon flash tubes. The 'scintillation counters' are slabs of scintillating material viewed by four photomultiplier tubes and the 'flash tube trays' contain a stack of neon flash tubes interleaved with electrodes. The neon flash tube, introduced by Conversi and Gozzini, (1955), discharges (or flashes) after the passage of an ionizing particle through the neon contained within the glass tube and the subsequent application of a high voltage ( $\sim 10$  KV) pulse. The trigger for the spectrograph to register and store data relevant to a muon event is provided by the coincidence of pulses from the scintillation counters placed at levels 1, 3 and 5 on both sides. The track location is provided by large diameter ( $\sim 1.5$  cm) flash tubes in trays at levels 1, 3 and 5 (the momentum selecting system) on the blue side and small diameter flash tubes ( $\sim .55$  cm) in trays at levels 1,2,3, 4 and 5 (the momentum measuring system) on both sides. (Figure 2.1).

Two modes of operation of the spectrograph have been used during the present experiment. Firstly, with the blue side operating independently the trigger condition is a coincident pulse from the 3 blue side scintillation counters. The momentum selector trays have a H.T. pulse applied ('pulsed') and information from the tracks in these trays is used electronically to determine whether the particle detected is of high momentum (in this case  $P_{\mu} > 100$  GeV/c) or not. If this condition is fulfilled then the five blue side measuring trays are pulsed and the track information from them sent to an on-line I.B.M. 1130 computer. Thus, rejection of low momentum events takes place and only potential high momentum data is stored for later analysis. Secondly, with the red and blue side operating together, the trigger requirement is that of coincident pulses from all six scintillation

counters in the spectrograph. This causes all ten measuring trays to be pulsed directly, without reference to the momentum selecting system. The track information from the five blue side trays is stored by the computer as before whilst the five red side measuring trays are photographed to provide a permanent record of which tubes flashed. The five trays on each side of the spectrograph enable measurements of the trajectory of muons to be made even if accompanied by air shower particles which obscure the muons track in the top measuring tray. Electromagnetic interaction of the muons in the iron blocks may also result in the obscuring of a measuring tray due to the electrons that accompany the muon out of the block.

These two modes of operation represent two independent experiments that can be run at the same time due to the low rate of collection of events for both. The former mode, the measurement of the rate of high momentum muons, was in operation from August, 1973, until May, 1976 during which time the only major alteration was the change from a Mk I momentum selector system to the Mk II system (see section 2.2.4). The latter mode, the measurement of the rate of coincident muon pairs, was in operation in conjunction with the former from September 1975 until May 1976. (see Figure 2.16).

The various parts of the spectrograph are now considered in more detail.

### 2.2.1 THE MAGNETIC FIELD

Each rectangular magnet block (3.66 m long, 2.13 m wide, 1.25 m high) is made up of 78,  $\frac{1}{2}$ " thick iron plates with a slot cut out of the centre (Figure 2.2). Wound around each arm of the resulting toroid is 4 swg copper wire. The coils on blocks A, B, C and D, bottom to top, (Figure 2.1) are wired such that the coils on B and D are in series and those on A and C are in series and each of these pairs are in parallel. The toroidal shape ensures a maximum magnetic flux density as the field is largely contained within the iron and necessarily the sense of the field is opposite in the

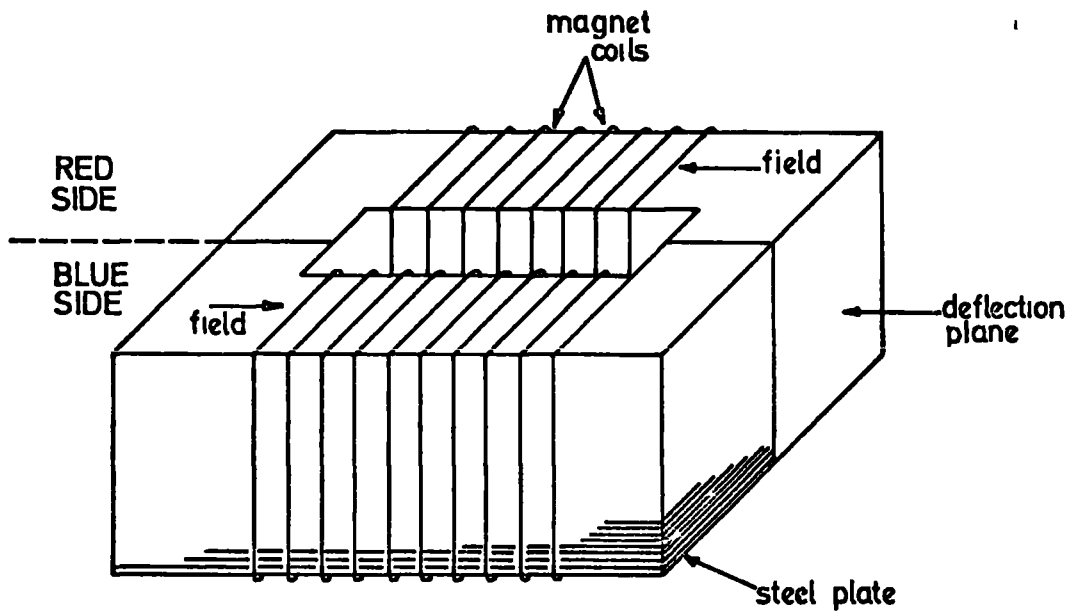


Figure 2.2. Schematic diagram of a magnet block.

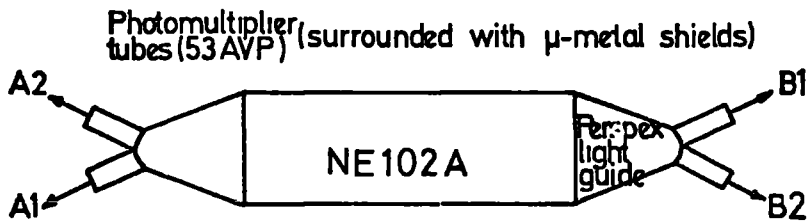


Figure 2.3a. Plan view of a scintillation counter.

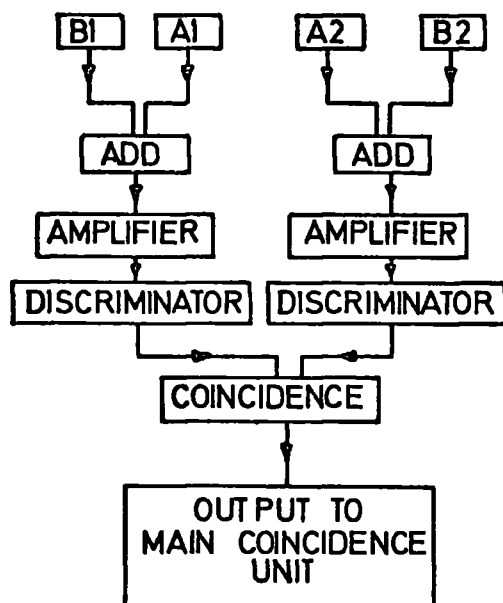


Figure 2.3b. Sequence of events following the passage of any charged particle through a scintillation counter.

two halves of the block. A 100 amp at 100 volts unstabilised D.C. supply feeds the combined resistance of 1 ohm of the total windings. The resultant field is  $16.3 \pm 0.1$  k gauss. The variation of the supply voltage and the non-uniformity of the field in the 'sensitive' volume of the block is estimated to lead to an error on the field of  $\pm 1\%$  k gauss (Whalley, 1974).

### 2.2.2 THE SCINTILLATION COUNTERS

The scintillator material (NE 102A), light guide and 4 photomultipliers, which constitute this type of detector, are contained inside a light tight aluminium box and are shown schematically in Figure 2.3a. The output pulses from diagonally opposite pairs of photomultipliers are added and after being amplified and discriminated, are fed into a coincidence unit with the other pair. (Figure 2.3b). A pulse results when a particle deposits enough energy in the material to pass the discrimination level set. The usual technique of gating a pulse height analyser with the output pulse from a 'telescope' placed above the scintillation counter was used to set the discrimination level. The output pulses from the 6 scintillation counters are fed into the main coincidence unit where the rate of coincidence between several different combinations of counters is continually monitored. A record of these rates is made every day to check the consistency of the counters. The measurement of the efficiency of the counters is discussed in Appendix H.

### 2.2.3 FLASH TUBE TECHNIQUES

A full description of the use of flash tubes in M.A.R.S. is given by Ayre (1971) and Ayre and Thompson (1969), and a more general review of their use in particle physics is given by Conversi (1973). In principle the flash tube is a long thin neon filled glass tube sealed with a flat end that is placed between two electrodes. If, within a few microseconds

of the traversal of a tube by an ionizing particle, a high voltage pulse is applied to the electrodes, the tube will discharge with the characteristic neon (red) colour suitable for photography. However, Ayre and Thompson (1969) discovered that it was possible to digitise the information from a flash tube by picking up the electric field associated with the discharge on a small brass probe connected electrically to an integrated circuit logic element memory. All the flash tubes in the trays on the blue side of the spectrograph are digitised in this way ; each tube having its own memory. The high voltage pulse applied to the electrodes of the flash tube trays is produced by discharging a delay line across a resistor. Each flash tube tray has its own delay line. The spark gaps used to discharge the delay lines for the measuring and momentum selecting trays are independent. Typically, negative, about 6 KV, rectangular pulses of duration about 3  $\mu$ s are used to ensure a sufficient discharge to set the tubes' memories via the probes. Slightly less field is needed to cause sufficient discharge for an accurate photographic record.

#### 2.2.4 THE BLUE SIDE MOMENTUM SELECTOR TRAYS AND ASSOCIATED LOGIC

The three blue side momentum selector trays consist of four layers of flash tubes (diameter  $\sim$  1.5cm., length  $\sim$  2 m.) arranged in a staggered pattern. (Figure 2.4). Between each layer of tubes are the earth and high voltage electrodes and in front are the digitising probes and memory logic. Each memory that is set corresponds to a discharged tube. The tray front is divided into 152 cells 0.5 cm wide ; each of which correspond to certain combinations of memories set, that is, certain combinations of tubes having discharged. This is achieved by a series of coincidence and anticoincidence gates through which the pulses from the 'set' memories pass. The cells that are allocated for different combinations of tubes discharged is hard-wired into the system. The logic was decided upon studying the response of arrays

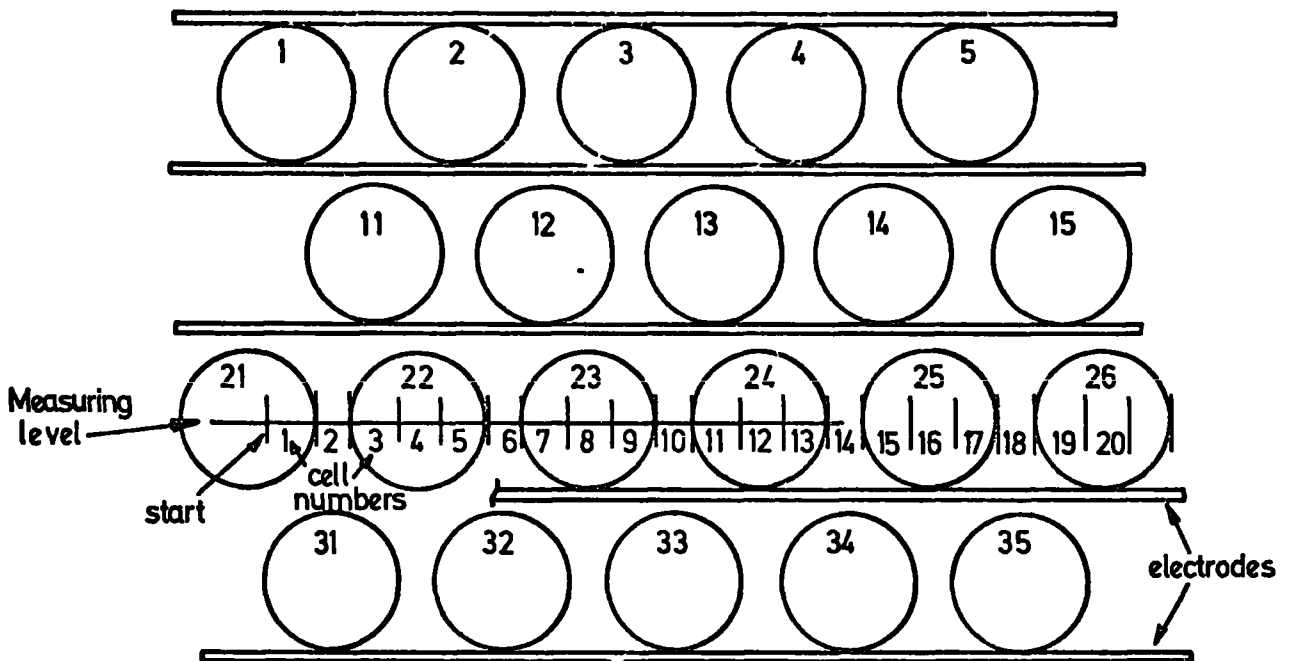


Figure 2.4. Schematic view showing momentum selector tray tube pattern and position of cells and electrodes.

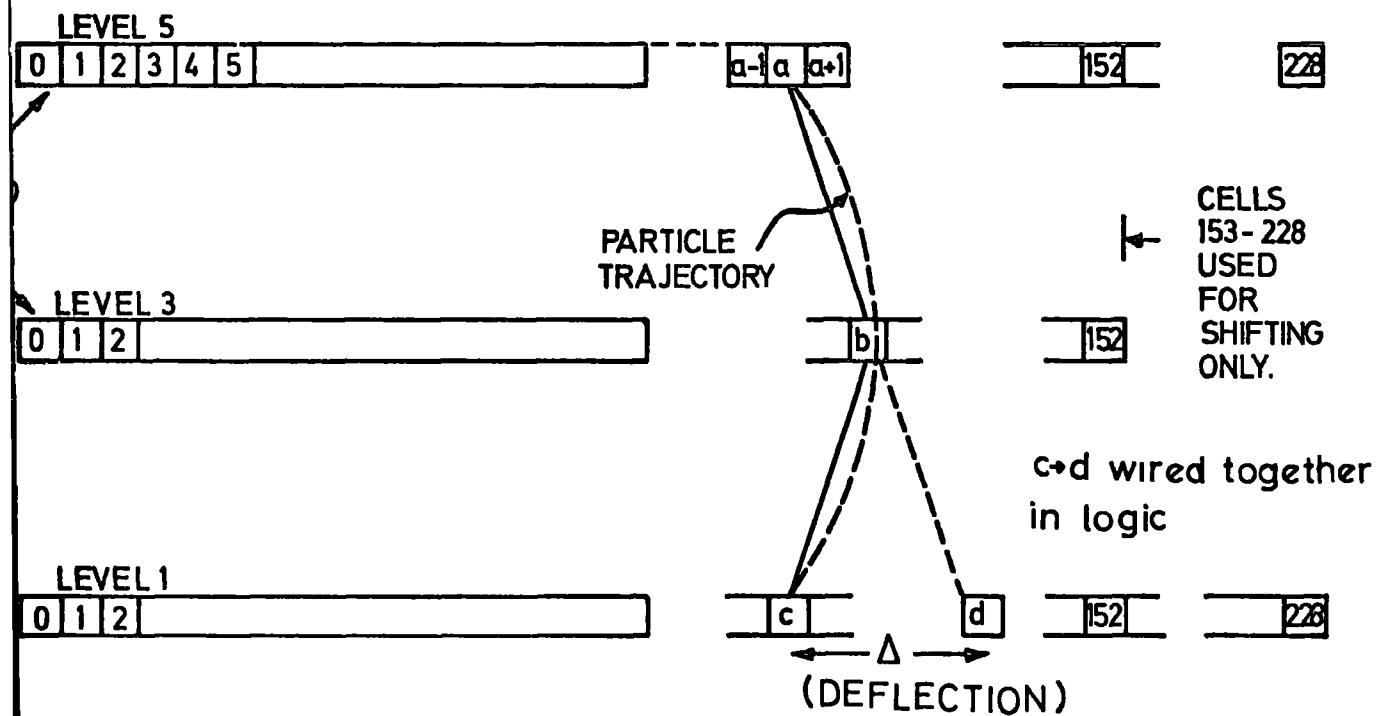


Figure 2.5. Principle of operation of Mk.1 momentum selector.

of flash tubes to particles arriving at up to  $\pm 7^\circ$  to the vertical. Any inherent wrong celling is allowed for by a subsequent overlapping of cells by the momentum selector logic, (Ayre, 1971). The original momentum selector, the Mk I, had 3 shift registers, one for each tray, in which each 'bit' corresponded to a cell on the tray front. After the passage of a particle and the pulsing of the tray a 'read' pulse sends data to the momentum selector shift register bits. A clock pulse at approximately 1MHz shifted the bits through a threefold coincidence circuit that represented all possible straight line configurations. The time for all possible combinations to be checked with this system was about 76  $\mu$ s, so that the measuring trays had to be pulsed at the same time as the momentum selector trays. This was because the flash tubes would be highly inefficient after the length of time needed to determine a high momentum combination. The Mk II momentum selector is a completely hard-wired device that enables a faster (about 1  $\mu$ s) determination of any possible high momentum combination of cells. Here the pulses that are gated down from the three tray fronts pass simultaneously through a series of threefold coincidence gates. A total of 6  $\mu$ s delay occurs after which the measuring trays are pulsed only if a high momentum combination is found. The different combinations of OR'ed cells for the Mk II momentum selector are shown in Table 2.1. The effect of a large number of particles passing through the momentum selector tray at level 5, as will happen when the core of an air shower falls nearby, is considered in Chapter 3. The principle of operation of the Mk I momentum selector is shown in Figure 2.5 and the correspondence between cells and flash tubes is shown in Table 2.2.

#### 2.2.5 THE BLUE SIDE MEASURING TRAYS

The five blue side measuring trays each have eight layers of flash tubes ( $\sim$  0.55 cm. diameter and  $\sim$  2m. long) with 89 tubes in each layer.

ORIGINAL CELL NUMBERS AND NEW GROUP NUMBERS  
FOR THE MKII MOMENTUM SELECTOR

CELL	A,B	C
1	1	1
2	1	1
3	1	1 and 2
4	1 and 2	1 and 2
5	2	1 and 2
6	2	2 and 3
7	2 and 3	2 and 3
8	3	2 and 3
9	3	3 and 4
10	3 and 4	3 and 4
11	4	3 and 4
12	4	4 and 5
13	4 and 5	4 and 5
14	5	4 and 5
15	5	5 and 6
16	5 and 6	5 and 6

(A,B and C represent levels 5,3 and 1 in logic system.)

TABLE 2.1

THE CORRESPONDENCE BETWEEN CELL ALLOCATED AND TUBES DISCHARGED

CELL No.	LAYER			
	1	2	3	4
	TUBES DISCHARGED			
1	1		21	31
1	1	11	21	31
1	1		21	
2	1	11		31
2		11		31
2	1			31
3	1	11	22	31
3		11	22	31
3	2	11	22	31
4	2	11	22	
4		11	22	
4		11	22	32
4	2	11	22	32

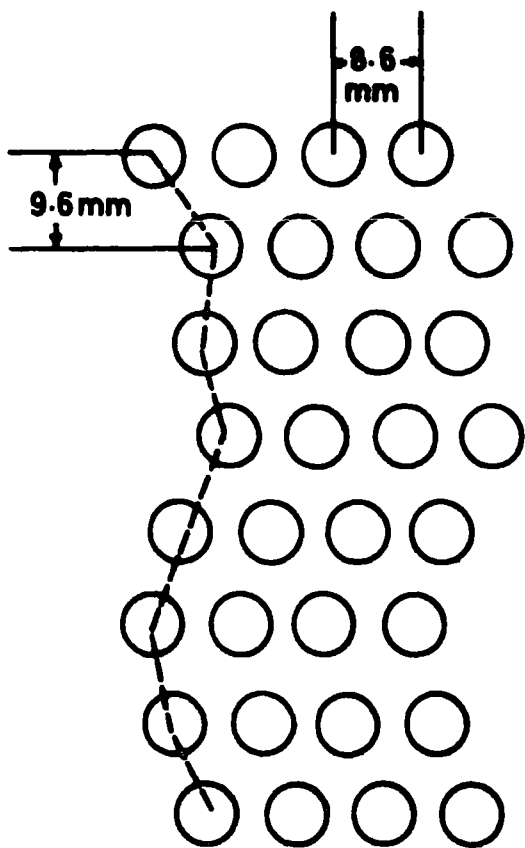
TABLE 2.2

The stagger pattern is shown in Figure 2.6, and is designed to have a uniform response to particles passing through at up to  $\pm 8^\circ$  to the vertical. For 100% efficient tubes the mean number discharging per vertical track is about 5.2. In a similar fashion to the momentum selector trays each tube has a probe and memory. The memories are grouped electronically in the same configuration as the flash tubes and are designated a number 2 to 90, whilst numbers 1 and 91 to 96 are used as 'dummy' columns by the controlling logic. The logic on the tray front supplies a column number followed by the tube pattern that has discharged. The data readout from these trays is automatic after the flash tube tray has been pulsed and proceeds via a core store (1024 x 8 bit word store) to an on-line I.B.M. 1130 computer. Data is stored in the core store in a predetermined sequence and alongside each event's data is information regarding the conditions under which the event was collected. This information is ; the trigger mode ; the event number ; the time; the date; the geiger counter information (see Section 2.2.7) ; the atmospheric pressure ; the field direction ; which comprises the event header. This is followed by the tube pattern information for just those tubes in each tray that have discharged. When this sequence is complete the computer reads the data from the core store to a file on a magnetic disc. An example of the format of this data as printed out by the computer is shown in Figure 2.7.

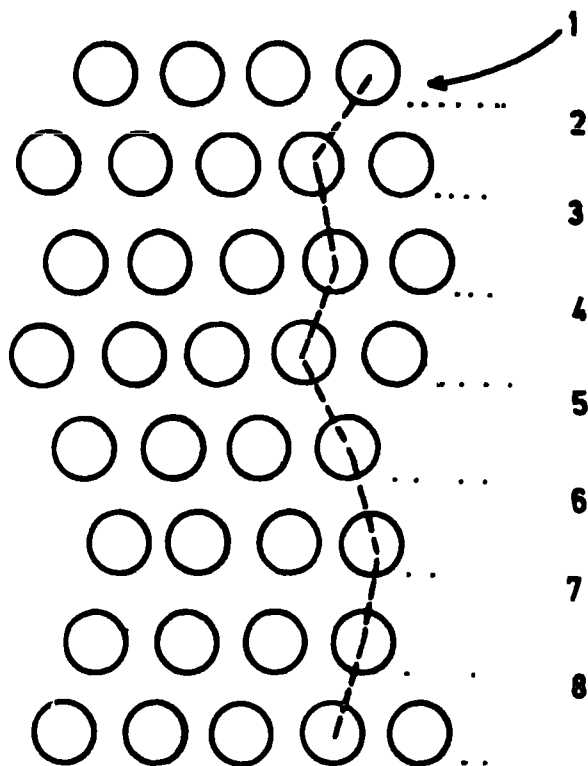
#### 2.2.6 THE RED SIDE MEASURING TRAYS

The tubes in the five red side measuring trays are not digitised but are photographed by two cameras which view the trays through a system of mirrors (Figure 2.8). The red side trays are only used in an experiment which has a data collection rate of one event in about 16 minutes, corresponding to about 50 events in an overnight run. At this rate, scanning of film is practicable and so it was not considered appropriate to digitise the red side





The Blue side measuring tray stagger pattern.



The Red side measuring tray stagger pattern.

Figure 2.6.

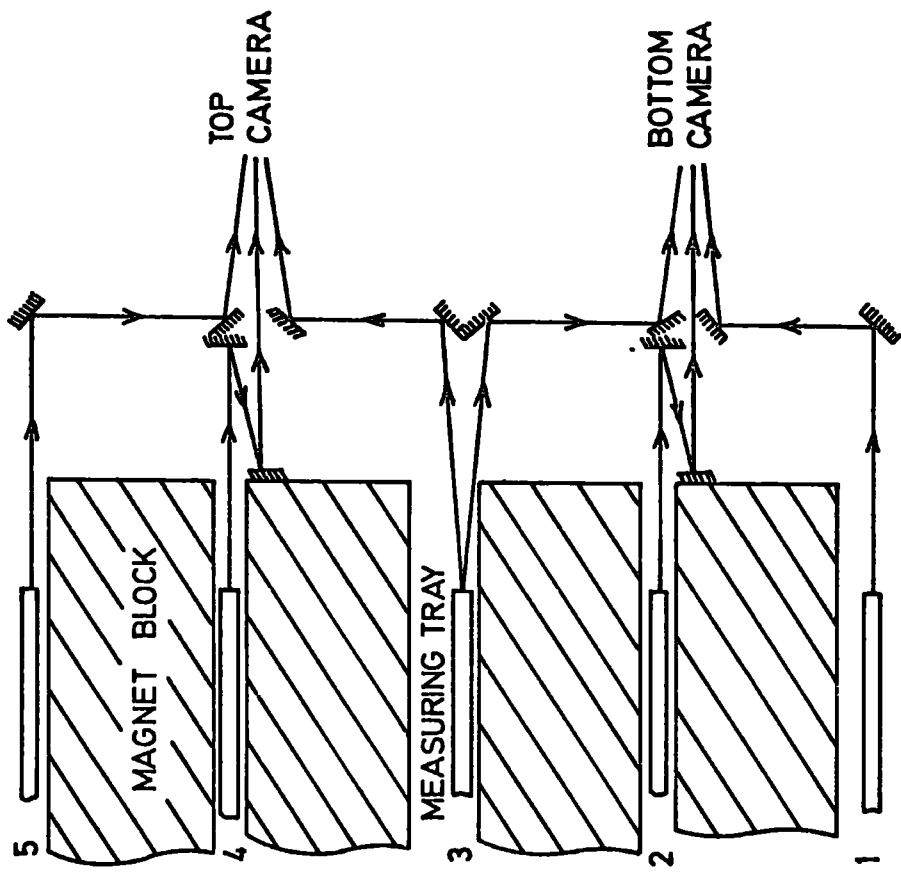


Figure 2-8. The mirror system for the red side measuring trays.

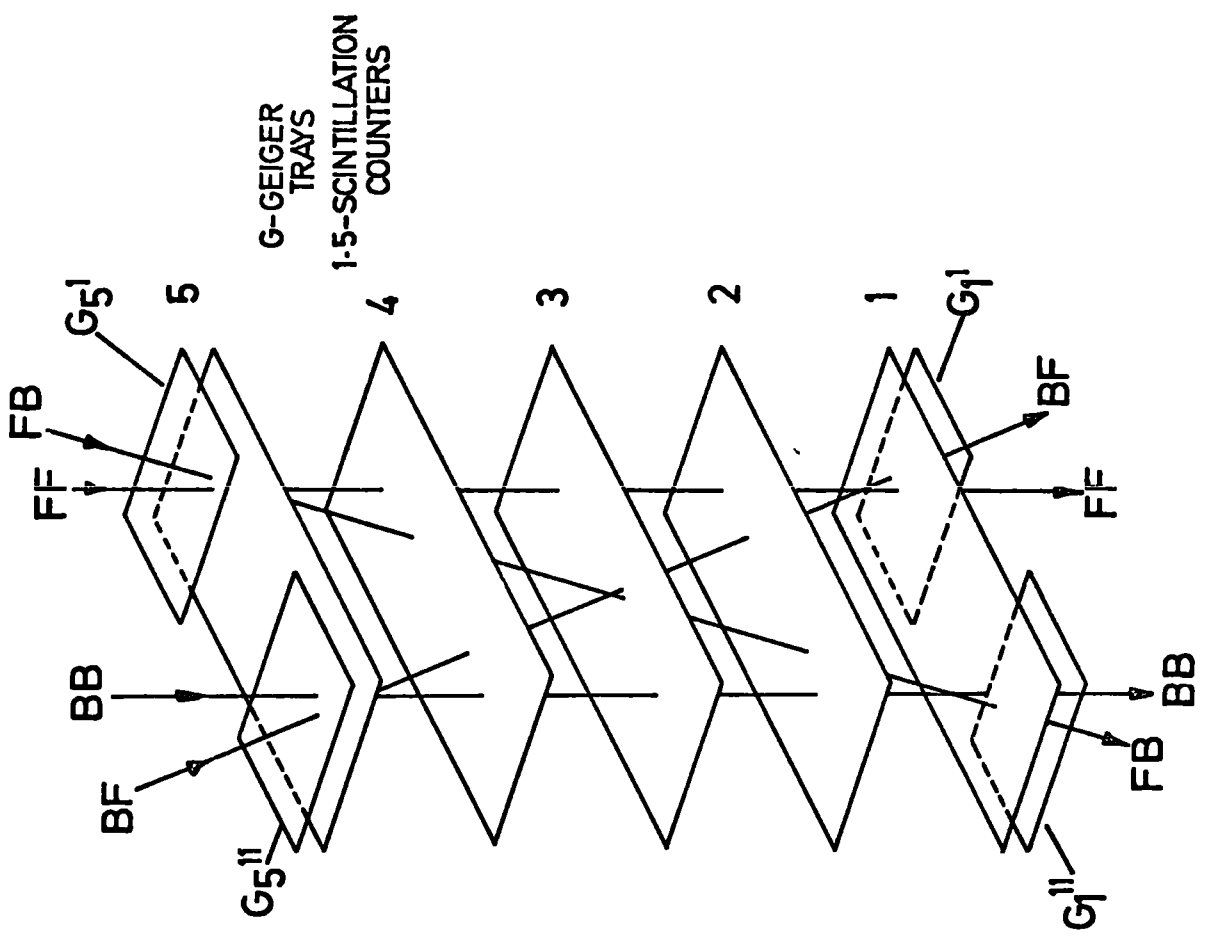


Figure 2-9 The geiger tray positions on the blue side.

flash tubes. However, the trays are pulsed in the same way as the blue side trays, and the stagger pattern of the tubes is the mirror image of the blue side pattern as can be seen in Figure 2.6. The mirror system consists of two mirrors for each flash tube tray, all of the mirrors being front silvered to keep distortion and loss of focus to a minimum. The light emitted by flash tubes is strongly collimated (Coxell, 1961) consequently the cameras were set to view the tubes normally from a total path length of about 4.25 m. A 135 mm. focal length lens set at its maximum aperture of f/1.8 was used for both cameras and kept on open shutter whilst viewing the trays in a darkened laboratory. With this system a well defined image of any discharged tube was achieved upon projection of the film. Immediately after each event a clock, event number and a run number board displaying the date and field direction were illuminated in the field of view of the cameras. Also, fiducial lights were used so that when the film is scanned it can be projected onto a pattern of the tray front showing the tube positions in relation to the bulbs.

In order to make use of the track fitting programs developed for the digitised blue side data, an accurate pattern was made of the tubes that had discharged for each event and a code written on a coding form for punching onto a computer card. An example of this code is shown with the tube pattern in Figure 2.10 and an accurate tube pattern of a complete event is shown in Figure 2.11. A program has been written which converts this code into a form suitable for the analysis programs. Plate 1 is an example of an event recorded on the red side which coincides with the computer picture of the same event on the blue side, Figure 2.12. During a paralysis of 2s the next frame of the film is wound into the gate of the camera ready for the next event.

PATTERN DATA: 6276 6491  
 ↑            ↙            ↘            ↑  
 COLUMN        TUBE PATTERN

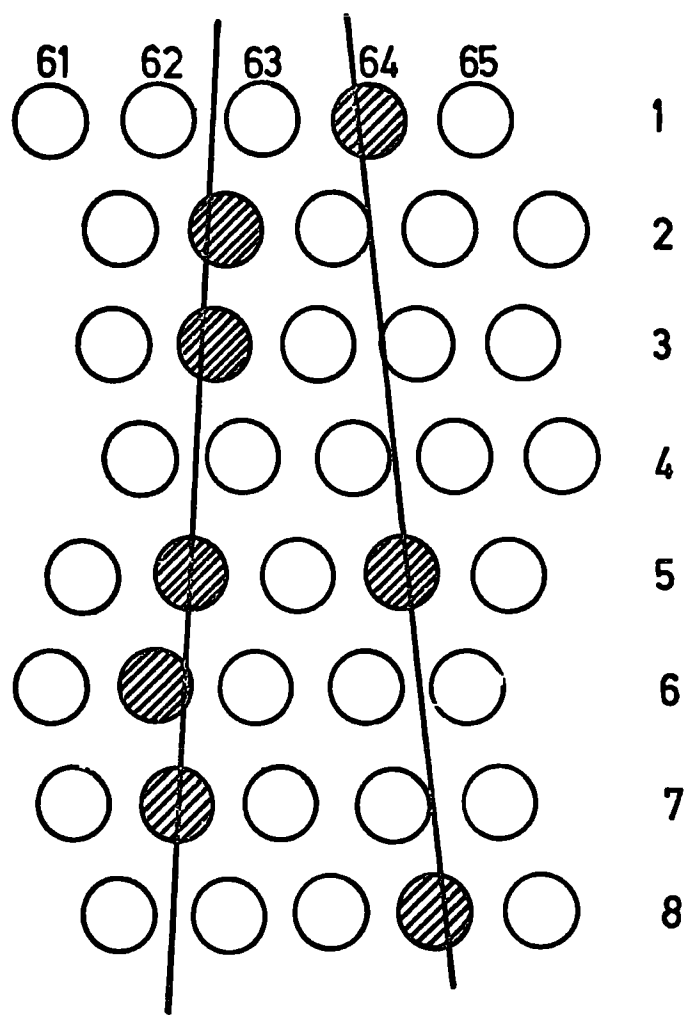


Figure 2-10. A muon event with an accompanying electron in a measuring tray presented with the computer pattern data.

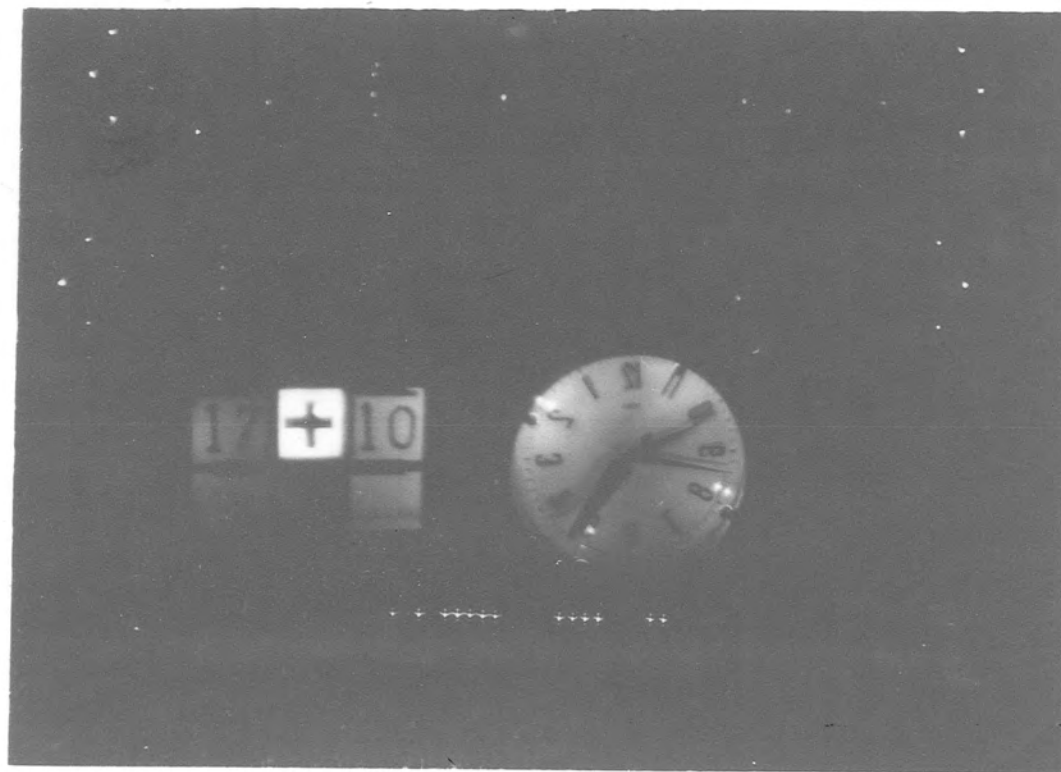


PLATE 1.

EVENT No. { 5751750  
5 7 C 3 C 6  
●●●|●●●|●●●|●●●|●●●|●●●

IE [2143] DATE [1711075] BLUE FIELD [ ]

Figure 2.11. An accurate reproduction of the event shown in Plate 1.



### 2.2.7 FLASH TUBE TRAY ALIGNMENT USING GEIGER TRAY INFORMATION

A correction for non-alignment of the mean position of the measuring trays vertically above one another is possible (during analysis) but skewness of the trays in relation to one another presents more difficulty. On the blue side initial alignment was achieved with a vertical plumb line, a square and a steel rule giving an estimated accuracy  $\pm 0.5$  mm. To assist further with the alignment Geiger-Muller (G.M.) tube trays were placed on top and below the spectrograph on the blue side (Figure 2.9). Four trays, two at the top and two at the bottom of the spectrograph supply pulses, on being traversed by an ionizing particle, which are put in coincidence with the trigger pulse from the 3 blue scintillation counters. This resulting coincidence, if any, is stored with the flash tube data as part of the event header information. With reference to Figure 2.9, it can be seen that particle trajectories that pass through all five measuring trays and one G.M. tray on the top and one G.M. tray on the bottom, can be defined as BB, FF, BF, or FB. Considering the situation of just one tray rotated about a vertical line through its centre with respect to all the others (i.e. skew) which are parallel, a track through the centre of this tray would appear straight but if it passed near one end of the misaligned tray it would appear as a curved trajectory. By considering the distributions of displacements of the position of the track as measured in any one tray compared with a straight line fit from the other trays (for a zero magnetic field situation) the alignment of the blue side trays was possible to better than 0.1 mm. and the skewness is less than  $\pm 0.2$  mm. over 133 cm. (Ayre et al., (1975)).

On the red side a more basic measurement of the tray position was relied upon. The method used for the blue side requires the analysis of many hundreds of events with the magnetic field reduced to zero. This would have been a time consuming process that was ruled out because of the need to

keep the field on in the spectrograph (for the high momentum spectrum determination taking place, using the blue side) at the time of completion of the red side. To measure the position of the red side trays as accurately as possible a steel rule was attached to the edge of the brass tray 'front' at both the front and back of the tray. The brass has been accurately drilled with holes to hold the tubes in position and determines the accuracy of flash tube location. A plumb line was then lowered to pass flush in front of the markings on the rule and was viewed with a travelling microscope. By this method it is estimated that the red side measuring trays were aligned to within  $\pm .25$  mm. and have a skewness of less than  $\pm 2.0$  mm. over 133 cm.

#### 2.2.8 THE ACCEPTANCE AND THE MAXIMUM DETECTABLE MOMENTUM OF THE SPECTROGRAPH

For one side alone the zero magnetic field acceptance approximates to a step function ; for muons with momentum greater than 7.2 GeV/c it has a value of  $408 \pm 2$  cm<sup>2</sup>. sr. and a value of zero for lower momenta. This corresponds to the minimum energy required (and lost) by a muon if it is to pass completely through the iron of the spectrograph and be detected at both extremities. The acceptance for pairs of coincident muons, both muons passing through one side, and one passing each side, will be considered in Chapter 5.

The maximum detectable momentum (m.d.m.) is defined as that momentum at which the uncertainty in the momentum of a particle is equal to the momentum of that particle. Using the method of Allkofer et al. (1971) and defining the particle path length in the magnetic field H gauss, as  $l$  cm, the m.d.m. can be written

$$300 \ l \ H / \Delta\theta \quad \text{eV/c}$$

where  $\Delta\theta$  is the rms uncertainty in the deflection of the particle, and is equal

to  $\theta$ , the magnetic deflection of the particle. Assuming a circular trajectory for the particle and an uncertainty in location of 0.3 mm. in a flash tube tray the m.d.m. for the five blue side measuring trays is calculated to be 5856 GeV/c, and for the four lowest trays, 3210 GeV/c. (Ayre et al., (1972)),

### 2.3 GENERAL DESCRIPTION OF S.A.R.A. (SHOWER AUTOMATED RESEARCH ARRAY)

In 1973 work began on an air shower array situated in the vicinity of the physics department in Durham. The stimulus for the array was helped by the presence of several other cosmic ray experiments in the Sir James Knott Laboratory. In the main, studies are undertaken on high energy muons and on hadrons for which details of the possible associated air shower could give valuable information about the true nature of the events. Placing the array, use was made of the physics building roof, as well as detector response considerations, resulting in an equilateral triangle geometry for the array. (Figure 2.13).

The design follows the pattern of placing detectors at many points in a large area to sample the shower particles at those points. The particle detecting elements of the array are 14 plastic scintillators viewed by photomultipliers. The area 'covered' is a circle of diameter 120 m. and the individual detectors range in size from  $0.75 \text{ m}^2$  to  $2.0 \text{ m}^2$ . The density of particles is measured at each detector and the relative time of arrival of the particles is measured by the 'fast timing' detectors. The parameters of the air shower thus obtainable are the electron size, the core location and the arrival direction of the shower front. The array responds to showers of size about  $5 \cdot 10^4$  to about  $10^7$  particles at sea level. The physical closeness of a building to the detectors limits successful analysis to showers falling within

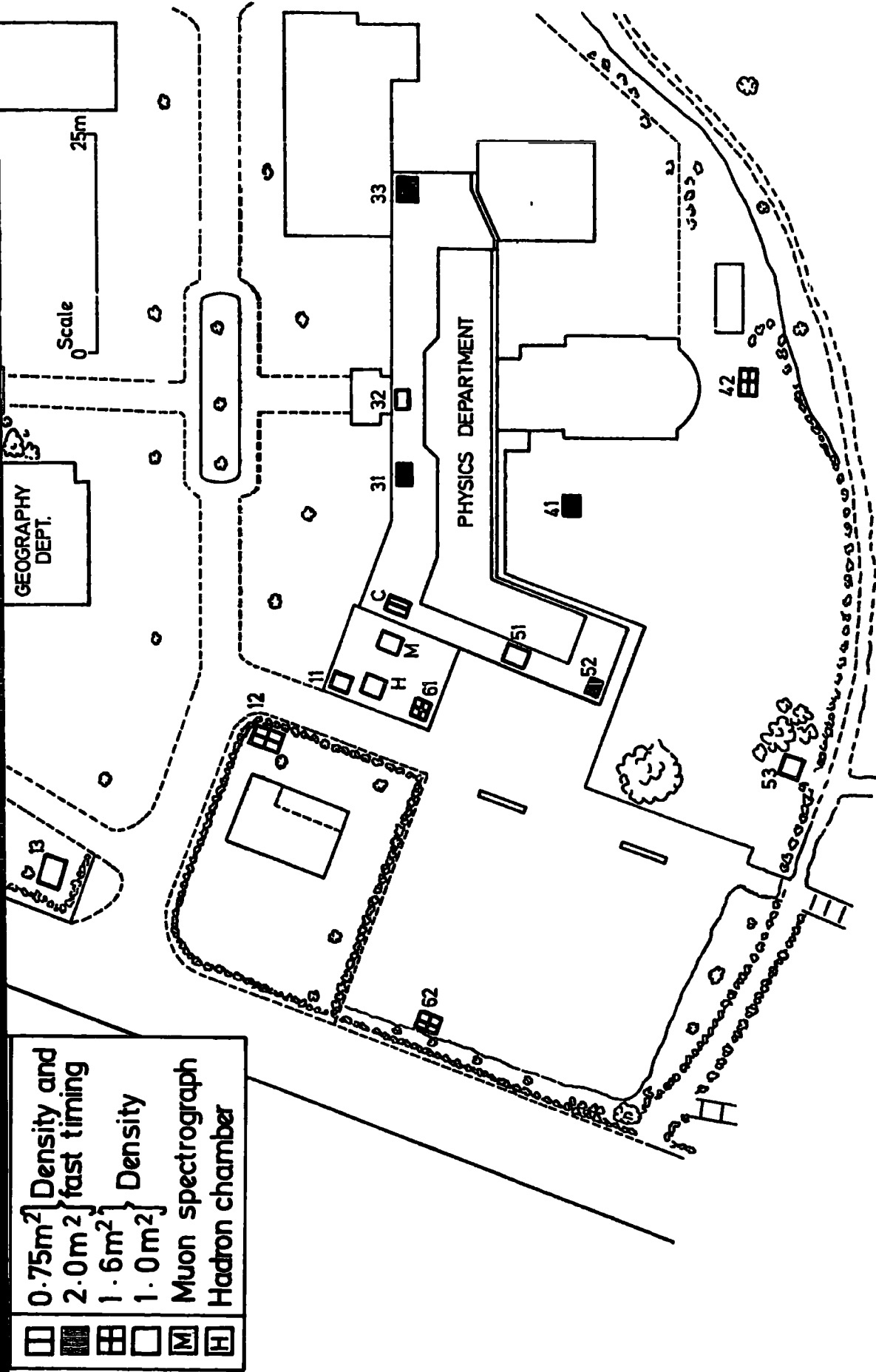


Figure 2-13. The Durham Extensive Air Shower Automated Research Array. (after Smith 1976).

30° of the Zenith.

The main feature of the array is the automatic nature of its data acquisition. The information from the detectors is 'digitised' on arrival in the laboratory and transferred automatically to a magnetic disc via an on-line I.B.M. 1130 computer for subsequent analysis. The digitisation process is completed and the information stored within about 2 ms of the arrival of an event enabling the array to have a 'live time' of greater than 99% of real time for the range of showers for which it is responsive. A further property of the array is 'interrogation' of the detectors. Here, the pulse heights in the laboratory due to particles passing through the detectors can be stored, in a similar fashion, by the application of an external trigger to the array electronics to initiate a data storage cycle.

A short account follows of the detecting elements of the array and the data handling electronics. In Chapter 3 the analysis of the data is considered. A full account of the array is given by Smith (1976).

### 2.3.1 THE DETECTING ELEMENTS

Four different types of plastic scintillation detectors are used in the array, distinguishable by size. Similar sizes of detector are placed in equivalent positions in the different arms of the array to maintain symmetry. All of the detectors are housed in weather-proofed wooden huts and serviced by high and low voltage power supplies via cables from the laboratory. Table 2.3 shows the format of the detectors. The response of the photo-tubes to light and of the head amplifiers to temperature was determined in the laboratory. The loss of signal in the coaxial cable was compensated for and the temperature coefficient determined to give a variation in arrival time of  $\pm 0.6$  ns, per 100 m. length of cable, of the signal (Smith, (1976)).

THE DETECTORS OF THE ARRAY

Number of Detectors	1	3	4	6
Geometrical Area	.75 m <sup>2</sup>	1.0 m <sup>2</sup>	1.6 m <sup>2</sup>	2.0 m <sup>2</sup>
'Slab' Depth	5 cm	5 cm	2.5 cm	2.5 cm
Scintillator Type	NE 102A	Unknown	NE 102A	NE 110
Position	Central	32,52,41	12,62,61,42	13,33,31,53, 51,11
Photomultiplier Tubes	Four 5" dia Phillips 53 AVP Two Phillips 56 AVP	Four 5" dia Phillips 53 AVP	Four 5" dia Phillips 53 AVP	Four 5" dia EMI 9579B One 2" dia Phillips 56 AVP
Measurements Taken	Density & Fast Timing	Density	Density	Density & Fast Timing

TABLE 2.3

### 2.3.2 DENSITY MEASUREMENTS

Calibration of the assembled detector involved the adjustment of the voltage supplied to each photomultiplier tube so that the tubes had similar responses. The summed pulse from all four tubes in the detector, when divided by 100 mV. gives the number of particles per square meter at the detector in the idealised situation. The experimental setting involved the use of a counter telescope and multichannel pulse height analyser (M.C.A.). By gating the M.C.A. with the telescope pulse a distribution of pulse heights can be 'built up' in the analyser from that region of the array scintillator defined by the position of the telescope. The minimum number of particles per square metre that can be recorded by a detector is about 1 and the maximum about 80.

### 2.3.3 FAST-TIMING MEASUREMENTS

The fast-timing pulses are  $\sim 5$ ns. f.w.h.m. and are used essentially to give a mark in time when the shower passed through the detector. Calibration is achieved by adjusting the counting rates of the fast tubes to be equal using some low discrimination level.

### 2.3.4 THE DATA HANDLING ELECTRONICS

The analogue signals arriving in the laboratory from the detectors are converted into digital information by the array electronics. Together with relevant information, date, time, event number, and so on, they are stored on a magnetic disc via an on-line computer. The sequence of the processes enabling this to occur are given below with reference to Figure 2.14.

### 2.3.5 DIGITISATION OF THE DETECTORS SIGNAL

The particle density data arrive as positive, 20  $\mu$ s decay time,

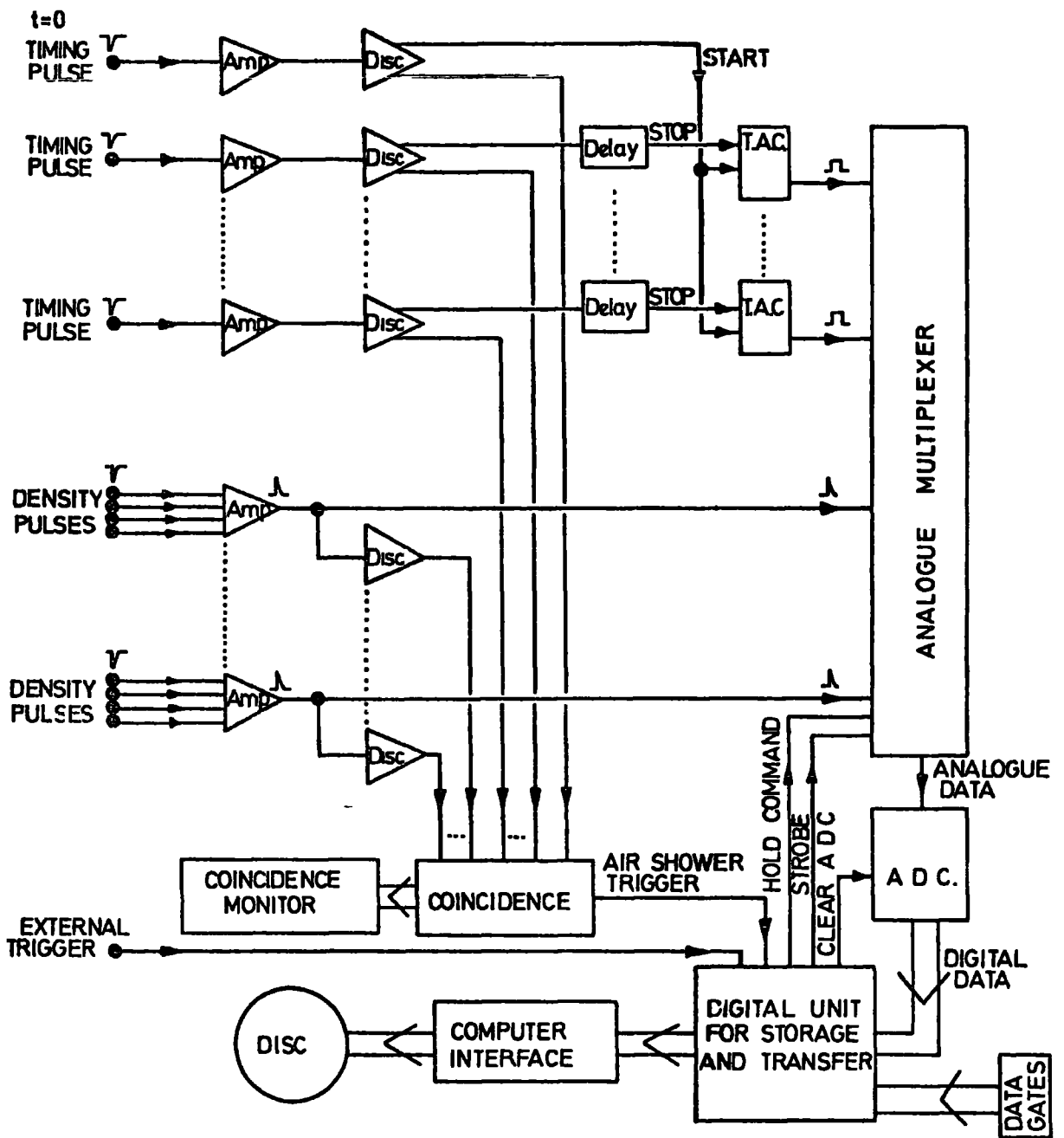


Figure 2.14. The event handling circuitry (after Smith, 1976).

exponential pulses. They are fed into an analogue multiplexer (A.M.) which is capable of holding the signal, as a voltage height, for an extended time. The timing pulses from each detector arrive at different times in the laboratory, in relation to each other. This difference is converted to an analogue signal by a time to amplitude converter (T.A.C.). Essentially a T.A.C. converts the difference in arrival time between 'start' and 'stop' pulses presented to it, into a voltage level, proportional to that time difference. The central detector's timing pulse is used to start all of the T.A.C.'s used, and no matter what arrival direction of shower sufficient delays are incorporated into the other detectors signals so that one T.A.C. is stopped for each subsequent fast timing signal received. These fixed delays must be removed in the analysis to render the true time differences. The T.A.C. outputs, 5  $\mu$ s wide rectangular pulses, go to the A.M. which acts as a 'multi-input' store for the signals. On receiving a 'hold' command the A.M. will store the voltage levels (pulse heights) present on its inputs. An externally applied hold command (an Interrogation) causes whatever voltages are present on the A.M. inputs to be stored.

### 2.3.6 THE STORAGE OF THE SHOWER DATA

The digital unit for storage and transfer (D.U.S.T.) controls the acquisition and passage of data to the computer. For each event an 'event header' is supplied which comprises relevant information, such as the date and run number. The analogue to digital converter (.A.D.C.) passes on the digitised form of the detectors' signals. These are stored in the memory (1024 x 8 bit word capacity) in D.U.S.T. until 11 events have been acquired (by which time the memory is full) where upon the events are all transferred consecutively, via the interface in the laboratory, to the computer.

### 2.3.7 THE INTERROGATION TECHNIQUE

After the arrival of the first signals in the laboratory that provide the basic air shower coincidence, a delay of about  $1 \mu\text{s}$  is incorporated before inhibiting the AM inputs and initiating the data storage cycle. This time is to ensure that the electronics respond fully and consistently to any signals. In order to emulate this with an interrogation pulse from the spectrograph a 'fast' counter telescope was placed on top of the spectrograph over the blue side, vertically above the three scintillation counters. A T.A.C. was started with the pulse from this telescope and stopped with the array coincidence pulse. The output of the T.A.C. was gated into a pulse height analyser with the threefold signal of the blue side scintillation counters. By considering the distribution of the delay of the array signal and also the distribution of the delay of the blue threefold coincidence, a suitable fixed delay was incorporated into the interrogation signal.

### 2.4 THE DAILY RUNNING OF THE SPECTROGRAPH AND ARRAY

In any twenty four hour period the spectrograph and array may 'run' automatically for up to about 22 hours. Switching 'on' and 'off', the experiments are mainly governed by the need to note accurately the run times and rates of the various monitoring counters and to store the data to a permanent form (a data file) on the computers magnetic disc. The spectrograph and array data are written as sequential core loads on to the disc. An example of the printout of successive events can be seen in Figure 2.7. At this time programs check the overall response of the detectors. For the spectrograph data, the efficiencies of each layer of flash tubes in the measuring trays is displayed, and for the array data, histograms of the pulse heights that have been stored in each separate

multiplexer channel are created. Any deviations of the distributions from those expected lead to a detailed check of the apparatus.

## 2.5 THE EXPERIMENTAL DESCRIPTION

### 2.5.1 THE RATE OF HIGH ENERGY MUONS IN AIR SHOWERS

The momentum spectrum of unassociated muons has been measured by the high resolution system of the spectrograph for about 2½ years from August, 1973, until May, 1976. A momentum selecting system has been in operation to select muons of greater than 100 GeV/c for analysis. However, the arrival of lower energy muons in air showers can provide sufficient conditions to trigger the spectrograph. Measurements on muons and the shower density in the region of the spectrograph thus gathered lead to the energy spectrum of muons in small air showers. These data are presented in Chapter 4 and the performance of the spectrograph is considered for the conditions under which such events occur.

### 2.5.2 AIR SHOWER ARRAY INTERROGATION

For a period of about 6 months from September, 1975, until March, 1976, the air shower array was interrogated when a coincidence occurred between a muon passing down the blue side of the spectrograph and a high particle density in the central detector of the array. This experiment was conducted by Mr. W.S.Rada. The data from it have been used in conjunction with the above mentioned air shower triggers of the spectrograph to determine the rate of high energy muons in air showers.

### 2.5.3 MUON PAIR EXPERIMENT

During the eight month period between September, 1975, and May, 1976, an experiment was conducted to measure the rate of arrival of coincident

vertical muon pairs. A coincident pulse from all six scintillation counters could be due to the passage of a muon through both sides of the spectrograph. Hence the measuring tray information was 'stored' from both sides on the advent of such a trigger. Necessarily the separation of the muon pair must be greater than or equal to about 38 cm. For comparison the rate of pairs, both passing down the blue side, is determined from the high momentum data. The results of this experiment are presented in this thesis with a discussion of the acceptance of the spectrograph for muon pairs unassociated or accompanied by a shower. For approximately half of the above mentioned period the air shower array was interrogated in the case of these events. A flow diagram is given in Figure 2.15 showing the mode of operation of the experiments.

## 2.6 THE ROLE OF THE AUTHOR

As one of the team of people working together in the cosmic ray group, the author assisted in maintaining and running the spectrograph and air shower array. In particular, it was the author's responsibility to complete and assemble the red side measuring trays and design and construct the photographic and film projection systems. The data referred to in this present work could not have been collected without the assistance of the other members of the group, but the author had responsibility for its collection, analysis and interpretation.

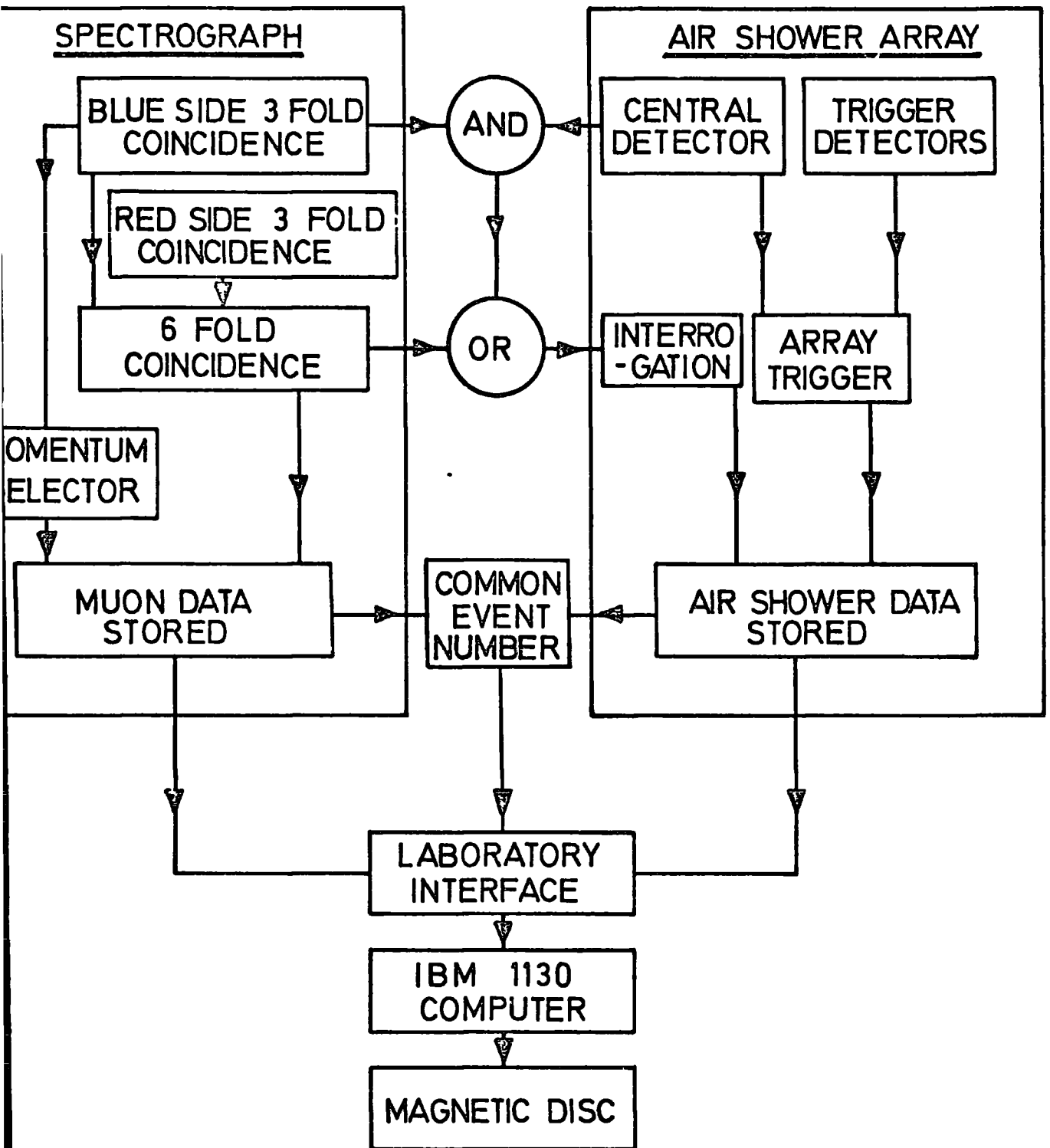


Figure 2.15. The mode of operation of the spectrograph and the array.

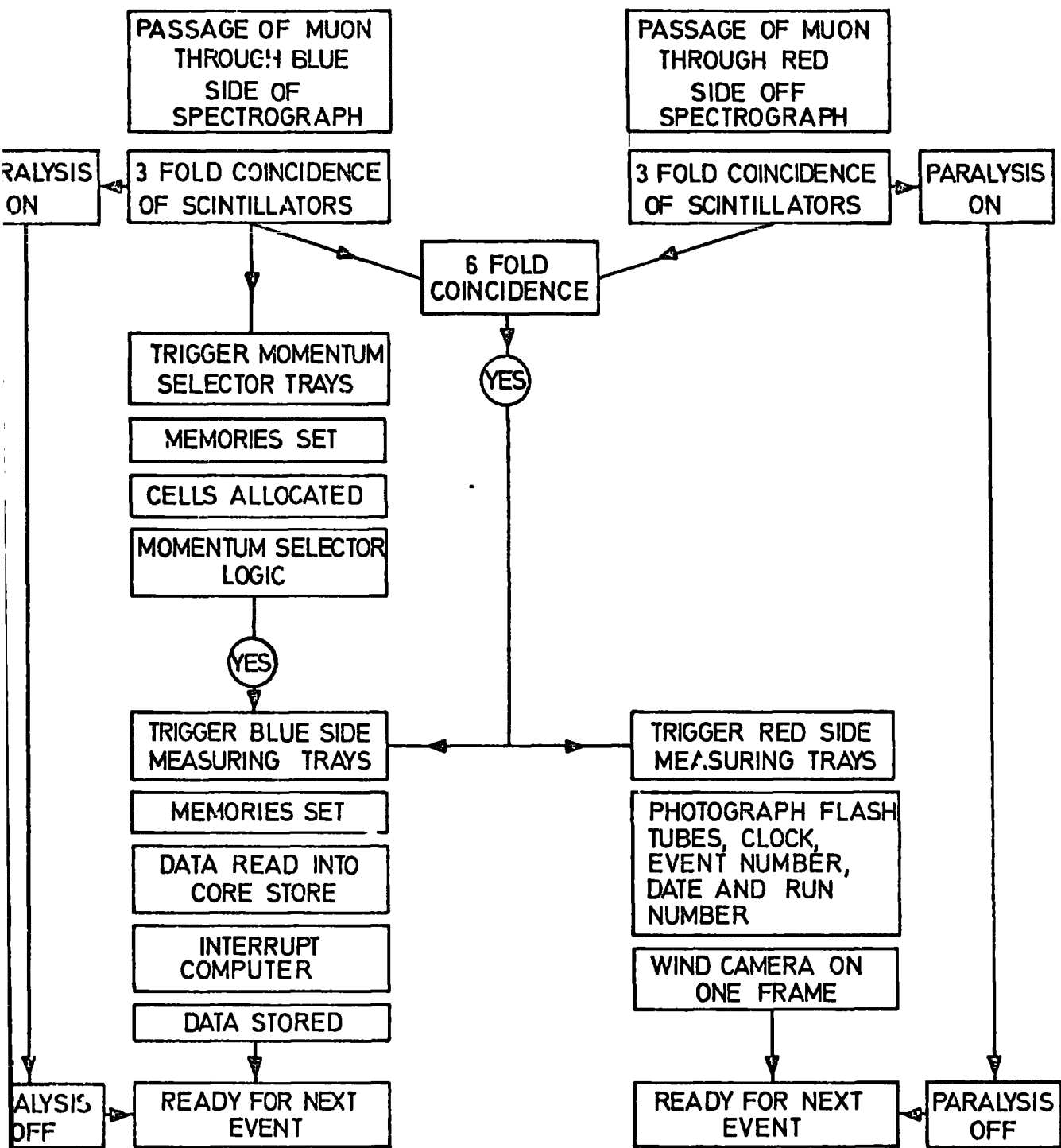


Figure 2-16 The spectrograph operating system.

CHAPTER 3

GENERAL ANALYSIS OF THE DATA

3.1 INTRODUCTION

This study of muons in air showers with the M.A.R.S. spectrograph and Durham Air Shower Array has led to several different types of data being gathered. The analysis of this data has required three separate procedures which are described in the following sections. The data to be analysed falls into the following categories.

(a) The muon data stems from the measuring trays of the spectrograph. The trajectory of the muon as recorded by these detectors leads to a momentum, charge and arrival direction for each muon.

(b) If the muon is accompanied by an air shower the unshielded measuring flash tube tray at level 5 of the spectrograph will show the passage of ionizing particles in the shower. Hence a measure of the local density of the air shower can be obtained.

(c) If triggered or interrogated the air shower array can provide the shower size, core location, and arrival direction of the accompanying shower.

All the data obtained from the different apparatus are stored either on magnetic tape or magnetic disc. The initial collection and storage of data is done in an I.B.M.1130 computer. Fortran and Assembler programs are then used to access and manipulate the data and render it into a suitable form for transfer to the Northumbrian Universities Multi-Access Computer (NUMAC) at Newcastle. This computer acts as the main data store and analysis of all data is achieved via remote 'job' submission from Durham using the Michigan Terminal System (M.T.S.).

The analysis programs for the spectrograph muon data were developed by Wells (1972), and Daniel. (private communication). The array data analysis programs have been developed by Smith (1976) whilst the interpretation of the 'shower' information from the top flash tube trays of the spectrograph has been the responsibility of the author.

### 3.2 THE ANALYSIS OF THE MUON DATA

#### 3.2.1 MUON MOMENTUM DETERMINATION

A charged particle moving in a static magnetic field experiences the Lorentz force according to

$$\underline{F} = e\underline{v} \times \underline{B} \quad (3.1)$$

where  $e$  is the electronic charge and  $v$  is the component of velocity that is perpendicular to the magnetic field of flux density  $B$ . The force is always perpendicular to the component of velocity and the direction of the field and so a circular motion ensues. If  $r$  is the radius of curvature then the centripetal force  $F$  maintaining circular motion is

$$F = \frac{Mv^2}{r} \quad (3.2)$$

for a particle of mass  $M$ .

Hence equating forces

$$Mv^2/r = eVB \quad (3.3)$$

or  $P = rBe$

or  $P = 300 rB$

where the momentum  $P$  is in  $eV/c$ ,  $r$  in  $cm.$ , and  $B$  is in gauss.

Application of the above equation, (3.3), to the passage of a muon through the spectrograph requires a correction for the gaps in the field due to the gaps between the blocks. In practice a parabolic trajectory of the form

$y = ax^2 + bx + c$  is fitted to the spectrograph data and Wells (1972) has shown that the constant  $a$  is related to the aforementioned radius of curvature by  $r = 1/2a$  which, including a correction for the gaps, corresponds to

$$p = 0.1949/a \text{ GeV/c}$$

which is the equation used to calculate the momentum of the muons.

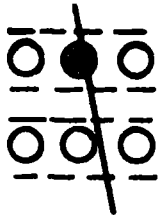
### 3.2.2 TRAJECTORY FITTING BY COMPUTER PROGRAMME

If, in an event, a single unaccompanied muon has discharged just one 'group' of flash tubes in each tray, a general region or 'channel' of the tray through which the muon passed is used. A group is defined as a cluster of greater than 2 discharged flash tubes in adjacent columns, and the channel is the lateral extent of possible movement of the track that would still give the same discharged tubes. The mid-point of this channel is used by the program as an approximate co-ordinate for the muon's position in each measuring tray. Using these co-ordinates a trajectory is fitted through all five trays and the approximate angle of the trajectory of the muon through each tray is determined. A new set of co-ordinates are obtained by using these angles to better locate the position that the muon passed through each group of discharged tubes. A final parabola is then fitted to these new co-ordinates. The momentum of the muon and projected Zenith angle in the bending plane are calculated from the coefficients of the parabola, whilst the charge of the muon is derived from the magnetic field direction and the direction of curvature of the muons track. For each event the standard deviation of the fit of the points in each tray to the final computed track is given as well as the fitting 'options', which are explained later. The M.A.R.S. 2 analysis program (Daniel, private communication) has been used to analyse the data for the present work.

Necessarily the situation is more complicated when there is more than

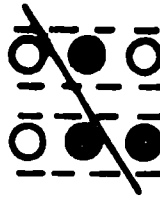
one group in a tray or if a group is very large ("a burst"). Generally all the possible combinations of groups in each tray are fitted and only the best fit is returned. Thus the program searches through the available data for a genuine trajectory. For all the events considered in the present work, a computer plot (for example see Figures 3.3 and 3.4) of the muons passage through the measuring trays of the spectrograph was studied with regard to the fit returned by the program. The reason for this is explained in Section 3.2.3, and in Section 3.4.3, the possibility of the chance alignment of tracks in different trays is considered.

The analysis program has the option to disregard a discharged tube, or tubes, and to consider a tube inefficient. Wells(1972) justifies this treatment of the data. Essentially if a muon is accompanied by an electron, or 'knocks-on' an electron which discharges a tube next to the muon's track, incorporating this tube in the trajectory determination would be erroneous. When a flash tube fails to discharge, despite a particle traversing it, a clear and obvious track would have to be disregarded due to the absence of one discharged tube through which the muon must have passed for that track. Hence a set of options are open to the program, to cope with these possibilities, which are used if necessary during the trajectory fitting. The fitting options are shown in Figure 3.1 and are used by the program starting with the lowest number, which corresponds to the least severe alteration to the data, and continuing until a satisfactory fit is obtained or the options are exhausted. If no option is found for a track in a particular tray, the corresponding co-ordinate is rejected from the parabola fit to the co-ordinates in the other trays. This rejection will also occur if there is no group of greater than 2 discharged flash tubes in a tray, or if the track cannot be placed through the configuration of discharged tubes at the right angle. If more than two trays are lost then the analysis terminates as a minimum of 3 co-ordinates are required to fit a parabola. For these and for other reasons the program may not satisfactorily fit a parabolic curve to the data. In these cases of failure the reason for



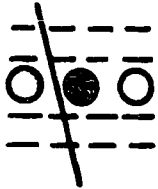
OPTION 0.

Good fit-no information has to be assumed.



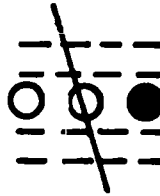
OPTION 6.

One single knock-on and one double knock-on are assumed in different layers.



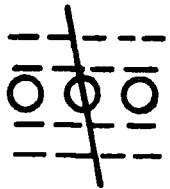
OPTION 1.

A knock-on electron is assumed ( a discharged tube is neglected ).



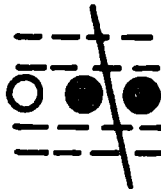
OPTION 7.

A tube inefficiency and a knock-on in the same layer are assumed.



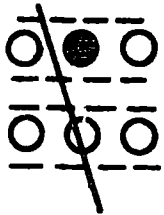
OPTION 2.

A tube inefficiency is assumed ( an undischarged tube is assumed to have discharged ).



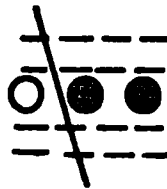
OPTION 8.

Two knock-ons in the same layer are assumed ( muon passed between them ).



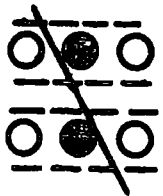
OPTION 3.

A knock-on electron and a tube inefficiency in different layers are assumed.



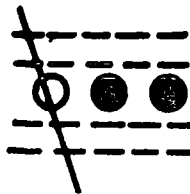
OPTION 9.

Two knock-ons in the same layer are assumed ( muon passed to one side of them ).



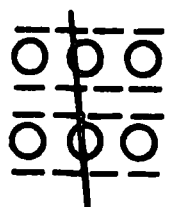
OPTION 4.

Two knock-on electrons in different layers are assumed.



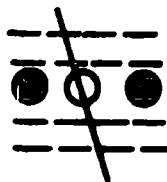
OPTION 10.

An inefficiency and a double knock-on are assumed in the same layer.



OPTION 5.

Two inefficiencies in different layers are assumed.



OPTION 11.

Assumes an inefficient tube between two knock-ons.

FIGURE 3.1. The fitting options available to the computer.

the failure is indicated by an error code. A summary of the error codes generated by the program and the reasons for them are given in the Table 3.1.

### 3.2.3 AIR SHOWER ACCOMPANIED MUONS

The distributions of the number of columns containing at least one discharged tube per recorded event in measuring trays 1 and 5 are shown in Figure 3.2. It can be seen that at about 30 columns of data, a marked separation of the two distributions occurs. This is the point where the accompaniment of the muon by air shower particles prevents the identification of the muons' track in tray 5. If tray 5 contains greater than 30 columns in which at least one tube has discharged (referred to as '30 columns of data') only a four tray fit is attempted (Trays 1,2,3 and 4). Notably, the mean momentum of muons in such events is lower than the mean for unaccompanied muons because the shower particles are providing part of the momentum selection condition necessary for the measuring trays to be triggered. A clear example of this can be seen in Figure 3.3 where the trajectory of the muon is marked in, as well as the position of the shower particle in tray 5 that probably caused the trigger, in conjunction with the low momentum muon. The acceptance of the spectrograph is larger for such accompanied muons and its calculation is somewhat complicated because of the chance nature of the momentum selector condition being satisfied. This is considered in detail in Chapter 4.

The suitability of these 'shower' accompanied muon events for analysis and subsequent evaluation depends upon the extent to which the muons trajectory can be discerned and successfully analysed. This shower data collected during the experimental runs of the spectrograph to determine the unassociated muon momentum spectrum falls into the following broad categories.

1. The mean number of events in which one or more flash tubes are discharged in more than 30 columns in measuring tray 5 is about 12% of all the events that trigger the momentum selector.

ERROR CODES FOR WHICH THE ANALYSIS PROGRAMME FAILS THE EVENT

<u>ERROR CODE</u>	<u>ERROR</u>
91	One or more flash-tube trays with no group in it
92	More than thirty columns of flash-tube data in tray 5 (i.e. incident extensive air shower)
93	More than ten group combinations successfully analysed
94	All the combinations of groups in the trays fail
95	Combination of groups fails the standard deviation or group-trajectory separation criteria
96	Possible multiple muons (3 or more successfully analysed independent combinations of groups)
99	More than twenty-five groups in all the trays combined

Error codes 91, 92 and 99 are generated before the analysis procedure commences, the remainder being generated after the analysis is complete.

ERROR CODES FOR UNUSED TRAYS

<u>ERROR CODE</u>	<u>ERROR</u>
20	No track can be fitted through the data without violating the flash-tube information
30	No group of discharged flash-tubes within one tube spacing of the fitted trajectory in an unused tray
40	No group of three discharged flash-tubes in a tray
60	No discharged flash-tube in the column indicated (i.e. electronics fault)
70	Trajectory failure due to the angle of the trajectory and the tube pattern in the tray being incompatible

TABLE 3.1

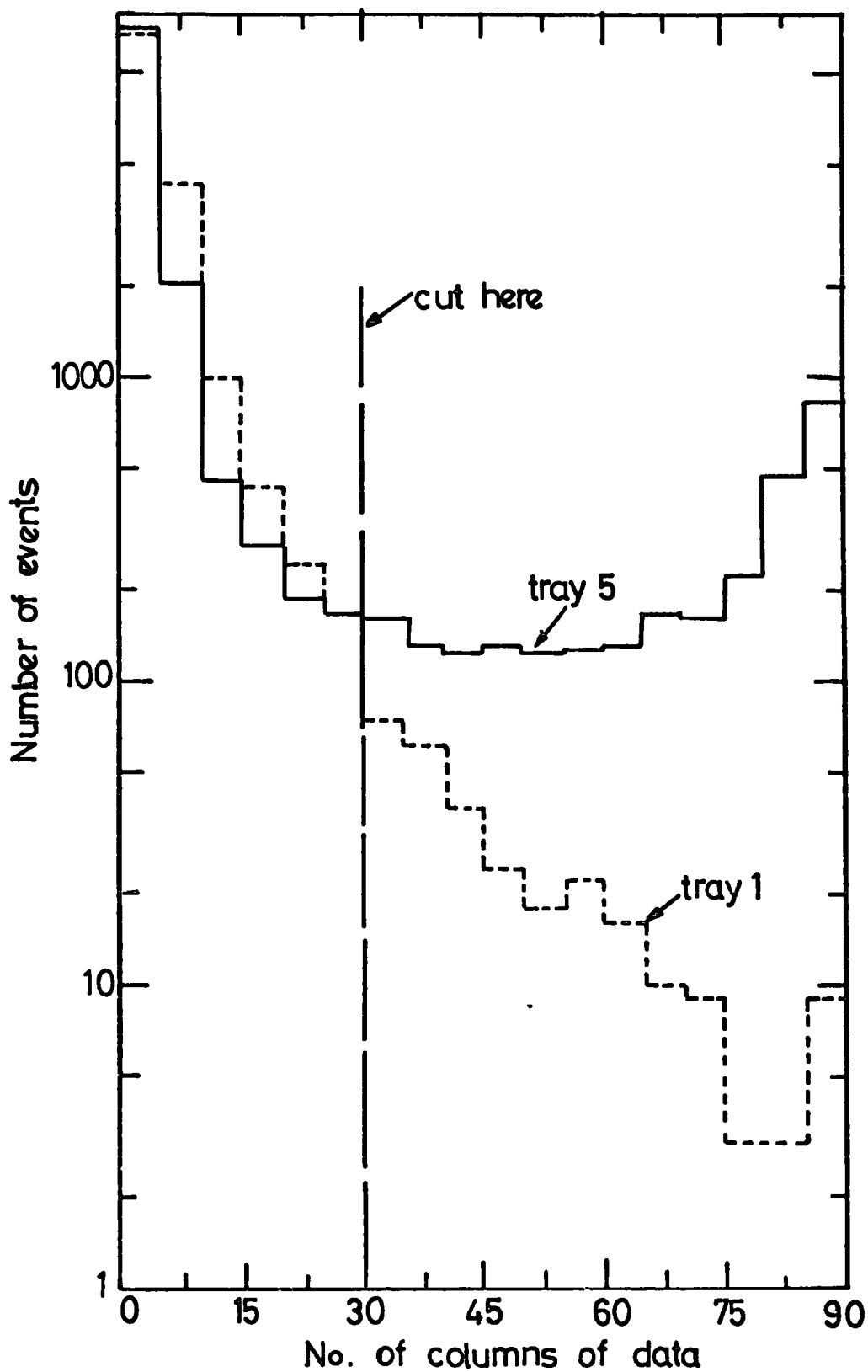


Figure 3.2. Distribution of number of columns of data per event in trays 1 and 5.



2. Of these events approximately 10% (about 1.2% of the total events) contain a muon passing the acceptance condition of traversing all of the lower four measuring trays.

3. Of the events containing a muon about 93% have at least one particle track apart from the muons track in one of the lower measuring trays.

4. About 0.05% of the shower events have such a high density of tracks in all the measuring trays that any possible muon trajectory is not discernible.

The analysis programs were not designed to cope with the number of separate tracks that occur in the lower trays in the shower events. Consequently the analysis program has been operated in an 'editing data' mode. Briefly this involves hand scanning of the computer plots (for example see Figure 3.3) of the events with greater than 30 columns of data in tray 5 and then splitting the data for each event into smaller sections across the trays before submitting the data to the analysis program. Thus the total number of possible combinations is reduced in any one attempt at analysis. NUMAC has been used to analyse the data and as this computer is programmed with MTS this allows an interactive mode of job submission. This is ideal for presenting the data to the analysis program in this 'editing mode'. Figures 3.4 and 3.5 show complicated situations involving more than one muon. The important criterion that must be met is that a single muon passed through all four lower flash-tube trays and that a chance coincidence of tracks of independent air shower particles did not occur. This will be discussed in Section 3.4.3. For all the 'shower accompanied' data, measuring tray 5 has not been used to determine the muons' momentum. Thus a maximum of 4 trays are available for momentum computation and to avoid the possibility of chance coincidence of particle tracks being used, all 4 lower measuring trays were used in the momentum analysis, whenever possible. Hence the following extra



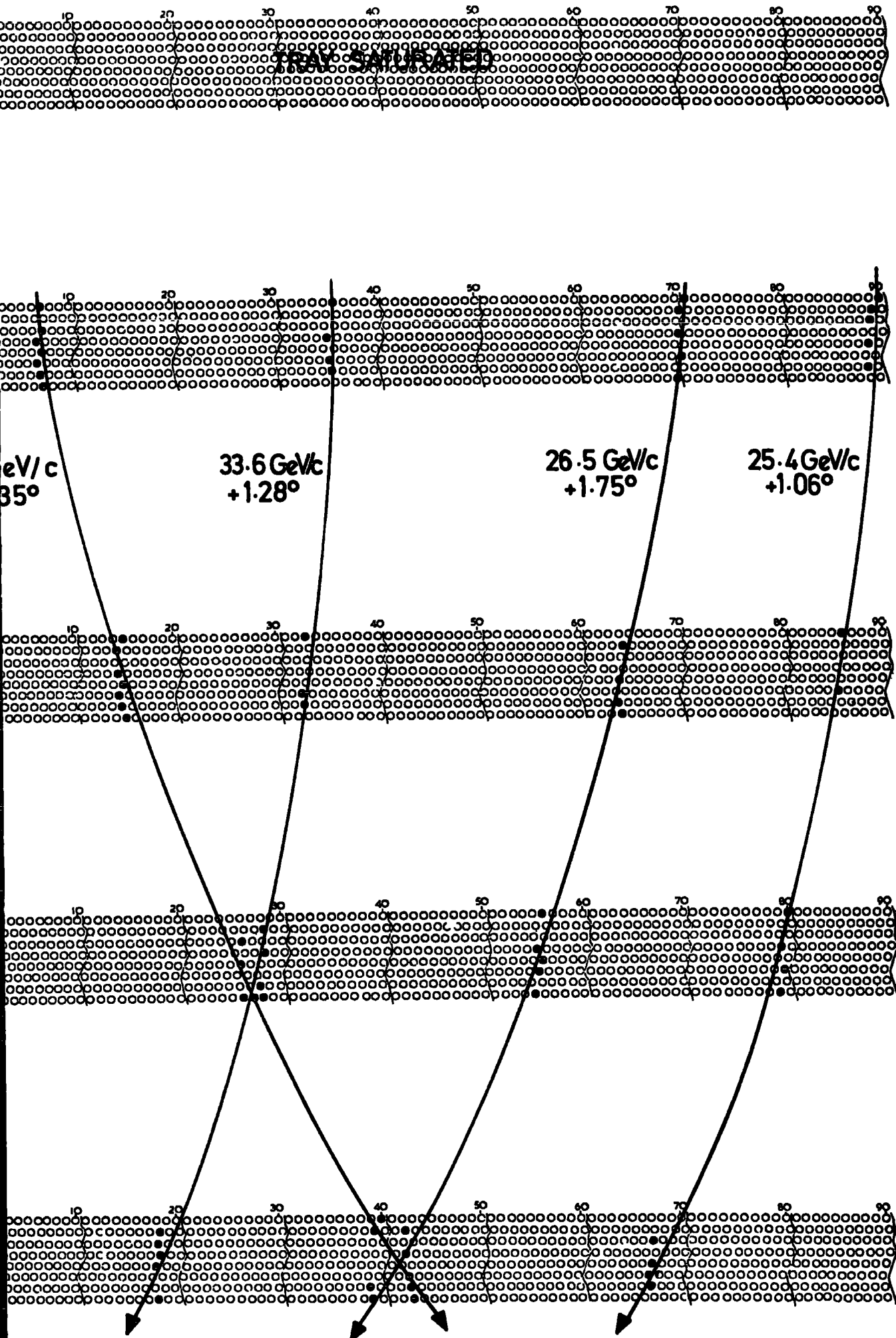


Figure 3.4a An event of 4 muons and >30 columns in tray 5. (Blueside)



TRAY SATURATED

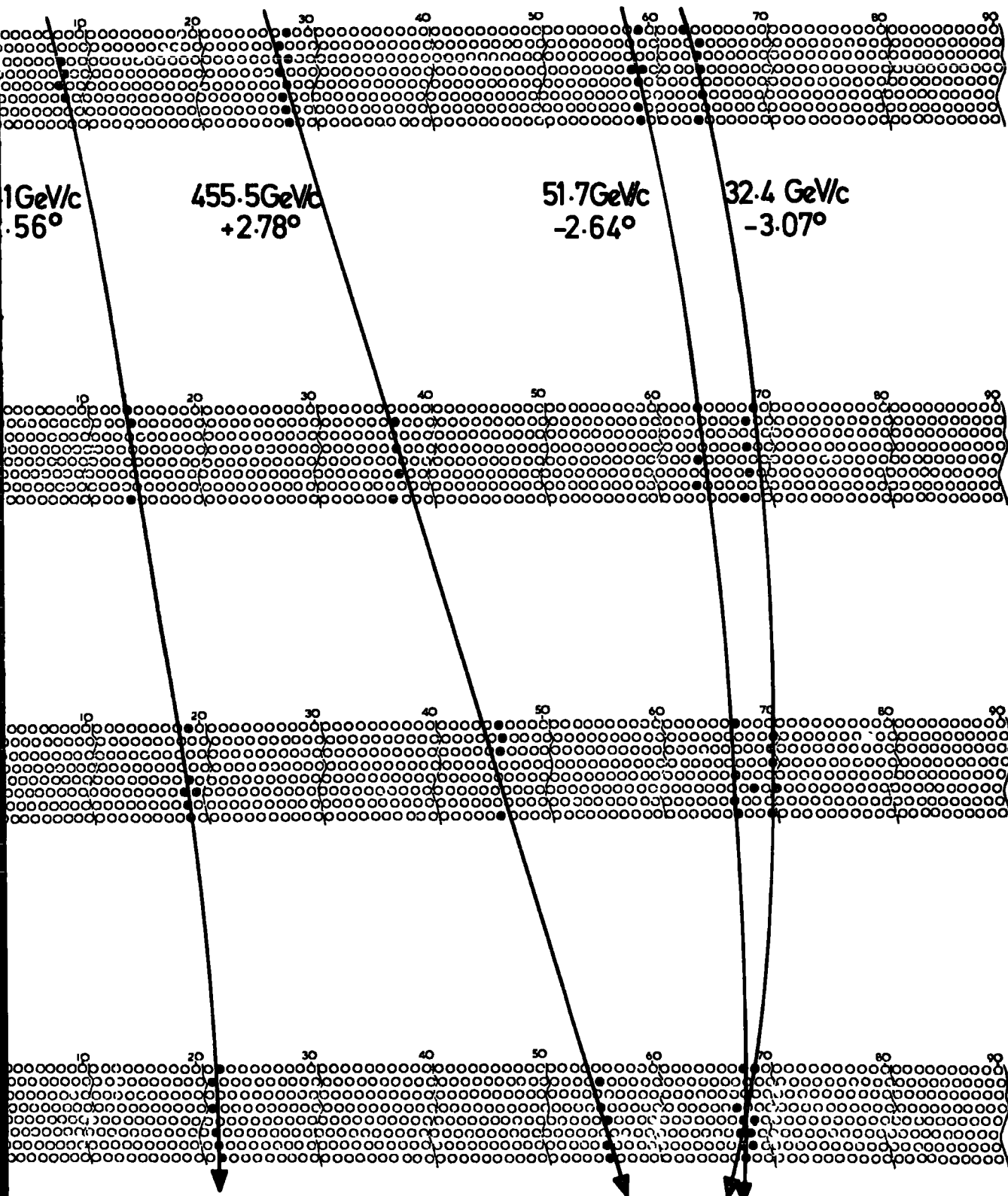


Figure 3.5a An event with 4 muons and >30 columns discharged in tray 5.

'error' codes have been introduced into the analysed event.

(a) ERROR CODE 66n (n, 1 - 4)

Initially the program fails to fit a track in tray n and a 3 tray fit is returned. The data is then edited and one, and only one, successful track is returned by the program giving a 4 tray fit. The code 66n is then stored with the event.

(b) ERROR CODE 88n (n, 1 - 4)

The program fails to find a track in tray n and a 3 tray fit is returned. The data is then edited and more than one possible successful track is found that satisfies the standard deviation and acceptance tests built into the program. The acceptance test is the requirement that a track must be present in each tray and the standard deviation of the points used to fit the parabola must be less than  $0.25 \cdot 10^{-3}$  m. for muons with momenta above 20 GeV/c and less than  $0.01 \cdot 10^{-1}$  m. for momenta below 20 GeV/c. The track with the lowest standard deviation and 'best' tray fit code is taken and the code 88n stored with that event.

(c) ERROR CODE 99n (n, 1 - 4)

Here a 3 tray fit to the muons trajectory is only possible as either a large unresolvable burst has occurred or there are only two tubes on the track in tray n. This is retained as a 3 tray fit and stored with the code 99n.

(d) ERROR CODE 55

To overcome the limitations of the analysis program when the particular configuration of discharged tubes cannot be interpreted by the analysis procedures (several 'knock-ons' or a crossing track overlaying the muons track) use was made

of an alternative technique developed by Whalley (private communication). Here the data in the tray in the region of interest (up to 10 columns wide) is 'scanned' at 1/10 tube spacings to find the ratio of the number of tubes discharged to the number that should have discharged for the given angle of track of the muon. Hence a probability distribution is built up across the tray. A diagram of this is given in Figure 3.6 alongside the tube pattern discharged for a single track. For the track in each tray the centre point of the distribution, the most probable value, is taken as the co-ordinate of the muons trajectory in that tray. A parabola is then fitted through the co-ordinates and the same standard deviation test is applied to the resulting fit as is applied to the M.A.R.S. 2 analysed events. The analysis of all the '4 tray' data is compared to the analysis of '5 tray' events of single, unassociated muons in Figure 3.7. This is a frequency histogram of the R.M.S. standard deviation of the fit of the points in each tray to a parabolic trajectory.

#### 3.2.4 THE ANALYSIS PROCEDURE

From the basic data file containing all the stored events, the events containing greater than 30 columns of data in measuring tray 5 were extracted to create a 'shower' data file. As mentioned above this constituted approximately 12 to 20% of the data depending upon the trigger conditions of the spectrograph. During the course of collection of these data different trigger conditions were in use. The consequence of this will

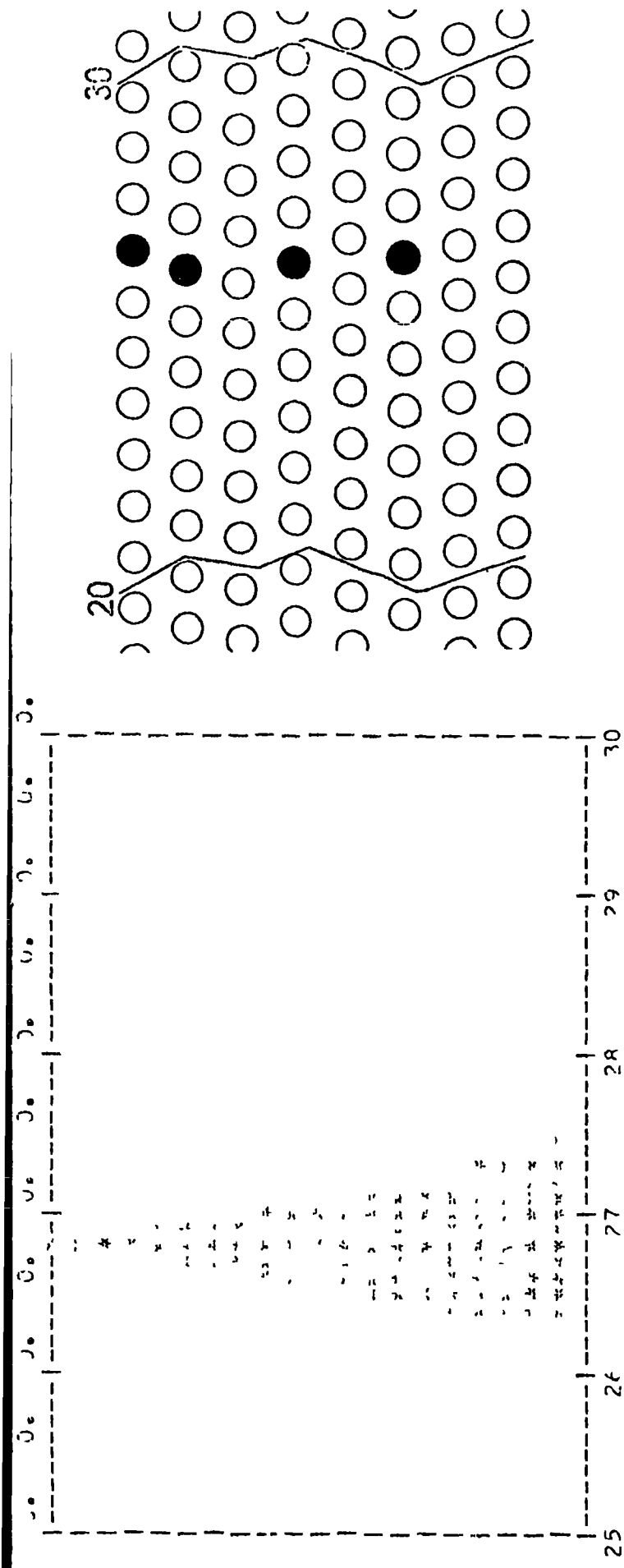


Figure 3.6 A 'probability' plot of the tube combination shown. The track angle is approximately +0.3 degrees

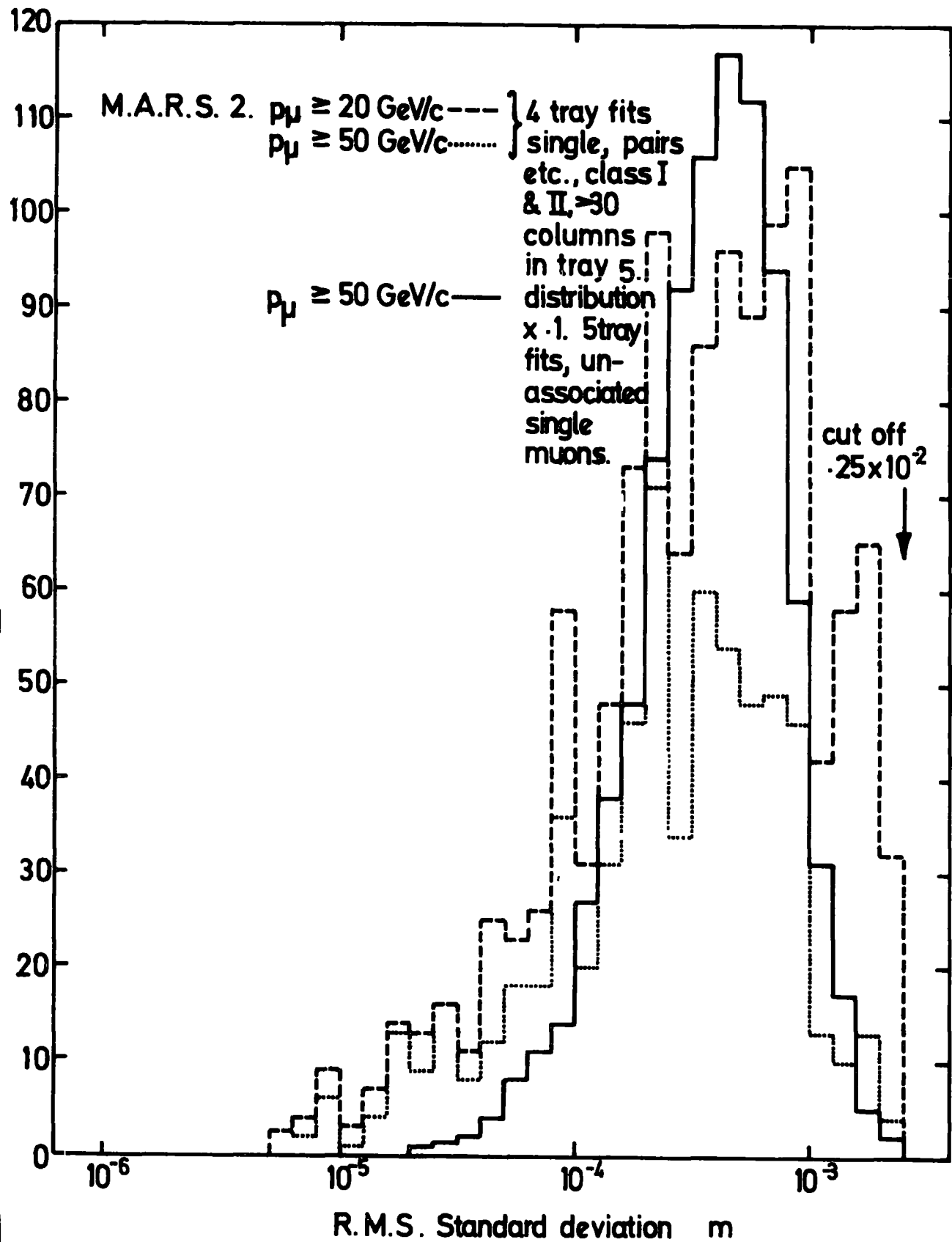


Figure 3.7 Standard deviation distribution.

be discussed in Chapter 4. All the events in the shower data file were analysed with a limit set on the maximum possible combinations of tracks. If no combination limit was set, certain events would have taken an excessive length of time to analyse. The same tests for acceptance and standard deviation were set as for the analysis of single, unaccompanied muons.

The first 1,000 events (irrespective of the analysis result returned by the program) were plotted by the computer (see Figure 3.5). These events were considered in detail and any confused or complicated event was replotted on a diagram of the trays of the spectrograph drawn oversize but in correct relative position. Figures 3.4 (a), and 3.5 (a), are examples of the events of Figures 3.4 and 3.5 replotted in this way. As a consequence of this detached analysis of individual events, it was considered necessary that all the events analysed as containing a muon, plus those returned with error codes 94, 95, 96 or 99, should be plotted using this computer routine. In the 1,000 trial events any event with other error codes never contained a muon, but the events containing a muon were frequently incorrectly analysed or returned with one or other of the error codes given above. Thus the edit mode was used extensively in the analysis of a total of 13,742 shower accompanied muon events. The corresponding run time was 5118.4 hours and the analysis produced 1650 events containing one or more muons of momentum over 6 GeV/c.

### 3.3 THE ANALYSIS OF THE AIR SHOWER ARRAY DATA

#### 3.3.1 INTRODUCTION

The analysis programs for the array data use a theoretical description (based on previous results of air shower arrays) of the structure of an air shower at sea level to fit a shower size, arrival direction and core location to the measured quantities. The data from the array, in digitised form, is transferred via the IBM 1130 computer to NUMAC for storage on magnetic tape

and magnetic disc. It contains experimental biases which must be removed or allowed for, prior to use. The first stage of the analysis is data calibration and conversion into usable quantities. Once this is done the program presents the data in suitable form to a minimisation routine called MINUIT. (A CERN program, James and Roos,(1971)). This then calculates the shower arrival direction followed by the core location and shower size. A full description is given by Smith (1976) and Smith and Thompson (1977).

### 3.3.2 THE ANALYSIS PROCEDURE

The full analysis of a data file begins by summarising all the data present in the data file including which run numbers are present and how many events are in each run. The program then histograms the data, and various statistical quantities are determined for each Analogue Multiplexer input. This acts as a monitor of the Analogue Multiplexer (A.M.) data and provides coefficients for internal calibration of the data. For instance at the next stage of analysis the inherent delays of the timing signals are allowed for by application of one of these coefficients. The delays are due to the detectors being non-coplanar, and speed differences in cable and electronic signal propagation. The mode of the distribution of delays of one detector for all the events in a run or runs, is subtracted from the value determined for this detector for each event. Thus the 'numbers' as presented by D.U.S.T. are converted into relative times of arrival of the shower front at the various detectors. In the case of the particle density data a conversion must be made from pulse height stored, into particle density. In this case a fixed combined A.D.C. and A.M. calibration factor is applied and the histograms are only used as a check of consistency. The extent of analysis possible depends on the quantity of data present for each event. Table 3.2 gives the options available.

THE ANALYSIS OPTIONS FOR THE ARRAY DATA

(AFTER SMITH, 1976)

ANALYSIS OPTION	MEANING	TIMES	DENSITIES
1	INSUFFICIENT DATA FOR ANALYSIS NO ANALYSIS DONE	<2	<5
2	INSUFFICIENT TIMING DATA FOR FULL ANALYSIS. THREE PARAMETER ( $X_c, Y_c, N$ ) FIT TO THE DENSITY DATA, $\theta$ ASSUMED TO BE $0^\circ$	<2	>5
3	TIMING DATA USED TO CALCULATE ( $\theta, \phi$ ).	>3	<3
4	FULL ANALYSIS. TIMING DATA USED TO CALCULATE ( $\theta, \phi$ ) DENSITY DATA USED TO CALCULATE ( $X_c, Y_c, N$ )	>3	>3

$\theta$   $\phi$  ZENITH AND AZIMUTH ANGLES

$X_c, Y_c, N$  CORE CO-ORDINATES AND SHOWER SIZE

TABLE 3.2

### 3.3.3 THE MINIMISATION OF THE ARRAY DATA

The arrival direction of a shower is determined by minimisation of the timing data (for those detectors that are operational) to a plane in three dimensions using a least squares technique. Infinite radius of curvature is assumed for the shower front as the small time differences due to any curvature are not detectable with the present array. The solution of the arrival direction is given by Smith (1976), for the case of 3 timing detectors. All the data considered here consist of 3 or 4 operational timing detectors.

A structure function of unknown age parameter ( $s$ ) is used to fit the density data for detectors with greater than or equal to  $0.5 \text{ particles m}^{-2}$ . A weighted least squares technique is used in the present experiment to fit the structure function due to Catz et al., (1975) to the experimental data. Detectors which have saturated or which have zero data are excluded from the analysis as non-measurements. Hence a complete disregard is taken of detectors not containing at least  $0.5 \text{ particles m}^{-2}$ .

Smith (1976) has checked the response of the program by simulating experimental data and analysing it with the analysis program. Errors on the times of arrival of the shower front and on the particle numbers were included and by examining the program's performance systematic effects introduced by the analysis could be identified and eliminated.

### 3.3.4 ACCURACY OF THE ARRAY ANALYSIS

The accuracy of the shower size, core location, and arrival direction, depends upon the shower size and arrival direction. It has been found, Smith (private communication) that for showers of greater than  $10^5$  and less than  $10^7$  particles, falling within less than  $30^\circ$  to the Zenith, a core location of about  $\pm 6$  metres can be obtained. The implications for analysis of data when the array is interrogated is considered in Chapter 5.

3.4 THE DETERMINATION OF SHOWER PARTICLE DENSITY FROM THE TOP  
MEASURING TRAY OF THE SPECTROGRAPH

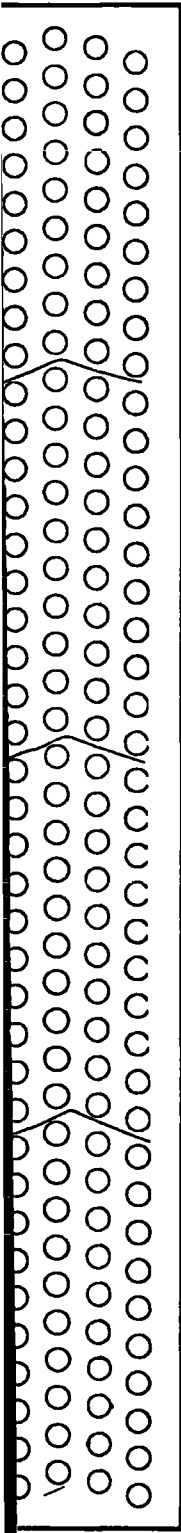
3.4.1 INTRODUCTION

The relative positions of the detecting elements at the top of the spectrograph can be seen in Figure 3.8. The measuring tray contains 8 by 89 flash tubes of internal diameter 0.55 cm of length 2m. filled with neon to a pressure of 2.4 atmospheres, and the momentum tray has 4 by 39 tubes of diameter 1.5 cm filled to 60 cm Hg. Typically a charged particle, such as a muon losing about  $2 \text{ MeV gm}^{-1} \text{ cm}^2$ , will deposit a few KeV in the gas of these types of flash tubes. In fact only about one electron need be released by ionization to start the avalanche on the application of a high voltage pulse, (Breare,1973). Thus when air shower particles accompany a muon through the top trays of the spectrograph, a measure of the density of shower particles is possible. Particle tracks can be seen in Figure 3.9 which shows an accurate reproduction of the tubes of measuring tray 5 for 3 separate events in which greater than 30 columns contained at least one discharged tube. Part of the present study is to determine the rate of arrival of muons of momentum greater than 20 GeV/c accompanied by a sufficiently high particle density to discharge tubes in more than 30 columns in measuring tray 5. The two conditions that have to be fulfilled for this data to be collected and analysed are :

1. If the muon is of low momentum (that is less than about 100 GeV/c) the shower particles must set off the appropriate cell in the momentum selector tray at level 5 so that a possible 'straight line' combination is passed to the momentum selector logic. If the muon is of sufficiently high momentum it may trigger the momentum selector.

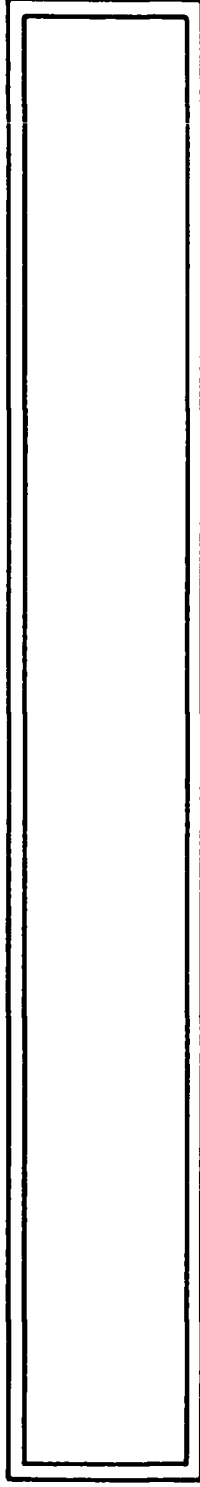
In Chapter 4 the details of these processes are given.

2. One or more tubes must be discharged in more than 30 columns in measuring tray 5. For a single ionising particle passing through the measuring tray there will be a discharged tube in an average of about



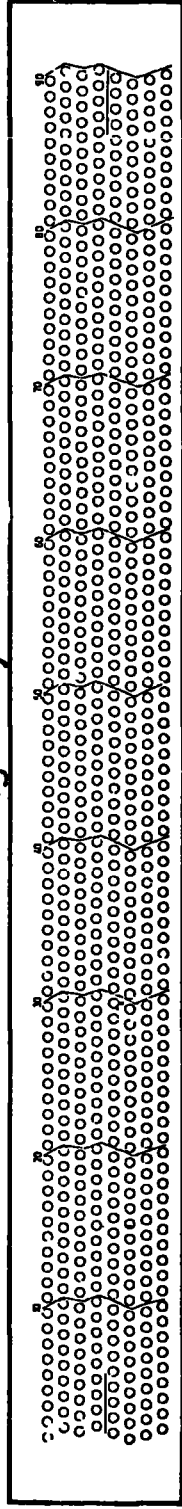
39.84 cm

Scintillator



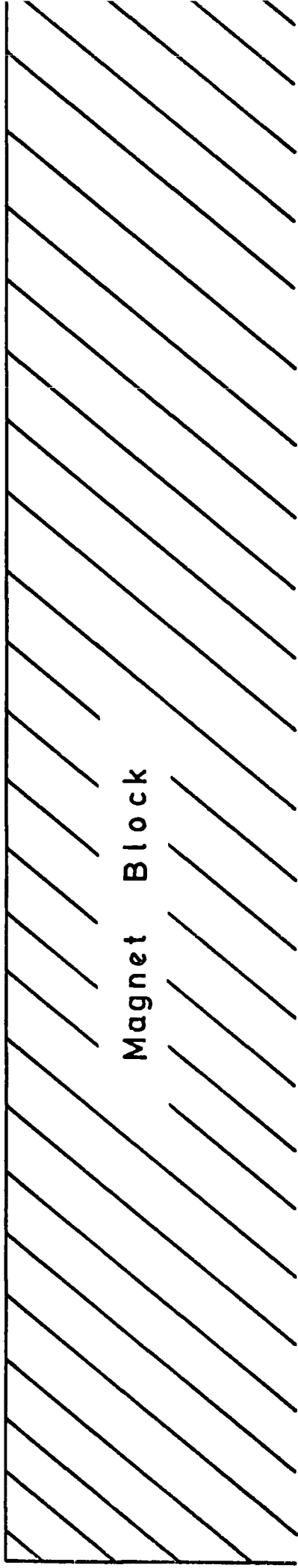
25.18 cm

Measuring Tray



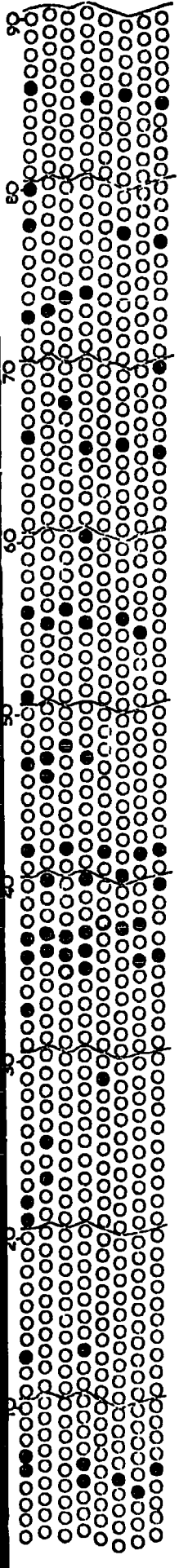
9.75 cm

0.0 cm

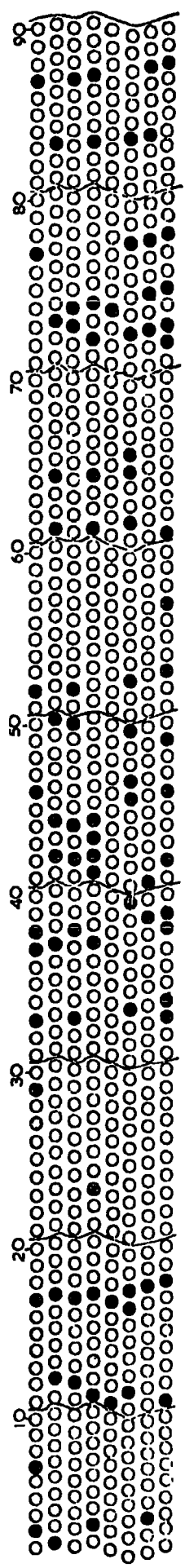


Magnet Block

FIGURE 3.8 BLUE SIDE OF MARS SPECTROGRAPH



EVENT No. 6148923 42 COLUMNS



EVENT No. 6174628 31 COLUMNS

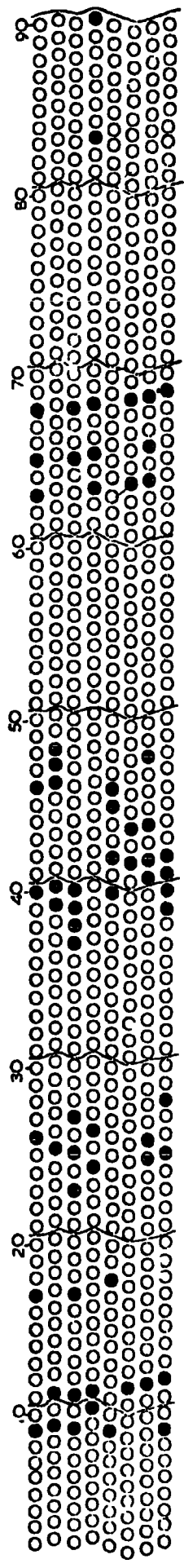


Figure 3.9. Measuring tray 5 for 3 different events

1.6 columns for a mean track angle of  $3.5^\circ$  to the Zenith.

Here consideration is given to determining the density of shower particles from a given number of columns of discharged tubes in measuring tray 5.

### 3.4.2 THE DENSITY OF SHOWER PARTICLES FROM FLASH TUBE DATA

Flash tubes have been used successfully to measure the density and structure of particles near to the axis of small air showers (Fukui, 1961). More recently searches for multiple air shower cores, and density measurements have been made at Kiel using flash tube "spheres". (Samorski, 1973), Blake et al., (1975), have investigated the response of flash tubes compared to scintillators at regions well away from the core of large air showers. These authors have also considered the differences in using both shielded and unshielded arrays of flash tubes, and they point out the importance of a knowledge of the threshold energy at which particles are detected for comparison to be made with theoretical predictions. Consideration of this for the present data will be given in Chapter 6. For the purpose of the following discussion, the top trays of the spectrograph are considered to be largely unshielded.

The number of shower particles passing through measuring tray 5 will be related to the number of columns containing a discharged tube, provided the density is sufficiently high to give a few particles passing through the tray, and sufficiently low not to saturate the tray. There are two steps in determining this relationship. Firstly, the distribution of the number of columns,  $c$ , containing at least one discharged tube compared to the number of tubes discharged in any one layer,  $n$ , must be determined. Secondly, a knowledge is required of the probability of  $n$  out of a total of  $m$  tubes of equal area in one layer being discharged when struck by a shower of particles of mean density,  $\rho$ .

Considering the first stage, the variation of  $c$  with  $n$  can be found from the experimental data. Every event collected by the spectrograph will have a specific number of tubes ( $n$ ) discharged in any one layer of measuring tray 5, and will also have a specific number of columns ( $c$ ) containing at least one discharged tube in measuring tray 5. Thus a histogram of the frequency of values of  $c$  for any given value of  $n$  can be compiled from the basic data files. Histograms have been generated for all values of  $n$ , from 1 to 89, for layer 4 of measuring tray 5, and the histograms for  $n = 7$  and  $n = 11$  are shown in Figure 3.10. Layer 4 was chosen as it was an efficient layer. However, for high densities of particles passing through the tray, a saturation effect occurs where alternate layers of flash tubes fail to discharge. This effect can be seen in Figure 3.5 where few tubes have discharged in layers 3, 5 and 7 despite a large number having discharged in the other layers. The tubes which apparently fail to discharge have the earth electrode above them. It was noticed by the author during the construction of the red side flash tube trays that the 'spacers', designed to keep the flash tubes apart and held in straight lines, tended to prevent the electrodes from actually touching the flash tubes. Work by Doe (private communication) has shown that the efficiency of the flash tubes drops about 30% if the electrode does not actually touch the tube. Consequently the spacers were adjusted for the red side but no change was possible on the blue side where this effect is seen to occur. However, the efficiencies of different layers of tubes for low densities of particles is fairly uniform. Table 3.3 gives the values for each layer in tray 5 which have been determined using the single particle data only. The mean spacing of the tubes is 0.86 cm, centre to centre, and the mean internal diameter, 0.55 cm. Thus if consideration is limited to densities of particles below the densities that cause this effect, then the probability of there being  $c$  columns containing at least one discharged tube can be determined as a function of  $n$ . In the case of layer 4 measuring tray 5,

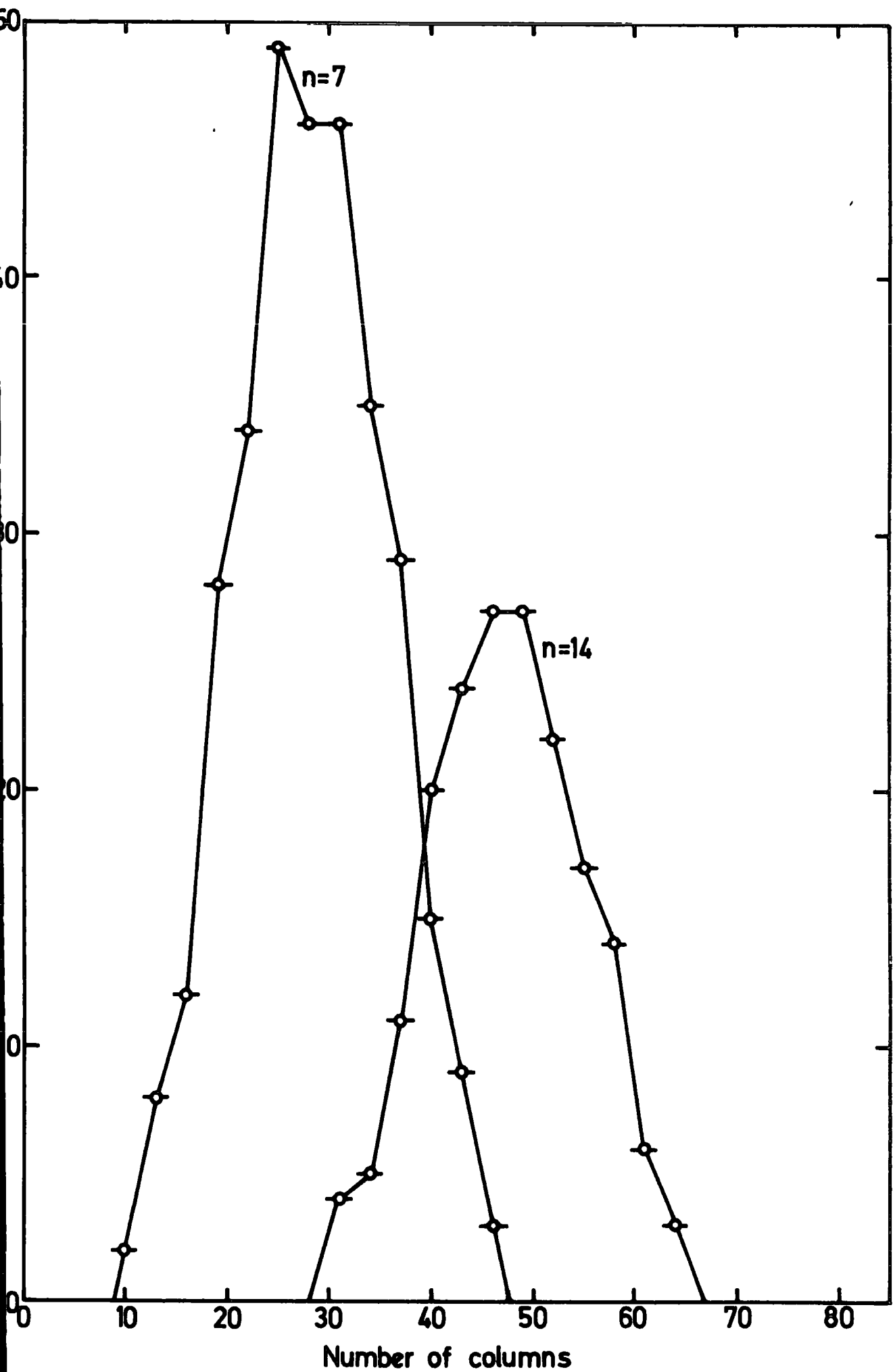


Figure 3.10 Experimental histograms of the frequency of number of columns in tray 5 for 7 and 14 tubes discharged in layer 4 of tray 5.

THE EFFICIENCIES OF THE FLASH TUBES IN MEASURING TRAY 5

TRAY	1 (top)	2	3	4	5	6	7	8
TRAY EFFICIENCY %	53.34	57.02	54.58	57.12	45.32	58.32	56.22	55.72
TUBE EFFICIENCY %	82.58	88.28	84.50	88.43	70.16	90.29	87.04	86.26

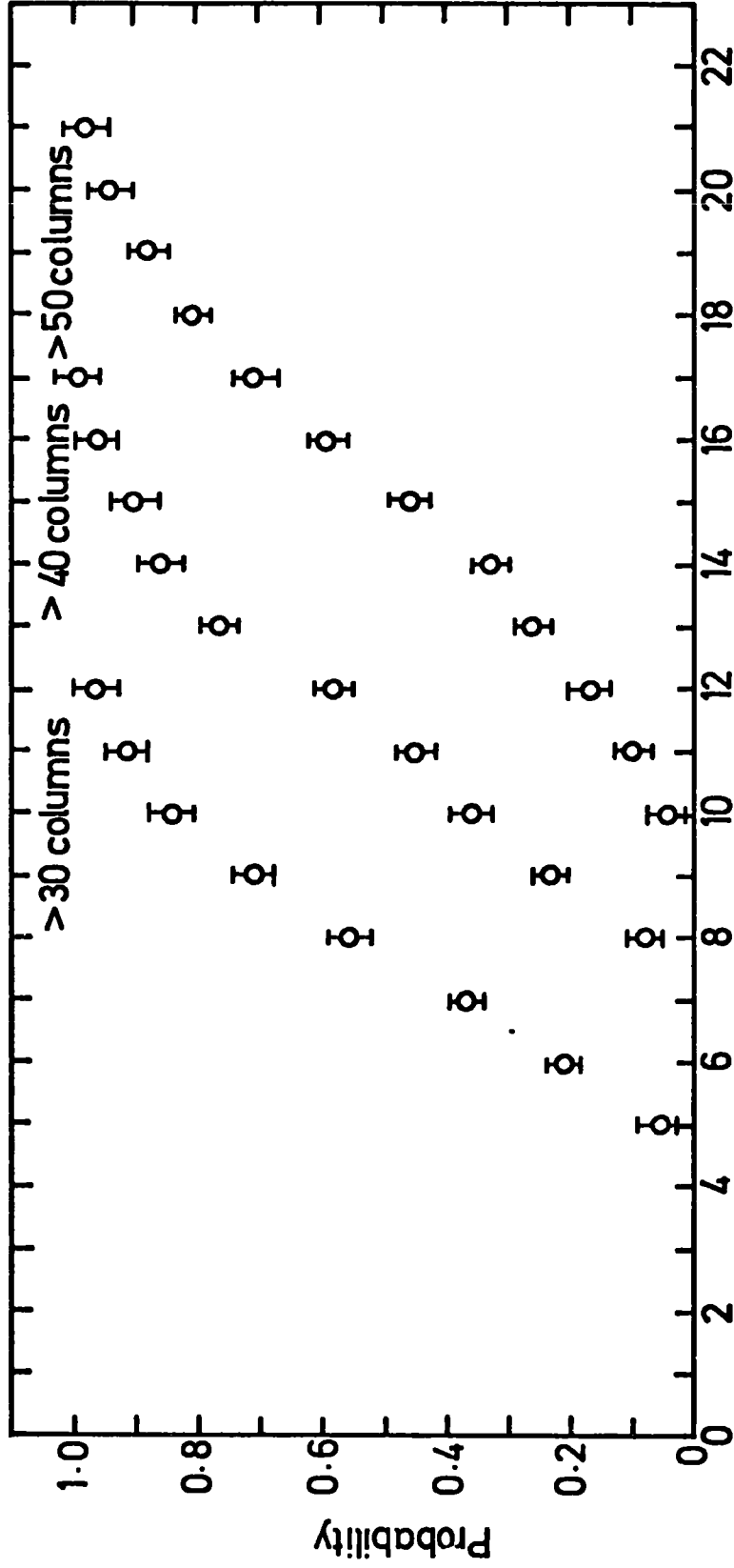
TABLE 3.3

the probability of there being >30 columns containing at least one discharged tube for any one value of n, is the ratio of the area beneath the curve of Figure 3.10 below the 31 column mark, to the total area beneath the curve. It must be emphasised that only one tube need have discharged in a column for the column to be considered as a column of data. From the set of histograms corresponding to all values of n, 1 to 89, the probability of there being >30 columns of discharged tubes can thus be obtained as a function of n. Figure 3.11 shows the probability of >30, >40 and >50 columns of discharged tubes as a function of n, determined in this way. Above about 60 columns containing discharged tubes, the onset of the saturation effect changes the relation of tubes discharged in layer 4 to the total columns containing discharged tubes. Hence 51 columns of data have been taken as the extreme limit for determining the particle density from the flash tube data.

The second stage in determining the relationship of columns discharge to the density of particles is the application of the Poisson probability formula, equation 3.4. This relates the probability, P (n), of n out of a total of m particle detectors, each of equal area S, being struck when the mean density of particles is  $\rho$ .

$$P_m(n) = \frac{m!}{n!(m-n)!} \left\{ 1 - e^{-\rho S} \right\}^n \left\{ e^{-\rho S} \right\}^{m-n} \quad (3.4)$$

Each flash tube is considered as a particle detector of area equal to internal diameter times the length of tube covered by the electrode. The efficiency of the tube, the probability of the tube discharging if a particle passes through the internal volume, is assumed to be uniform over its length. Thus for a given particle density the probability of n tubes being discharged in layer 4 of measuring tray 5 can be determined.



n number of tubes in layer 4 measuring tray 5

Figure 3.11 Probability of >30, >40, and >50 columns discharged in the whole of measuring tray 5 vs. number of tubes discharged in layer 4 of that tray.

To combine the two stages into a probability of a given number of columns of data ensuing from a mean density of particles a computer program was constructed that employed the Monte Carlo technique. This technique is discussed below and explained in more detail in appendix A. For each value of density the number of tubes discharged in layer 4 was selected from the probability distribution, equation 3.4. The shape of the distribution for different values of mean density  $\rho$  is shown in Figure 3.12 where the number,  $n$ , of discharged tubes was generated by the Monte Carlo technique. The probability,  $P_{3|}$ , of getting greater than or equal to 3| columns of data for  $n$  tubes discharged in layer 4 is used next by the program. If a number selected randomly between 0 and 1 is greater than  $P_{3|}$  the program records a 'failure' and if the number is smaller than  $P_{3|}$  the program records a 'success'. In a program cycle of 10,000 trials for each value of mean density the ratio of success to the total number of trials gives a value of the probability of 3| or more columns of data. This process was repeated for 4| or more and 5| or more columns of data in measuring tray 5 for each value of mean density,  $\rho$ . The variation of probability with mean density is shown in Figure 3.13 for each of these cases.

A further check on the ratio of the density of shower particles passing through the tray to the number of columns containing a discharged tube was made by a more direct simulation of particles passing through a computer model of a tray. In this computer simulation an arrival direction was selected for each shower of particles considered. The selection was made, again by the Monte Carlo technique, from a non-isotropic distribution in Zenith angle. The frequency of arrival was considered to vary as the cosine raised to the power eight of Zenith angle. Each particle was assigned a random position along the top edge of the measuring tray and considered to travel undeviated down through the eight layers of flash tubes. For each

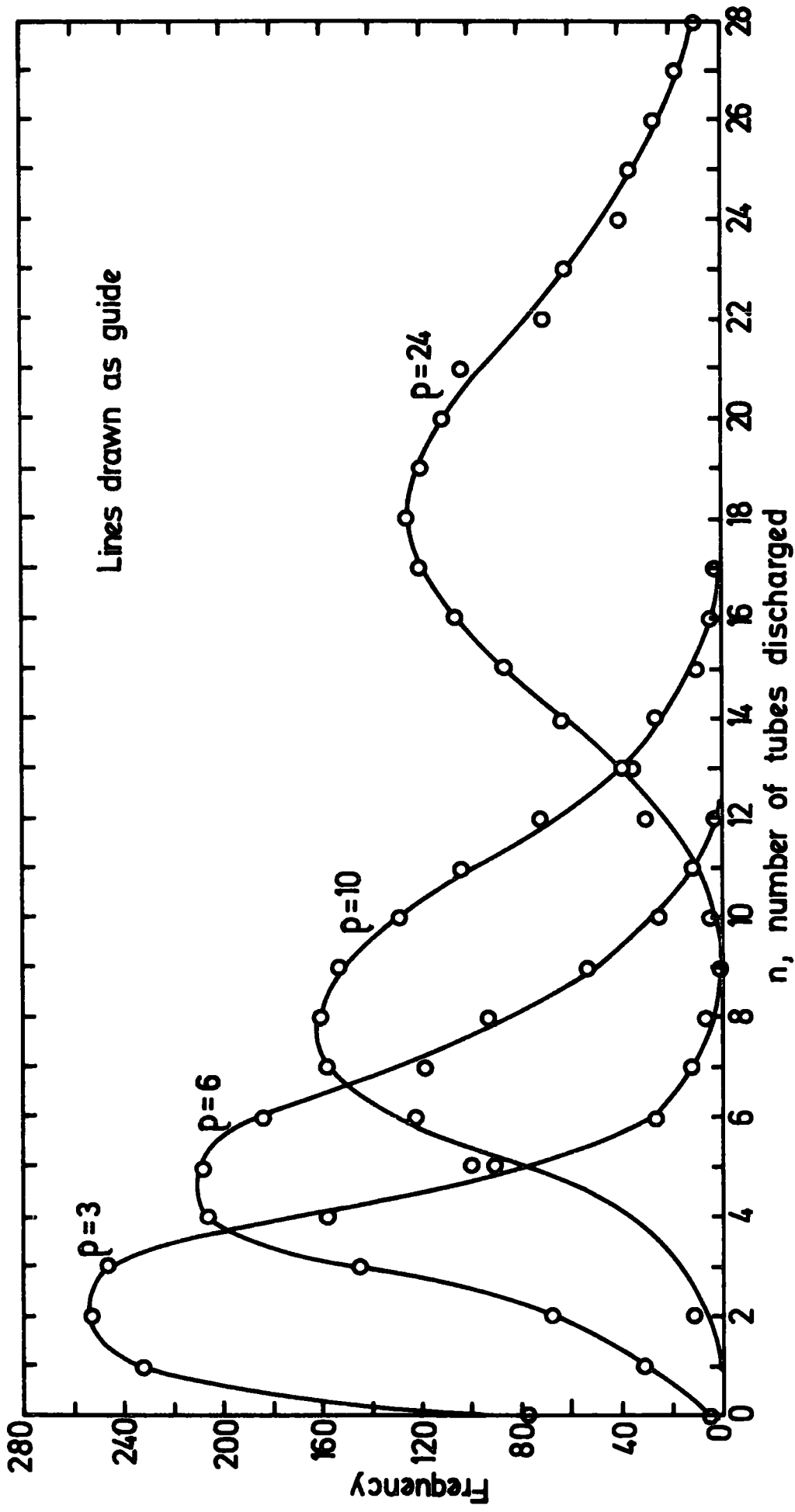


Figure 3.12. Frequency of tubes discharged ( $n$ ) for particle density ( $p$ ). Monte Carlo generated values.

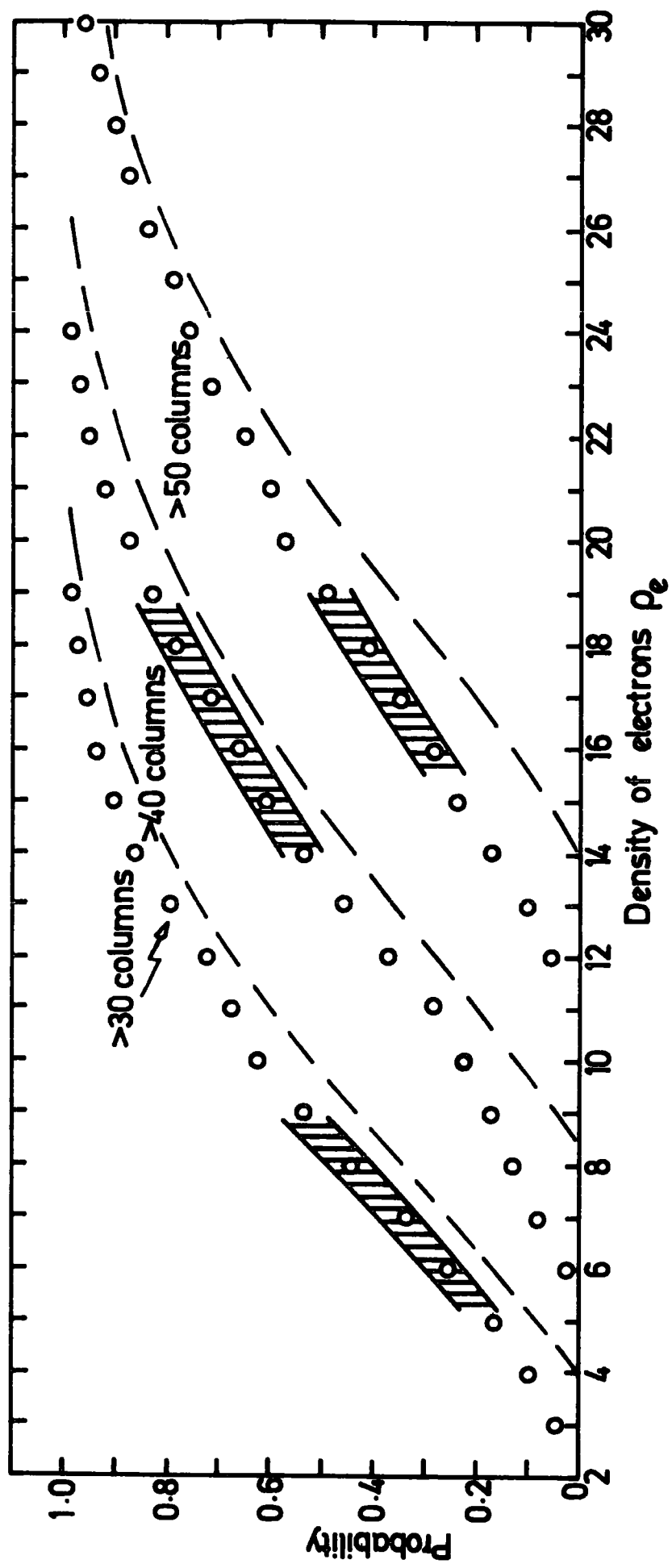


Figure 3.13 Probability of getting greater than a given number of columns from a given density of electrons.

simulated event of  $n_e$  particles a total of  $C$  columns containing a discharged tube was obtained. The distribution of the values of  $C$  for the values of density,  $n_e$  divided by the area of the tray, agrees with the relationships of Figure 3.13 in general shape but is about 10% lower in probability for each value of density. (The dashed curve). A possible source of this discrepancy may be the method used to allow for the efficiency of the tubes in the two methods. In the first method the tube efficiency of layer 4 was used to reduce the density in equation 3.4 to give an effective density for producing the probability distributions shown in Figure 3.12. In the latter method of determining the number of columns from the number of particles the tube efficiencies for each layer were used to reduce, via the Monte Carlo technique, the probability of a tube discharging. Part of the discrepancy may be due to individual 'extra' tubes which have discharged. Figure 3.9 shows the tubes discharged in measuring tray 5 for 3 separate events, where a number of single tubes appearing not to lie on any track can be seen. Some discharges are presumably due to low energy knock-on electrons that are generated by the shower passing through the material above and in the measuring tray. Consequently the probabilities of the number of columns for different densities as determined by the first method discussed (relying more heavily on the experimental data) have been used for the theoretical calculations given later.

A comparison of the density of shower particles as measured by this technique and by the air shower array is shown in Figure 3.14. This figure is a plot of the number of tubes discharged in layer 4 of measuring tray 5 against the density of particles in the region of the spectrograph as calculated using the array measured densities and the Greisen (1960) semi-empirical structure function (equation 4.4 in the next chapter). The events plotted correspond to the data from the experiment under conditions where the air shower array was interrogated on a master pulse from M.A.R.S. In all these

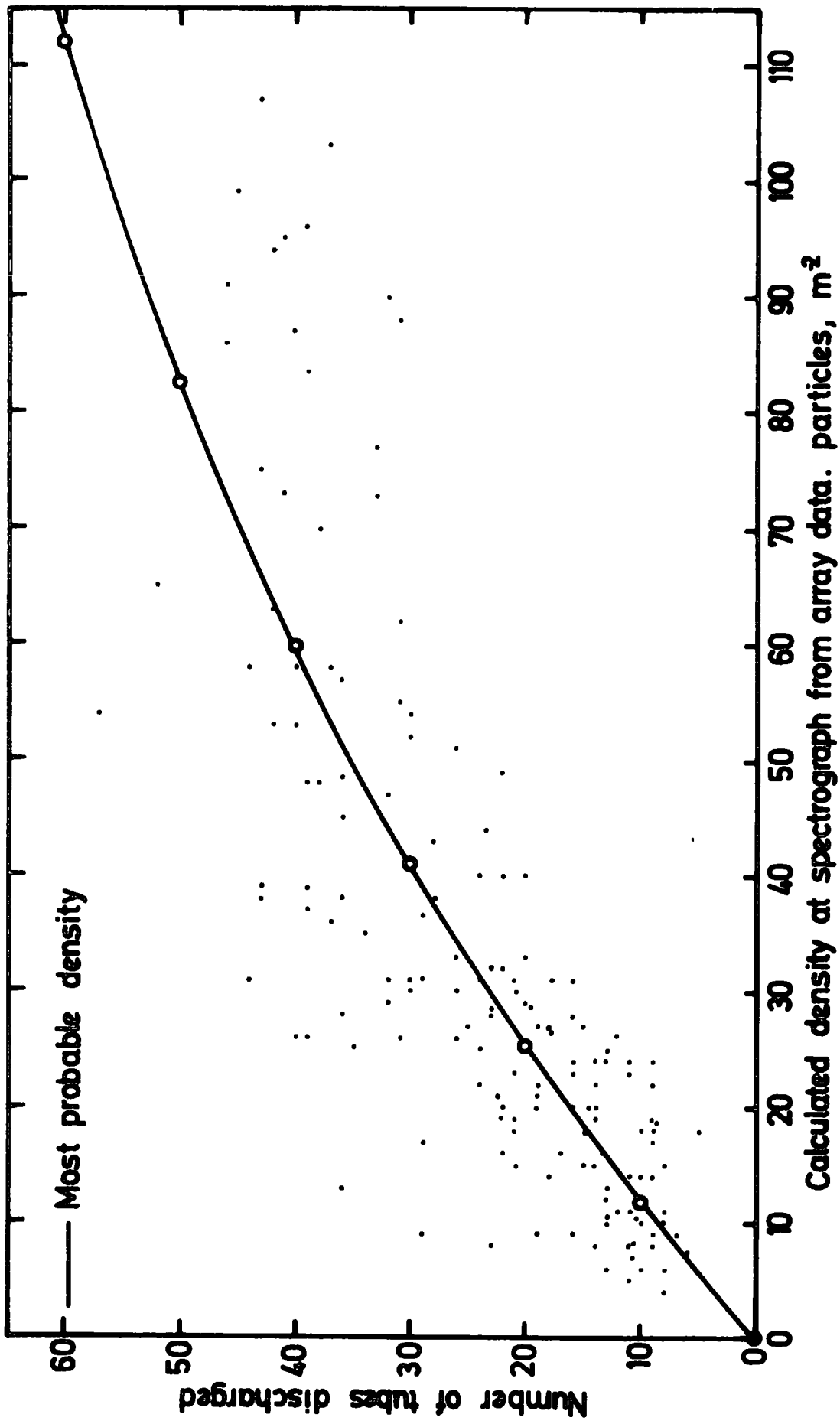


Figure 3.14. Comparison of the density of particles at the spectrograph determined from the array measurements with the number of tubes discharged in layer 4 of tray 5.

events a muon of momentum greater than 6 GeV/c traversed the spectrograph and a shower of greater than  $10^5$  particles fell within 50 metres of the centre of the array according to the subsequent muon and shower analysis. The line in Figure 3.14 is the most probable density for the number of tubes discharged. Differentiating equation 3.4 with respect to density,

$$\frac{\partial P_m(n)}{\partial \rho} = \frac{m!}{n!(m-n)!} \left\{ \left\{ 1 - e^{-\rho s} \right\}^n \left\{ -s(m-n) \right\} e^{-(m-n)\rho s} + e^{-(m-n)\rho s} n s e^{-\rho s} \left\{ 1 - e^{-\rho s} \right\}^{n-1} \right\} \quad (3.5)$$

and the most probable density  $\rho_p$  will be when

$$\frac{\partial P_m(n)}{\partial \rho} = 0$$

so

$$\frac{m}{m-n} = e^{-\rho_p s} \quad (3.6)$$

Further consideration of these density measurements is given in Chapter 6.

### 3.4.3 THE VALIDITY OF THE MUON DATA

In order to determine as accurately as possible the absolute rate of muons accompanied by air showers using the spectrograph, consideration must be given to the possibility of the chance alignment of tracks being analysed as events, and of genuine trajectories being missed due to the density of accompanying particles. A computer simulation of the spectrograph measuring trays was used in order to determine the probability of chance alignment of tracks occurring. For each tray in turn a random point was selected along the top edge. A track was then constructed down through the eight layers of tubes and the resulting pattern of tubes traversed, was stored. The direction of the tracks in all the trays was selected from a distribution as described in Section 3.4.2. Again, a non-isotropic distribution was used ranging over  $\pm 7^\circ$  to the Zenith. However, in each tray

approximately 25% of the tracks were directed randomly. This extent of tracks not following the general direction of the air shower was determined from studying computer plots of genuine events that have a large number of tracks. The stored tube patterns for each event were then analysed by the M.A.R.S. 2 analysis program. The result of this investigation was that for the lower 4 measuring trays, each containing up to six tracks, the probability of chance alignment was less than 0.2% if a standard deviation of less than  $0.25 \cdot 10^{-2} \text{ m}$  was required for trajectories corresponding to a momentum of greater than 20 GeV/c. However, when only 3 trays were considered the probability of chance alignment was about 20% for only a total of 3 tracks in each tray. This is largely because of the relative ease with which a parabola can be fitted to 3 points. Hence a 4 tray fit has been achieved whenever possible and for this reason data from the lower 3 trays alone has not been considered. With regard to obscuration of trajectories, 0.05% of all the events that triggered the momentum selector and discharged more than 30 columns of tubes cannot be deciphered for this reason. The events are mainly showers arriving at large angles. (for example Figure 3.15). The particle tracks appear to be highly inclined and if the particles are electrons they must arrive at large angles in order to penetrate into the trays between the magnet blocks. For large angle showers a muon is most unlikely to pass through all 4 lower measuring trays. Consequently no correction has been applied for this possibility.

0000 0000 0000 0000 0000 0000  
0.0 0.0 0.0 0.0 0.0 0.0



Figure 3.15 A large angle ( $\sim 30^\circ$ ) shower causing a high density of discharged tubes in all the measuring trays.

## CHAPTER 4

### THE RATE OF MUONS IN AIR SHOWERS

#### 4.1 INTRODUCTION

During the experimental runs of the M.A.R.S. spectrograph performed to determine the unassociated muon momentum spectrum, data was collected that corresponded to small air showers falling near the spectrograph. These showers triggered the spectrograph in conjunction with a muon traversing it. The spectrograph was not designed to detect muons with air showers, but with an understanding of its performance for such events valuable information may be gained about muons of momentum in the range 20 GeV/c to 1000 GeV/c in showers of size ranging from  $10^3$  to  $10^7$  particles. The integral rate of such events is presented in this chapter together with calculations of the expected rate using two different approaches.

The first determination of the expected rate of events makes use of the sea level shower size spectrum, and essentially empirical structure functions for the muon and electron densities in air showers. The second approach is based on results of calculations on the expected characteristics of muons generated by primary nucleons using the 'usual' C.K.P. model for high-energy interactions as put forward by Cocconi et al, (1961), and the scaling model of Feynman (1969). The calculations are due to Goned, (1975), and Fishbane et al., (1974) and have been applied to the present work by the author.

#### 4.2 THE EXPERIMENTAL RESULTS

The data presented in this chapter was collected from September 1973 until March 1976. For convenience of handling, the data was stored and analysed in five separate files. The run time and total events in each file can be seen in Table 4.1a. The rate of events can be seen to have decreased in the middle period of data collection, but returned to its former value toward the end. The increase from about 12% to 20% in 'shower triggers' of the spectrograph is the result of the additional experiments conducted as mentioned

THE SHOWER DATA

Data File Name	Run Time h, m, s	% Shower Events	No. Events >20 GeV/c	Rate h <sup>-1</sup>
A 4-5-6	1209:55:09	14.1	280	.232
A 7-8 M1	1649:01:54	12.1	317	.192
M2	697:17:51	12.2	141	.202
M3	467:19:06	19.9	96	.206
M4	1094:50:31	23.1	246	.224
TOTAL	5118:24:31	16	1080	.211

TABLE 4.1a

in Chapter 2. Shower triggers are defined as events with 31 or more columns of data in measuring tray 5. A cut at a minimum muon momentum of 20 GeV/c has been made for events considered in this chapter. Notably, the rate of events of momentum less than 20 GeV/c has increased substantially during the course of the additional experiments. The 'overall' acceptance of the spectrograph has reached its limiting value for muons of momentum greater than 20 GeV/c. A detailed discussion of the acceptance of the spectrograph for all the situations relevant to this thesis is given in Chapter 5 and Appendices B, C and D.

The results of the 'data editing' described in Chapter 3 are given in Table 4.1b. The '3-tray' fits have been divided into those events with only two tubes discharged in any tray and those events with a burst in any tray. Measuring tray 3 has inefficient layers of tubes and contributes most heavily to the 'two tube' events. As this instrumental effect is largely momentum independent, the integral rate has been adjusted for these events, as opposed to adding them to the spectrum according to the '3-tray' computed momentum. The adjustment has been done according to the percentage of events above any integral point. Thus at greater than 20 GeV/c the increase is 62 and at greater than 100 GeV/c the increase is 24, and so on. The probability of '3-tray' fits resulting from bursts will be momentum dependent, as the probability of the muon being accompanied by a large number of electrons out of a magnet block is momentum dependent. (Hansen, (1975) Hansen and Thompson, (1976)). The integral rate for these events is given in Table 4.1c. No correction has been applied to the presented data for these events. The events corresponding to error codes 66n, 88n, and 55, have all been used and are included in the experimental values used later in this chapter.

A correction must be applied to the computed momentum as returned by the analysis programs to allow for the gaps in between the blocks and the energy lost by the muon. Wells, (1972) gives the value of momentum that must

THE 'EDIT-MODE' DATA

ERROR CODE	Number of Events in Each Condition				Total for all Trays
	<u>Tray No.</u>				
	1	2	3	4	
4 Tray Fits { 66 88 55	68	58	73	60	259
	16	12	17	31	76
					65
3 Tray Fits { 99 2 tubes 99 burst	11	4	41	6	62
	8	5	2	5	20

TABLE 4.1b

INTEGRAL SPECTRUM FOR 3 TRAY FITS (BURSTS)						
$P_{\mu}$ GeV/c	>20	>50	>100	>200	>500	>1000
Number	20	17	15	8	4	2

TABLE 4.1c

be added to the computed momentum for a muon arriving at  $\pm 6^\circ$  and  $0^\circ$  to the vertical in the bending plane. The mean of these values is given in Table 4.1d for five different values of momentum. The technique used here was to compile the computed values of momentum into an integral rate above a given momentum and then adjust this momentum point according to the appropriate correction. The results are presented as the integral rate of arrival of muons of momentum in the range 20 GeV/c to 1000 GeV/c accompanied by shower particles discharging tubes in greater than a given number of columns. The rates for  $>30$ ,  $>40$  and  $>50$  columns in measuring tray 5, having at least one discharged tube, are shown in Figures 4.10, 4.11 and 4.12.

#### 4.3 THE CHARGE RATIO OF MUONS IN AIR SHOWERS

The charge ratio of muons,  $N_{\mu^+}/N_{\mu^-}$ , in the events which have more than 30 columns of data is presented in Figure 4.1. The charge ratio of muons near the core of showers is expected to be unity on the theoretical grounds that most muons are secondary to pions which are the products of successive interactions, thus masking any possible charge asymmetry. Measurements by Machin et al., (1969) on muons greater than 150 m from the core gave an overall charge ratio of  $1.00 \pm .03$  for muon momenta greater than 1 GeV/c and Orford et al., (1967) found the ratio to be near unity (see Figure 4.1). The muons studied were in the momentum range 10-100 GeV/c at 10-100 m. from the core of showers produced by primaries in the range  $10^{14}$ - $10^{17}$  eV and with zenith angles less than  $45^\circ$ . However, the ratio above a muon momentum of 100 GeV/c was noted to increase. The overall ratio was found to be unity by Bennett & Greisen (1961). In small showers, the charge ratio of very high energy muons might begin to show the positive charge excess of unassociated muons if the muons are from one of the very first interactions.

#### 4.4 THE NATURE OF THE MUON EVENTS ACCOMPANIED BY PARTICLES

During the latter part of the experimental run described above, the Durham air shower array was in operation. From those times that the experiments

CORRECTION TO BE ADDED TO COMPUTED MOMENTUM

Computed Momentum GeV/c	Correction Fit to Trays 1, 2, 3 & 4. GeV/c
20	5.3
50	5.2
100	5.2
200	5.0
500	4.5

TABLE 4.1d

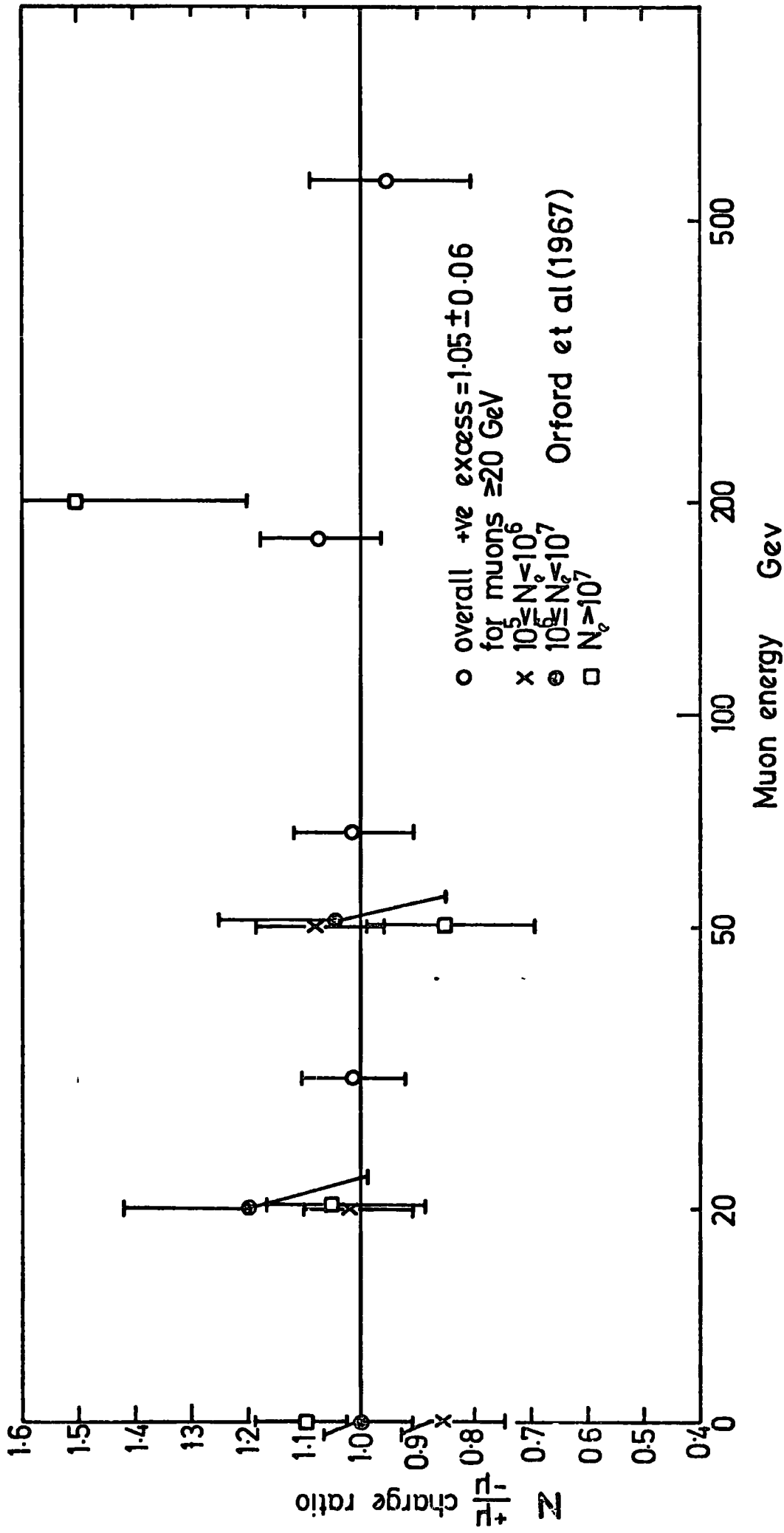


Figure 4.1 Charge ratio of muons accompanied by shower particles discharging  $> 30$  columns.

were operating concurrently, the common 'event number scaler' enables matching of events from one experiment to the other. An indication that events, in which muons are accompanied by particles discharging a large number of flash tubes in the top tray of the spectrograph, are air shower events and not local showers induced by the muon, is given by Figures 4.2a and 4.2b. These figures show the distribution of shower sizes and radial distances for 175 events. For all these events the array detected a shower of size greater than  $10^5$  particles within a distance of 50 metres of the spectrograph, and a muon traversed the spectrograph. A further 410 events were registered by the array in which particles were detected but either the shower was too small or the core was too far away from the centre of the array to give a 'successful' analysis of the event. In Figure 4.3 an event is shown in which the bulk of the columns, in which tubes are discharged in tray 5, are due to a burst produced by the muon. This type of event has been rejected using the criterion that if 50% of the tubes discharged are within 10 tube spacings of the projection of the muons track into tray 5, then the shower is assumed local.

#### 4.5 THE PROBABILITY OF THE SPECTROGRAPH BEING TRIGGERED

In order to determine the rate of arrival of muons in air showers an important quantity that must be known is the probability of a given density of electrons and a muon of a given momentum triggering the momentum selector. In practice an air shower falling in the proximity of the spectrograph will trigger it if either a traversing muon is of sufficiently high momentum, or if shower particles in conjunction with a muon set off "sufficient" cells in the momentum selector. For the purpose of this study at least one tube must be discharged in more than 30 columns in measuring tray 5 before the event is considered for analysis. This total probability of 'selection' is considered in two parts,  $P_M$  and  $P_T$ .

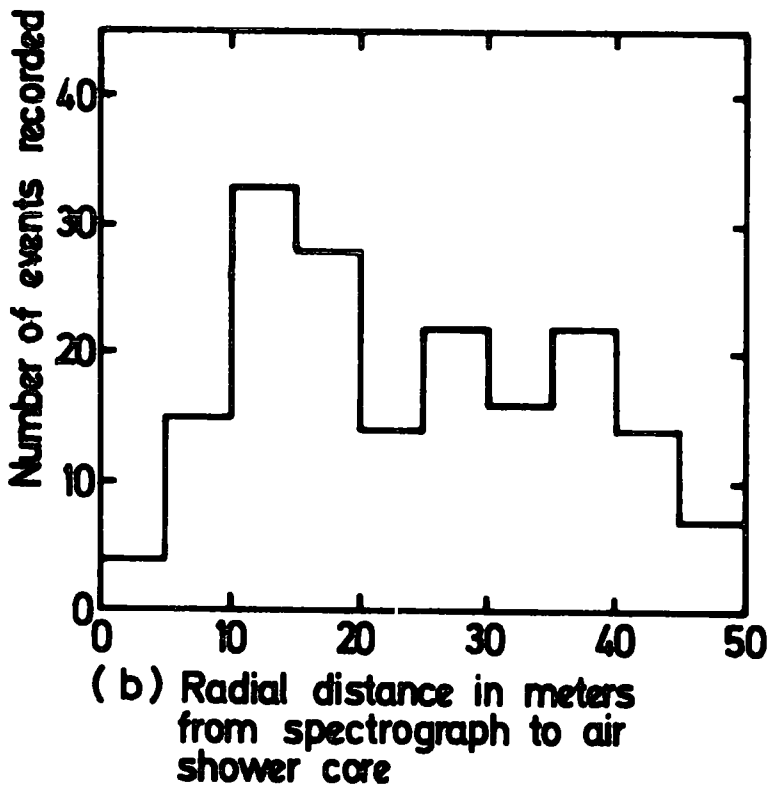
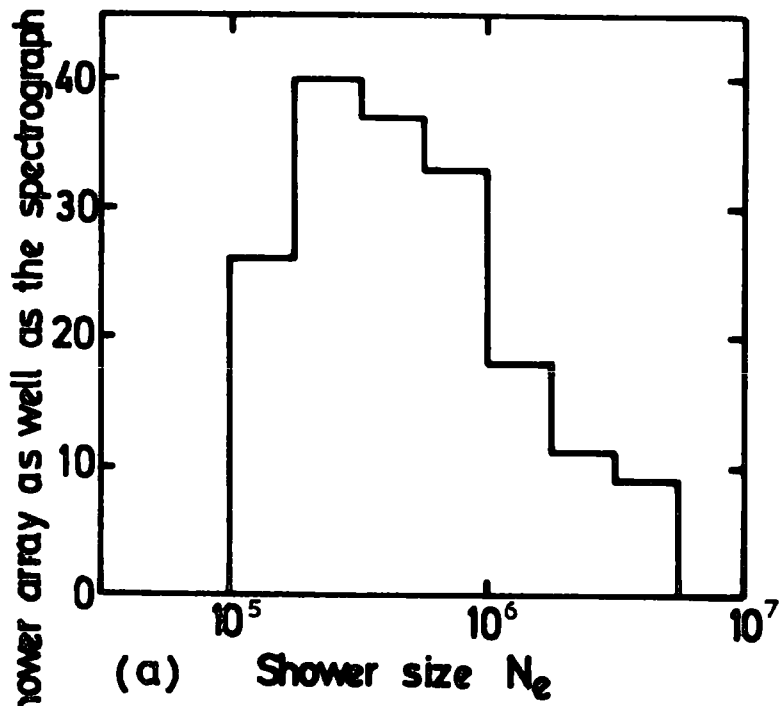


Figure 4.2 Events common to air shower array and the spectrograph.

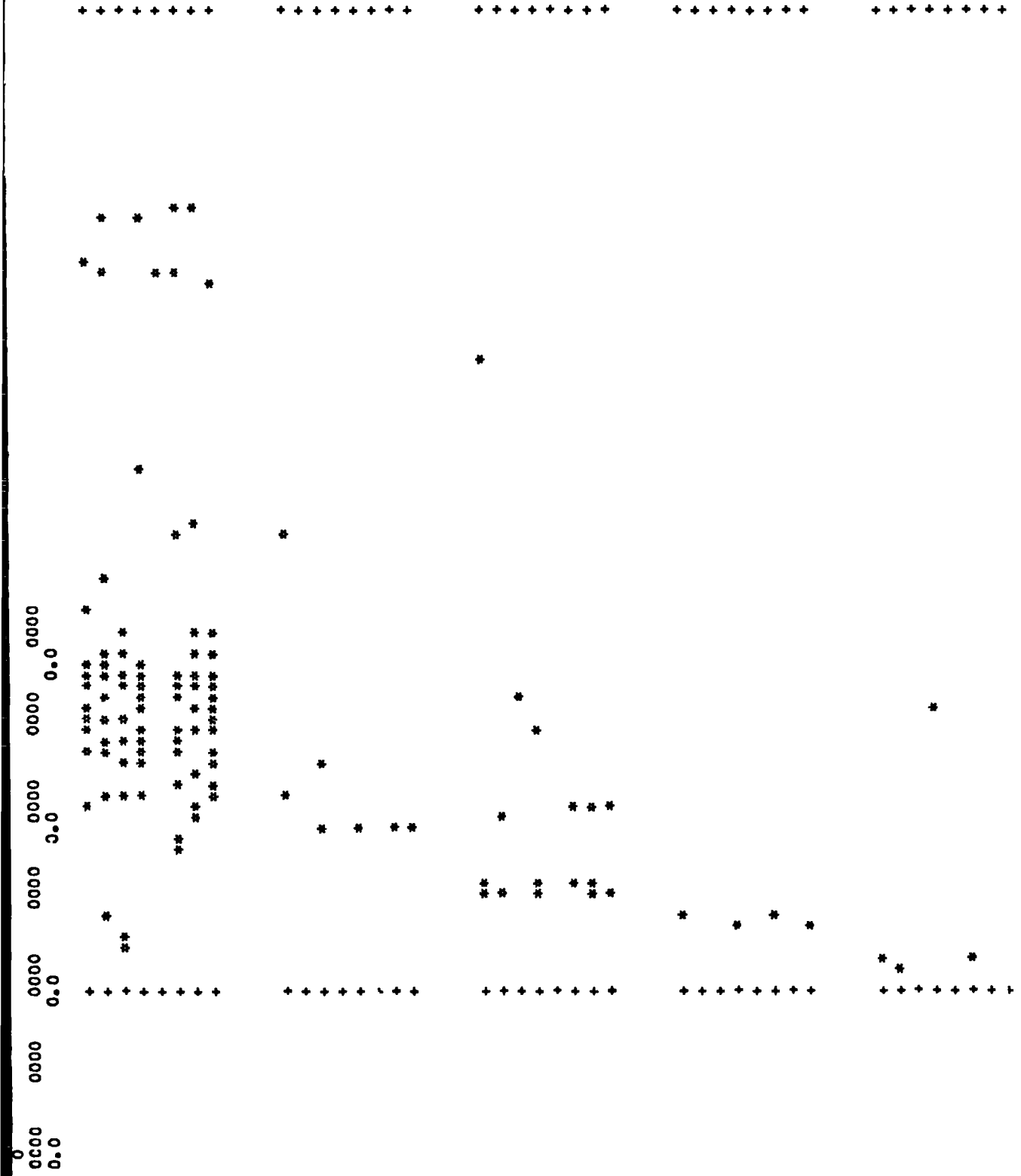


Figure 4.3. A computer plot of a rejected event in which >30 columns contain a discharged tube in tray 5.

$P_M$  is defined as the probability of one or more muons passing through the 'area' of the top of the spectrograph. To convert the rate of events per steradian per second into a rate per second, the effective 'solid angle' of the spectrograph under these shower conditions must also be known. The determination of the relevant area at the top and solid angle is given in Appendix D.

$P_T$  is defined as the probability of both the spectrograph being triggered and at least one tube being discharged in more than 30 columns in measuring tray 5.

The spectrograph can be triggered in two different ways. If the muon traversing the spectrograph is of sufficiently high momentum, the momentum selector cells set will satisfy the 'straight line' condition in the momentum selector logic as described in Chapter 2. The probability of this trigger is shown as a function of the muon's momentum in Figure 4.4. However, if the muon is of low momentum but accompanied by air shower particles, the cells set by the muon in the momentum selector trays at levels 1 and 3 may 'line up' with the cell set by a shower particle in the momentum selector tray at level 5. This trigger is independent of the muon's momentum but will be a function of the density of shower particles.

Thus  $P_T$  is a complex function depending upon the momentum of the muon and the density of shower particles. For muons of momentum below about 100 GeV/c the probability of 3 or more columns of tubes being discharged depends only on the density of shower particles, whilst the probability of triggering the momentum selector depends on the chance alignment of the muon's track in the lower momentum selector trays with the track of a shower particle in momentum selector tray 5. For muons of momentum above about 100 GeV/c the probability of 3 or more columns of tubes being discharged still depends only on the density of shower particles, but the probability of triggering the momentum

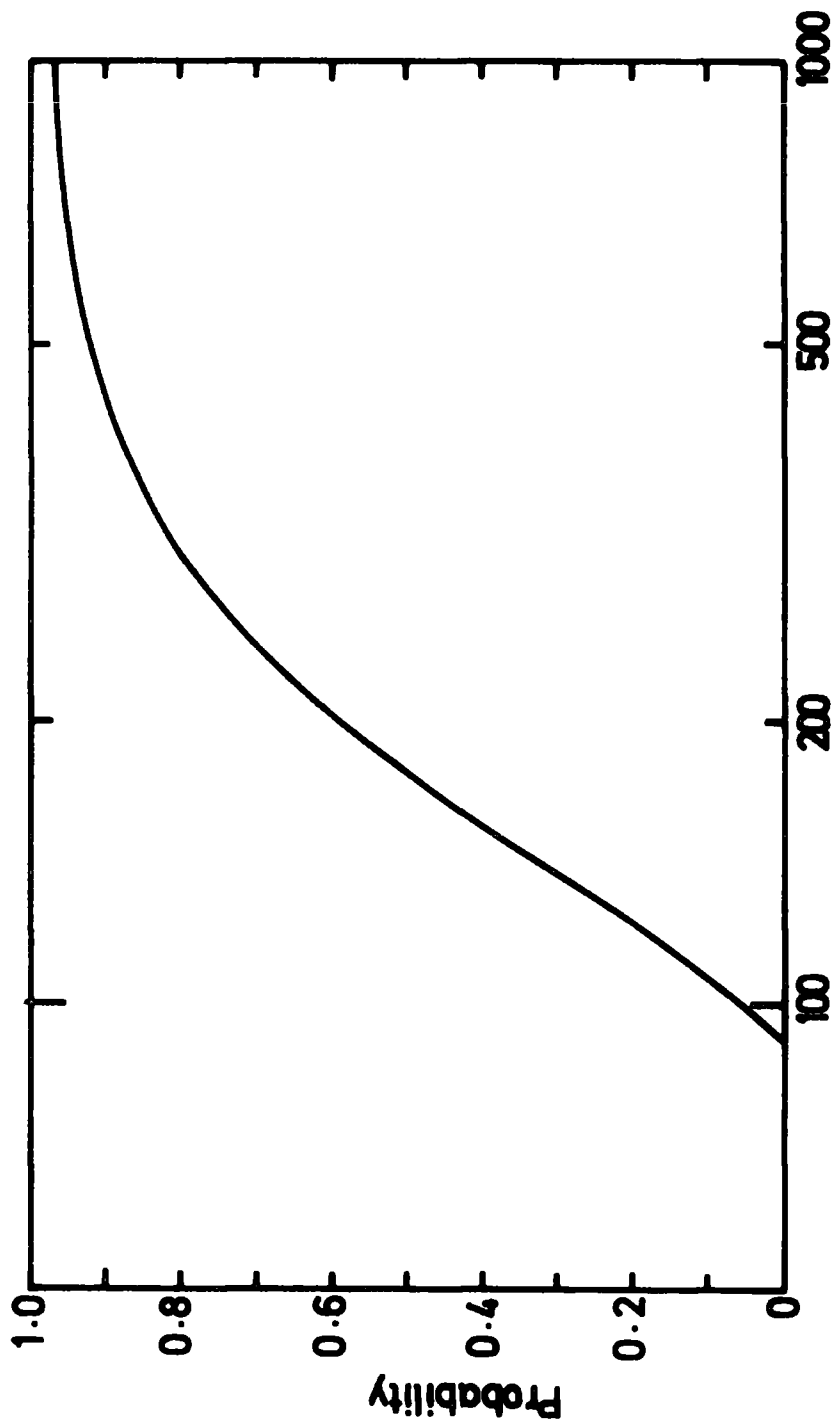


Figure 4.4 Incident muon momentum GeV/c

Probability of muon triggering the spectrograph vs. incident momentum, (after Piggott, 1976.)

selector will be the combination of the probability of chance alignment as above and the probability of a muon 'alone' trigger.

Therefore

$$P_T (P_\mu, \rho_e) = P_C (\rho_e) \left\{ P_{\mu ms} (P_\mu) + P_{ems} (\rho_e) - P_{\mu ms} (P_\mu) P_{ems} (\rho_e) \right\} \quad (4.1)$$

where,

$P_C (\rho_e)$  is the probability of one or more tubes discharged in more than 30 columns in measuring tray 5, and it is a function of the density of shower particles  $\rho_e$ , as shown in Figure 3.13.

$P_{\mu ms} (P_\mu)$  is the probability of the muon triggering the momentum selector and it is a function of the momentum of the muon,  $P_\mu$ , as shown in Figure 4.4.

$P_{ems} (\rho_e)$  is the probability of the chance alignment of a shower particle track with the muon's track in the momentum selector system. It is not a function of the momentum of the muon but depends upon the density of shower particles. The probability of a muon traversing the spectrograph is taken account of in  $P_M$  and thus  $P_{ems} (\rho_e)$  must be determined given that a muon has passed through all the detecting elements of the spectrograph but not caused a momentum selector trigger.

For muons of momentum below about 100 GeV/c equation 4.1 reduces to,

$$P_T (P_\mu, \rho_e) \rightarrow P_T (\rho_e) = P_C (\rho_e) P_{ems} (\rho_e), \quad (4.2)$$

A computer simulation of particles passing through the spectrograph was used to determine the variation of  $P_{ems}(\rho_e)$  with the density of shower particles,  $\rho_e$ . To achieve this, a program duplicated the logic of the electronic 'celling' and deflection determination of the momentum selector. The mode of operation of the program was as follows.

For a given density,  $\rho_e$ , of shower particles falling on the spectrograph the angle of incidence of the shower was selected assuming the shower intensity varies as  $\cos^n \theta$ ,  $\theta$  being the shower zenith angle,  $n$  being 8. The number of electrons within the area ( $S$ ) of the top momentum selector tray of the spectrograph was selected from a poissonian distribution having a mean value equal to  $\rho_e S$ . The co-ordinate of each particle was selected randomly along the top edge of the top tray and the particles passed down through a two dimensional model of the tubes. A 95% tube efficiency was included (Whalley, (1974)), and any tube was considered to have flashed if a particle passed within 0,75 cm. of the tubes centre. The corresponding cells were allocated and passed to the simulated momentum selector logic. Given that a muon had traversed the spectrograph but not triggered the momentum selector, two tracks were selected at random co-ordinates above the simulated momentum selector trays at levels 3 and 1. However, after the selection of the first of these tracks at level 1, the co-ordinate of the track at level 3 was constrained within a limit such that the projection of a straight line through the two co-ordinates passed into the tray at level 5. If the projection to level 5 were to go outside the extent of tray 5, there would be no possible straight line combination in the logic. This is to match the test that was applied to the experimental data that excluded any event in which the muon entered the spectrograph from the side below measuring tray 5. For a very high momentum muon entering below tray 5 the trajectory will hardly be bent and the cells the muon sets in the lower momentum selector trays will have no cell that can be 'aligned' in tray 5. Thus for increasing muon momentum the

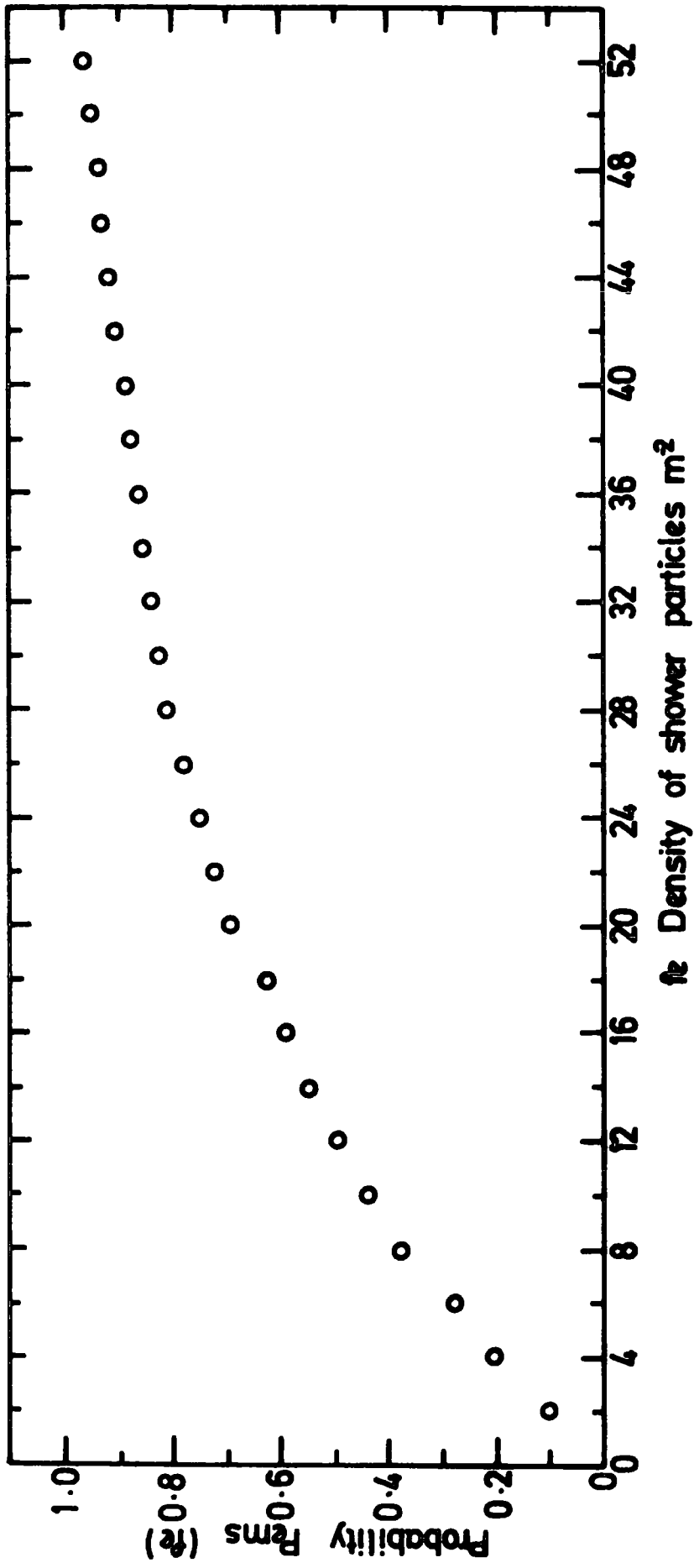


Figure 4-5. The probability of triggering the momentum selector vs density of shower particles.

probability of triggering the spectrograph will decrease for this situation. In the simulation the cell or cells corresponding to the muon's co-ordinates were passed to the simulated logic and together with the cells set by the shower particles the combinations were tested for linearity. For 10,000 such simulations for each value of density the probability of triggering the momentum selector was thus determined as a function of the density of shower particles. The variation of  $P_{ems}(\rho_e)$  is shown in Figure 4.5.

To obtain some internal consistency the computer program just described was combined with the program described in Section 3.4.2, which had been used to determine the variation of  $P_c(\rho_e)$  with density,  $\rho_e$ . This joint routine was used to determine the combination of  $P_{ems}(\rho_e)$  and  $P_c(\rho_e)$  and the values are shown as a function of  $\rho_e$  in Figure 4.6. In this figure the product of  $P_{ems}(\rho_e)$  and  $P_c(\rho_e)$  determined separately is shown as a dashed line.

#### 4.6 THE RATE OF EVENTS DETERMINED FROM THE SEA LEVEL SHOWER SIZE SPECTRUM

To predict the rate of events using the above derived probabilities the passage of a muon through the apparatus was assumed. The acceptance of the spectrograph for a shower accompanied muon merely requires the muon to pass through the lower two scintillation counters as the shower particles will strike the top scintillation counter. However, the situation considered here is somewhat more complicated as the momentum selector must be triggered and for the analysis reasons explained in Chapter 3, the muon must pass through all 4 lower measuring trays. The muon can thus enter the spectrograph below level 5 only from the back or front. This situation is shown schematically in Figure 4.7. The acceptance of the spectrograph for this situation has been determined by a Monte Carlo technique which is explained in Appendix A and B. For an assumed intensity variation with zenith angle  $\theta$ , of cosine  $\theta$  raised to the power 8, the relevant acceptance is  $487 \pm 3 \text{ cm}^2 \text{ sr}$ .

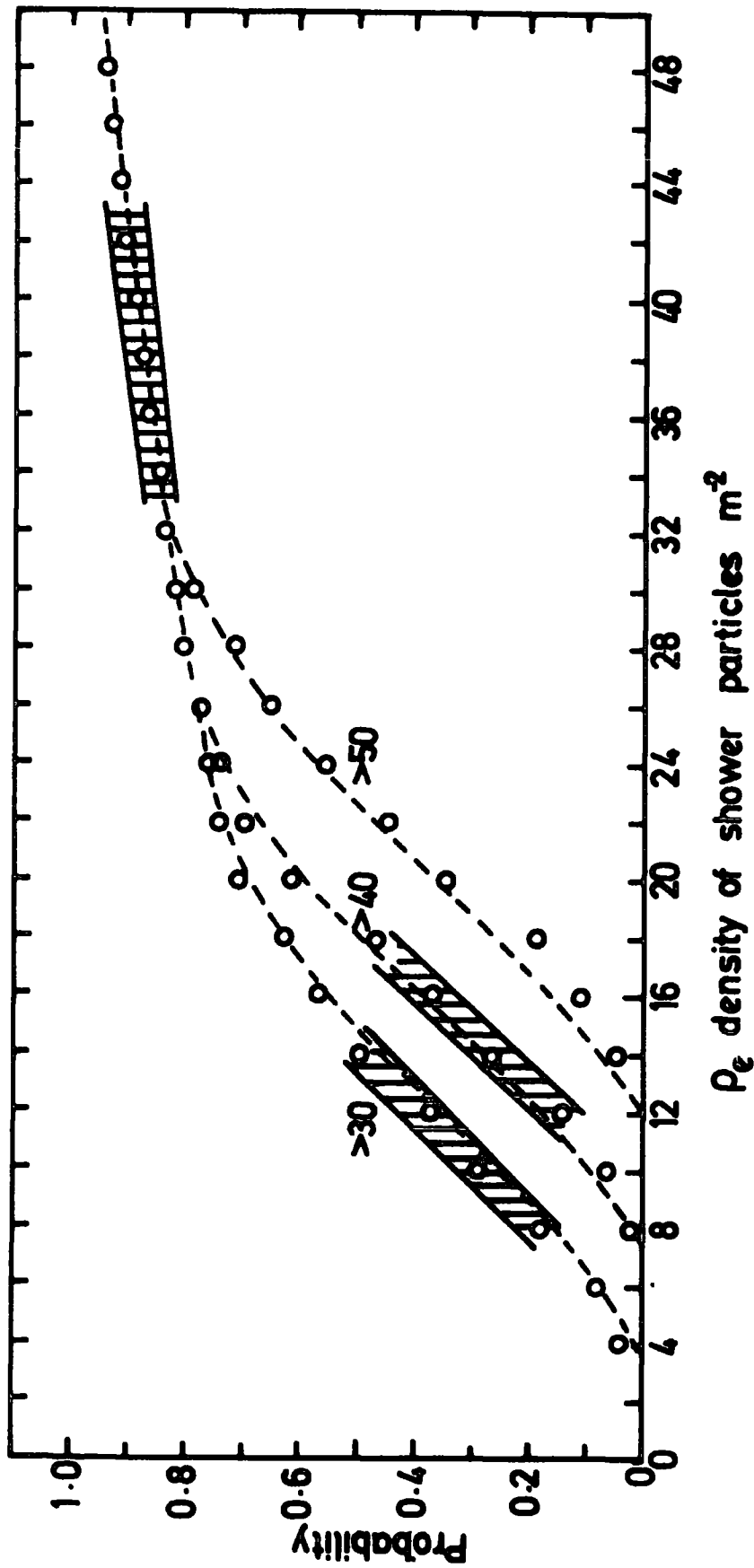
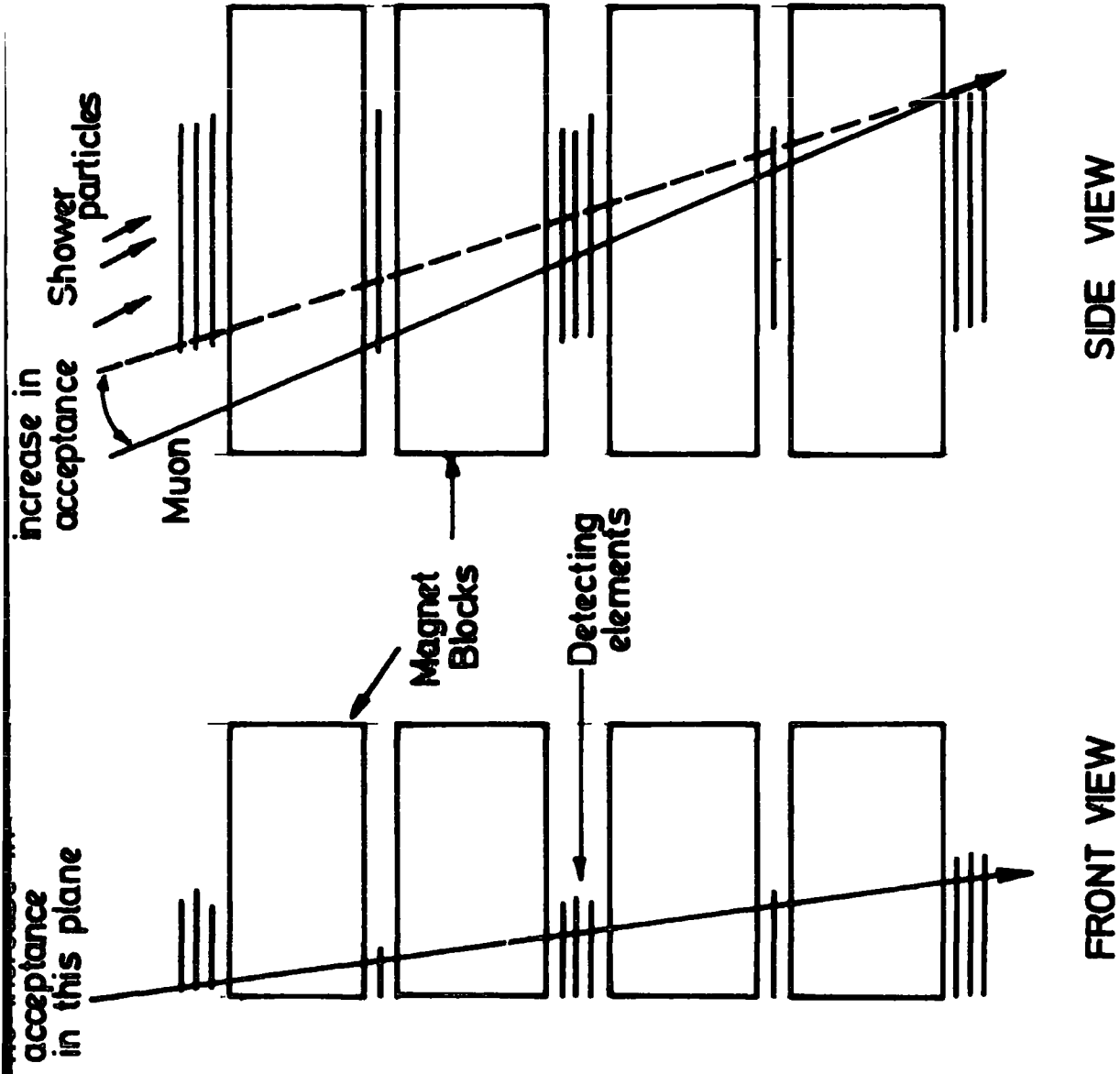


Figure 4.6 Probability of discharging  $>30$ ,  $>40$  and  $>50$  columns in level 5 measuring tray and triggering the momentum selector in conjunction with a muon of momentum  $\leq 100$  GeV/c vs. density of shower particles.



**Figure 4.7** The Spectrograph showing schematically the increase in overall acceptance due to shower particles.

The rate of events will depend on the rate at which air showers fall close enough to the spectrograph to cause the required trigger conditions. Clearly the axis of small air showers must fall nearby whereas larger (but more infrequent) showers can fall at greater distances and still provide the necessary conditions. A survey of the integral sea level shower size spectra is shown in Figure 4.8. The two straight lines drawn through the data points are due to Bell, (1974). They have been determined as the integral slope well away from the 'knee'. The integral spectrum taken from these data for the present work is

$$F(>N_e) = 6.3 \cdot 10^1 N_e^{-1.5} \text{ m}^{-2} \text{ s}^{-1} \text{ Sr}^{-1} \text{ above } N_e = 5 \cdot 10^3, \quad (4.3)$$

and

$$F(>N_e) = 8.48 \cdot 10^4 N_e^{-2.034} \text{ m}^{-2} \text{ s}^{-1} \text{ Sr}^{-1} \text{ above } N_e = 7 \cdot 10^5, \quad (4.4)$$

For the lateral distribution of electrons in air showers Greisen (1960) has suggested an empirical analytic function for the electron density of the form,

$$\rho_e(N_e, r) = \frac{0.4}{r_1^2} N_e \left\{ \frac{r_1}{r} \right\}^{0.75} \left\{ \frac{r_1}{r + r_1} \right\}^{3.25} \left\{ 1 + \frac{r}{11.4 r_1} \right\}^{-2} \quad (4.5)$$

Where  $N_e$  is the shower size and  $r$  the radial distance in m, and where  $r_1$  is the Moliere unit for which at sea level Greisen gives a value of 79 m. This expression, without the last factor, is a close approximation to the theoretical expression for an electromagnetic cascade with an age parameter  $S = 1.25$  as derived by Kamata and Nishimura (1950), and has been used for all the predictions of the present work.

Two different radial structure functions have been used for the muon

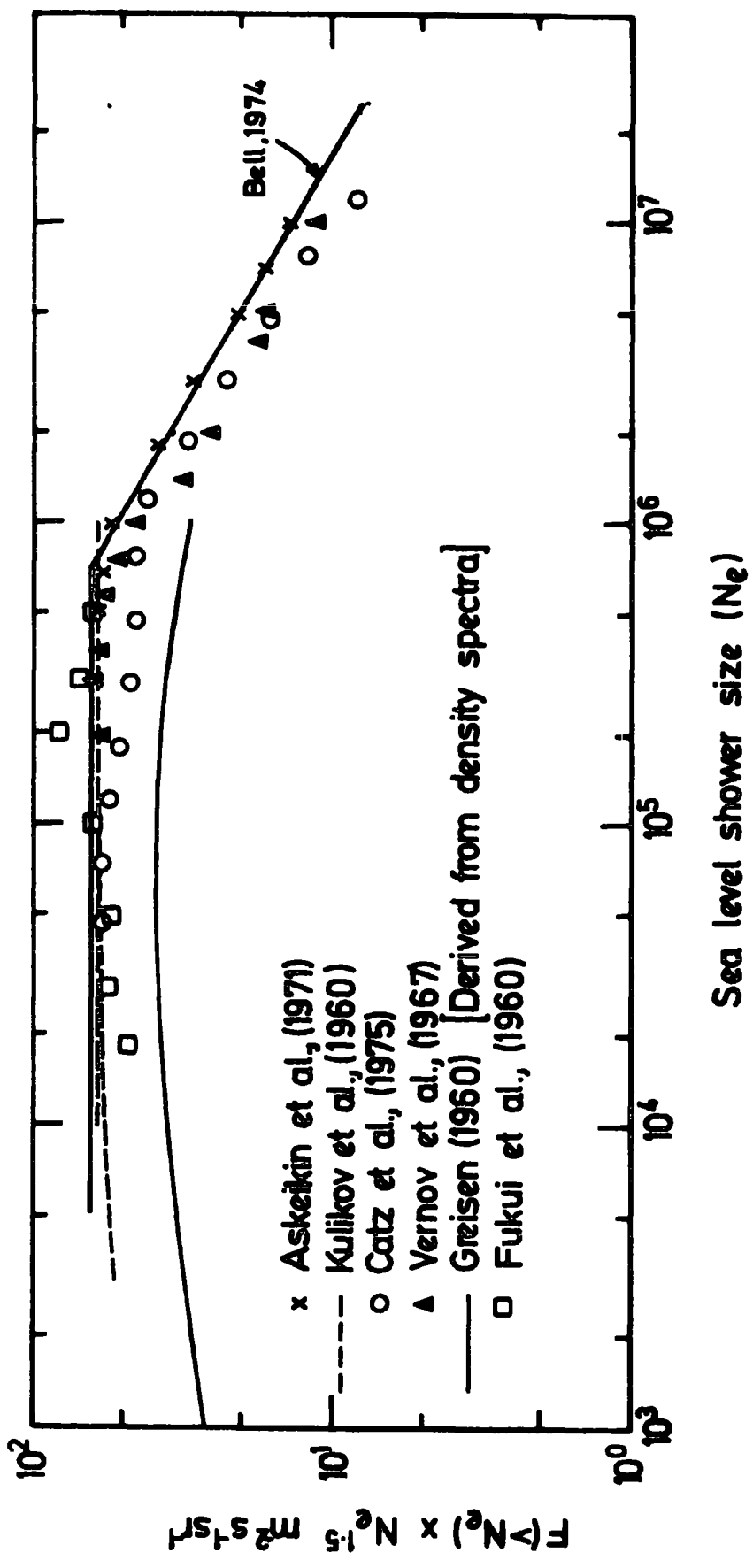


Figure 4.8. Integral size spectrum of air showers at sea level.

component of air showers. The first is due to Greisen (1960) where the density of muons,  $\rho_\mu$ , is of the form,

$$\rho_\mu (N_e, r, >E_\mu) = \frac{14.4r^{-0.75}}{(1 + r/320)^{2.5}} \left( \frac{Ne}{10^6} \right)^{0.75} \frac{51}{E_\mu + 50} \left( \frac{3}{E_\mu + 2} \right)^{0.14r^{0.37}} m^{-2} \quad (4.6)$$

Where  $E_\mu$  is the threshold energy of the muons in GeV and  $r$  is the radial distance in m., and  $Ne$  the shower size. This expression is based on measurements of muon spectra in air showers in the range from  $10^3$  particles to  $10^7$  particles at sea level. (Bennett and Greisen, 1961). The range of muon energies studied was from 1 to 20 GeV and the range of radial distances from 10 to 500 m. This upper value of muon energy is the lowest energy of muon considered here but Earnshaw et al., (1967) find general agreement with this expression (except for large distances from the core) in studies of muons of momentum up to 100 GeV/c.

The second analytical form of muon structure function has been derived by the present author from the experimental values produced by the Moscow-Lodz collaboration (Rozhdestvensky et al., (1975)). Khrenov (private communication, 1975) suggests a fit to these values (for a muon energy,  $E_\mu$ , greater than 10 GeV) for the density of muons,  $\rho_\mu$ , of the form

$$\rho_\mu (E_\mu > 10 \text{ GeV}, r, Ne) = 1.210^{-4} Ne^{0.8} r^{-0.5} e^{-r/80}, m^{-2} \quad (4.7)$$

where again,  $r$  is the radial distance in m., and  $Ne$  is the shower size.

(See also Kulikov et al., 1974). The following momentum dependent muon structure function,  $\rho_\mu$ , was fitted by the present author to the Moscow-Lodz data points :

$$\rho_\mu (>P_\mu, r, Ne) = A P_\mu^B Ne^{0.8} r^{-0.5} e^{-CP_\mu^D r}, m^{-2} \quad (4.8)$$

the constants

in the expression having the values

$$A = 2.124 \cdot 10^{-4} \text{ m}^{-3/2}, \quad B = -0.27, \quad C = 3.74 \cdot 10^{-3}, \quad D = 0.56,$$

r being measured in metres.

The experimental values and the form of equation 4.8 for 4 values of muon momentum are shown in Figure 4.9. Energy and momentum have been considered as equivalent in magnitude ; the error thus introduced is less than about .05% for values of energy above 10 GeV.

The predicted rate of events in which at least one muon of momentum greater than  $P_\mu$  crosses the 'area' of the top of the spectrograph and the instrument is triggered, and at least one flash tube is discharged in more than 30 columns in measuring tray 5 is then

$$R (>P_\mu) = \int_{\text{All shower sizes}} \int_{\text{All radial distances}} P_M P_T F(\text{Ne}) 2\pi r dr d\text{Ne} \text{ s}^{-1} \text{ sr}^{-1} \quad (4.9)$$

Thus the measured rate will be  $R(>P_\mu) \times$  'solid angle' of the instrument. The appropriate 'area' and 'solid angle' is determined in Appendix D. The differential shower size spectrum  $F(\text{Ne}) d\text{Ne}$  is determined from the integral spectrum such that below the 'knee',

$$F(\text{Ne}) d\text{Ne} = 9.45 \cdot 10^1 \text{ Ne}^{-2.5} d\text{Ne} \text{ m}^{-2} \text{ s}^{-1} \text{ sr}^{-1} \text{ GeV}^{-1} \quad (4.10)$$

and above the 'knee',

$$F(\text{Ne}) d\text{Ne} = 1.724 \cdot 10^5 \text{ Ne}^{-3.034} d\text{Ne} \text{ m}^{-2} \text{ s}^{-1} \text{ sr}^{-1} \text{ GeV}^{-1} \quad (4.11)$$

The probability,  $P_M$ , of one or more muons passing through an area  $s \text{ m}^2$  where the mean density of muons is  $\rho_\mu \text{ m}^{-2}$ , is given by the Poission formula,

$$P_M = 1 - e^{-\rho_\mu s} \quad (4.12)$$

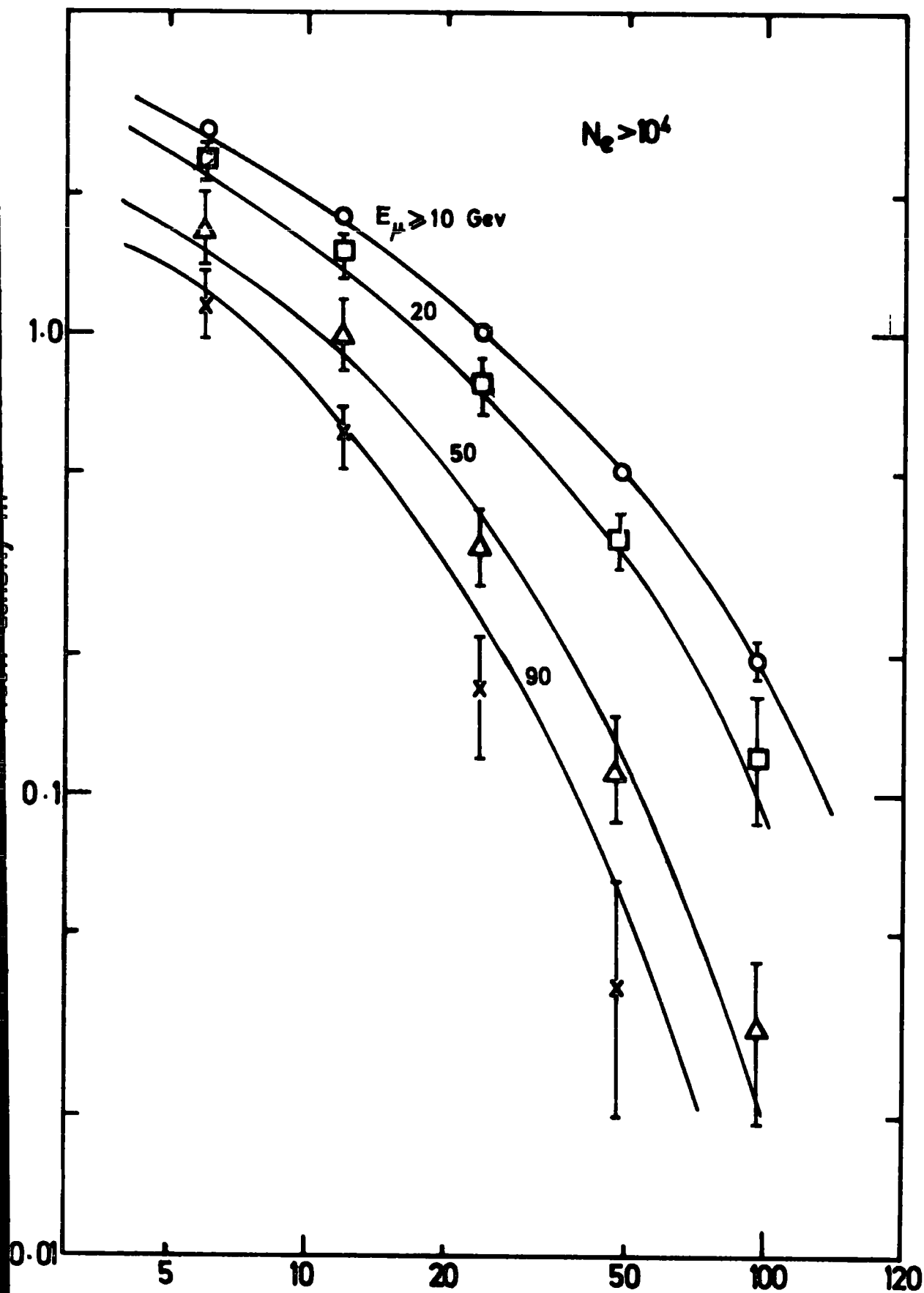


Figure 4.9 R, radial distance, m

Experimental values due to  
et al (Munich 1975)

Rozhdestvensky

$P_T$  is the probability of triggering the spectrograph as described in the previous section.

To evaluate this expression the limits of integration must be set and must include all shower sizes and all radial distances that contribute significantly to the rate. The range of radial distance used was from 0.1 m. to 100.0 m. out from the centre of the spectrograph. The determination of the density of electrons and density of muons from equations such as 4.5, 4.6 and 4.7 is discussed in Appendix F, where the correction for a finite size of detector is also considered. A lower shower size limit of  $5 \cdot 10^3$  particles and an upper shower size limit of  $10^7$  particles was also used.

A computer program evaluated equation 4.9 within the limits given and calling from a subroutine the probability,  $P_T$ . Within the subroutine,  $P_T$  was determined according to the shower size, radial distance and muon momentum as given by equation 4.1. In Figure 4.10 are shown the experimental values of the integral rate of events as well as the predicted rate using the two muon radial structure functions. In Figures 4.11 and 4.12 are the corresponding values for the situation where one or more flash tubes have been discharged in respectively more than 40, or more than 50 columns in measuring tray 5. Notably, the extrapolation of the structure function for muons due to Greisen (1960) into a region of muon momentum above 100 GeV/c still broadly agrees with the experimental data. The width of uncertainty on each line that corresponds to a 5% change in  $P_T$  is shown as a 'hatch' area.

In order to determine from which radial distances the contribution to the rate of events is greatest the following integral has been evaluated.

$$I(r, >P_\mu) = 2\pi r \int_{5 \cdot 10^3}^{10^7} P_T P_M F(Ne) dNe \quad (4.13)$$

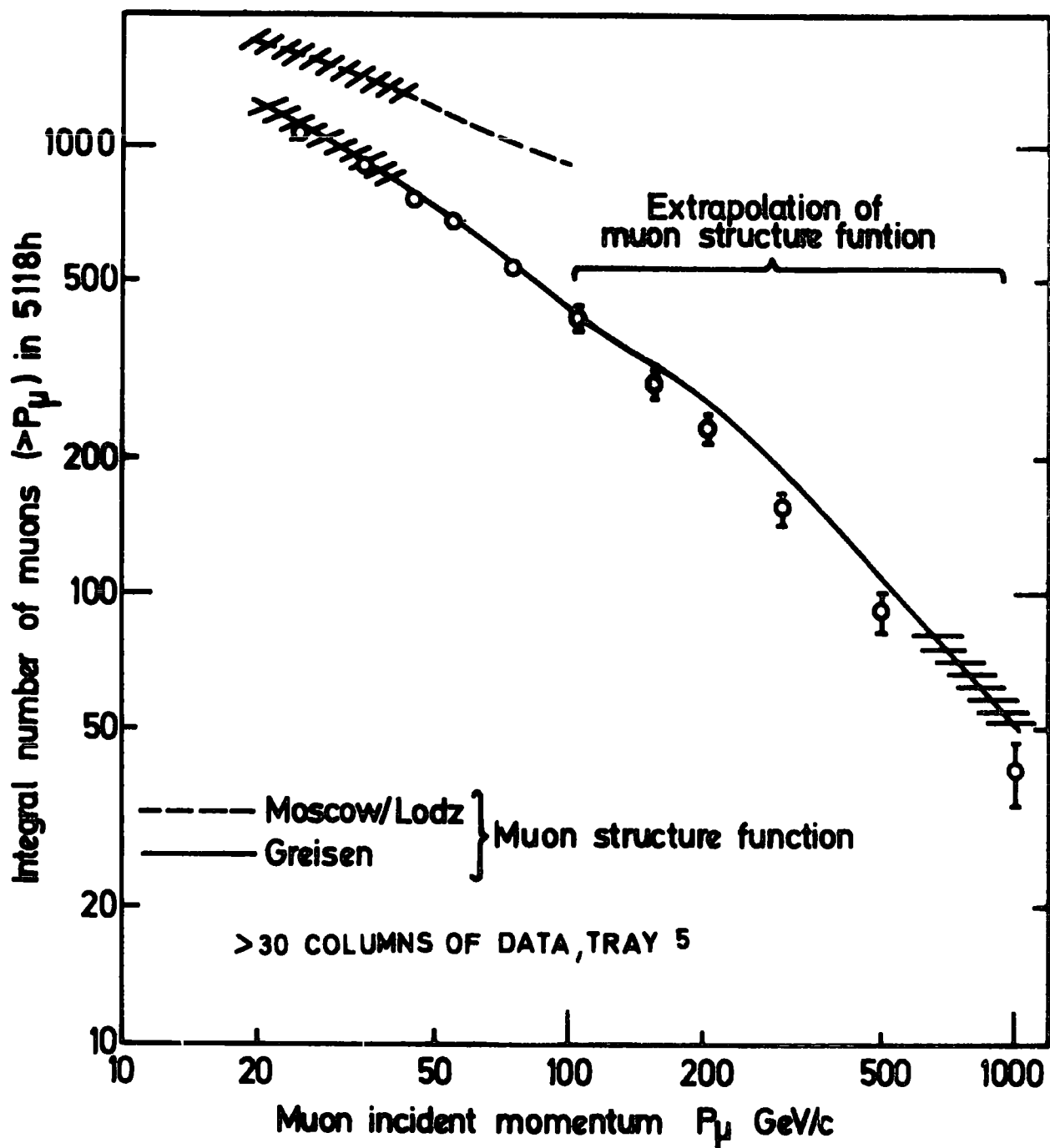


Figure 4.10. The rate of events determined from the shower size spectrum.

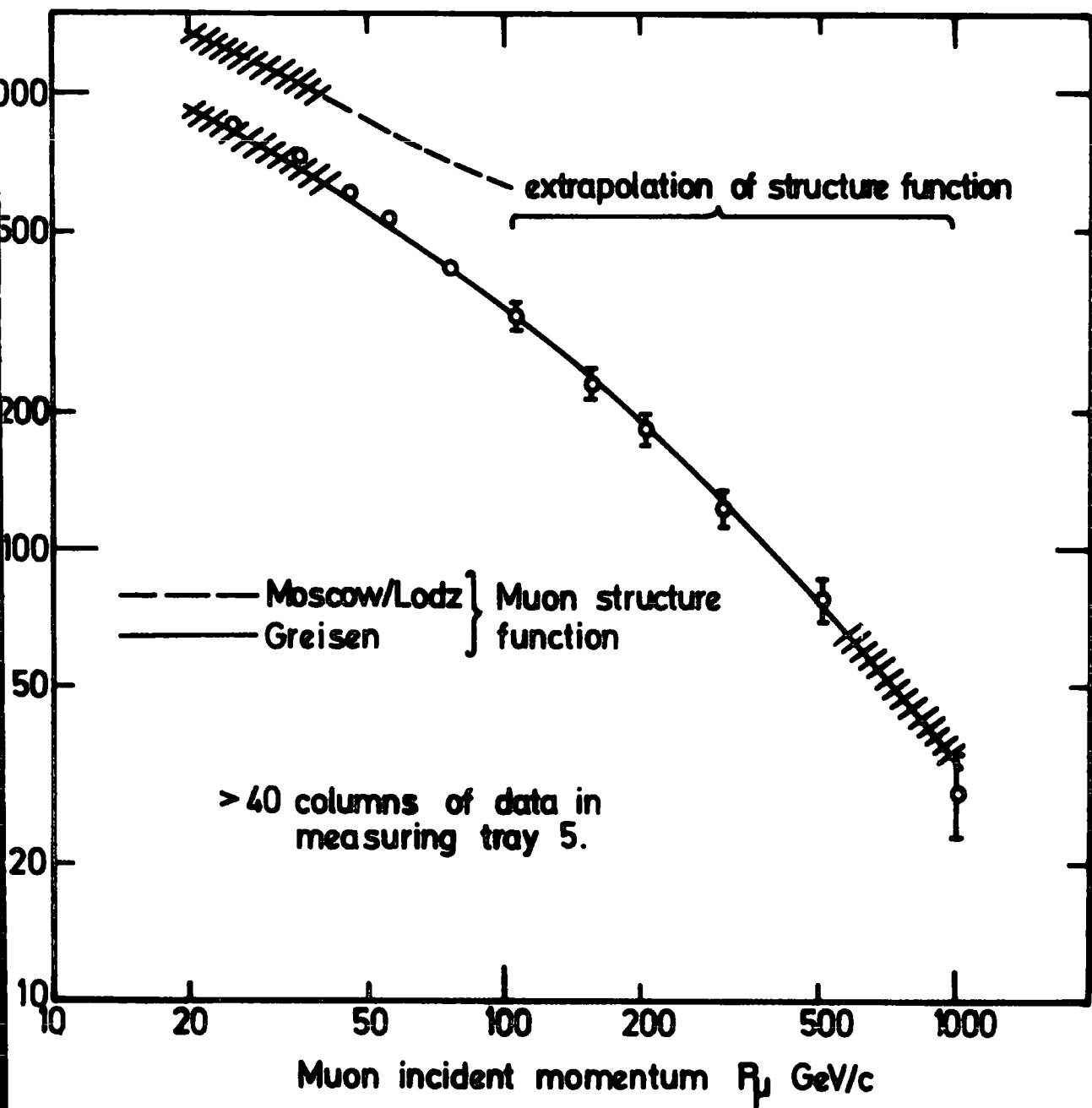


Figure 4.11. The rate of events determined from the shower size spectrum.

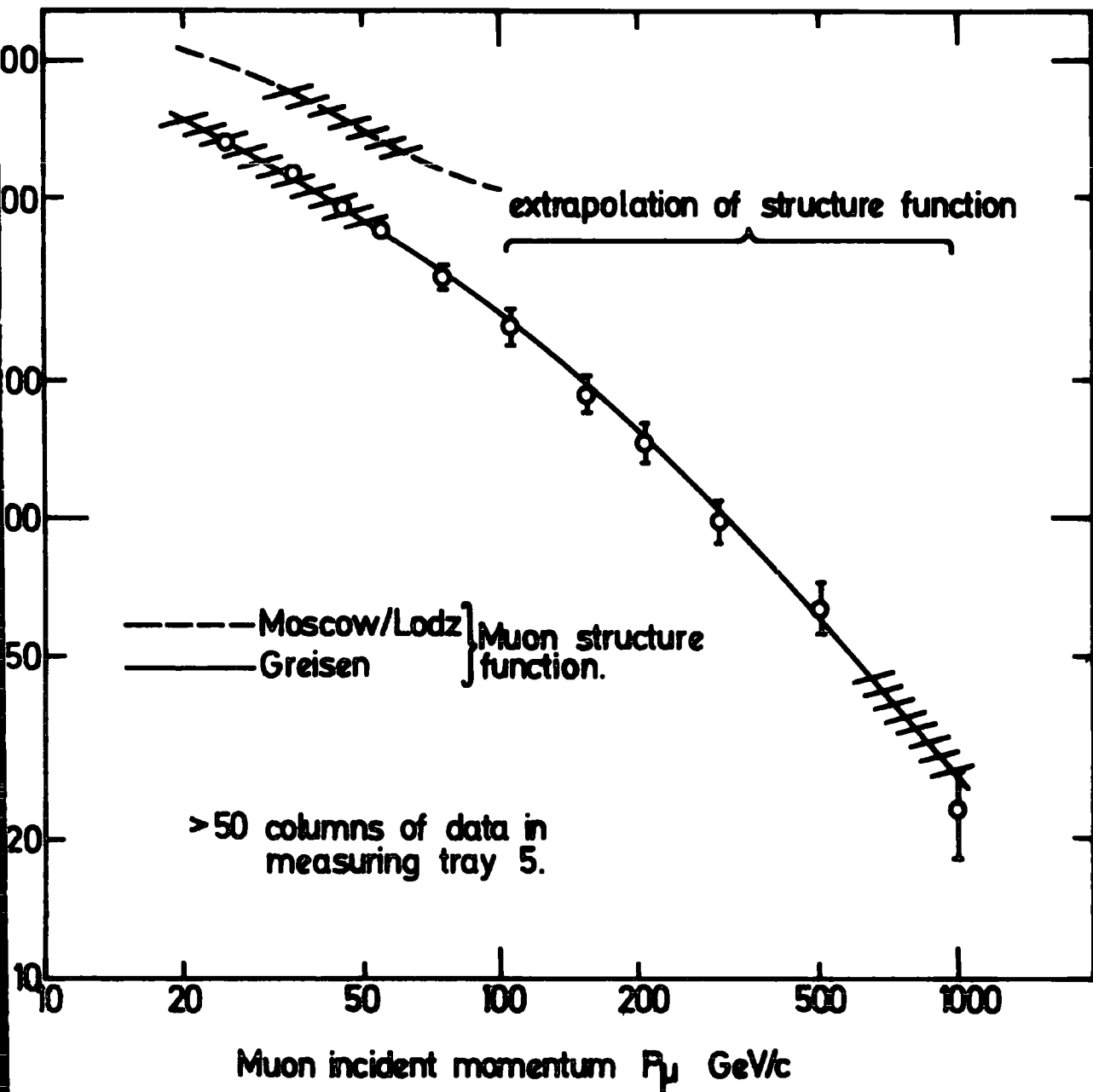


Figure 4.12. The rate of events determined from the shower size spectrum.

In figure 4.13  $I(r, >P_\mu) \times r$  is shown as a function of  $r$  for two values of threshold momentum,  $P_\mu$ , and for the situation of more than 30 and more than 50 columns of discharged flash tubes. The structure function of equation 4.6 has been used for these figures.

The contribution to the rate of events from different shower sizes is indicated by evaluation of

$$I (Ne, >P_\mu) = F(Ne) \int_{0.1}^{100.0} P_T P_M 2\pi r \quad dr \quad (4.14)$$

In Figure 4.14  $I(Ne, >P_\mu) \times Ne$  is shown as a function of  $Ne$  for four values of threshold momentum,  $P_\mu$ , again for the more than 30 and more than 50 columns of data situations.

#### 4.7 THE PREDICTIONS OF THE C.K.P. AND SCALING MODELS

##### 4.7.1 INTRODUCTION

In this section the predictions of two models of high energy nuclear collisions are compared to the measured rate. The models chosen are due to Cocconi, Koester and Perkins, (1961), the so-called C.K.P. model, and Feynman (1969), the scaling model. The models are used to give the number and energy distribution of the secondary particles produced in high energy collisions of cosmic ray primary particles with air nuclei. No new calculations have been performed by the present author, but the relationships due to Goned (1975), de Beer et al., (1966), (1968), Gaisser (1974), (1974a), and Fishbane et al., (1974) are interpreted with respect to the present results. In the main the predictions of the two models differ with regard to the ratio of electron number to muon number in air showers at sea level. For the present experiment the influence of each model is through the momentum and lateral structure of the muon component of the air shower and the total shower size

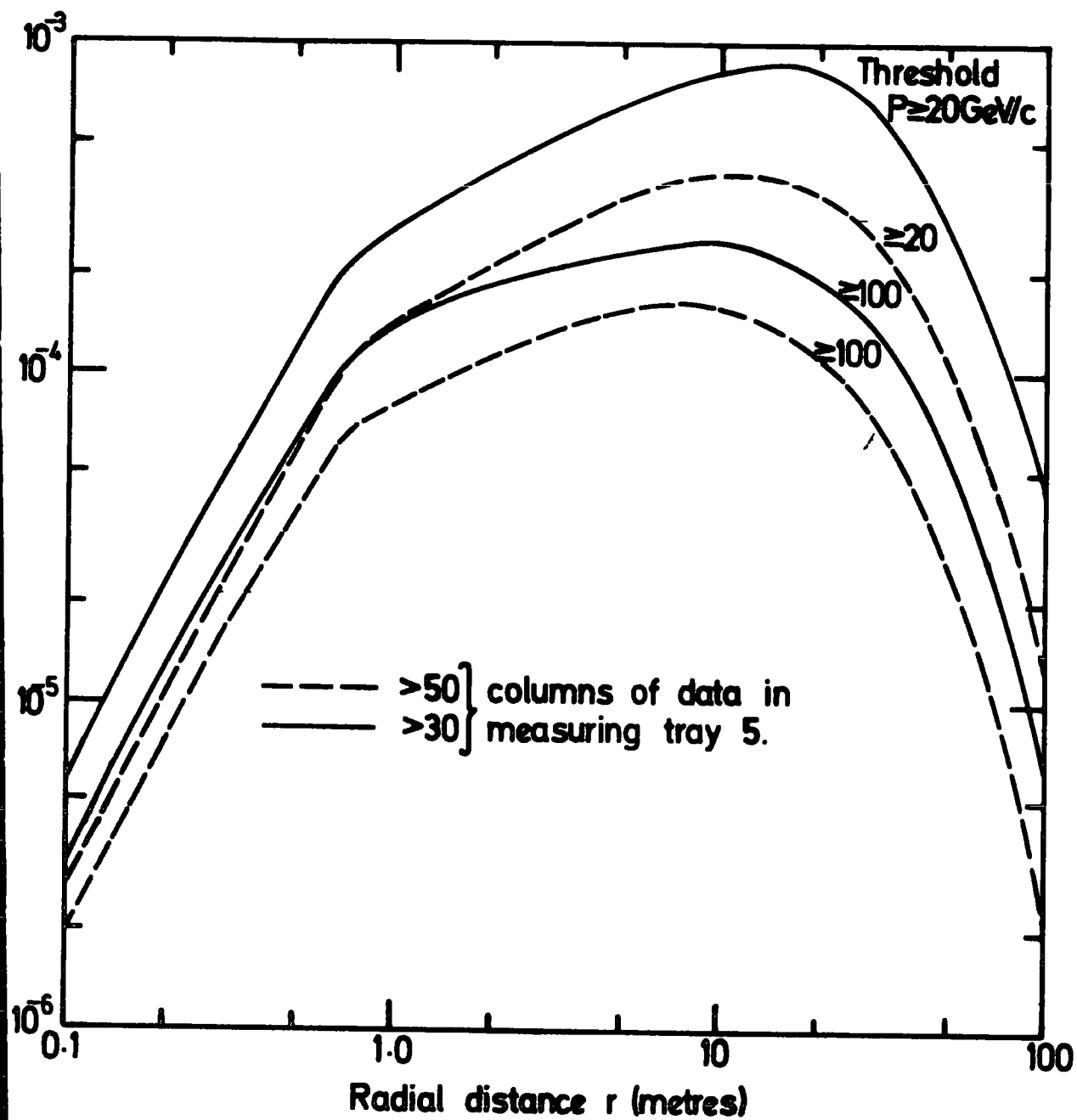


Figure 4.13. Contribution to the predicted rate of events from different radial distances.

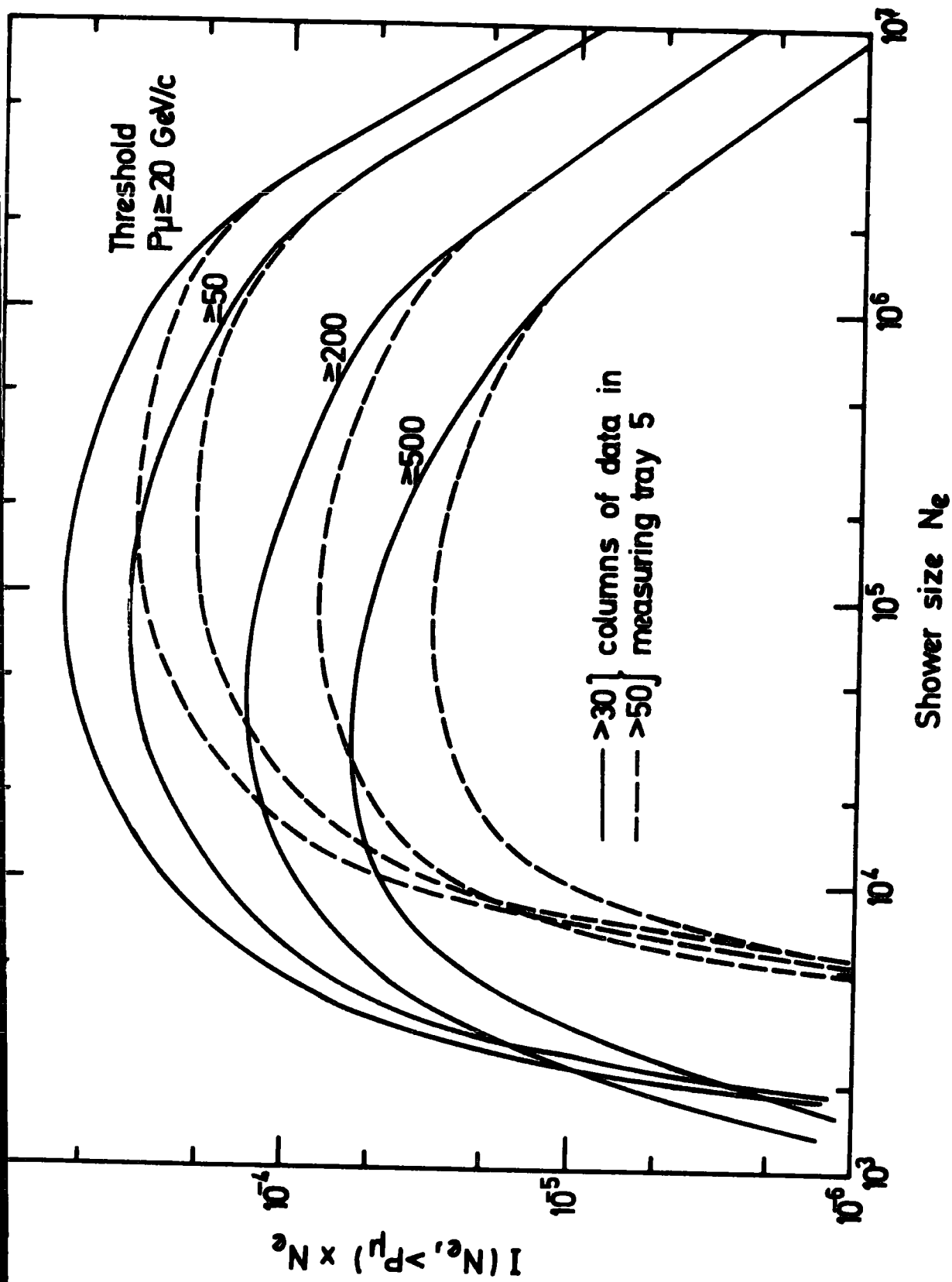


Figure 4.14. Contribution to the predicted rate of events from different shower sizes.

for a given initiating primary particle. The empirical electron structure function, equation 4.5, due to Greisen (1960) is considered to hold true.

In the main, for the muon component of air showers the work of Goned (1975) is taken for the predictions of both models. The starting point in the present work is the predicted total muon number and their first two radial moments for the lateral distribution. For the electron component the relation of shower size to primary energy has been taken from de Beer et al., (1966) and Dixon et al., (1973) for the C.K.P. model, and from Gaisser (1974), and Fishbane et al., (1974), for the scaling model.

Various primary spectra are taken to test and compare the predictions of the models. These vary with regard to spectral slope and composition, but are designed to give agreement with the measured shower size spectrum at sea level for each combination of model and primary spectrum.

#### 4.7.2 THE MUON COMPONENT DETERMINED FROM NUCLEAR INTERACTION MODELS

The basic common features that are incorporated with both the C.K.P. and scaling models when applied to air showers are :

1. Pions are considered to be the main source of muons, neglecting anti-nucleons and strange particles (Kaons). Leading particle effects have also been ignored.
2. The inelasticity is assumed to be independent of energy, being 0.5 for nucleon interactions and 1, that is catastrophic, for pion interactions.
3.  $\pi^+$ ,  $\pi^-$  and  $\pi^0$  are assumed to be produced in equal numbers.
4. The transverse momentum,  $p_t$ , of produced secondaries has a mean value,  $\bar{p}_t$ , of 0.4 GeV/c. The distribution in  $p_t$  is represented by the expression suggested by Cocconi et al., (1961)

$$f(p_t) = \frac{p_t}{p_0} \exp \left\{ -\frac{p_t}{p_0} \right\} \quad \text{with } \bar{p}_t = 2 p_0 \quad (4.15)$$

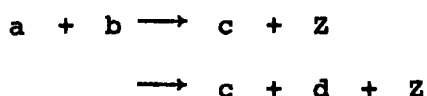
5. The inelastic interaction cross-sections are assumed to be independent of energy. For protons the interaction length  $\lambda_p$  is taken as  $80 \text{ gm cm}^{-2}$  and for pions the attenuation length  $\lambda_\pi$  is taken as  $120 \text{ gm cm}^{-2}$ .

The consequences of these assumptions for any predictions will be considered in Chapter 6. The parameters given here are similar to values used by other authors, (see for example Grieder, (1976) and Table 1 of the survey of computer simulation of air showers made by Turver, (1973)).

#### 4.7.3 THE SCALING MODEL

Feynman scaling is exhibited by inclusive proton-proton collisions at a centre of mass energy of 28 GeV. This has been observed in the C.E.R.N. Intersecting Storage Rings (I.S.R.).

This centre of mass (c.m.) energy available is equivalent to a laboratory energy of about  $2 \cdot 10^3$  GeV for a proton colliding with a stationary target. The assumption used is that scaling continues up to the high energies of the cosmic ray primary interactions of interest here. Inclusive means that only one or two (c or c and d) particles are detected in a reaction like



where the nature of a, b and c (and d) is known and Z is everything else which goes 'unseen'. Exclusive reactions imply full information on all (or all but one) of the outgoing channels. When c is of the same nature as a or b, it is called leading, if it is not it is considered as a produced particle. In inclusive reactions the measured values of the invariant (inelastic) cross section,  $f$ , are considered in the Feynman variable  $x$  and

the rapidity  $Y$ , where for a c.m. energy of  $s^{\frac{1}{2}}$ ,

$$f = \frac{\text{single rate of } c \text{ scattered into an element of solid angle}}{\text{flux}}$$

$$x = 2 P_L s^{-\frac{1}{2}} \quad (-1 < x < 1) \quad (4.16)$$

$$\text{and } Y = \frac{1}{2} \ln \frac{E + P_L}{E - P_L} \quad (\text{or } P_L = E \operatorname{tgh} Y) \quad (4.17)$$

and where  $P_L$  is the c.m. longitudinal momentum and  $E$  is the c.m. energy of the detected particle. Expressing the differential cross section in the Lorentz-invariant form,

$$f = E \frac{d^3 \sigma}{d^3 p} = E \frac{d^2 \sigma}{dP_L dP_T} \quad (4.18)$$

where  $P_T$  is the c.m. transverse momentum of the detected particle. Neglecting spin effects  $f$  is a function of three variables, which may be chosen to be  $(s, P_t, x)$  or  $(s, P_t, Y_L)$

$$\text{where } Y_L = Y_p - \frac{1}{2} \ln \frac{E + P_L}{E - P_L} \quad (4.19)$$

and  $Y_p$  is the c.m. rapidity of the projectile, a. Scaling predicts that at high energies the cross-sections become independent of the energy variable,  $s$ ,

$$f = F(s, P_T, X) \xrightarrow{s \rightarrow \infty} F(P_T, X) \quad (4.20)$$

$$f = G(s, P_T, Y_L) \xrightarrow{s \rightarrow \infty} G(P_T, Y_L) \quad (4.21)$$

For the case in point the requirement is to determine the multiplicities of charged pions in the reaction



Various I.S.R. groups (Antinucci et al.,(1973), Albrow et al.,(1974) and others reported by Morrison,(1973)) who have studied these single inclusive reactions show that expression 4.21 can be factorised as

$$G(P_T, Y_L) = G'(P_T) G''(Y_L) \quad (4.22)$$

such that  $f(Y, P_T) = G''(Y_L) \exp(-bP_T)$  (4.23)

with  $b = 6 \text{ (GeV/c)}^{-1}$  for  $\pi^+$  production,

(Antinucci et al., 1973)

This is found to be valid for the central region of rapidity ( $Y_L > 2$ ) where a plateau occurs in the plot of invariant cross-section vs. laboratory rapidity,  $Y_L$ .

Goned (1975) uses the data of these I.S.R. groups to calculate the laboratory differential cross-section  $d\sigma / dx$  at  $P_T = 0.4 \text{ GeV/c}$  which is close to the mean value of transverse momentum. The ratio ( $X$ ) of the secondary pion energy  $E_\pi$  to the incident proton energy in the c.m. system, is taken as being equal to the corresponding value in the laboratory system. For high energy particles produced in the forward hemisphere in the c.m. system,

$$X = \frac{2 P_L}{\sqrt{s}} \approx \frac{P_L}{P_{L \text{ max}}}$$

where  $P_{L \text{ max}}$  is the maximum value of longitudinal momentum which is therefore half the c.m. energy. Thus for the fast pions in the c.m.,  $X$  is approximately the ratio of the secondary pions laboratory energy to the incident proton energy. Wdowczyk and Wolfendale, 1972, point out that this model resembles the isobar model of Khristiansen et al., 1965, in that the multiplicity of secondaries carrying a significant fraction of the incident energy is sensibly independent of the incident energy although the mean total number of secondaries

increases as  $\ln s$ .

Goned obtains

$$\frac{d\sigma}{dx} = \int_0^{\infty} f^{(Y_L, P_T)} \frac{\pi t g h Y_L}{x} dP_T^2 = \frac{2\pi t g h Y_L}{b^2 \exp(-0.4b)} x f^{(Y_L, 0.4)} \quad (4.24)$$

for the laboratory differential cross-section where momenta are in GeV/c.

#### 4.7.4 THE C.K.P. MODEL

Studies of the interactions of protons with light nuclei led Cocconi, Koester and Perkins, (1961) to suggest an energy distribution for produced pions of the form,

$$S(E_p, E_0) = \frac{1}{2} \left\{ \frac{n(E_0)}{T} \exp\left\{-\frac{E_p}{T}\right\} + \frac{n(E_0)}{G} \exp\left\{-\frac{E_p}{G}\right\} \right\} \quad (4.25)$$

where  $n(E_0)$  is the multiplicity of pions produced,  $E_0$  is the transferred energy, and

$$T = 2 \left\{ E_0 - \frac{1}{2} n(E_0) G \right\} / \left\{ n(E_0) \right\} \quad (4.26)$$

is the average energy of the pions in the forward cone in the laboratory system and  $G$  is the average energy of pions in the backward cone in the laboratory system. The forward core of secondary particles only is considered, as the pions emitted in the backward core will have low energies in the laboratory system, and will not contribute to the high energy muon component. The justification for using this model stems from the success in recent years of the application of it to the air shower situation. (see for example the review by Grieder, 1976).

The form  $N_s = 1.35 E_p^{1.4}$  is taken for the multiplicity dependence on primary energy,  $E_p$ .

#### 4.7.5 THE METHOD OF CALCULATION

Following the method of de Beer et al., (1966) Goned solves the diffusion equations which govern successive generations of pions in the atmosphere. To a first approximation these spectra of pions resemble multifireball systems. The scaling model can, in principle, be approximated to a multifireball model, since (in both models) the basic feature is the existence of a central plateau in the rapidity distribution. In the C.K.P. model the energy spectrum given above results in a multifireball system of multiplicity  $N_s$  for each fireball and average pion energy  $T_n$  in the  $N^{\text{th}}$  fireball. The calculations are extended to 5 pion generations and 5 interactions of the primary.

#### 4.7.6 APPLICATION TO THE PRESENT EXPERIMENT

The lateral muon density distributions,  $\rho_\mu(r)$ , have been calculated from the total muon numbers and two radial moments for proton primaries, given by the calculations described above. The lateral distributions are represented by

$$\rho_\mu(r) = \frac{1}{2\pi} \int_0^\infty \frac{f(r_0)}{r_0^2} \exp\left\{-\frac{r}{r_0}\right\} dr_0 \quad (4.27)$$

where  $f(r_0)$  is the radial distribution for a fixed transverse momentum  $p_0$  and has the form

$$f(r_0) = C r_0^\alpha \exp\left\{-\beta r_0\right\} \quad (4.28)$$

Figure 4.15 shows the predicted total muon numbers and Table 4.2 gives the parameters of the muon radial distributions (for a primary proton of  $10^5$  GeV) for the two models. Thus for a given primary nucleon the distribution of muons of greater than a threshold energy,  $E_T$ , can be determined

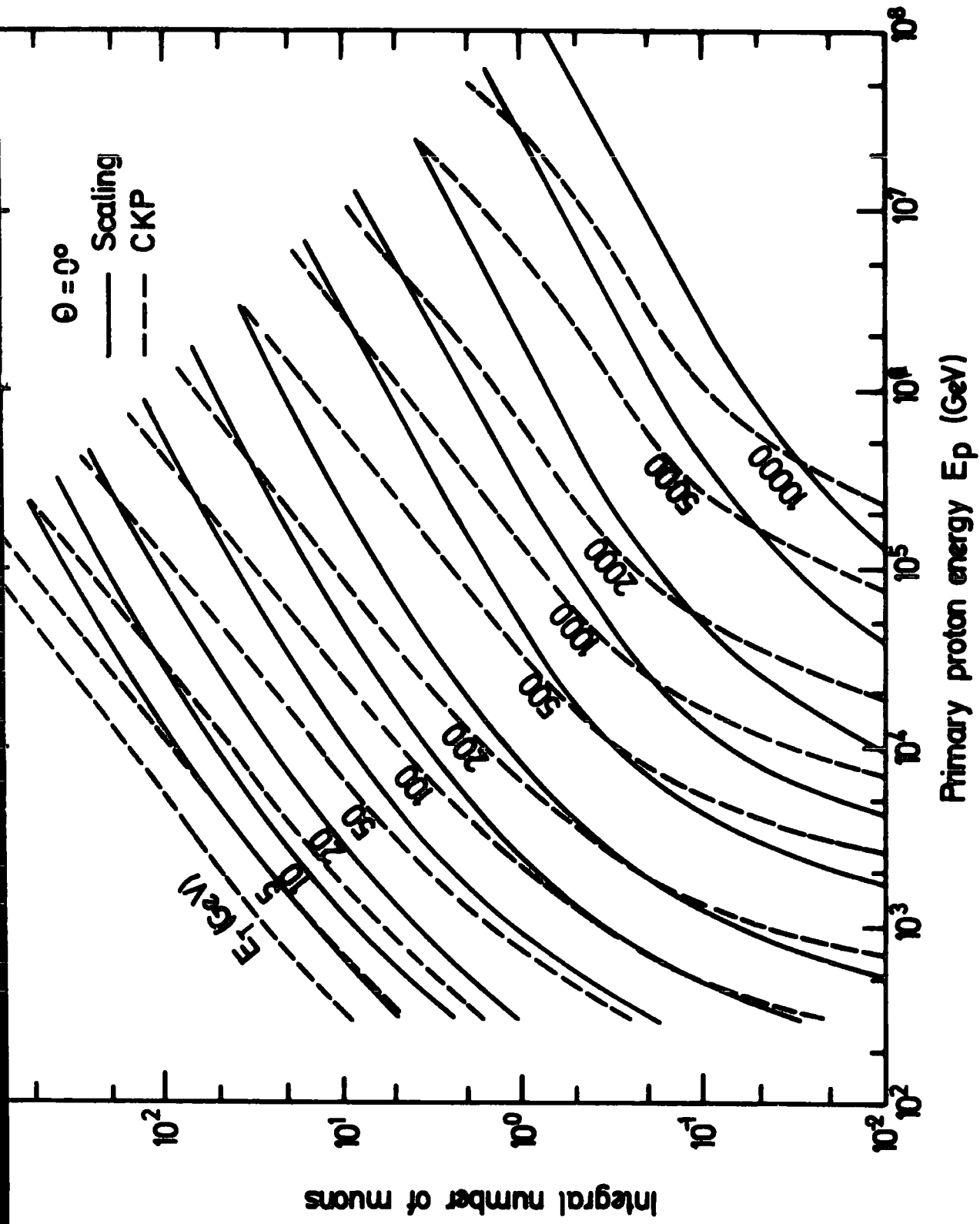


Figure 4.15 Predicted total muon number at sea level for proton primaries (after Goned, 1975)

PARAMETERS OF MUON RADIAL DISTRIBUTIONS FOR  $E_p = 10^5$  GeV AND  $\theta \neq 0^\circ$  WITH

$\langle p_t \rangle = 0.4$  GeV/c (After Goned, 1974)

	C.K.P.			SCALING		
	c	$\alpha$	$\beta$	c	$\alpha$	$\beta$
50	$2.7810^{-3}$	4.244	0.274	$4.4910^{-2}$	2.428	0.194
100	$1.3310^{-2}$	4.274	0.455	$1.2610^{-1}$	2.318	0.319
500	$2.9710^{-1}$	4.100	1.269	$4.9510^{-1}$	3.110	1.198

MUON  
THRESHOLD  
ENERGY  
, GeV

PROTON  
PRIMARY  
ENERGY  
 $= 10^5$  GeV

TABLE 4.2

for both models.

#### 4.7.7 THE ELECTRON COMPONENT

To complete the calculation of the expected rate of events in which one or more muons are detected with an associated electron density, the electron shower size,  $N_e$ , predicted by each model must be known. The present experimental situation can be seen as a test of the overall muon to electron ratio,  $N_{\mu}/N_e$ , in small air showers as all parts of the shower are sampled to some extent, although there is a bias toward the centre of showers. A low  $N_{\mu}/N_e$  ratio implies a low multiplicity model for pion production, because fewer charged pions will lead to fewer muons. In such a model as scaling the charged pions are on the average more energetic and because of time dilation are more likely to interact before they decay to muons. However, the number of electrons will be approximately proportional to the amount of energy that goes into the neutral pion component (which decays promptly) which is about the same in the C.K.P. and scaling models.

The structure function used throughout, for the electrons, is that due to Greisen (1960), (equation 4.5) who suggests a very extensive range of application extending from showers of  $2 \cdot 10^3$  to  $2 \cdot 10^9$  particles and over distances from 5 cm. to 1500 m. However, recently Allen et al., (1975) have suggested that electron lateral distributions have less lateral spread by a factor of about 2 than given by Nishimura and Kamata (1958). This would imply a higher density near the axis of the shower, the consequence of which is considered in Chapter 6.

Some primary spectrum of given composition and intensity must be used with each model to predict the rate of events. To enable consistent comparison to be made, a datum of the measured sea level shower size spectrum has been used. Thus, for each model the prediction of mean shower size for a given primary energy, is used with the measured sea level shower size spectrum to generate a

primary spectrum. This primary spectrum is then used with the model to predict the experimental rate. This approach has been used because the primary spectrum has been measured directly with accuracy and by more than one experiment only up to the energy region of about  $10^3$  GeV/nucleon (Ryan et al., (1972) for example) but not beyond. Primary energies of greater than this are required to give a shower of greater than about  $10^3$  particles at sea level. However, the sea level shower size spectrum has been measured by many authors (see Figure 4.8) over the range of interest of the present experiment which is from showers of  $5 \cdot 10^3$  particles to showers of over  $10^7$  particles.

If, in a region of constant exponent, the differential shower size spectrum is

$$F(N_e) dN_e = AN_e^{-\beta} dN_e$$

where A and  $\beta$  are constants, and  $N_e$  is the shower size, and for the model in question the mean shower size is (assuming one component, say protons only),

$$N_e = C E_p^\alpha \tag{4.29}$$

where  $E_p$  = primary particle energy,  
and C and  $\alpha$  are constants

then

$$dN_e = \alpha C E_p^{\alpha-1} dE_p \tag{4.30}$$

so

$$J(E_p) dE_p = A (CE_p^\alpha)^{-\beta} \alpha C E_p^{\alpha-1} dE_p \tag{4.31}$$

is the corresponding primary differential spectrum.

#### 4.7.8 THE MEAN SHOWER SIZE PREDICTED BY THE C.K.P. MODEL

For the relationship of mean shower size, for a given primary energy as predicted by the C.K.P. model, the work of de Beer et al., (1966), has mainly been used. This work has, to a large extent, been superseded by more refined calculations (Dixon et al., (1973) Greider, (1976)) but is considered suitable for the present work. Firstly, the predictions of the original work (de Beer et al., (1966) the model called I) are in broad agreement with a number of latter calculations.

Secondly, the model parameters match those used by Goned (to predict the muon numbers) except that fluctuations are allowed for to the extent of variations in the inelasticity (K) of nucleon air-nucleus collisions. The form of the fluctuations assumed is that of (Brooke et al., 1964) where the inelasticity distribution is

$$f(K) = - (1 + \alpha)^2 (1 - K)^\alpha \ln(1 - K)$$

with  $\alpha = 1.414$ ; which is chosen to fit the work of Dodd et al., (1961) on low energy (24 GeV) proton-proton interactions observed in a hydrogen bubble chamber. De Beer et al., point out the importance of shower size fluctuations when considering the action of one primary particle. Considering showers at a fixed size,  $N_e$ , the steep primary spectrum favours fluctuations that produce a given size with unusually low primary energy relative to the primary energy giving that shower size considered at fixed primary energy,  $E_p$ . The parameter most often measured by air shower arrays is the shower size which is then placed with showers of similar size into a bin of finite width, the number in each bin leading to the spectrum. Thus the measurements tend to be at fixed shower size. Two of the main causes of fluctuations are the depth of first interaction of the primary particle and the fraction of energy carried off by produced  $\pi^0$ 's in the early interactions. In Figure 4.16 the relation of mean shower size to primary proton energy for a proton incident at  $0^\circ$  to the

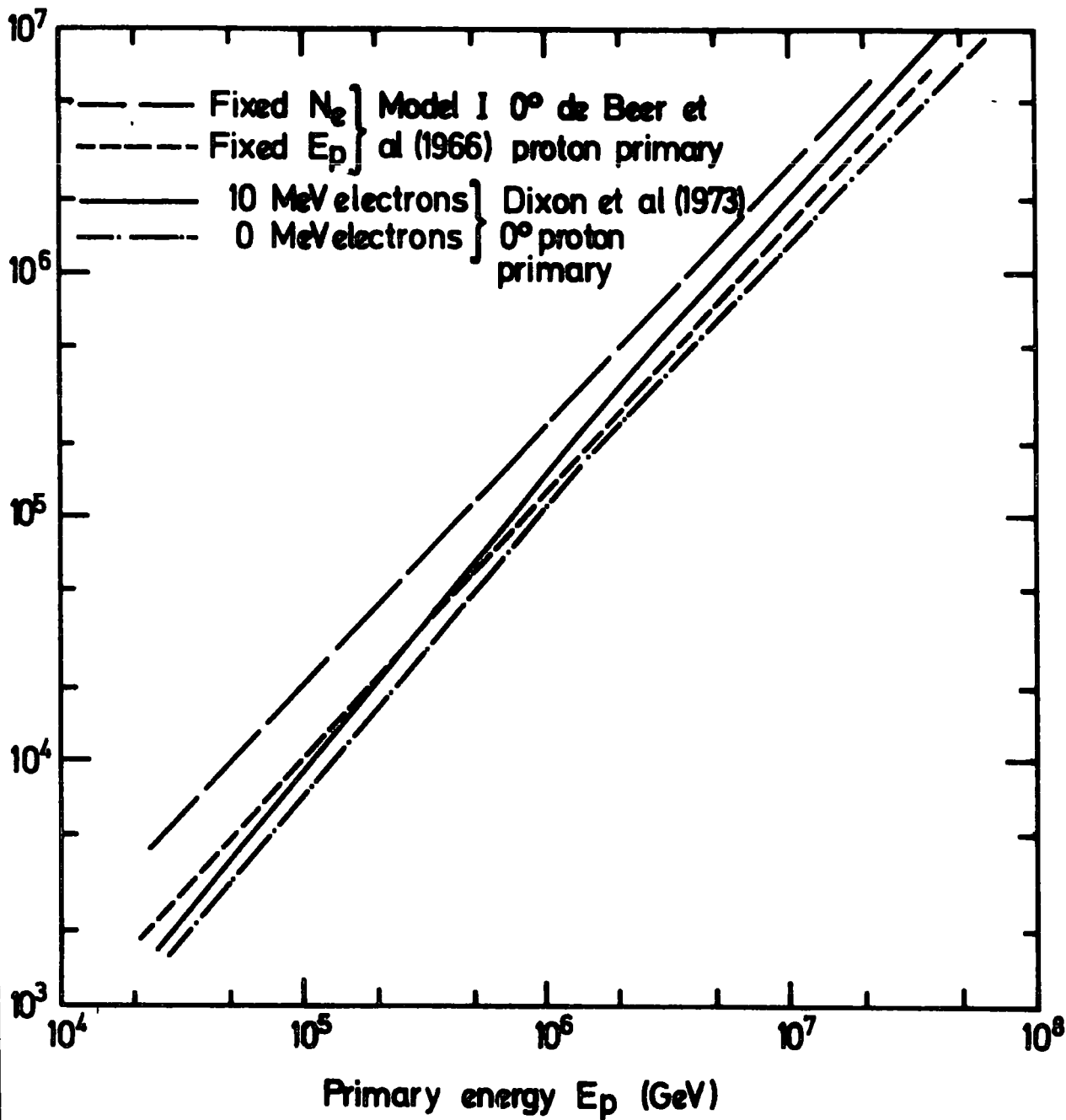


Figure 4-16 Sea level shower size spectrum Vs primary energy for the CKP model.

Zenith is shown as determined from model I, for both fixed  $N_e$  and fixed  $E_p$  situations. Shown also are the relations due to Dixon et al., (1973) of shower size to primary energy at fixed  $E_p$ , for two different energy thresholds for electron detection. Agreement can be seen to be good and these authors (Dixon et al., (1973) Turver, (1973) and Grieder, (1976)) conclude that many of the small differences which do occur in simulations using this type of model may be accounted for by differences in the parameters used. Greider finds that differences in the sensitivity of the 'observables' to model and parameter variations can be ranked as 'local and total energy spectra of distinct groups of particles within a shower', followed by 'particle ratios and numbers' and finally by 'lateral density and arrival time distributions'. The relevant relations of shower size to primary energy are given in Table 4.3, where the conversion from fixed  $E_p$  to fixed  $N_e$ , as determined by de Beer et al., has been applied to the relationship of Dixon et al., for shower size to primary energy for both electron detection thresholds

#### 4.7.9 THE MEAN SHOWER SIZE PREDICTED BY THE SCALING MODEL

The relationships of sea level shower size and muon number to primary particle energy for the scaling model as calculated by different authors, show marked differences. This is reflected in Figure 4.17 where the relationship between muon number and electron number in showers at sea level as determined by several workers is shown.

The initial calculations performed in the early 1970's not long after Feynman suggested that the energy spectrum of particles emitted in high energy nucleon-nucleon collisions may 'scale' (for example, Gaisser and Maurer, (1972) Wdowczyk and Wolfendale, (1972)) indicated that the  $N_\mu/N_e$  ratio predicted by scaling is too low for assumed proton primaries in comparison with experiments. However, more recently, calculations which take into account the possible effects of (1) rising cross section for proton-proton interactions, and thus for

THE RELATION OF SEA LEVEL SHOWER SIZE TO PRIMARY ENERGY FOR THE C.K.P. MODEL

N <sub>e</sub> MEAN SEA LEVEL SHOWER SIZE, E <sub>p</sub> IN GeV			
	Fixed E <sub>p</sub>	Fixed N <sub>e</sub>	Conversion from Fixed E <sub>p</sub> to Fixed N <sub>e</sub>
de Beer et al., 1966 MODEL I O	N <sub>e</sub> = 3.466 10 <sup>-2</sup> E <sub>p</sub> <sup>1.095</sup>	N <sub>e</sub> = 9.706 10 <sup>-2</sup> E <sub>p</sub> <sup>1.064</sup>	2.8 E <sub>p</sub> <sup>-0.031</sup>
DIXON et al., 1973 E <sub>e</sub> > 0 Mev	BELOW E <sub>p</sub> ~ 2 10 <sup>6</sup> N <sub>e</sub> = 6.08 10 <sup>-3</sup> E <sub>p</sub> <sup>1.233</sup>	ABOVE E <sub>p</sub> ~ 2 10 <sup>6</sup> N <sub>e</sub> = 3.24 10 <sup>-2</sup> E <sub>p</sub> <sup>1.113</sup>	
DIXON et al., 1973 E <sub>MIN</sub> ELECTRON > 10 Mev	BELOW E <sub>p</sub> ~ 1.5 10 <sup>6</sup> N <sub>e</sub> = 9.41 10 <sup>-3</sup> E <sub>p</sub> <sup>1.177</sup>	ABOVE E <sub>p</sub> ~ 1.5 10 <sup>6</sup> N <sub>e</sub> = 4.67 10 <sup>-2</sup> E <sub>p</sub> <sup>1.064</sup>	

TABLE 4.3

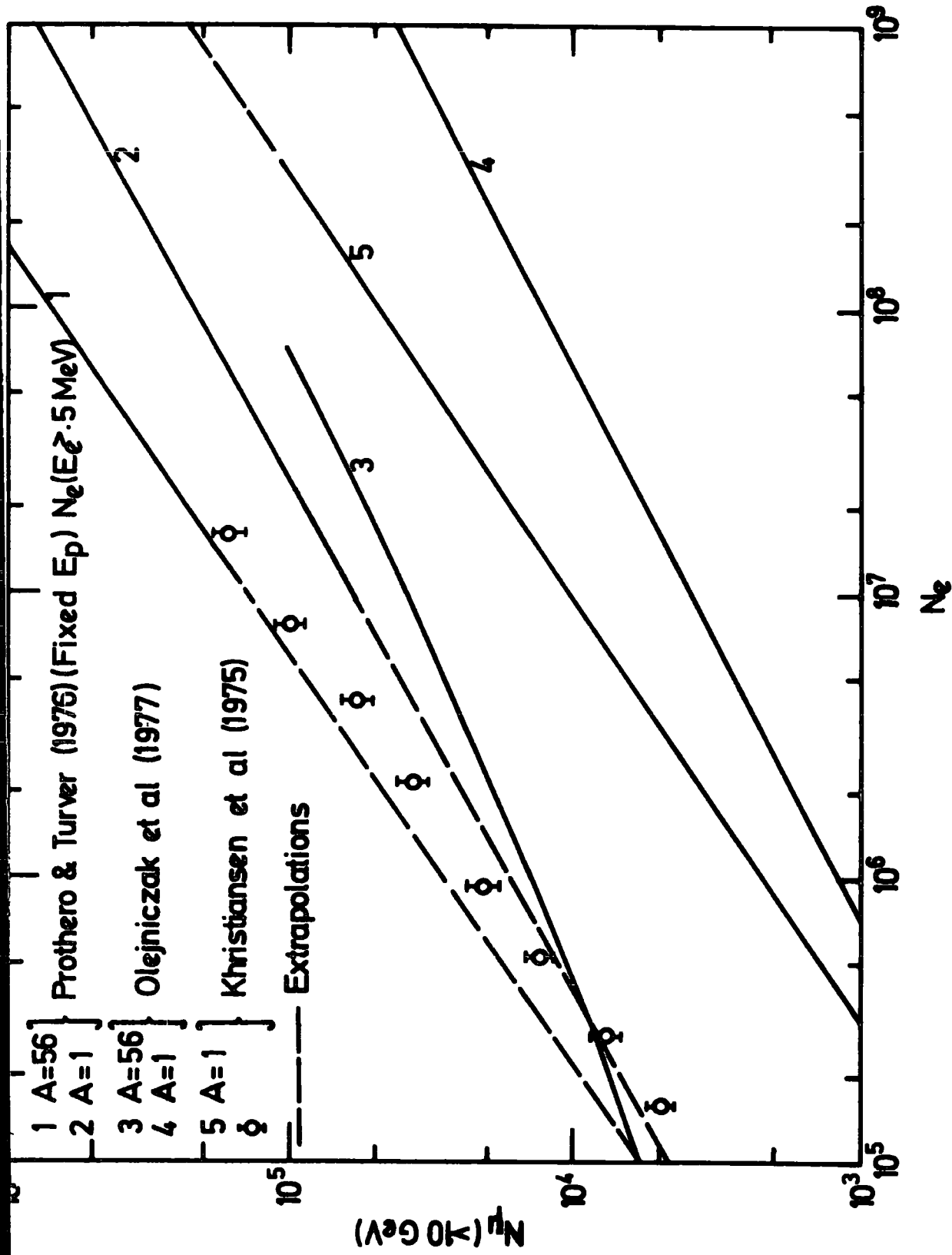


Figure 4.17 The ratio of muons to electrons predicted by scaling models applied to air showers.

proton-air nucleus interactions, (2) intra nuclear cascading, and (3) heavier (probably iron) primaries, can give a satisfactory fit to the experimental data. (Gaisser,(1974) Turver,(1974) Prothero and Turver, (1976)).

The approach adopted here has been to use the relationships reported by Gaisser (1974), Fishbane et al., (1974) and Gaisser (1974 a) for the sea level shower size dependence upon different primary energy as predicted by a scaling model. In Figure 4.18 the calculations of these workers of shower size vs depth are superimposed on data points due to Bradt et al.,(1965) and La Pointe et al.,(1968). The aim of Fishbane et al., (see also Gaisser and Maurer,(1972)) has been mainly to determine the  $\frac{N_{\mu}}{N_e}$  ratio as predicted by a scaling model. The atmospheric cascade of successive generations of pions was approached by the use of a similar diffusion equation to that used by Goned. Other similarities include, the neglect of Kaons (assumed as pions), the use of a mean transverse momentum for the secondaries of 0.4 GeV/c, and a nucleon inelasticity of 0.5. However, they extend the calculations to determine the effects of intra-nuclear cascading and a possible increase in the pion-air nucleus and proton-air nucleus cross-section.

Their calculations include the region  $X = 0$  ( $X = 2P_L S^{-1}$ , that is the pionization region) as pions produced here will have a sufficiently high 'laboratory' energy to contribute to the extensive air shower. The intra-nuclear cascade has been allowed for by an incoherent production model (I.P.M.) The nucleon is considered to interact several times within the nucleus as opposed to just one nucleon-nucleon collision as is the case in a more conventional model. Thus, particles rescatter independently within the nucleus and build up a cascade. Consequently the  $\frac{N_{\mu}}{N_e}$  ratio as measured beyond shower maximum will increase because this greater production of particles will cause a more rapid development of the air shower.

Three different combinations of these processes as developed by Gaisser and co-workers are considered here, and are summarised below.

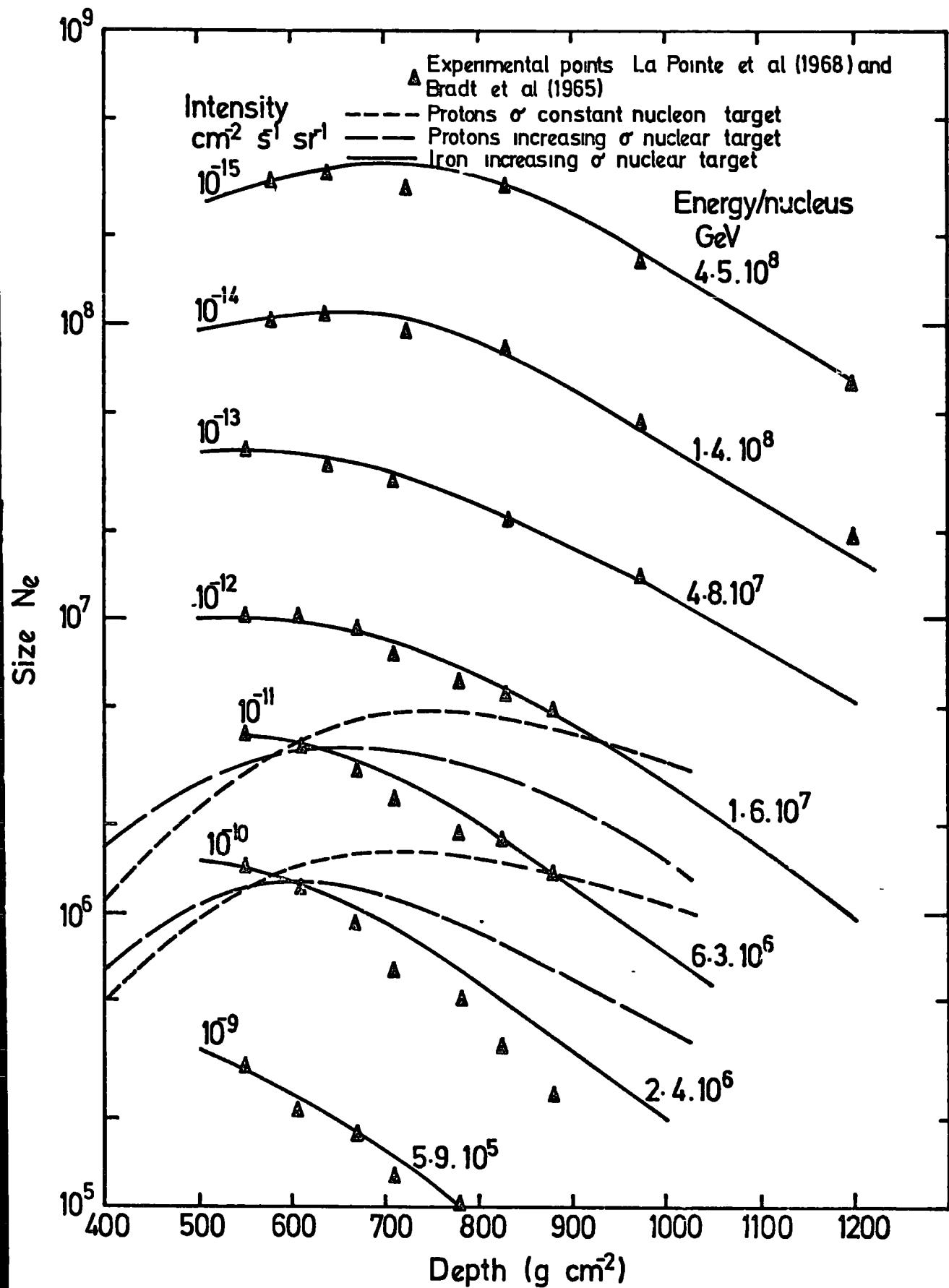


Figure 4.18 Shower size vs. depth (after Gaisser (1974) and Fishbane et al. (1974))

1. 'Proton primaries strike a nucleon target, that is one nucleon within the nucleus ; and the interaction cross-section is constant with primary energy.'

The variation of shower size with depth for primary particle energies of  $2.4 \cdot 10^6$  GeV and  $6.3 \cdot 10^6$  GeV, which correspond to intensities of  $10^{-10}$  and  $10^{-11}$   $\text{cm}^{-2} \text{s}^{-1} \text{sr}^{-1}$ , are shown as curves of short-dotted lines in Figure 4.18.

2. 'Proton primaries striking a nucleus and intra-nuclear cascading taking place ; a rising proton-air nucleus cross-section ( $\sigma_{\text{p-air}}$ ) is assumed and is taken directly from the cosmic-ray data of Yodh et al., (1973).'

This is consistent with a  $(\ln s)^2$  extrapolation of I.S.R. measurements of the proton-proton cross-section ( $\sigma_{\text{p-p}}$ ) when allowance is made for the nuclear target. The pion-air cross-section ( $\sigma_{\pi\text{-air}}$ ) is taken as  $0.7 \sigma_{\text{p-air}}$ . The predicted variation of shower size with depth is shown as two curves of long-dashes in Figure 4.18.

3. The remaining curves showing the shower size depth relationship in Figure 4.18 (the most successful fits to the data) are obtained with the assumption of 'intra-nuclear cascading, rising cross-section and all iron primaries,' at the same energy per nucleus as the prediction for proton primaries. In this case the superposition principle was used where a primary particle of size A (a nucleus) and of total energy E, is equivalent to A times as many nucleon primaries each of energy E/A.

The curves are normalized to the data points at about  $600 \text{ g/cm}^2$ . In order to determine the relation of shower size to primary energy as predicted by each of these different applications of the scaling model the following deductions have been made :

(a) Fishbane et al., (1974) give for showers of fixed size

$N_e$  of  $10^6$  particles, a mean primary energy of  $\bar{E}_{\text{p } N_e} = 2.4 \cdot 10^6$  GeV

for the scaling model assuming a constant cross-section and a nucleon target. (The subscript  $N_e$  implies fixed shower size, whilst the subscript  $E_p$  implies fixed primary energy.)

(b) Figure 4.18 is a plot of the atmospheric variation of shower size for fixed primary energy,  $N_e E_p$ . This is because the size versus depth experimental points are determined by taking cuts of constant intensity of showers at different Zenith angles, which relate directly to the primary energy. This is because the same intensity will be due to the same energy primary. For the particular curves given for proton primaries ( $\sigma_{p\text{-air}}$  considered constant and a nucleon target) the increase in shower size at sea level ( $1033 \text{ g/cm}^2$ ) is a factor of 3.05 from  $N_e E_p$  equal to  $10^6$  to  $3.05 \cdot 10^6$ .

This corresponds to an increase of 2.625, from  $E_p$  equal to  $2.4 \cdot 10^6$  GeV to  $6.3 \cdot 10^6$  GeV, in primary energy. This is for fixed energy of the primary. The corresponding increase in shower size at fixed shower size, has been determined by applying the transformation from fixed  $E_p$  to fixed  $N_e$ , a factor of  $2.8 E_p^{-.031}$ , as determined by de Beer et al., (1966). Although this transformation was determined from considering showers using the C.K.P. model, it has been assumed to apply here as the major cause of fluctuations (the steeply falling spectrum and the height of first interaction) will be model independent. Thus the increase in  $N_e$  at fixed  $N_e$  is a factor 2.96, for an increase of 2.625 in primary energy.

Point (b) above leads to Table 4.4 where the values of increase in shower size for an increase in primary energy are given for the three different processes under fixed  $N_e$  conditions. Combining points (a) and (b) the equations of mean shower size for given primary energy can be determined. In Table 4.4 the parameters  $K$  and  $\alpha$  in the relation of shower size to primary energy,  $N_e = K E_p^\alpha$ , at fixed  $N_e$ , are given for the three processes described,

Primary Energy at Intensity $10^{-10}$ & $10^{-11}$ $\text{cm}^{-2} \text{s}^{-1}$	Shower Size $N_e$ Fixed $E_p$	Shower Size $N_e$ Fixed $N_e$	Ratio Energy Increase Size Increase at Fixed $N_e$	Primary Energy for Fixed Size $N_e = 10^6$	Primary Energy $\sim$ Shower Size $N_e = KE^\alpha$
$2.4 \cdot 10^6$ Gev	$1.0 \cdot 10^6$	$1.775 \cdot 10^6$	.886	$2.4 \cdot 10^6$ Gev	$6.66 \cdot 10^{-2}$
$6.3 \cdot 10^6$ Gev	$3.05 \cdot 10^6$	$5.256 \cdot 10^6$			1.125
$2.4 \cdot 10^6$ Gev	$3.5 \cdot 10^5$	$6.22 \cdot 10^6$	.739	$3.9 \cdot 10^6$ Gev	$2.194 \cdot 10^{-3}$
$6.3 \cdot 10^6$ Gev	$1.28 \cdot 10^6$	$2.21 \cdot 10^6$			1.314
$2.4 \cdot 10^6$ Gev	$1.32 \cdot 10^5$	$2.35 \cdot 10^5$	.739	$5.5 \cdot 10^6$ Gev	$1.373 \cdot 10^{-3}$
$6.3 \cdot 10^5$ Gev	$4.85 \cdot 10^5$	$8.36 \cdot 10^5$			1.314

PRIMARY PROTONS  
 $\sigma = \text{CONST.}$   
NO INTRANUCLEAR  
CASCADE

PRIMARY PROTONS  
INCREASING  $\sigma$   
INTRANUCLEAR  
CASCADE

IRON PRIMARIES  
INCREASING  $\sigma$   
INTRANUCLEAR  
CASCADE

TABLE 4.4

and in Figure 4.19 these are compared to the simulations due to Turver, (1975).

The integral muon energy spectra, predicted by Goned, (1975) and by Fishbane et al., (1974) are shown in Figure 4.20, for a shower size of  $N_e$  equal to  $10^6$  particles. The lines due to Fishbane et al., are a direct translation of their  $N_\mu/N_e$  ratio predictions at a shower size of  $10^6$  particles. The line corresponding to Goned's calculations is taken from the data (see Figure 4.15) at a fixed  $E_p = 3.95 \cdot 10^6$  GeV. This energy corresponds to a shower of size  $N_e$  equal to  $10^6$  particles at a fixed  $E_p$  for the case of primary protons,  $\sigma_{p-air}$  considered constant and a nucleon target from the work of Fishbane et al., (1974).

The predictions of Goned's calculations and those of Fishbane et al., for protons for which both a constant cross section and a nucleon target are assumed are considered close enough (at least for muons of energy in the range 100 to 1000 GeV) to be used together to predict the rate of events for the present experiment. They are combined such that the shower size for each primary energy is taken from the work of Fishbane et al., and the muon component is taken from the work of Goned.

In Section 4.7.11 the use of a primary spectrum comprising different elements is considered. In Section 4.7.12 the possibility of using Fishbane et al.'s predictions for rising cross section and intranuclear cascading, is also considered. The main problem with these predictions is that although the expected increase in total muon number and reduction in electron size, at sea level, can be taken from their work, the muon lateral structure is only given by Goned. This is only for the constant  $\sigma_{p-air}$ , nucleon target case, which will give too narrow a distribution if applied to the rising  $\sigma_{p-air}$ , nuclear target case.

#### 4.7.10 THE PRIMARY COSMIC RAY COMPOSITION

As indicated in Section 4.7.8 the intensity of the primary spectrum has been determined for each model used so that the sea level shower size spectrum

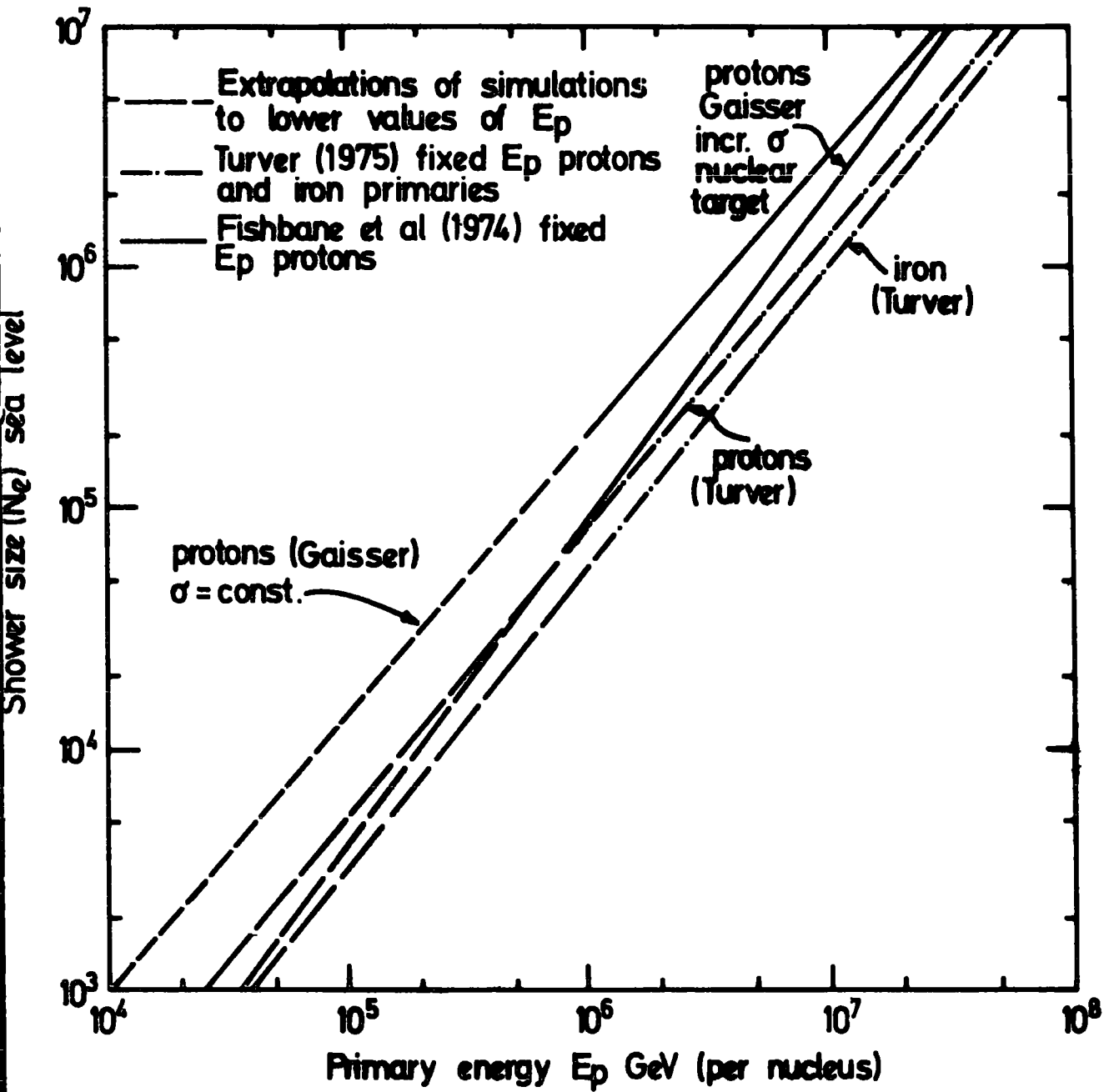


Figure 4.19 Sea level shower size vs primary energy for the scaling model

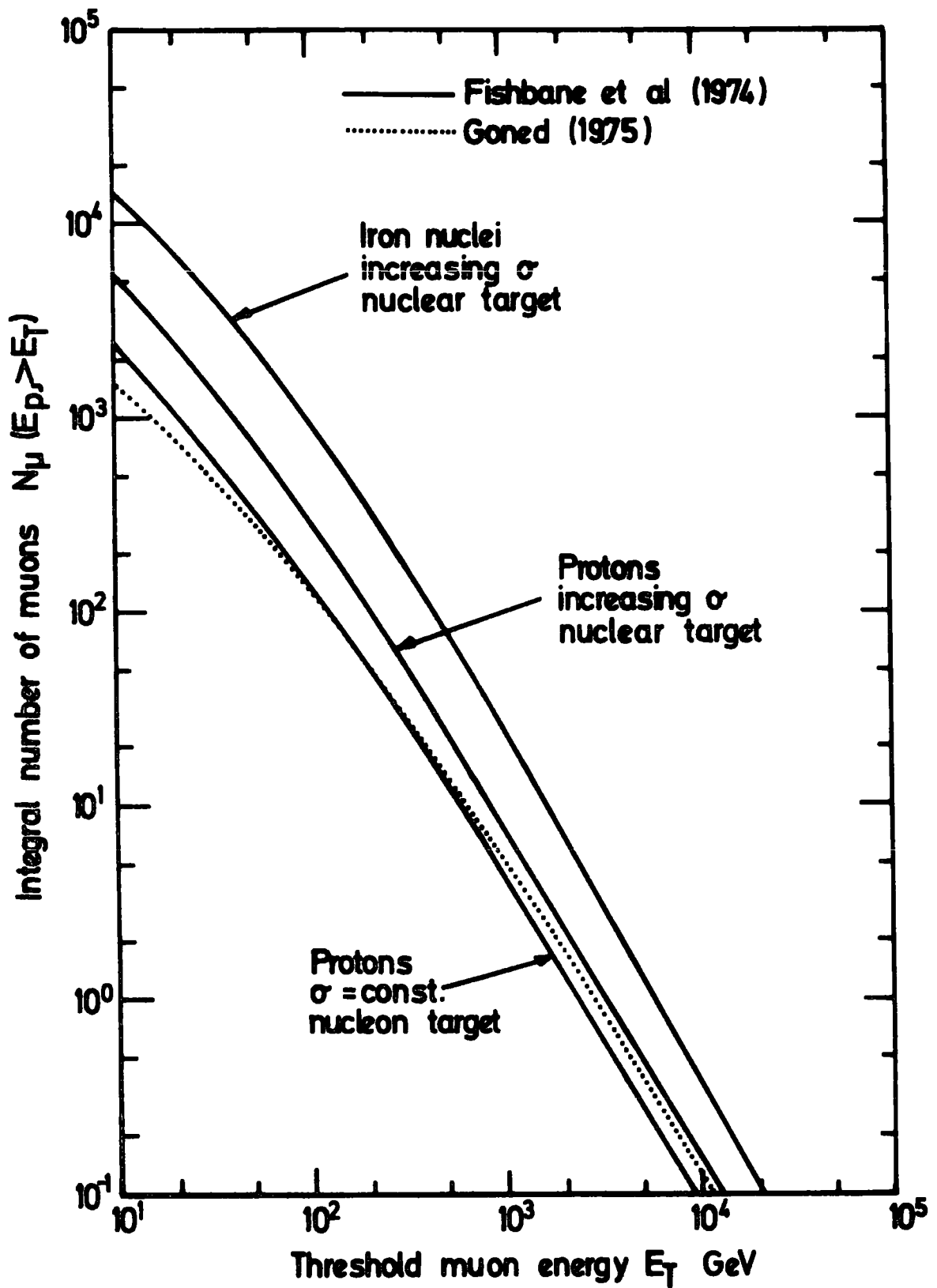


Figure 4.20 Integral muon energy spectra at  $\theta = 0^\circ$  for shower of size  $N_e = 10^6$

that is predicted is consistent with the measured spectrum. For all the models considered two different compositions have been used.

1. A proton only spectrum.

For energies of up to about  $5 \times 10^3$  GeV, the region of direct measurement of the spectrum, protons dominate. The use of a proton only spectrum should give a lower bound to the  $N_\mu/N_e$  ratio. The shower size fluctuations and age fluctuations (Khristansen et al., (1971) and Catz et al., (1973) seen in showers from primaries of  $10^5$  to  $10^7$  GeV suggest protons as at least part of the primary spectrum up to these energies. So the lead of many workers has been taken and a proton only spectrum is used as a datum.

2. A composition spectrum.

Here seven main constituent nuclei are taken and all are assumed to follow a power law of the form  $I_0 E^{-\gamma}$  with a break occurring in the spectral shape of each mass component at a constant rigidity. The proton spectrum is taken from Ryan et al., (1972) who give the exponent  $\gamma$  as 2.75, and the proportions of heavier nuclei are taken from a survey by Elbert et al., (1974). This survey has taken measurements in the range 2 to 500 GeV/nucleon made by Ryan et al., (1972) for Z equal to 2, Cartwright et al., (1971) for Z 2 to 9, Shapiro and Silberberg, (1970) for Z 10 to 28, and Balasubrahmanyam and Ormes, (1972) for Z equal to 26. The spectral break is assumed to occur at a rigidity of  $2 \times 10^6$  GeV as given by Hasegawa et al., (1962). In Table 4.5 the proportions and mean charge (Z) and weight (A) of the different components of the spectrum are given.

The hypothesis of superposition has been assumed to hold for the region of primary energy of interest in the present work. This requires that the interaction of a heavy nucleus of mass A and total energy E is equivalent to the 'superposition' of A times as many showers each of energy E/A. This implies complete fragmentation of the incident nucleus in the first interaction. The validity and effect of this assumption will be considered in Chapter 6. Most showers in the range of  $10^3$  to  $10^7$  particles have developed beyond their

THE COMPONENTS OF THE PRIMARY SPECTRUM

USED FOR THE C.K.P. AND SCALING MODELS.

	P	$\alpha$	L	M	LH	H	VH ( $F_e$ )
N Z	1	2	4	7	11.5	19	26
N A	1	4	8	14	23	40	56
PORTION E ENERGY NUCLEON	1	.042	$7.1 \cdot 10^{-4}$	$2.92 \cdot 10^{-3}$	$9.1 \cdot 10^{-4}$	$2.97 \cdot 10^{-4}$	$4.89 \cdot 10^{-4}$
E ENERGY NUCLEUS	1	.475	.027	.296	.220	.189	.561
CTION OF TOTAL ( $= 5.536 \cdot 10^4$ )	.361	.172	.010	.107	.079	.068	.203

TABLE 4.5

maximum when detected at sea level. The higher the energy of the primary the further the maximum moves down toward sea level and the total number of particles detected increases. Hence shower size  $N_e \propto E_p^\alpha$  where  $\alpha$  is greater than unity. However, the number of muons reaching sea level will tend to decrease because as the energy of the interaction rises, the energy given to the pions produced will increase and hence they will tend to interact rather than decay to muons. So the number of muons  $N_\mu \propto E_p^\beta$ , where  $\beta$  is less than unity. Consequently for a primary of mass  $A$ , using the superposition model,  $N_e \propto A (E/A)^\alpha = E^\alpha A^{1-\alpha}$ , hence  $N_e$  decreases as  $A$  increases and  $N_\mu \propto A (E/A)^\beta = E^\beta A^{1-\beta}$  so  $N_\mu$  increases as  $A$  increases. Using the C.K.P. model of de Beer et al., (1968), Turner (1969) finds that the shower size varies as  $A^{-0.33}$ . Allowance was made for fluctuations which for the C.K.P. model results in a relative width  $\sigma_{N_e}/N_e = 7.0 E_p^{-0.15}$ , where  $\sigma_{N_e}$  is the standard deviation of the shower size distribution and  $N_e$  is the average value for a primary proton of energy  $E_p$ . The width of the fluctuations for heavy particle initiated showers is given by

$$\left\{ \frac{\sigma}{N_e} \right\}_A = \left\{ \frac{\sigma}{N_e} \right\}_P A^{-1/2}$$

which decreases as  $A$  increases. Figure 4.21 shows the sea level shower size as a function of nucleus energy, the corrections for fluctuations implying that the relations are for fixed shower size,  $N_e$ .

For the application of the different models discussed to the present experimental data the actual intensity and composition of the primary spectrum used for each of the models will be different. This is because each model plus primary spectrum is constrained to predict the shower size spectrum. For the proton only spectra the parameters are given in Table 4.6. For the spectra composed of different nuclei, the parameters are given in Table 4.7, and the inter-relation of the different components is shown in Figures 4.22 and 4.23. These parameters are fixed by the proportions of the different nuclei as given

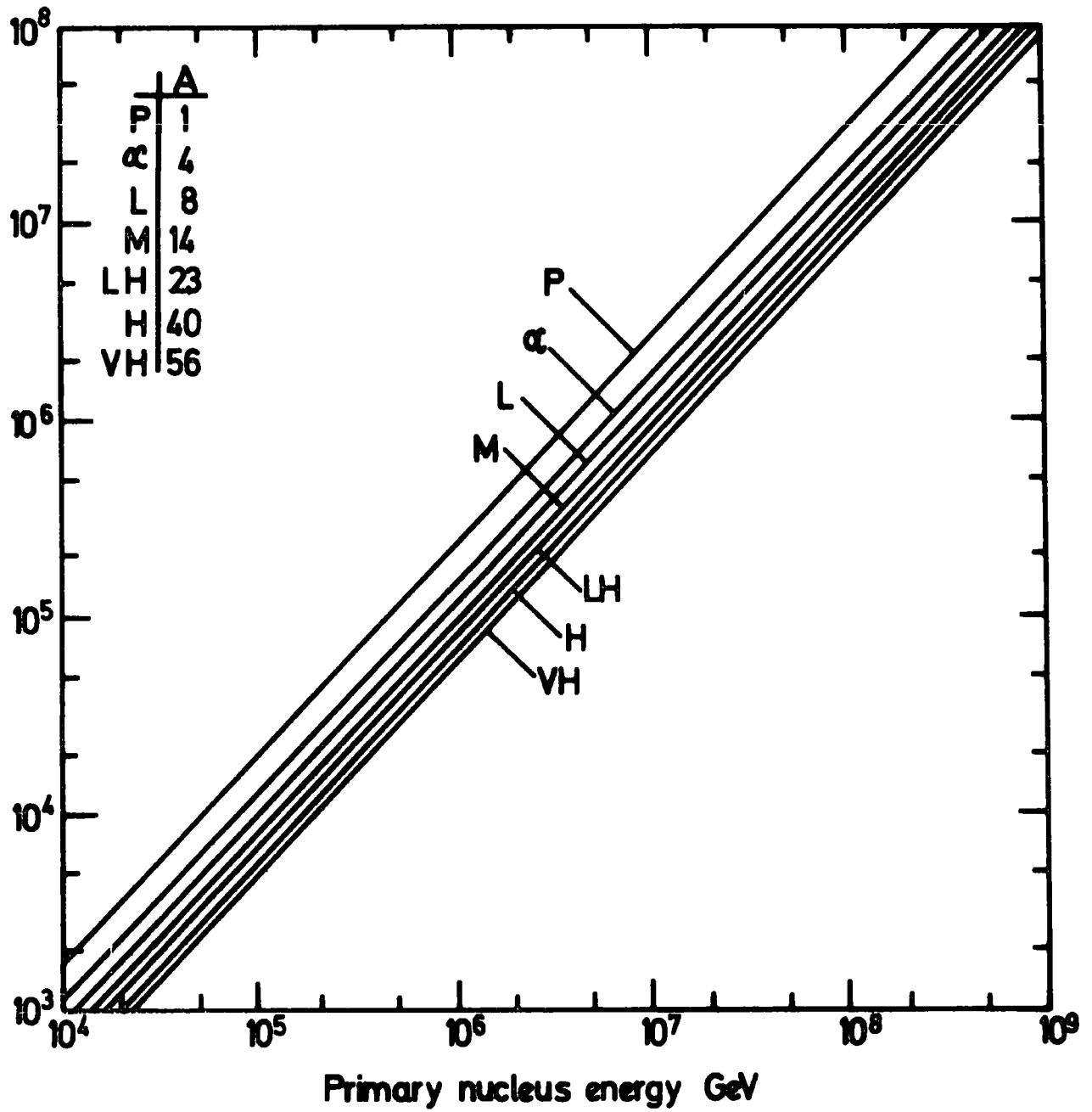


Figure 4.21. Sea level shower size vs. primary nucleus energy for the CKP model.

THE PARAMETERS FOR THE PROTON ONLY SPECTRA

USED FOR CKP AND SCALING MODELS, WHERE

$$\frac{J(E_p) dE_p}{M s^{-1} sr^{-1} GeV^{-1}} = K E_p^{-\alpha} \frac{dE_p}{p}$$

	Below Break Point		Break Point	Above Break Point	
	K	$\alpha$	GeV	K	$\alpha$
	$M^{-2} s^{-1} sr^{-1} GeV^{-1}$			$M^{-2} s^{-1} sr^{-1} GeV^{-1}$	
MODEL A (CKP, see figure 4.21)	$3.33 \cdot 10^3$	2.596	$2.79 \cdot 10^6$	$2.11 \cdot 10^7$	3.164
MODEL B (Scaling, see figure 4.23)	$6.18 \cdot 10^3$	2.687	$1.75 \cdot 10^6$	$4.79 \cdot 10^7$	3.289
MODEL C (Scaling)	$1.72 \cdot 10^5$	3.034	$2.96 \cdot 10^6$	$5.80 \cdot 10^{10}$	3.670

TABLE 4.6

**THE PARAMETERS FOR THE COMPOSITION OF THE PRIMARY SPECTRUM**

	P	$\alpha$	L	M	LH	H	VH	
A	1	4	8	14	23	40	56	
Fraction of Total Spectrum	.361	.172	.010	.107	.079	.068	.203	
MODEL A $A^{\alpha(1-\gamma)}$	1	.472	.324	.239	.183	.135	.113	
Fraction $x A^{\alpha(1-\gamma)}$	.361	.081	.003	.026	.015	.009	.023	$\Sigma=.518$

Below Break Point  $I_0 = 6.414 \cdot 10^3 M^{-2} s^{-1} sr^{-1} GeV^{-1}$ ,  $\gamma = -2.596$

Above Break Point  $I_0 = 6.635 \cdot 10^7 M^{-2} s^{-1} sr^{-1} GeV^{-1}$ ,  $\gamma = -3.164$

MODEL B $A^{\alpha(1-\gamma)}$	1	.484	.337	.251	.194	.145	.122	
Fraction $x A^{\alpha(1-\gamma)}$	.361	.083	.003	.027	.015	.010	.247	$\Sigma=.524$

Below Break Point  $I_0 = 1.1986 \cdot 10^4 M^{-2} s^{-1} sr^{-1} GeV^{-1}$ ,  $\gamma = -2.687$

Above Break Point  $I_0 = 2.326 \cdot 10^8 M^{-2} s^{-1} sr^{-1} GeV^{-1}$ ,  $\gamma = -3.288$

MODEL C $A^{\alpha(1-\gamma)}$	1	.785	.695	.631	.578	.525	.495	
Fraction $x A^{\alpha(1-\gamma)}$	.361	.135	.007	.067	.046	.036	.101	$\Sigma=.716$

Below Break Point  $I_0 = 1.685 \cdot 10^5 M^{-2} s^{-1} sr^{-1} GeV^{-1}$ ,  $\gamma = -2.971$

Above Break Point  $I_0 = 1.813 \cdot 10^{11} M^{-2} s^{-1} sr^{-1} GeV^{-1}$ ,  $\gamma = -3.673$

**TABLE 4.7**

in Table 4.5 and by the sea level shower size spectrum. In Appendix G the determination of the parameters for a given relation of shower size to primary energy is given. The choice of models is given in the next section.

#### 4.7.11 THE TRIAL MODELS AND PRIMARY SPECTRA

To compare the predictions of the C.K.P. model and the scaling model three different lines of investigation are followed, and are referred to as Model A, B and C.

##### 1. Model A

This involves the proton only spectrum of Figure 4.22. With this the shower size to primary energy relation for the C.K.P. model (for fixed  $N_e$ ) due to de Beer et al., (1966) (Figure 4.16) is used. The muon component is determined from the total muon number and radial moments from the calculations by Goned (1975). To consider the effects of different nuclei in the primary spectrum, the primary nucleus spectra of Figure 4.22 are used with the shower size to primary nucleus relations of Figure 4.21. The muon component is again based on the work of Goned and the superposition principle is applied.

##### 2. Model B

The calculations based on scaling of Fishbane et al., and Goned are combined to consider scaling with a constant proton-air cross section and a nucleon target. For the proton only spectrum the relation of shower size to primary energy of Figure 4.19 is taken in conjunction with the proton only spectrum of Figure 4.23 and the predictions for total muon number and radial muon structure of Goned. To determine the effect of heavier nuclei, the same shower size dependence on mass ( $N_e \propto CA^{-0.33}$ ) as predicted by the C.K.P. model is assumed to apply to the scaling situation. The corresponding primary nucleus spectra are shown in Figure 4.23.

##### 3. Model C

To allow for the possible influence of a rising proton-air nucleus

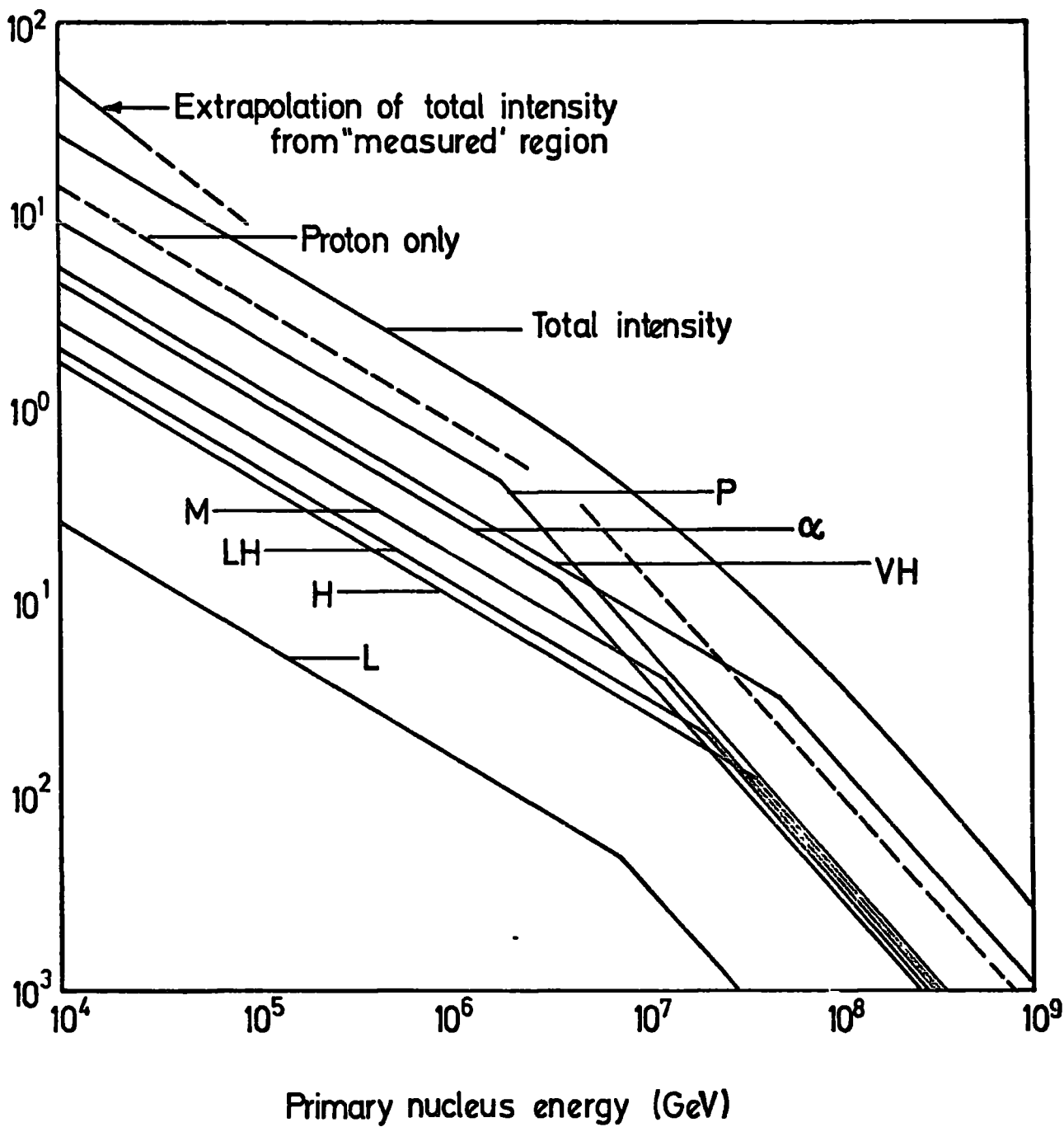
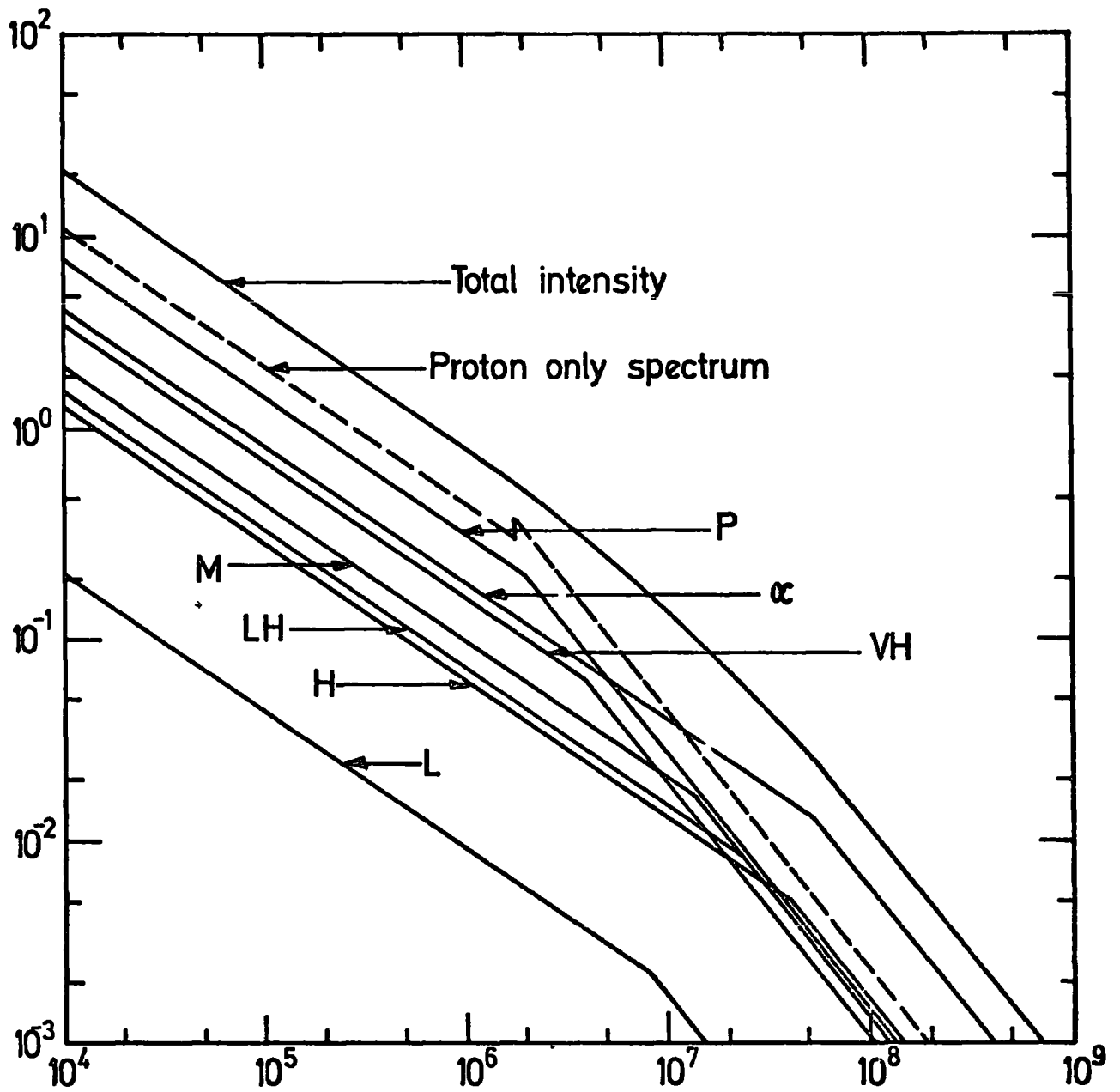


Figure 4.22 The primary spectrum used for the CKP model calculations (model A)



Primary nucleus energy. GeV.

Figure 4.23. The primary spectrum used for the Scaling Model calculations. (Model B).

cross-section and of intranuclear cascading. The results of Fishbane et al., for the scaling model are again combined with the muon predictions of Goned. However, although it is possible to determine the increase in the total number of muons and the decrease in shower size (see Figures 4.19 and 4.20) the effect on the lateral structure of the muons is not determined. Turver, 1975, has extended the basic model of Fishbane et al., to a three-dimensional development model of showers. This author incorporates slight differences in the model, for example, the fragmentation process, but reaches the same conclusions as Fishbane et al., with regard to the longitudinal development of the electron cascade and the integral energy spectra of muons. Figure 4.24 is the lateral distribution of muons (in fact of lower muon energy than considered in the present work) predicted for the scaling model compared to a conventional C.K.P. model as given by Turver, 1975. These functions are for a  $\sigma_{p-air}$  rising with energy and intranuclear cascade. The lateral distribution for proton initiated showers is still somewhat narrower than for a 'conventional' model, but that for iron initiated showers is about the same. Thus as a first approximation (to give an upperbound to the predictions for the present work) the muon lateral structure functions corresponding to constant  $\sigma_{p-air}$  and no nuclear target effects are taken and the density is considered to increase. The total muon number corresponds to the number predicted by Fishbane et al., (1974), when rising cross-section and nuclear target effects are taken into consideration. Table 4.8 shows the factor by which the total muon number increases as a function of muon threshold energy. The decrease in shower size because of the more rapid development of the shower is determined from Figure 4.19 to be a function of primary mass such that,  $N_e \propto A^{-0.116}$ . The lateral structure will in fact be broader than considered here (if rising cross-section and nuclear target effects do occur) and the predictions of this 'hybrid' model must be considered

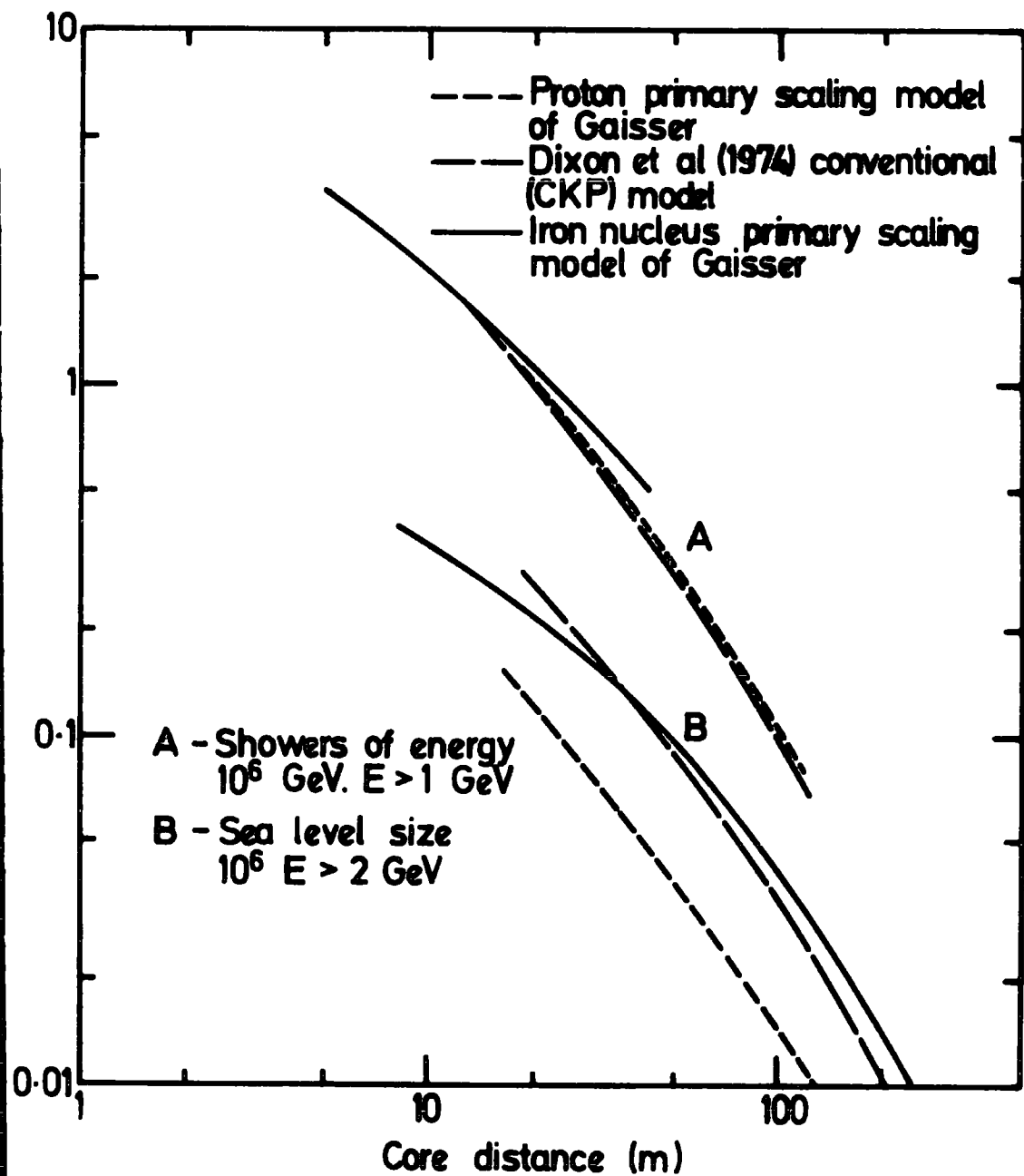


Figure 4.24. Muon lateral distribution functions (after Turver 1975).

THE PREDICTED INCREASE IN TOTAL MUON NUMBER FOR RISING  $\sigma_{P-AIR}$

AND NUCLEAR TARGET EFFECTS

MUON ENERGY	$E_T$ GeV	20	50	100	200	500	1000
Increase due to $\sigma_{p-air}$ Rising and Nuclear Target	Protons	2.4	2.4	2.4	2.0	1.8	1.66
	$F_e$	6.5	7.5	7.6	7.2	6.66	4.0

TABLE 4.8

in this light.

In the next section the method of applying the predictions of these three models to the present experimental results will be given.

#### 4.7.12 THE PREDICTED RATE OF EVENTS USING THE C.K.P. AND SCALING MODELS

The application of the predictions of the models discussed in the immediately preceding sections follows closely the method used involving the empirical particle structure functions and sea level shower size spectrum as discussed in Section 4.6. In this case, however, the rate of events will be the summation over all primary energies modulated by the primary spectrum as opposed to the summation over all shower sizes modulated by the shower size spectrum. Thus the predicted rate of events in which at least one muon of momentum greater than  $P_\mu$  crosses the area  $S$  of the top of the spectrograph and the instrument is triggered and there are at least 31 columns of data, is

$$R (>P_\mu) = \int_{\text{All Primary Energies}} \int_{\text{All Radial Distances}} P_M P_T J(E_p) 2\pi r dr dE_p \text{ s}^{-1} \text{ sr}^{-1} \quad (4.32)$$

On this occasion  $P_m$  is as defined in equation 4.12 but  $\rho_\mu$ , the radial density of muons, is taken from the model predictions.  $P_T$  is as defined in equation 4.1 where the shower size for each primary energy is given by the model under consideration but the lateral structure of electrons has been determined by the structure function due to Greisen (1960), equation 4.5. The differential primary spectrum,  $J(E_p) dE_p$ , varies according to the model under consideration and also varies according to the composition of the spectrum.

To evaluate expression 4.32, 15 steps in primary nucleon energy from an energy of  $1.0 \cdot 10^3$  GeV to  $1.0 \cdot 10^8$  GeV, were used for each threshold value of muon moment,  $P_\mu$ . The integration ranged from 0.1 m to 100.0 m. in radial distance from the centre of the spectrograph, and the expected rate was evaluated

for six values of threshold momentum for each combination of spectrum and model (muon momentum greater than or equal to 20, 50, 100, 200, 500 and 1000 GeV/c).

The results of these calculations are shown in Figures 4.25 to 4.28. In these figures the two lines indicated as C.K.P. correspond to model A as described in Section 4.7.11. The lines have been drawn smoothly through the six points at which the integral rate was evaluated. The extent of change in computed values corresponding to a 5% change in  $P_T$ , as described in Section 4.6, is indicated by the region of 'hatch.' The lines corresponding to the predictions of scaling are derived using model B as described in Section 4.7.11. In Figure 4.28 is shown the results of using model C, the last model given in Section 4.7.11. For all these predictions the primary spectrum used differs according to the conditions given previously. The discussion of the merit and closeness of fit to the experimental points of these predictions will be left until Chapter 6. For the present an indication of the primary nucleus energy contributing to these predicted rates is shown in Figures 4.29 to 4.31. These plots correspond to evaluation of the following integral for different values of primary nucleus energy :

$$I(E_p, >P_\mu) = J(E_p) \int_{0.1}^{100.0} P_M P_T 2\pi r dr$$

In Figure 4.29,  $I(E_p, >P_\mu) \times E_p$  has been plotted as a function of primary proton energy,  $E_p$ , for different threshold values of muon momentum,  $P_\mu$ , for both model A and B. These relationships are for a spectrum comprising protons only. In Figures 4.30 and 4.31 are shown  $I(E_N, >P_\mu) \times E_N$  as a function of primary nucleus energy,  $E_N$ , for model A and B with a spectrum of different nuclei. These figures indicating the range of primary energy contributing to the predicted rate have been evaluated for the probabilities associated with more than 30 columns of data in measuring tray 5. Table 4.9 shows the

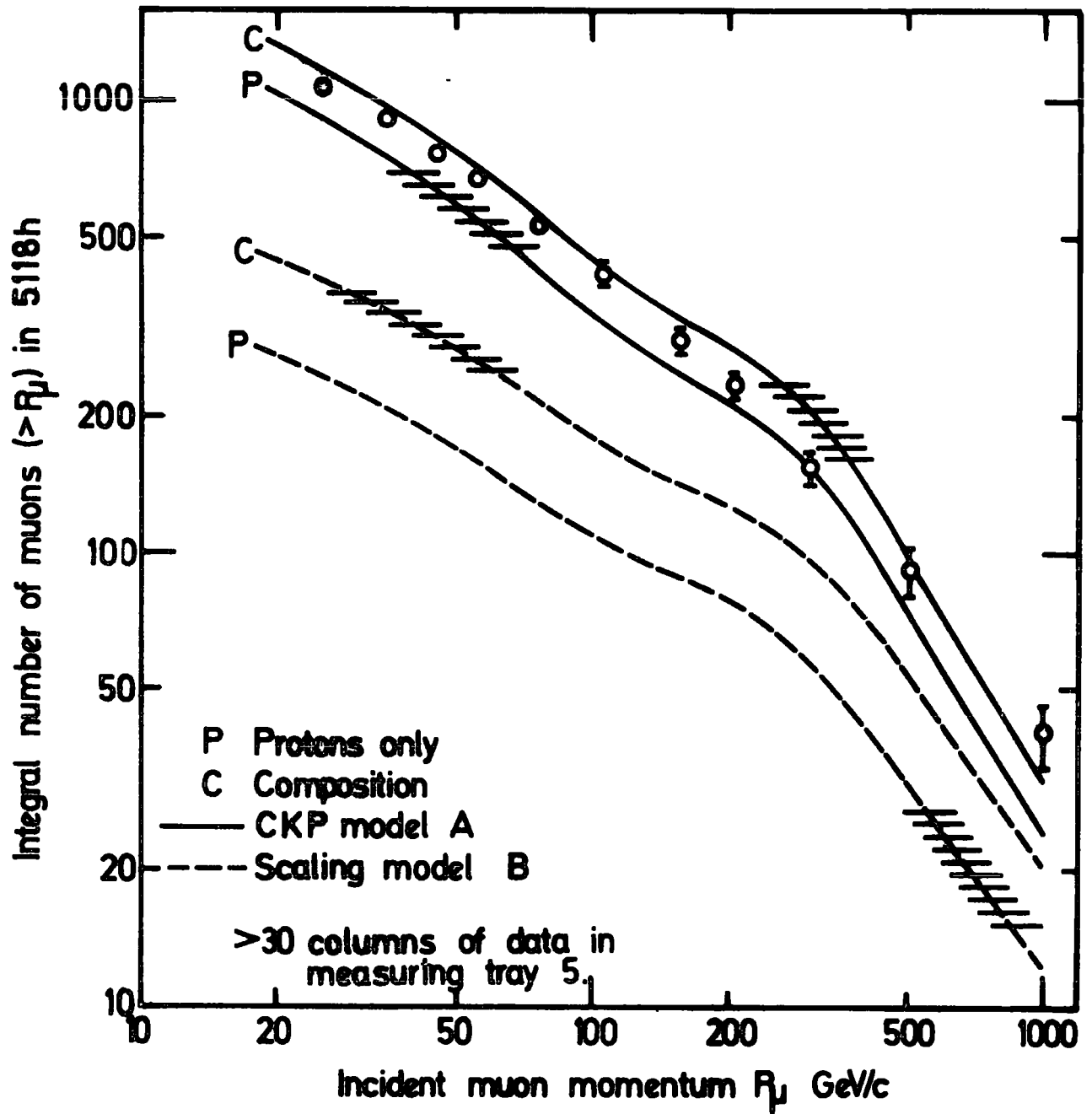


Figure 4-25. Model A and B predictions.

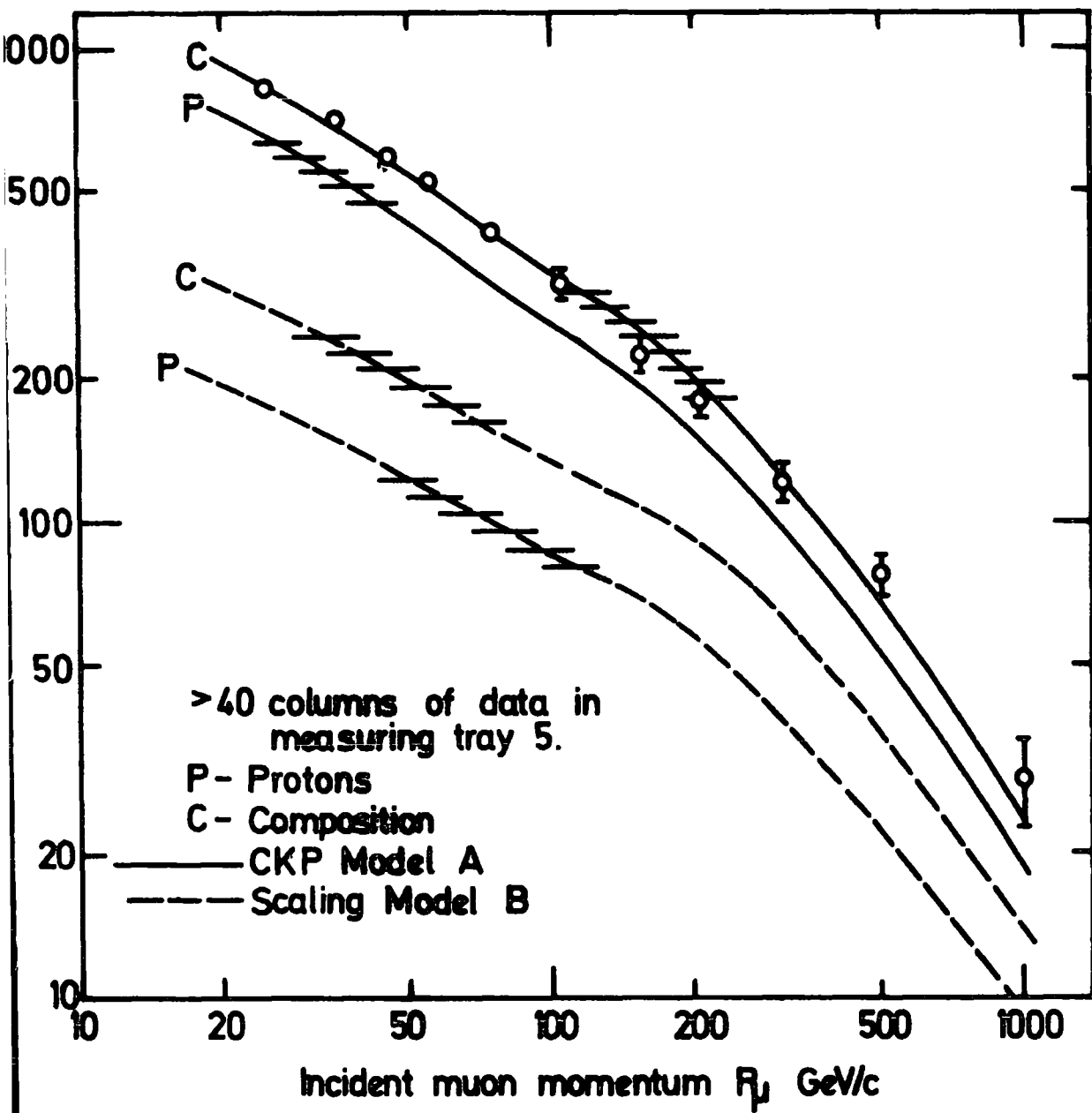


Figure 4.26. Model A and B predictions.

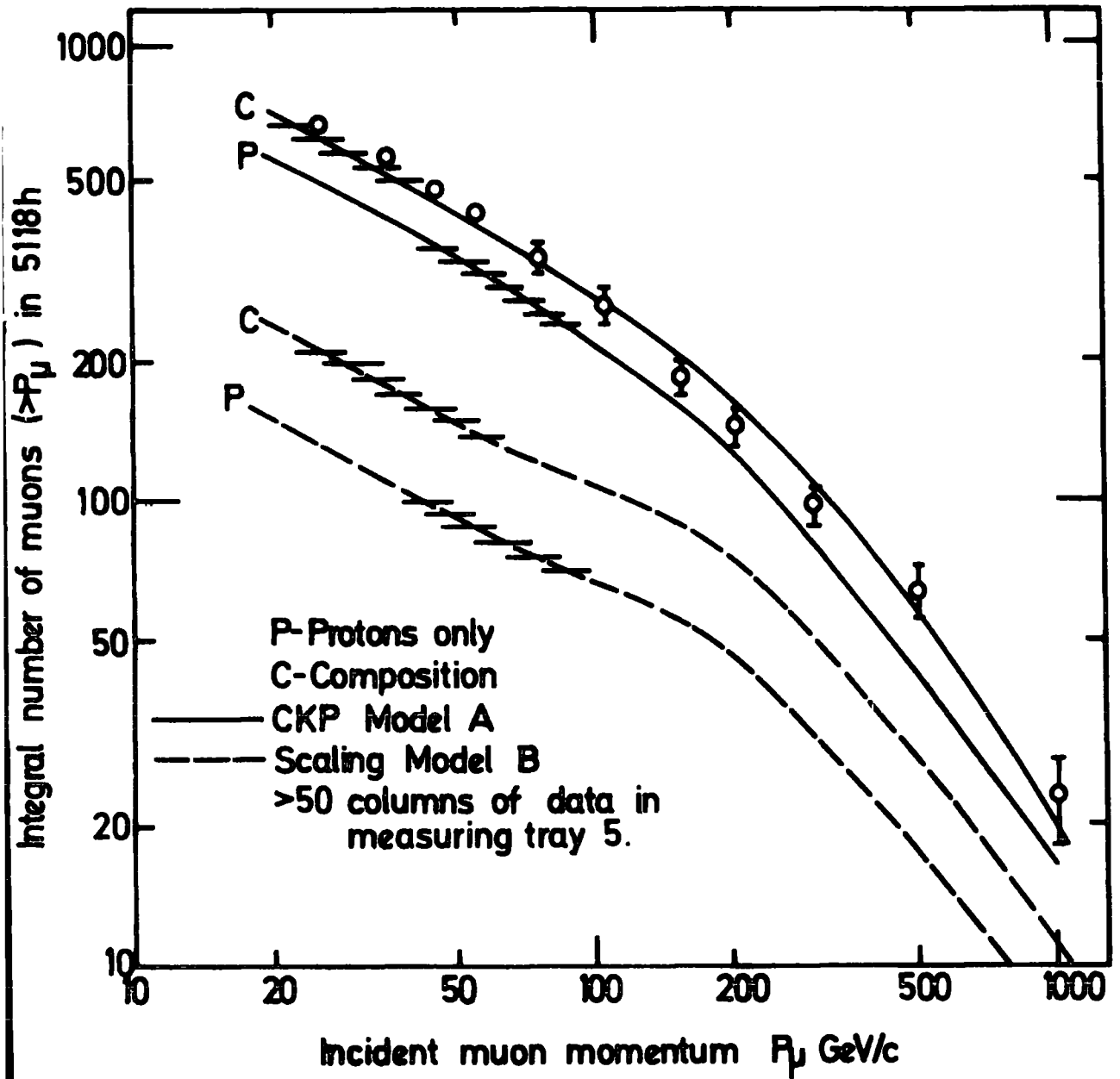


Figure 4.27. Model A and B predictions.

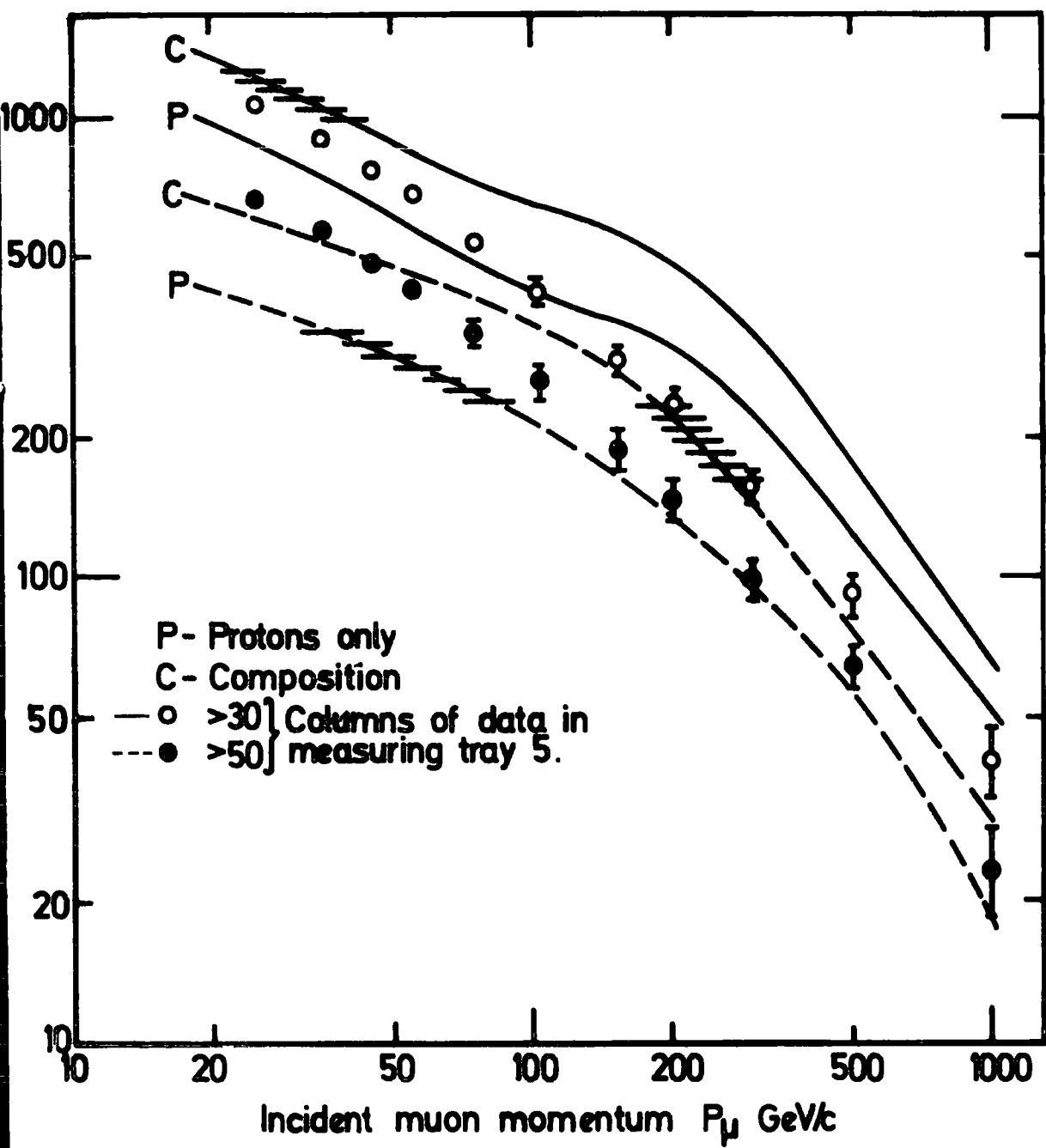


Figure 4.28. Scaling Model C.

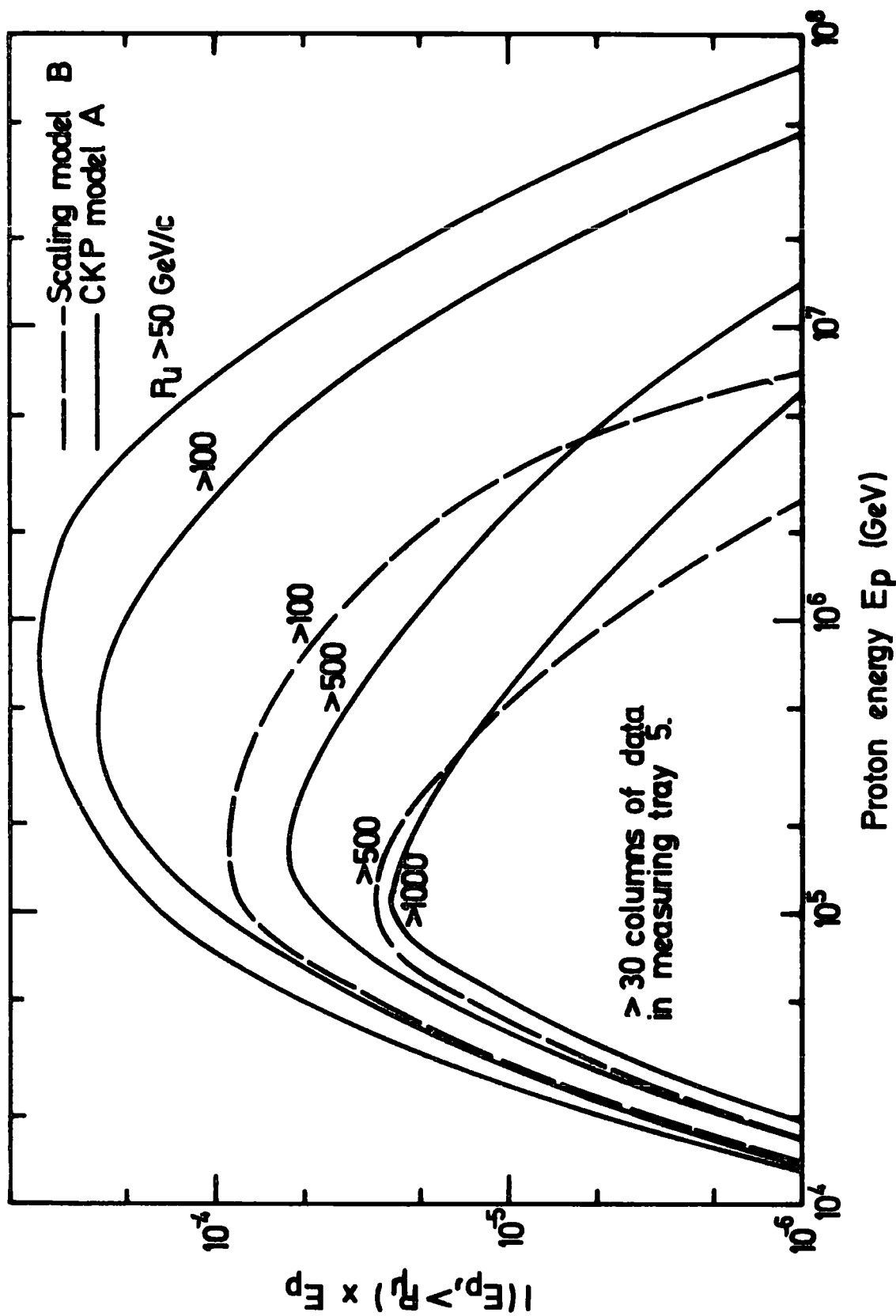


Figure 4.29. Contribution to predicted rate of events from proton only spectrum.

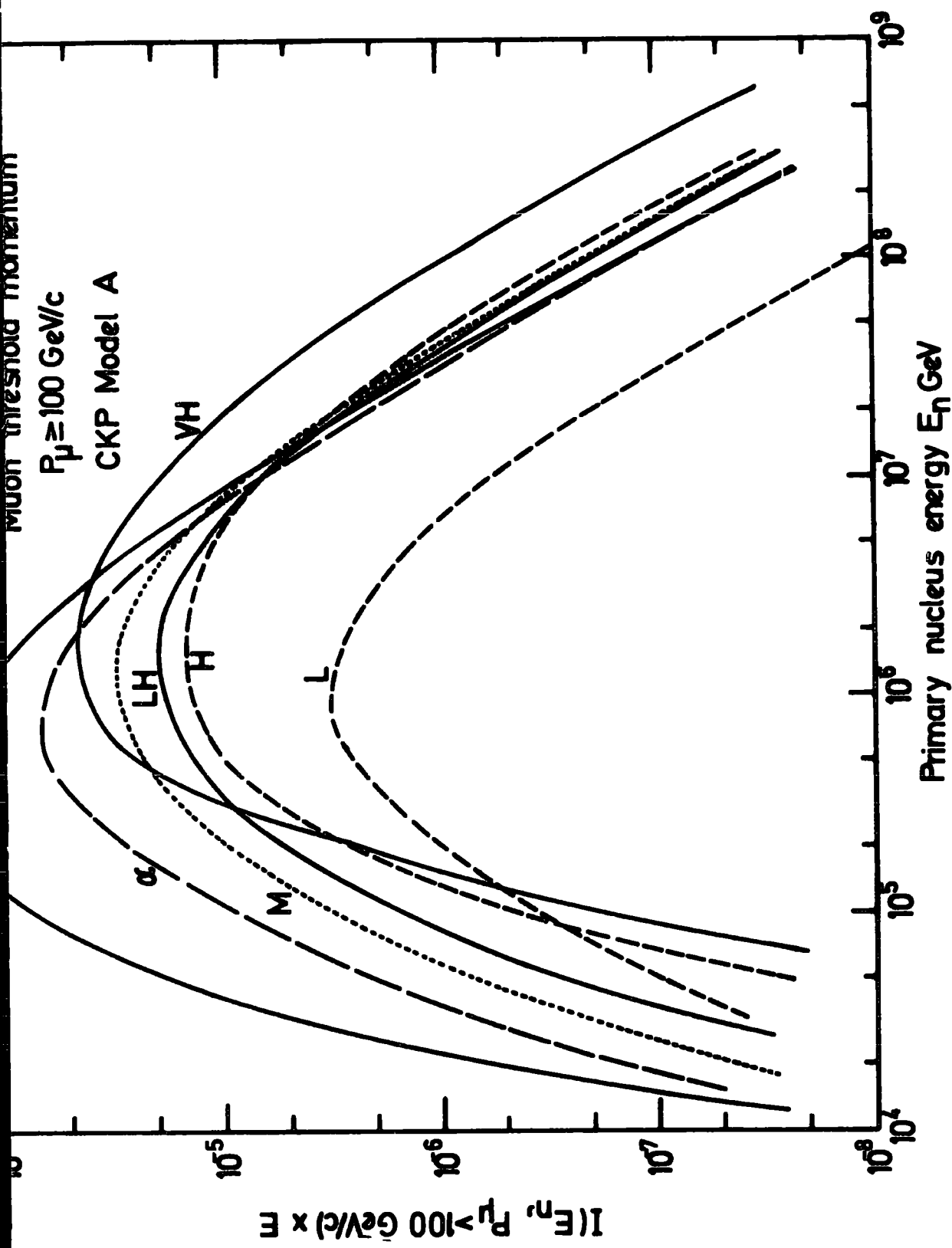


Figure 4.30. Contribution to the predicted rate of events from different components in primary spectrum.

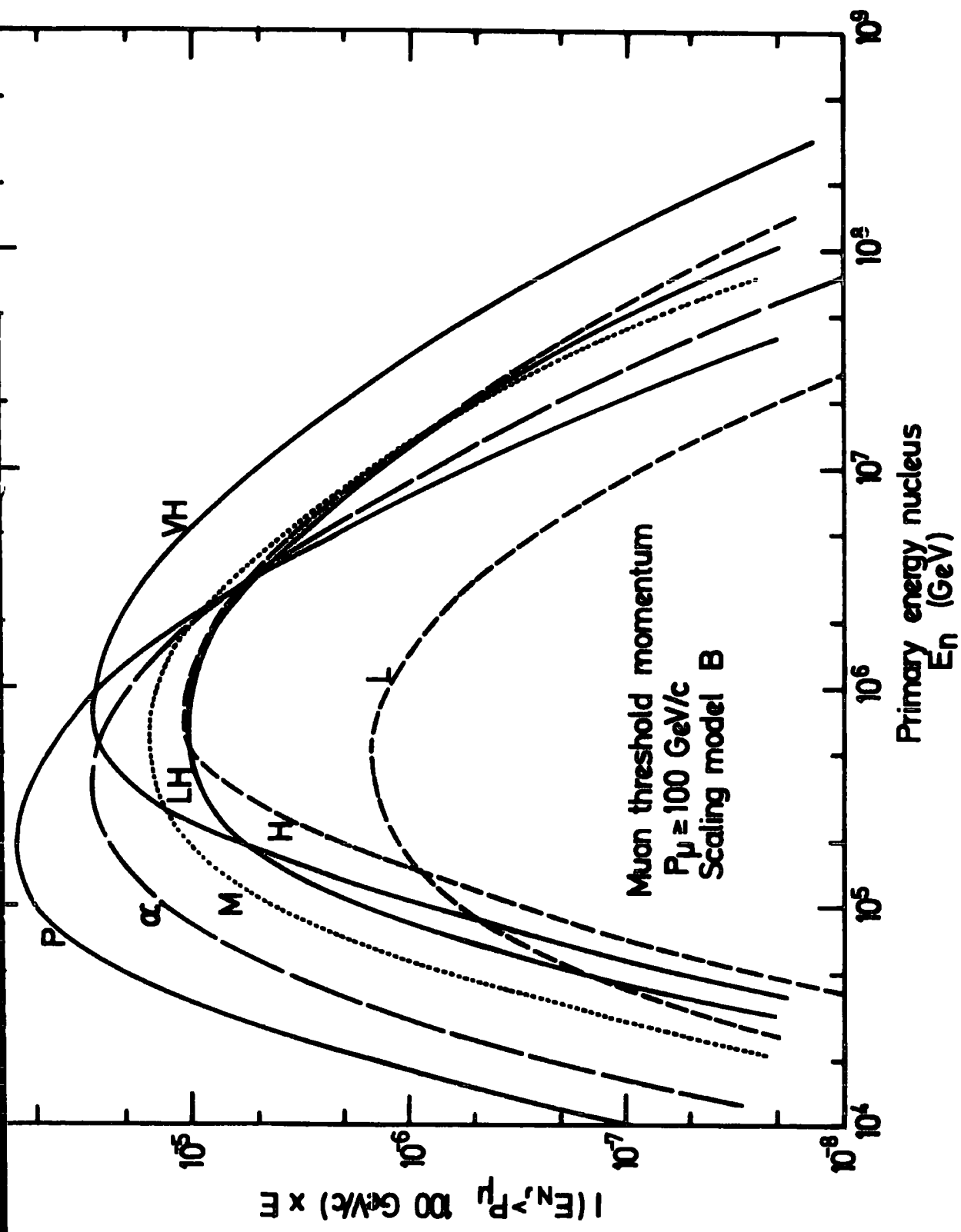


Figure 4-31. Contribution to the predicted rate of events from different components in the primary spectrum.

PROPORTION OF CONTRIBUTION TO PREDICTED RATE

FROM DIFFERENT NUCLEI IN THE PRIMARY SPECTRUM.

COMPONENT		P	$\alpha$	L	M	LH	H	VH
MEAN A		1	4	8	14	23	40	56
Muon Threshold Momentum	100	.482	.185	.010	.092	.060	.046	.126
GeV/c	1000	.560	.195	.009	.078	.047	.032	.079
CKP, MODEL A, >30 COLUMNS OF DATA								

Muon Threshold Momentum	100	.418	.188	.010	.101	.067	.057	.158
GeV/c	1000	.482	.195	.010	.098	.063	.043	.109
SCALING, MODEL B, >30 COLUMNS OF DATA								

Muon Threshold Momentum	100	.490	.182	.009	.091	.061	.045	.122
GeV/c	1000	.523	.194	.009	.086	.536	.037	.097
CKP, MODEL A, >50 COLUMNS OF DATA								

Muon Threshold Momentum	100	.416	.180	.105	.108	.074	.057	.154
GeV/c	1000	.464	.158	.010	.098	.069	.054	.147
SCALING, MODEL B, >50 COLUMNS OF DATA								

TABLE 4.9

proportions of contribution to the predicted rate from each primary mass component for two values of muon threshold momentum, and for both more than 30 and more than 50 columns of data.

## CHAPTER 5

### THE COINCIDENT MUON PAIR EXPERIMENT

#### 5.1 INTRODUCTION

Multiple pion production in very high energy hadron-hadron collisions can be studied by consideration of the pion decay products. For any event resulting from an interaction the more decay products seen the more information might be expected about the basic interaction. In the case of high energy cosmic ray primary interactions high in the atmosphere, the resulting coincident muons have been studied to investigate not only the multiplicity of particles, (see for example Lowe, et al.,(1975) Rogers, et al.,(1969)) but also the particle transverse momentum distribution (Bergeson, et al.,(1975)). An extensive study of muon groups deep underground has been performed by the University of Utah cosmic ray group, (see the Proceedings of the International Conference on Cosmic Rays from Denver, 1973, and Munich, 1975). Notably, measurements on the multiplicity of muons deep underground are some of the few cosmic ray experiments that show broad agreement with the predictions of a scaling model for hadron-nucleus interactions, (Elbert, et al.,(1975),Goned, et al.,(1975)). Ideally a measurement of any accompanying air shower should be made with the muon measurements to give as full a picture of the products of the fundamental interaction as is possible. In the light of this, a study of coincident muon pairs has been undertaken using the M.A.R.S. spectrograph, and S.A.R.A. air shower array.

As was described in Chapter 2, the spectrograph has two symmetric halves as a consequence of the magnet block design. Each half has 3 separate scintillation counters which provide the basic trigger pulses for the spectrograph. A coincident pulse from all 6 counters may be due to the traversal of each side of the instrument by coincident muons. From September, 1975,

until April, 1976, in over 3000 hours of recording, approximately 14400 triggers resulted in 380 events analysed as two or more coincident muons. For approximately half of this period the air shower array was operational and any air shower particles associated with the muon events were recorded. The rate of two muons traversing the blue side of the spectrograph is also considered in this chapter.

In the following section the acceptance of the spectrograph for coincident muons is considered. Paramount to any considerations of the data collected is an understanding of the operation of the instrument under the conditions of collection of the data. In this context coincident muon detection represents a complex mode of operation of the instrument as the momentum, sign and separation of the muons can all vary. In the following sections, information about any associated air shower as determined by the air shower array is discussed, and a possible correlation between the muons of a pair detected without an associated shower is considered.

Finally a comparison is made between the measured rate of events and the rate of events as predicted by using the models as described in Chapter 4.

## 5.2 THE ACCEPTANCE OF THE SPECTROGRAPH FOR MUON PAIRS

### 5.2.1 THE ACCEPTANCE FOR TWO MUONS TRAVERSING THE BLUE SIDE

In this section the acceptance of the blue side of the spectrograph for two muons traversing the lower 4 measuring trays plus a coincident shower striking the top will be considered. The acceptance is considered for pairs incident with parallel trajectories and is defined so as to be consistent with the pair intensity. Thus the measured counting rate, CR, is

$$CR = A_p \times I_p$$

where the acceptance  $A_p$  has dimensions of  $m^4 \text{ sr}$ , and the intensity  $I_p$  has dimensions  $m^{-4} \text{ sr}^{-1} \text{ s}^{-1}$ . In Appendix E the acceptance of a counter telescope

for muon pairs is determined following the method of Barton,(1971).

In order to determine the acceptance for pairs of muons account must be taken of the spectrograph triggering conditions. This applies because of the operation of the muon momentum selector. The triggering probability of the momentum selector will be greater for two muons than for one muon when accompanied by an air shower. This is due to the additional cells set in the momentum selector by the second muon. The probability of satisfying the momentum selector condition was determined in a similar way to the determination for single muons by the use of a computer simulation of the operation of the momentum selector. For any given density of shower particles which set cells in the momentum selector tray at level 5, two trajectories were considered passing through the lower 2 momentum selector trays. However, neither track was constrained to project into the momentum selector tray at level 5. With 2 low momentum tracks not only is there a chance that the cells set by each muon will separately line up with the cells set by the shower particles but every possible combination of cells will be tested by the logic for the straight line condition. Thus in determining the acceptance for pairs of muons accompanied by showers a 4 tray acceptance has been used, where the upper defining element for the muons is measuring tray 4 and the lower one is scintillation counter level 1. This defines a rectangular box of dimension 1.76 m by 0.75 m of height 4.89 m. Equation E 1.4 from Appendix E has been used to determine the values of acceptance for straight line tracks, which correspond to the limiting case of 'infinite' momentum muons. The values given in Table 5.1 correspond to a pair intensity variation, with zenith angle ( $\theta$ ), of  $\cos^n \theta$ . The Monte Carlo technique described in Appendix B and E has been used to determine the acceptance of muon pairs of momenta less than this limiting value. In Figure 5.1 the variation of relative acceptance with momentum for equal momentum muons is shown. As can be seen there is a marked difference between a muon pair having the same charge and a pair having different charges. This effect is discussed in detail in the next section as such an

THE ACCEPTANCE FOR PAIRS OF MUONS THROUGH THE LOWER 4 MEASURING TRAYS  
OF THE BLUE SIDE

n	ACCEPTANCE $M^4 \text{ sr}$
0	4.149 $10^{-2}$
2	4.091 $10^{-2}$
4	4.034 $10^{-2}$
6	3.980 $10^{-2}$
8	3.927 $10^{-2}$

TABLE 5.1

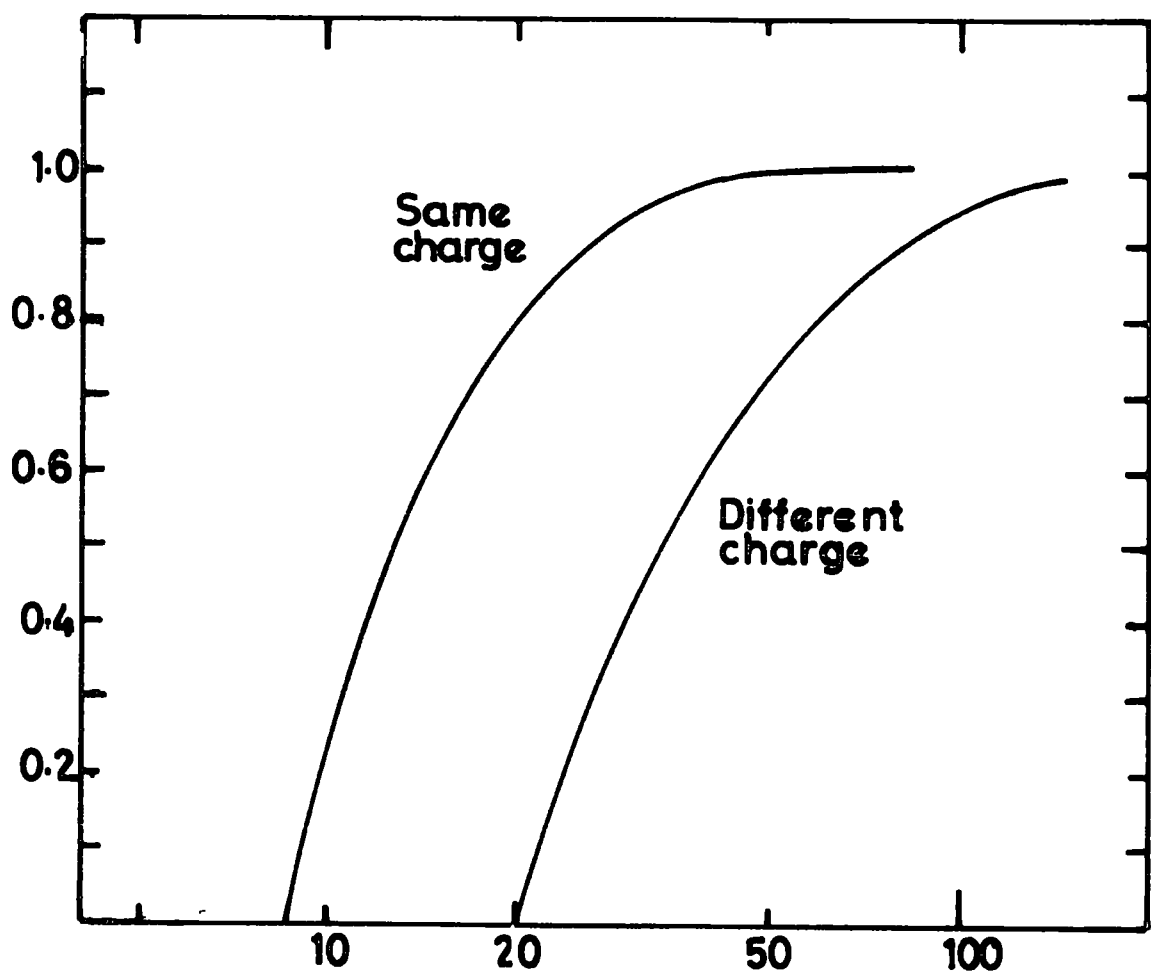


Figure 5.1 Incident momentum Gev/c

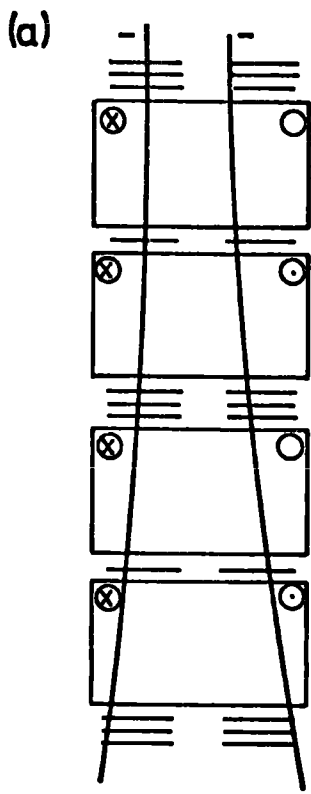
5 Tray acceptance for equal momentum muons.

effect will also apply to two muons when one traverses each side of the spectrograph. For shower accompanied muon pairs traversing the blue side the limiting value of acceptance is reached for any combination of charge when both muons are above a momentum of about 60 GeV/c.

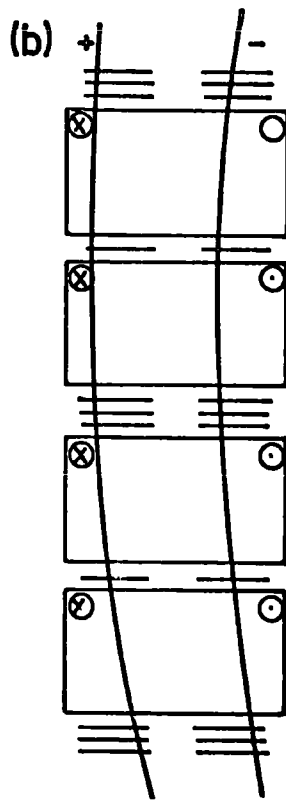
### 5.2.2 ONE MUON TRAVERSING EACH SIDE OF THE SPECTROGRAPH

If two muons are incident on the spectrograph they will be accepted and trigger the instrument, if one muon passes down each side through the three scintillation counters. For muons arriving parallel the acceptance will depend not only on the direction of arrival but also on the separation, charge and momentum of the two muons. Considering first the situation of an unassociated muon pair arriving parallel where both strike the top of the spectrograph. The four possible configurations under which the muons will be accepted are shown schematically in Figure 5.2 (a), (b), (c) and (d). There will be four further mirror image configurations when the field direction is reversed. Of these eight possibilities there are 3 uniquely different situations for two muons of given momenta. They will either diverge, as in Figure 5.2 (a) ; or they will bend in the same direction, as in Figure 5.2 (b) and 5.2 (c) ; or they will converge as in Figure 5.2 (d). A Monte Carlo computer program was used to investigate all these possibilities by simulating muon pairs incident on a computer model of the spectrograph. The general technique used is explained in Appendix E. An area incorporating the gap between the detecting elements on the top of the spectrograph was used to initialise the trajectories of the muons. All three possible arrival combinations were tested by allowing the two muons to fall anywhere over the whole area and the trajectories computed to determine if one muon passed either side of the spectrograph. The three possible combinations are that both muons can be positive, both negative, or one of each charge.

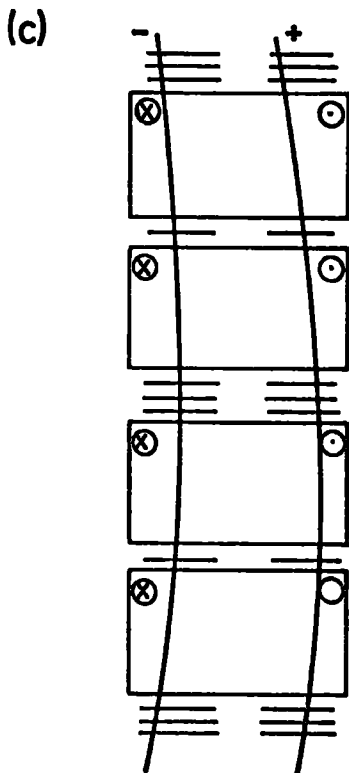
The results of this analysis can be seen in Figure 5.3 where the relative acceptance is plotted as a function of the momentum of one of the



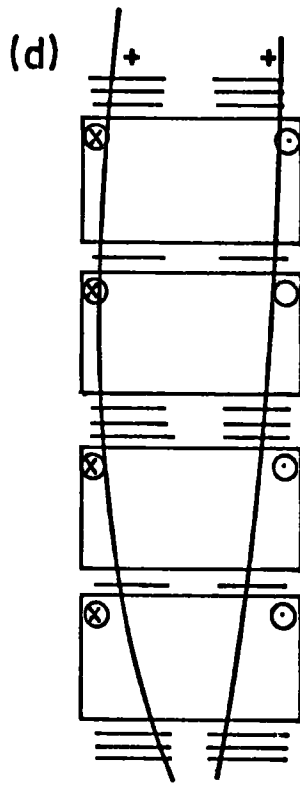
2 negative muons.



negative muon on the red side,  
positive muon on the blue side.



positive muon on the red side,  
negative muon on the blue side.



2 positive muons.

⊗ field direction  
into paper  
⊙ field direction  
out of paper

The four possible directions of bending for two muons - one passing down each side for one field configuration.

Figure 5-2

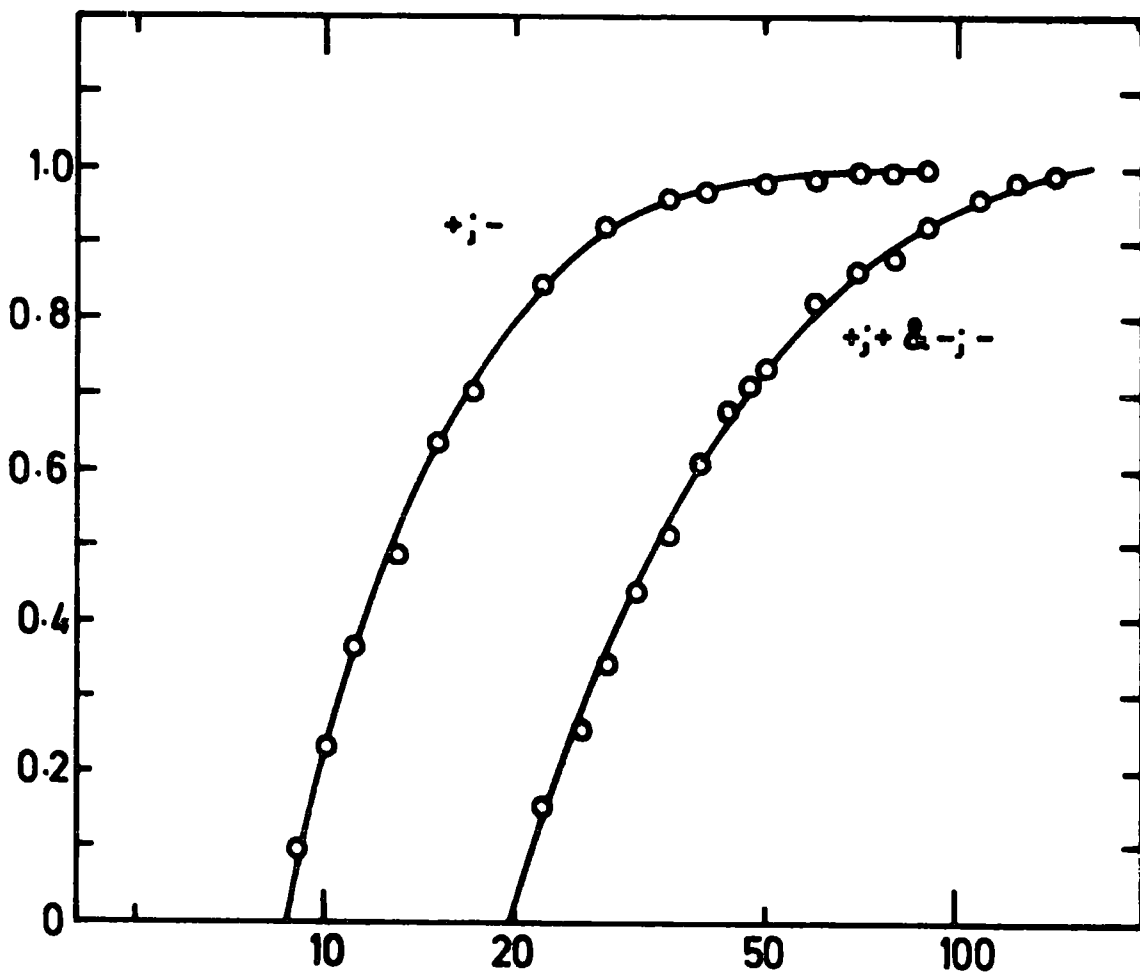


Figure 5.3 Incident momentum GeV/c  $P_{\mu_1} = P_{\mu_2}$

5 Tray acceptance for muon pair  $P_{\mu_1} = P_{\mu_2}$   
 No arrival direction dependence.

incident pair of muons. The variation obtained for both two positive and two negative muons was the same. Also the same variation of acceptance for the case of divergence of the muons, as in Figure 5.2 (a), was found as for the case of convergence of the muons, as shown in Figure 5.2 (d). In Figure 5.3 the open circles represent the acceptance as determined by the Monte Carlo program and the lines are drawn smoothly through the points to act as a guide.

The acceptance for muons accompanied by air shower particles will be of the same form except that the muons need only traverse the lower 4 detecting elements on either side of the spectrograph as the shower particles will trigger the top scintillation counters. This increase in acceptance is shown in Figure 5.4. In Figure 5.5 the variation of acceptance is shown as a function of the momentum of one muon of a positive pair and in Figure 5.6 the variation of acceptance is shown for two muons of opposite charge. The acceptance for muon pairs detected with a shower becomes constant with momentum when both muons have a momentum of over about 60 GeV/c whilst for unassociated pairs the limiting value is reached when both muons have momentum over about 100 GeV/c. These limiting values are independent of the charge of the muons.

The acceptance described above has been considered relative to the acceptance for two 'infinite' momentum muons incident on the spectrograph. In order to make some comparison with the rate of events of two muons traversing the blue side, a calculation has been made using a hypothetical instrument which has a sensitive volume equal to both halves of the spectrograph considered joined. Thus a rectangular box of dimensions 1.76 m. by 1.888 m. of height 6.49 m. is considered. The area of the top is given by the area of both adjacent detecting elements plus the gap between them. This is shown in Figure 5.12 and discussed in Section 5.4.2. For the shower accompanied case the height of the box thus considered will be 4.89 m. with the same top and bottom areas. Table 5.2 gives the values of acceptance

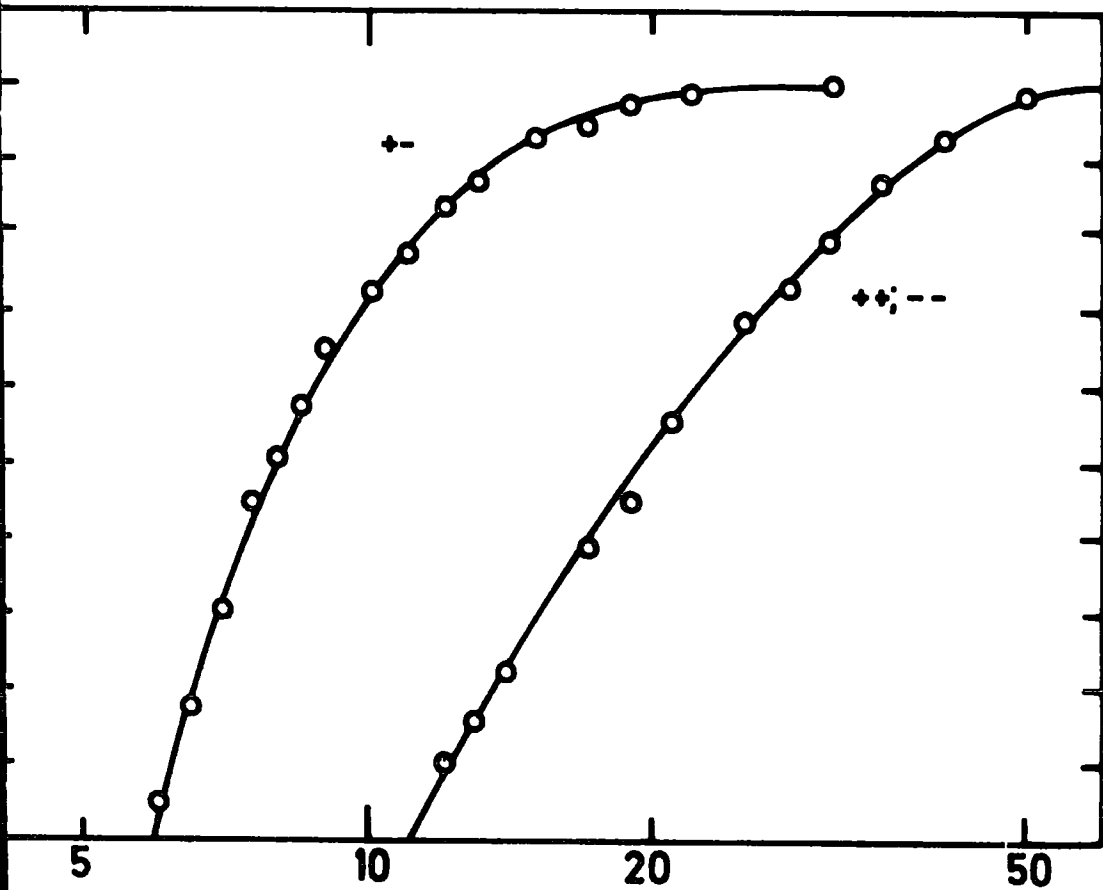


Figure 5.4 Incident momentum GeV/c  $P_{\mu_1} = P_{\mu_2}$

4 Tray acceptance for muon pair  $P_{\mu_1} = P_{\mu_2}$   
 $\cos^2 \theta$  arrival direction dependence.

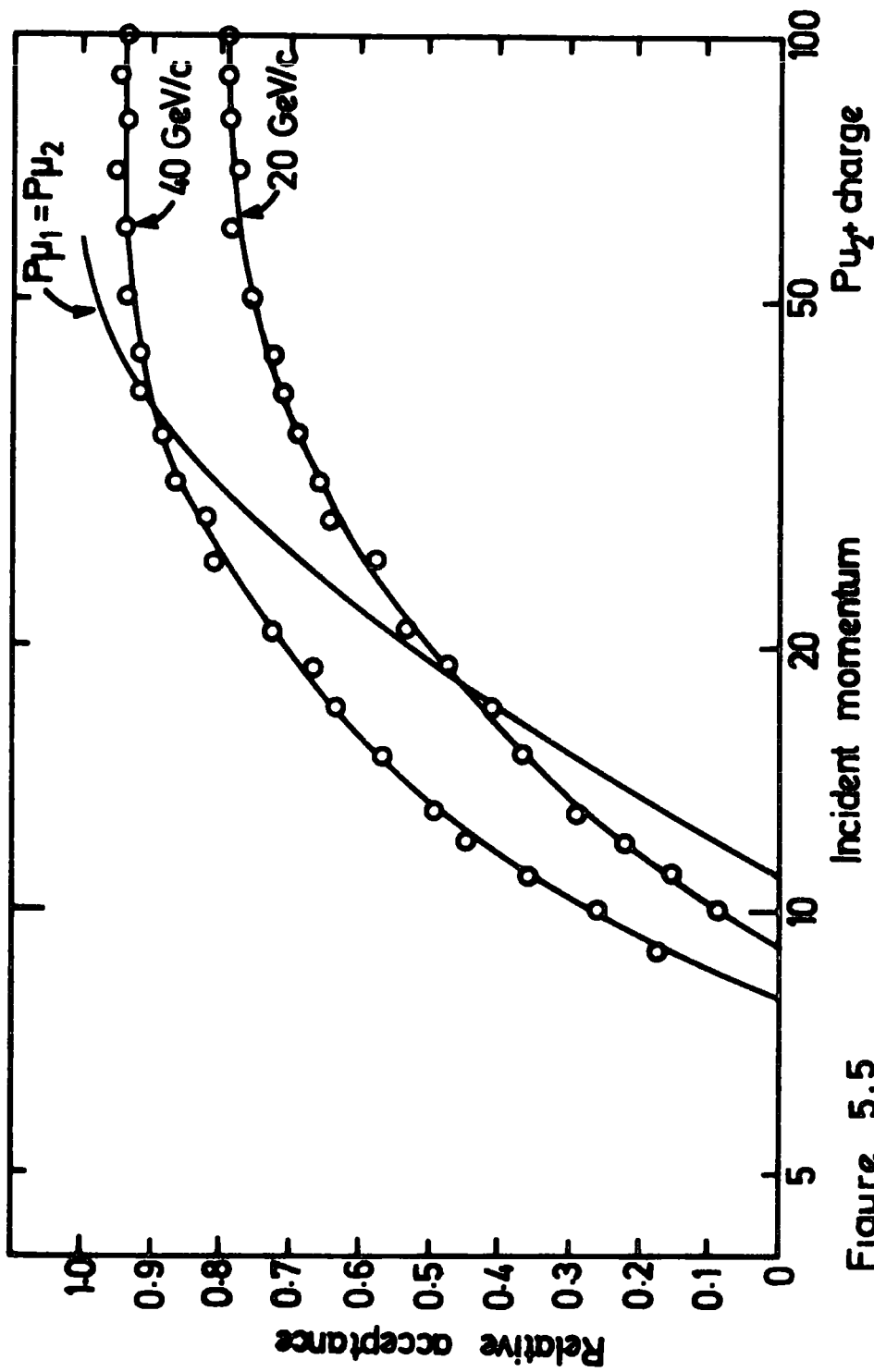


Figure 5.5

4 Tray acceptance for muon pair  $P_{\mu_1} = 20$  GeV/c, 40 GeV/c.  
Both muons + (or both -).

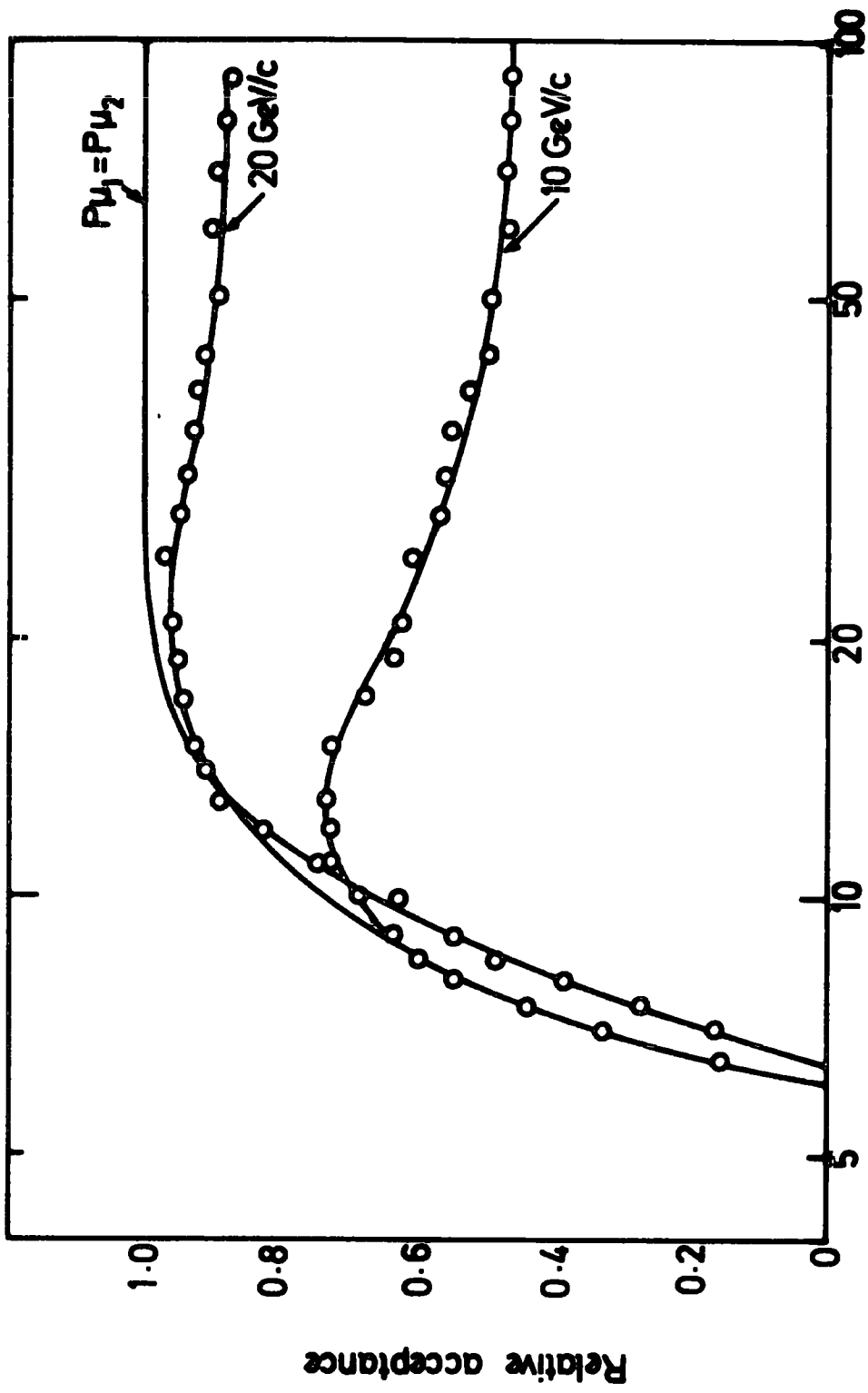


Figure 5.6  
 4 Tray acceptance for muon pair  $P_{\mu_1} = 10 \text{ GeV/c}$   
 and  $20 \text{ GeV/c}$ . muon  $1^+$ , muon  $2^-$ .

THE ACCEPTANCE OF A RECTANGULAR BOX OF DIMENSIONS AS GIVEN IN THE TEXT,

AS A FUNCTION ZENITH ANGLE INTENSITY

n	ACCEPTANCE M <sup>4</sup> sr	
	5 TRAYS	4 TRAYS
0	.3751	.6429
2	.3696	.6269
4	.3642	.6117
6	.3590	.5971
8	.3539	.5833

TABLE 5.2

of this box as a function of variation in zenith angle ( $\theta$ ) intensity, such that intensity is proportional to  $\cos^n \theta$ . It should be pointed out that the muon pairs actually detected must arrive with a minimum separation of about 0.39 m.

### 5.3 GENERAL DATA OF THE MUON PAIR EXPERIMENT

#### 5.3.1 INTRODUCTION

In the following sections the parameters of the events in which one muon traversed each side of the spectrograph are given. For some events the data includes the shower size and arrival direction of any air showers that accompanied the muons, which were large enough and close enough to the centre of the array to be successfully analysed. All the muon data refers to a muon traversing both sides of the spectrograph (thus causing a coincident signal from all six scintillation counters), and all the air shower data refers to shower information obtained from the array by interrogation (initiated by the coincident signal of all the scintillation counters in the spectrograph). The data analysis programs developed by Smith, (1976) for analysing air shower triggered events has been used to analyse all the array data reported here.

The relative positions of the central detector of the array and of the spectrograph are shown in Figure 5.7.

#### 5.3.2 THE EXPERIMENTAL DATA

The total number of muon pairs, and higher multiplicities, collected in 3066.7 hours are shown in Table 5.3 (a).

The 60 events in which more than two muons traversed the spectrograph are also shown as well as the frequency of different combinations of charge of the muons for the pair events. The momentum threshold for all the events is 6 GeV/c. During the time these events were collected the array was operational and sensitive to interrogation for 2007.8 hours. The distribution of the analysis options ascribed by the analysis program to the data collected

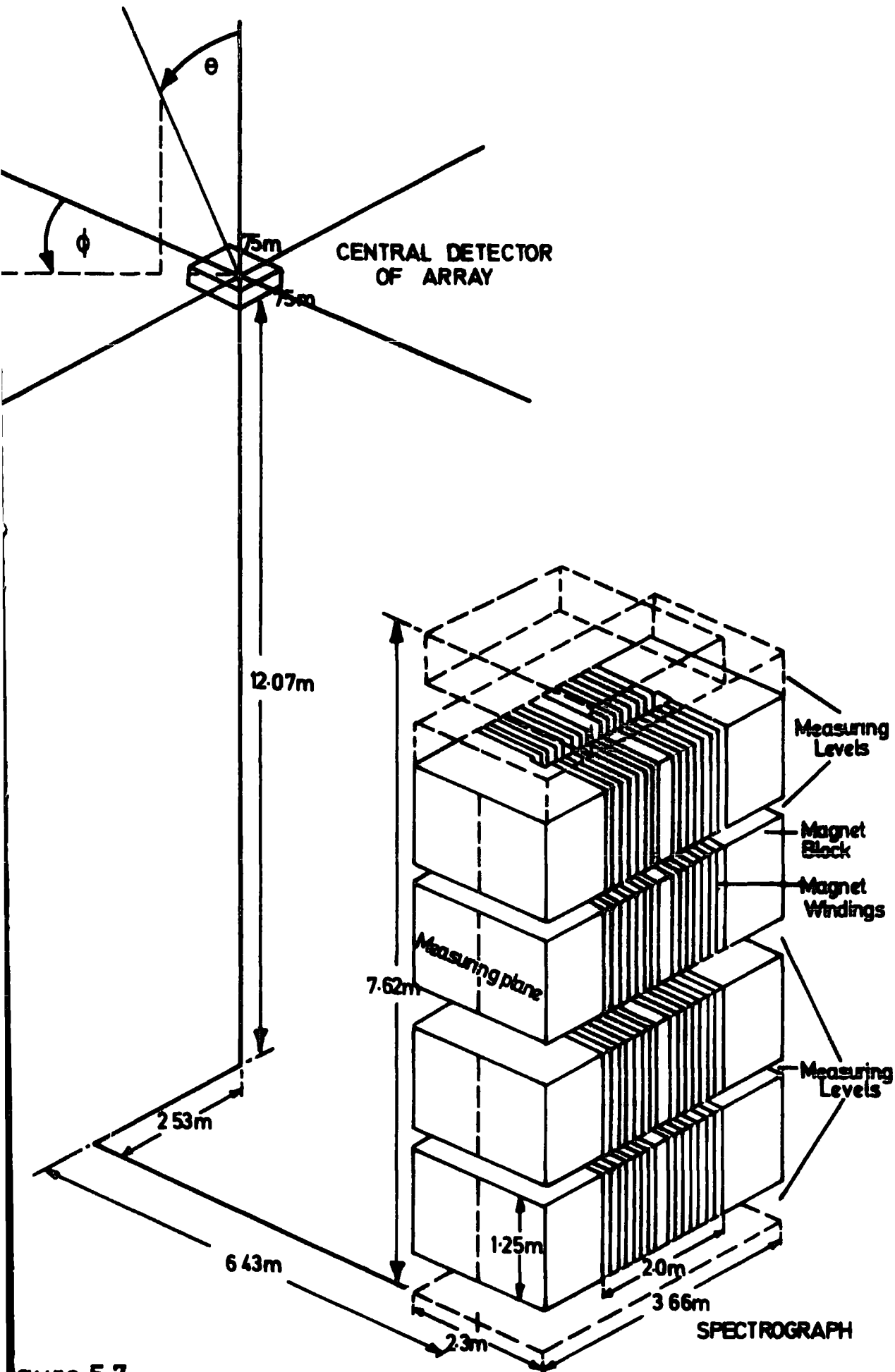


Figure 57

The relative position of the central detector of the array and the spectrograph.

THE MUON AND SHOWER DATA FOR THE MUON PAIR EXPERIMENT

		TOTAL RUN TIME 3066.7 h				CHARGE DISTRIBUTION FOR PAIRS			
		Number of Muons of Each Multiplicity							
(a) MUON PAIR DATA	2's	3's	4's	5's	6's	++	--	+ -	
	320	49	10	0	1	67	72	181	
Number of Events in each Category									
		TOTAL SENSITIVE TIME FOR ARRAY 2007.8 h							
		DISTRIBUTION OF 255 ANALYSED EVENTS							
(b) AIR SHOWER DATA	ANALYSIS OPTION					1	2	3	4
	NUMBER OF EVENTS					73	100	5	77

TABLE 5.3

in this period is shown in Table 5.3 (b). Of the 73 events given option 1, 47 correspond to particle densities of less than  $0.5 \text{ particles m}^{-2}$  in all the array detectors. For all these 47 events there were also no air shower particle tracks in the top measuring tray of the spectrograph. Of the other events, 78 were analysed as showers of more than  $10^5$  particles whose axis fell within 50 m. of the centre of the array, 45 events were determined as showers of less than  $10^5$  particles, and for 40 events the axis fell more than 50 m. from the centre of the array. Figure 5.8 shows the normalized acceptance of the array, (Smith and Thompson, 1977). This was determined by simulating the response of the array detectors as well as the performance of the analysis programs. The acceptance as given in Figure 5.8 depends on the probability of the array being triggered but when the array is interrogated this probability will be unity. However, the successful analysis of an interrogated event will depend upon the size of the shower and the distance of the axis of the shower from the centre of the array. The integral spectrum of showers above a size of  $4 \times 10^5$  particles and accompanied by two muons of momentum above 6 GeV/c is shown in Table 5.4. Reference will be made to this spectrum when consideration is given to the shower sizes predicted to contribute to the measured rate of muon pairs. For this purpose only those events for which there were also more than 30 columns of data in measuring tray 5 on both the blue and red side of the spectrograph have been included in this table.

### 5.3.3 ANGULAR SEPARATION OF MUONS

The muon trajectory analysis program determines the arrival direction of the muon in the bending plane of the spectrograph by fitting a tangent to the track at the point of entry into the spectrograph. Figure 5.9 shows the distribution of angular difference of the arrival direction of the two muons for muons of momentum over 40 GeV/c. The distribution has been split into those events in which the incident directions converge and those events in which the incident directions diverge. The mean of the combined distributions

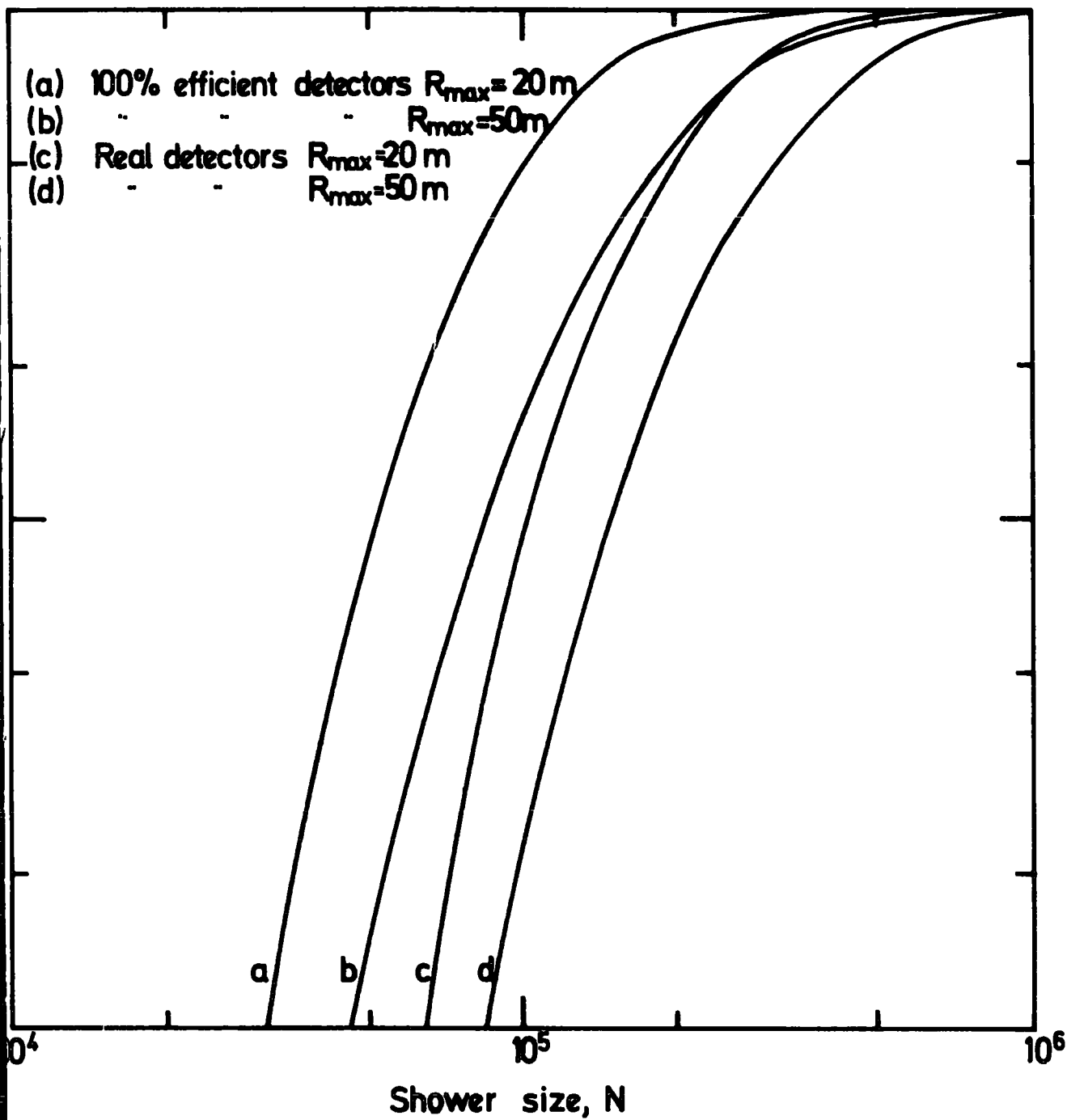


Figure 5.8. The response of the array.

THE INTEGRAL SIZE SPECTRUM OF AIR SHOWERS ASSOCIATED WITH TWO MUONS

BOTH OF MOMENTUM GREATER THAN 6.0 GeV/c TRAVERSING THE SPECTROGRAPH

SIZE $N_e$	$4.0 \cdot 10^5$	$7.87 \cdot 10^5$	$1.55 \cdot 10^6$	$3.05 \cdot 10^6$
NUMBER ( $>N_e$ )	34	19	8	3

TABLE 5.4

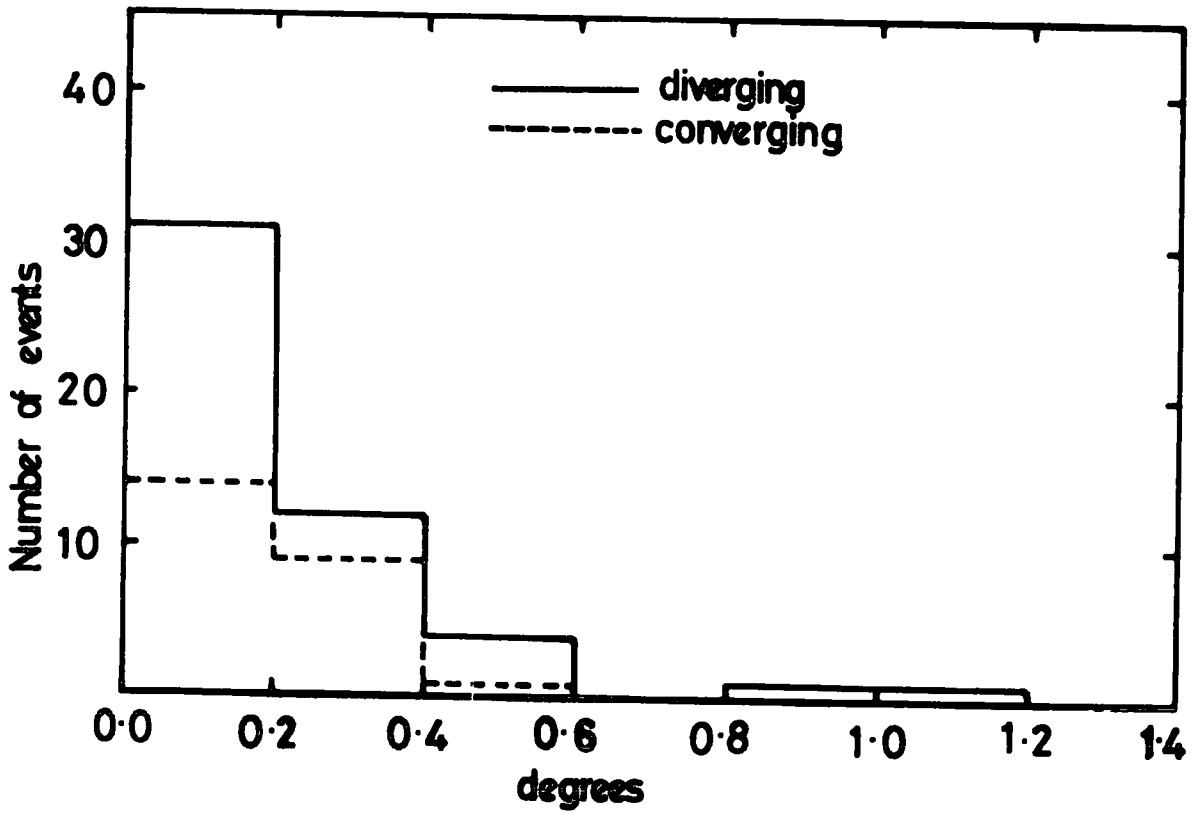


Figure 5.9. Measured angle between arrival directions of muon pair.

(convergence plus divergence) is 0.19 degrees nett divergence and the r.m.s. standard deviation is 0.22 degrees. Summing overall and considering convergence as negative and divergence as positive, the nett divergence is then  $8.3^\circ$  for the 113 events. Not included in this are 3 events in which the two muons arrived with angles differing by more than 2.0 degrees. It should be stressed that the computed muon angle requires a correction, which is momentum dependent, to give the true arrival angle. Wells (1972) has determined the correction to be as much as  $-7.2$  degrees for a muon with momentum 10 GeV/c arriving at  $-6$  degrees to the vertical. Hence muons of momentum of less than 40 GeV/c have not been considered for parallel incidence because even for the same approximate arrival direction the correction required will be different if the muons momenta are different. Even at a momentum of 40 GeV/c a small correction is required which has not been applied to these events. Thus Figure 5.9 acts only as an indication of the extent to which the incident muons have parallel tracks but a slight nett divergence can be concluded for these coincident muons.

#### 5.3.4 SPACIAL SEPARATION OF THE MUON PAIR

The maximum and minimum separation of the two muons as measured in the bending plane of the spectrograph is limited approximately by the width of the gap between, and the extreme edges of, the measuring trays. In shower accompanied events the muons can enter the spectrograph below the top tray, at inclined angles, and initially be separated by more than this width. The distribution of separation of the recorded pairs of muons is shown in Figure 5.10 where the data has been split into those events where the muon pair have the same charge and those events where the charge is different. Shown also is the expected distribution for 'infinite' momentum muon pairs with a completely random separation. This was determined by simulating the arrival of muon pairs on a model of the spectrograph. However, the rate of coincident muon pairs has been shown to be a function

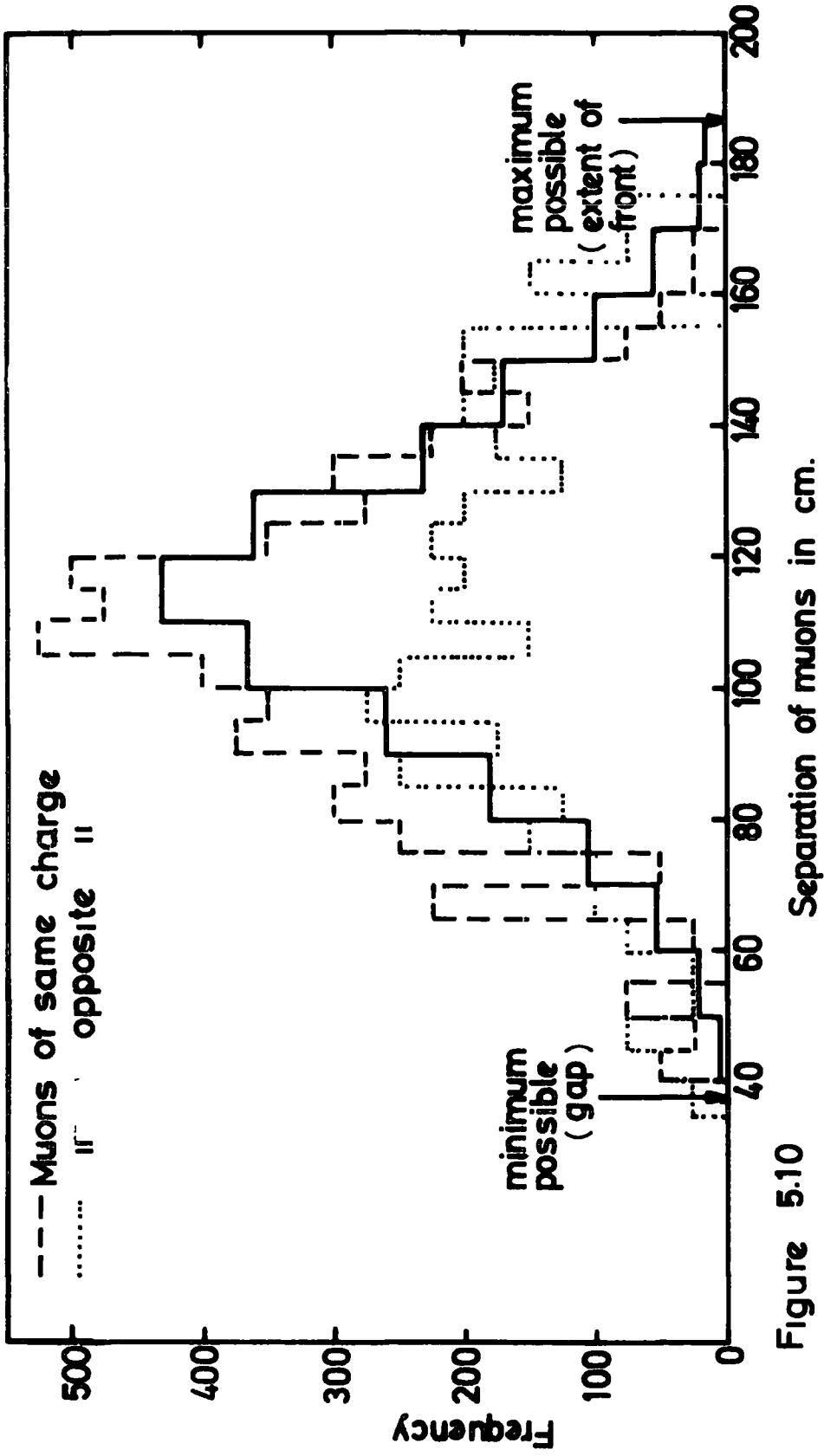


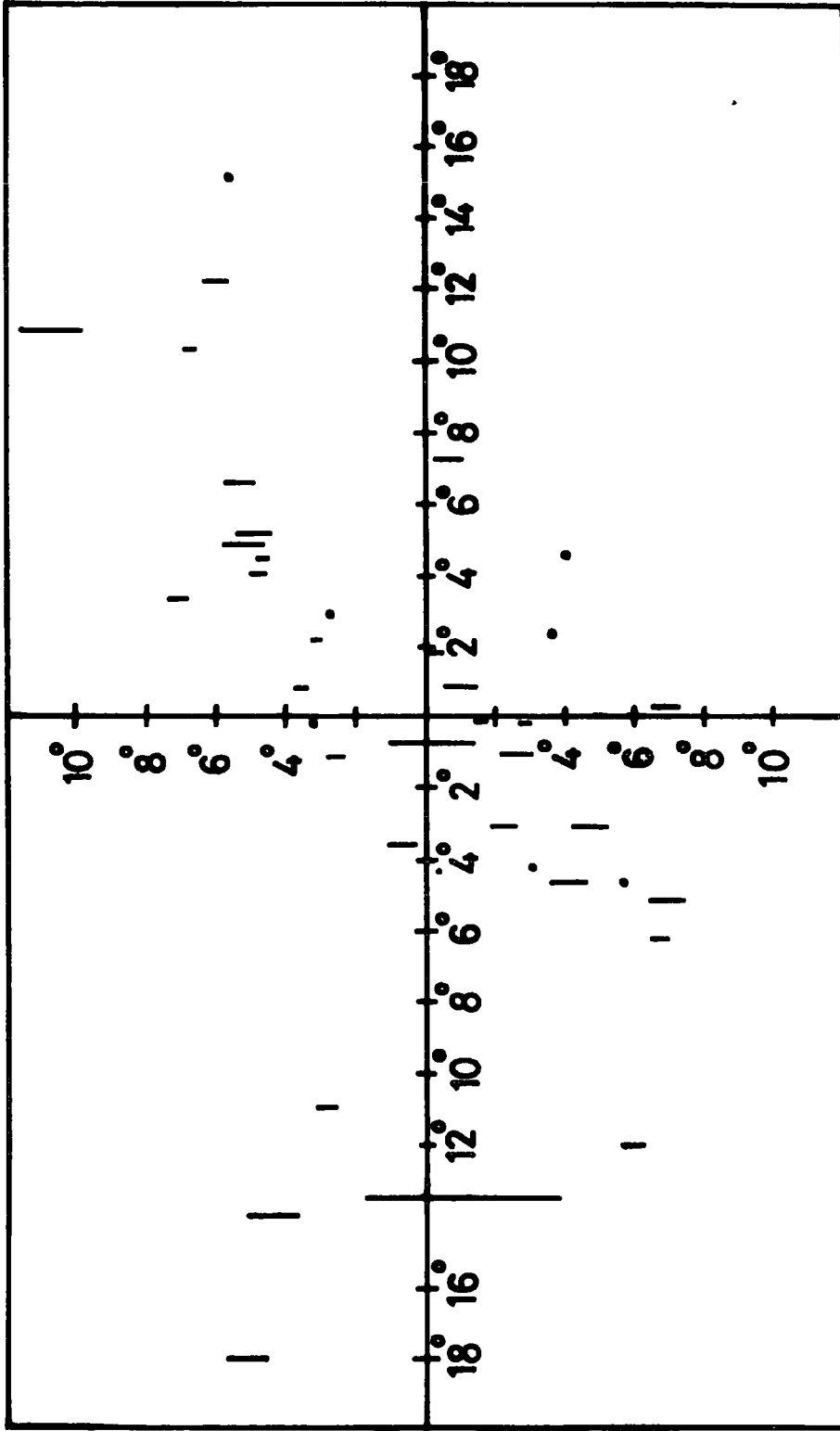
Figure 5.10 Separation of muons in cm.

Distribution of separation of muons of infinite momentum that are accepted assuming random separation of arrival, ( — ) and experimental values.

of the separation of the muons. (George et al., (1952) Hunter and Trent, (1962) Porter and Stenerson (1968) Bergeson, et al., (1975)). This decoherence has been determined for muon pairs at several different depths underground where a significant decrease in the rate of events is seen for an increase in separation. The extent of this variation is a function of the depth below ground of detection of the muon pair, and hence of the energy of the muons. Barrett, et al., (1952) determined the decoherence curve at a depth of 1600 metre water equivalent (m.w.e.) for muons of energy of at least  $3 \times 10^2$  GeV at ground level. Their results approximate well to the assumption that the lateral distribution of muons about the shower core is flat out to a radius of about 13 metres and zero at larger radii. George et al., (1952) working at a depth of 60 m.w.e., conclude that for muons of energy over 12 GeV the density is uniform over a circle of radius of about 60 metres. The data presented in Figure 5.10 includes events for which the energy of the muons range from below 12 GeV to over  $3 \times 10^2$  GeV. As the detection of two muons depends on the relative charge and separation as well as the momentum of the muons, no attempt has been made to discern the decoherence of the muon pairs. However, in Sections 5.4 and 5.5 it has been assumed that the muon pairs arrive with completely random separations. In order to make some comparison with predictions, the experimental rate of events has to be restricted to those events for which both muons have a momentum in excess of 60 GeV/c.

#### 5.3.5 ANGULAR DEVIATION OF MUON PAIR FROM SHOWER AXIS DIRECTION

If, when the air shower array is interrogated, shower particles had passed through the timing detectors the arrival direction of the shower can be determined. Figure 5.11 shows the arrival direction of the muon pair in comparison to the shower arrival direction projected into the bending plane of the spectrograph. For these events 4 of the array timing detectors recorded the shower event and the two muons had momenta of over 10 GeV/c. The lines on the figure join the angle as determined for the blue side



Angle of blueside and redside muon in spectrograph bending plane

Component of shower direction in spectrograph bending plane determined by the array

Figure 5-11.

muon to the angle as determined for the red side muon. The correction has not been applied to the angles of arrival of the muons as described in Section 5.3.3 , hence this figure acts only as an indication of the general correlation of the muons with the air shower.

5.4 THE PREDICTED RATE OF COINCIDENT MUON PAIRS ACCOMPANIED BY AN AIR SHOWER

5.4.1 INTRODUCTION

In the following sections the two methods developed in Chapter 4 are used to predict the rate of coincident muon pairs. The predictions, which use the semi-empirical structure functions and particle interaction models, are compared with the rate of events in which two muons traverse the blue side and as well as the events in which a muon traverses both the red and blue sides. For both cases the measured rate of pair events has been converted into an intensity of pairs using the techniques described in Section 5.2 and Appendix E. The need to remove the effect of the instrument's geometry before comparing measurements with predictions has been pointed out by Barton (1968), and Porter and Sternerson (1968), and has led to some misunderstanding as reported by Barton (Castagnoli, et al., 1969).

5.4.2 THE CONVERSION OF THE RATE OF EVENTS INTO THE INTENSITY OF MUON PAIRS

A total of N pair events recorded by the spectrograph in a total time T hours corresponds to a measured rate R of  $R = N/T \text{ h}^{-1}$ . The intensity of events I will be

$$I = R/A(n) \text{ m}^{-4} \text{ sr}^{-1} \text{ h}^{-1}$$

where A(n) is the acceptance of the spectrograph for pairs of muons for which the intensity varies with zenith angle ( $\theta$ ) as  $\cos^n \theta$ . A value of  $n = 8$  has been used for the muons, when they are accompanied by air showers.

Considering first the events in which a muon pair traverse the blue side of the spectrograph, which are accompanied by shower particles discharging one or more flash tubes in more than 30 columns in measuring tray 5. A total of 105 events were recorded in about 5118 hours for which both muons had momentum of over 20 GeV/c. However, the acceptance for pairs varies with momentum if one or either of the muons is of momentum less than

about 60 GeV/c. Thus the expected integral rate has been compared to the measured integral rate of two muons for two higher threshold values of momentum. The measured rate of muon pairs for which both muons have momenta greater than 60 GeV/c and for which both muons have momenta greater than 100 GeV/c are shown in Table 5.5. The corresponding intensities which are shown have been determined using an acceptance of  $3.927 \cdot 10^{-2} \text{ m}^4 \cdot \text{sr}$ . for the lower 4 measuring trays.

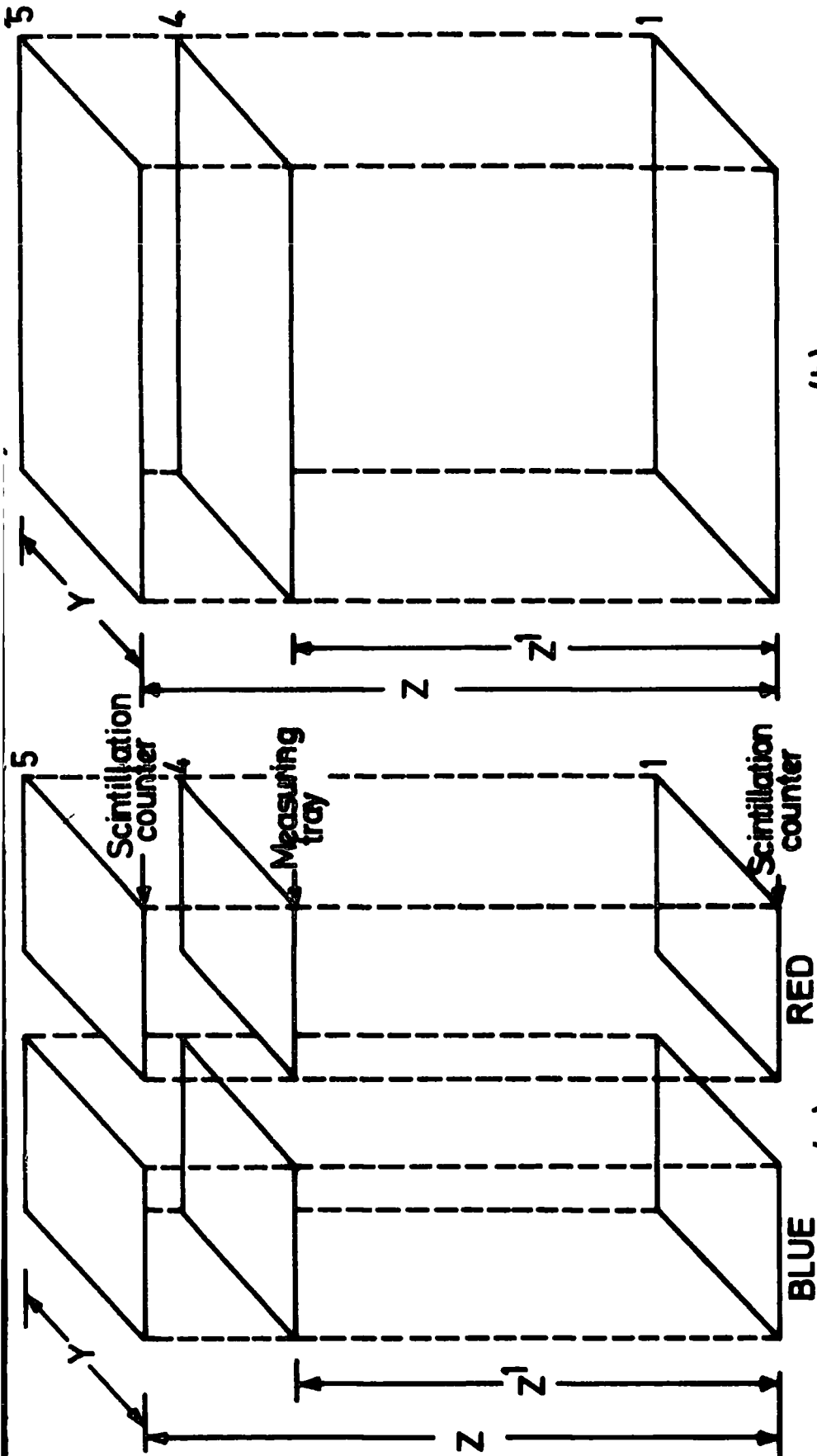
To consider the rate of events in which one muon traverses each side of the spectrograph an analogy of the experimental situation has been used. Two computer models were constructed in which the spectrograph was represented by the positions of the scintillation counters at levels 1 and 5 and measuring tray 4. Figure 5.12 (a) shows schematically the actual relationship of the detecting elements considered whilst Figure 5.12 (b) shows a rectangular box equivalent to both halves of the spectrograph plus the gap in between. Considering only the case of 'infinite' momentum muons, both of these models were used in a computer simulation in which muons were incident with an intensity that varied as  $\cos^n \theta$ ,  $\theta$  being the zenith angle. The entire area of the top at level 5 (X times Y, Figures 5.12 (a) and (b) ), was used in both simulations, and the simulations were repeated for muons incident on level 4. In this way the response of the spectrograph to pairs of muons was compared to the response of a spectrograph of dimensions similar to those of Figure 5.12 (b) and for which the acceptance has been calculated by integration and is shown in Table 5.6. Also shown in the table are the number of successful simulated events in  $10^6$  trials for both of these shapes of instrument. A description of this type of Monte Carlo simulation is given in Appendix B. Thus, assuming a completely flat decoherence curve (that is a completely random value of separation of the muons on arrival) the percentage decrease in measured events expected will be the ratio of the successful events for the simulation of the actual spectrograph to the successful events for the simulation of the hypothetical instrument.

THE INTENSITY OF MUON PAIRS TRAVERSING THE BLUE SIDE OF THE

SPECTROGRAPH

THRESHOLD MOMENTUM	NUMBER OF EVENTS IN 5118 h	INTENSITY $m^{-4} sr^{-1} h^{-1}$
60 GeV/c	43	0.214
100 GeV/c	20	0.100

TABLE 5.5



(b)

Schematic view of 'box' used to determine acceptance for pairs.

(a)

Schematic view of system used for simulation of the spectrograph.

Figure 5.12.

n	VALUES FOR RECTANGULAR BOX			VALUES FOR SPECTROGRAPH	
	Acceptance of 'Rectangular Box' Determined by Integration $m^4$ sr	Number of Successful Events in $10^6$ Trials	Acceptance Determined from Monte Carlo $m^4$ sr	Number of Successful Events in $10^6$ Trials	% for Actual Spectrograph
0	.6429	73647	.6390	20392	27.7 %
4	.6117	91658	.6130	12924	14.1 %
8	.5833	110850	.5863	14670	13.2 %
0	.3751	43220	.3750	11813	27.3 %
4	.3642	53813	.3599	7480	13.9 %
8	.3539	67310	.3560	8750	13.0 %

TABLE 5.6

The acceptance of the two halves of the spectrograph varies according to the momentum of the incident pair of muons for muons of momentum less than 60 GeV/c. The variation of acceptance with momentum can be seen in Figures 5.4, 5.5, 5.6, and accordingly the predicted rate will only be compared with the experimental rate of muon pairs when both the muons have momentum of over 60 GeV/c and also when both are over 100 GeV/c. In Table 5.7 the number of events recorded in 3066 hours for these two threshold values of momentum is shown. Also shown is the number that would have been recorded by a rectangular spectrograph, as described, which has been determined by multiplying the measured rate by the percentage increase as shown in Table 5.6. These events were all accompanied by shower particles which discharged one or more tubes in more than 30 columns in both measuring tray 5 on the blue side and measuring tray 5 on the red side. Hence the values of acceptance appropriate have been taken from the row corresponding to ; 4 trays and  $n = 8$ , of Table 5.6. Table 5.7 also shows the number of events where both muons recorded were of momentum over 100 GeV/c and no shower particles was detected by the array or by the top measuring trays of the spectrograph. A value of 100 GeV/c has been used as a threshold for this situation, because the acceptance varies for values of momentum less than this (Figure 5.3). The value taken to adjust to the expected rate is from Table 5.6 in the row corresponding to ; 5 trays and  $n = 4$ . Barton, (1968) suggests that this  $\cos \theta$  exponent of 4 for the angular distribution of muon groups (as reported by Higashi, et al., 1962) may be expected as muons will be less strongly collimated than the electron component of showers.

#### 5.4.3 THE MUON PAIR INTENSITY PREDICTED FROM THE SHOWER SIZE SPECTRUM

An attempt has been made to predict the intensity of coincident muon pairs using the measured sea level shower size spectrum and the electron and muon structure functions due to Grøisen (1960), equations 4.5 and 4.6. The method used follows closely the method developed in Chapter 4 for single muons.

THE NUMBER OF MUON PAIR EVENTS IN WHICH ONE MUON PASSED EACH SIDE OF THE

SPECTROGRAPH

	THRESHOLD MOMENTUM GeV/c	NUMBER OF EVENTS IN 3066 h	ADJUSTED NUMBER OF EVENTS FOR BOX	INTENSITY CORRESPONDING TO ADJUSTED NUMBER $m^{-4} sr^{-1} h^{-1}$
TRAYS LOWER MOMENTUM EVENTS	60	46	348	0.195
	100	26	197	0.110
TRAYS LOWER MOMENTUM EVENTS	7	47	-	-
	100	7 (1725 h)	50	0.080

TABLE 5.7

The probability of two or more muons striking the top of the spectrograph must be determined. The probability that  $n$  particles cross a detector of area  $S \text{ m}^2$ , when the mean density is  $\rho \text{ m}^{-2}$  is given by the Poisson formula,

$$P_n = (\rho s) \frac{e^{-\rho s}}{n!} \quad (5.1)$$

so that the probability of at least two particles crossing the area is

$$P_2 = 1 - (1 + \rho s)e^{-\rho s} \quad (5.2)$$

Thus the predicted rate of events in which at least two muons of momentum greater than  $P_\mu$  cross the area  $S \text{ m}^2$  of the spectrograph top is

$$R_2(P_{\mu_1} > P_\mu, P_{\mu_2} > P_\mu) = \int \int P_2 P_{T2} F(N_e) 2\pi r dr dN_e s^{-1} \text{sr}^{-1} \quad (5.3)$$

All shower sizes,  $N_e$       All radial distances,  $r$

where  $F(N_e) dN_e$  is the differential shower size spectrum which can again be determined from the integral shower size spectrum.  $P_2$  is as given in equation 5.2, and  $P_{T2}$  is the probability that the spectrograph will be triggered. For predicting the rate of pair events on the blue side,  $P_{T2}$  has been determined as described in Section 5.2.1. However, the events in which a muon passes either side of the spectrograph will be triggered independently of the momentum selector as only the six scintillation counters need provide a coincident signal to trigger the spectrograph. The probability of getting more than 30 columns of flash tubes in measuring tray 5 in which at least one tube had discharged was determined in Section 3.11 as a function of particles hitting the blue side. This can be extended to the red side as well.

Thus a prediction can be made for events in which a muon of greater than a given threshold momentum traverses each side of the spectrograph and more than 30 columns contain at least one discharged tube in the top measuring trays on both sides of the instrument. In this case,

$$P_{T2} = P_{CB}(\rho e) \times P_{CR}(\rho e) \quad (5.4)$$

where  $P_{CB}(\rho e)$  is given by  $P_C(\rho e)$  and is defined as the probability of getting one or more flash tubes discharged in more than 30 columns in measuring tray 5 on the blue side ; and it has been assumed that  $P_{CR}(\rho e)$ , the probability of one or more flash tubes discharged in more than 30 columns in measuring tray 5 on the red side, is approximately equal to  $P_C(\rho e)$ .

To evaluate equation 5.3 the differential shower size spectrum, expression 4.10 and 4.11 have been used and the limits of integration were set as described in Section 4.6, with the exception that the upper shower size limit was set to  $10^8$ . The results of this calculation for both the blue side events and 'both' side events are shown in Table 5.8. In the case of the predictions for the blue side events the intensity corresponds to the rate of events in which two muons pass through  $1.32 \text{ m}^2$  and the corresponding predicted number of recorded events is determined by the acceptance of  $3.927 \times 10^{-2} \text{ m}^4 \text{ sr}$  and the run time of 5118 hours. For one muon each side equation 5.3 was evaluated for an area of  $3.322 \text{ m}^2$  and the number in the run time of 3066 h corresponds to an acceptance of  $0.5833 \text{ m}^4 \text{ sr}$ . The number of events actually expected has been determined as 13.2 % of this number. Comment on the agreement of these predictions with the values of Tables 5.5 and 5.7 will be made at the end of the next section.

The contribution predicted to come from different radial distances is shown in Figure 5.13 for both cases. This figure is a plot of  $I(r, >P_\mu) \times r$

THE PREDICTED RATE OF PAIRS USING THE SEA LEVEL SHOWER SIZE SPECTRUM

MUON THRESHOLD MOMENTUM Gev/c P <sub>μ1</sub> and P <sub>μ2</sub>	Predicted Rate of Two Blue Side Muons		Predicted Rate One Muon Each Side of Spectrograph		
	Rectangular Box		Number in 3066 h	Number Adjusted for Experimental Situation (13.2%)	
	Intensity m <sup>-4</sup> h <sup>-1</sup> sr <sup>-1</sup>	Number in 5118 h			
60	2.03 10 <sup>-1</sup>	41	1.546 10 <sup>-1</sup>	277	37
100	9.95 10 <sup>-2</sup>	20	7.88 10 <sup>-2</sup>	141	19

TABLE 5.8

where

$$I(r, >P_\mu) = 2\pi r \int_{5 \cdot 10^3}^{10^8} P_2 P_{T_2} F(N_e) dN_e \quad (5.5)$$

Notably the predicted contribution is from smaller radial distances for the pair events than for the single muon events, Figure 4.13.

In order to contrast the size of the showers predicted to contribute to the rate with the integral shower size spectrum of Table 5.4, the integral equation 5.3 was solved with a shower size lower limit of  $4 \cdot 10^5$ ,  $7.87 \cdot 10^5$ ,  $1.55 \cdot 10^6$  and  $3.05 \cdot 10^6$ . In each case the integral was solved for muons of momentum greater than 20 GeV/c, and Table 5.9 shows the result in comparison with the normalized measured rate. The agreement is reasonable given that the measured events correspond to a muon momentum threshold of 6 GeV/c but cannot be considered conclusive because of the small size of the sample of air showers.

5.4.4 THE INTENSITY OF MUON PAIRS PREDICTED BY THE INTERACTION MODELS

The method used to predict the rate of muon pairs in air showers using the CKP and scaling models follows the arguments as given in Sections 4.7.1 to 4.7.13 of Chapter 4. The predicted rate of events in which at least two muons of momentum greater than  $P_\mu$  cross an area of  $\pi m^2$  is

$$R_2(P_{\mu_1} > P_\mu, P_{\mu_2} > P_\mu) = \int_{\substack{\text{Primary} \\ \text{Spectrum}}} \int_{\substack{\text{Radial} \\ \text{Distances}}} P_2 P_{T_2} J(E_p) 2\pi r dr dE_p s^{-1} sr^{-1} \quad (5.6)$$

Models A, B and C as detailed in Section 4.7.11 have been used in evaluating equation 5.6 to predict the rate of blue side muon pairs as well as the rate of pairs through the box described in Section 5.4.2.  $P_2$  and  $P_{T_2}$  are as

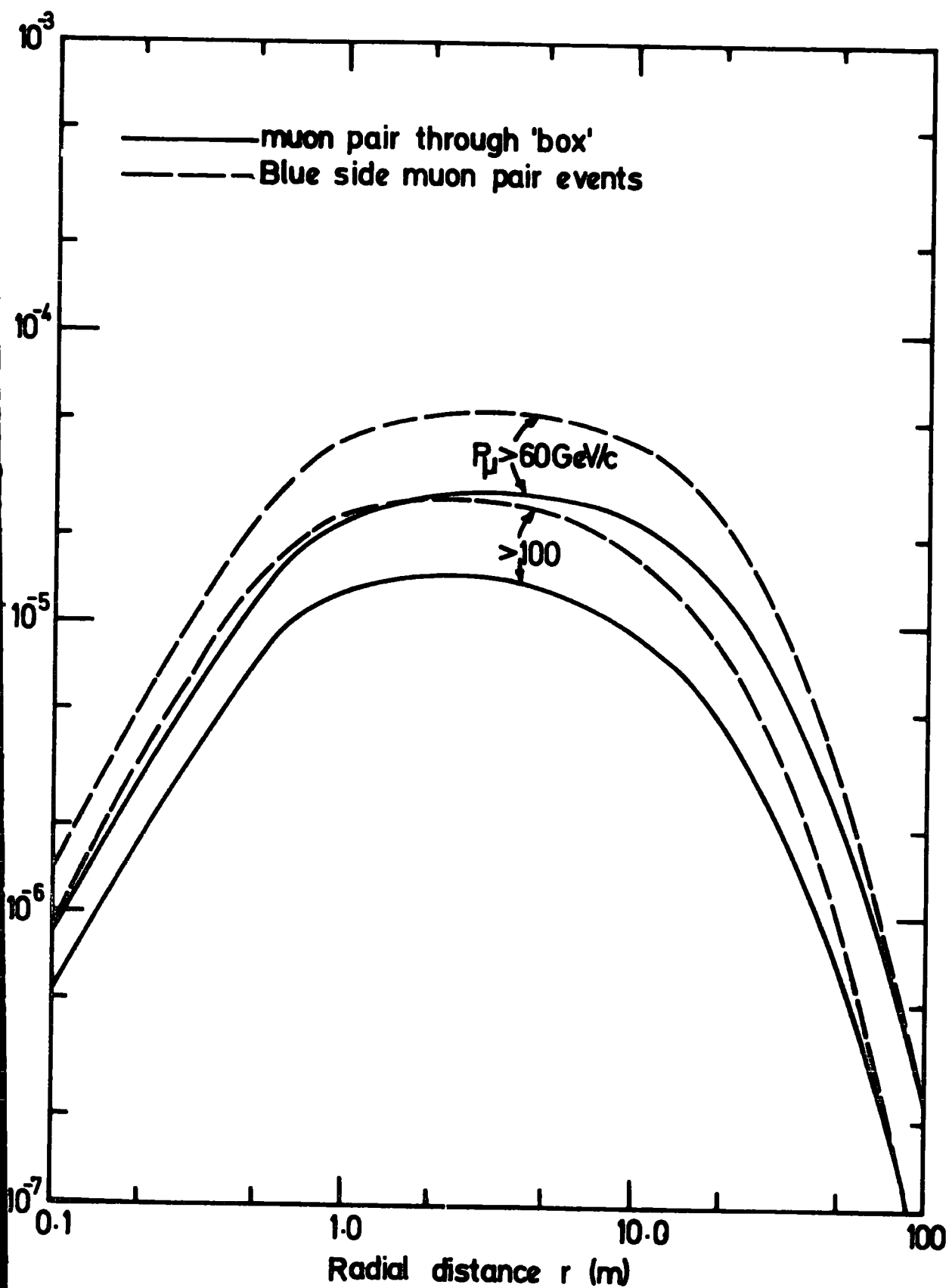


Figure 5.13. The contribution to the predicted rate of pairs from different radial distances.

THE MEASURED AND PREDICTED CONTRIBUTION FROM SHOWERS OF DIFFERENT SIZES  
TO THE SHOWER ACCOMPANIED MUON PAIR RATE. (NORMALISED TO INTEGRAL  
SHOWER SIZE  $4 \cdot 10^5$ )

$N_e$	$4 \cdot 10^5$	$7.87 \cdot 10^5$	$1.55 \cdot 10^6$	$3.05 \cdot 10^6$
MEASURED INTEGRAL NUMBER OF SHOWERS ( $>N_e$ )	1	.56	.24	.09
PREDICTED INTEGRAL NUMBER OF SHOWERS ( $>N_e$ )	1	.57	.27	.12

TABLE 5.9

defined in Section 5.4.3. The intensities thus determined are shown in Tables 5.10 and 5.11. The intensities in Table 5.10 are computed for an area of  $1.32 \text{ m}^2$  and the corresponding number is determined by the acceptance of  $3.927 \cdot 10^{-2} \text{ m}^4 \text{ sr}$ , and the experimental run time. These predicted values can be contrasted with the values given in Table 5.5 and the left-hand side of Table 5.8. The rates predicted by the calculation involving Greisen's air shower particle structure functions and the sea level shower size spectrum, and the CKP model calculations are in broad agreement with the measured rates. The measured rate of events lies somewhere in between the proton only and mixed composition predictions of the CKP model. The scaling model predictions are all too low compared to the measured rate with the exception of the mixed composition of model C which predicts a rate too high by a factor of 2. Table 5.11 can be interpreted in much the same way for the predicted rate of events in which a muon passes either side of the spectrograph. Here the combination of mixed composition and CKP model is the nearest to the values of Table 5.7. However, there are some serious qualifications of these results, and any conclusion will be reserved until the end of Chapter 6.

## 5.5 MUON PAIR PRODUCTION

Following Yukawa,(1935) many suggestions have been made concerning the possible existence of a 'carrier' of the weak force in direct analogy with the photon or quanta which mediates the electromagnetic force. (See for example Lee and Yang,(1957) Feynman and Gell-Mann,(1958) Weinberg,(1967) Salam,(1968)). The intermediate Vector boson has been proposed in both charged ( $w^\pm$ ) and neutral ( $Z^0$ ) form and estimates of the mass of each form are model dependent. Theories that unify the weak and electromagnetic interaction yield

$$\begin{aligned} M_w &\sim 37 \text{ GeV}/c^2 && \text{(See Weinberg, 1967 and Salam,1968)} \\ M_z &\sim 75 \text{ GeV}/c^2 \end{aligned}$$

THE RATE OF BLUE SIDE MUON PAIRS PREDICTED BY THE CKP AND SCALING MODELS

THRESHOLD MOMENTUM FOR MUON PAIR GeV/c		MODEL A CKP		MODEL B SCALING		MODEL C SCALING	
		Protons Only	Mixed Composition	Protons Only	Mixed Composition	Protons Only	Mixed Composition
60	Intensity $m^{-4} s^{-1} sr^{-1}$	$1.61 \cdot 10^{-1}$	$3.41 \cdot 10^{-1}$	$1.21 \cdot 10^{-2}$	$5.19 \cdot 10^{-2}$	$3.14 \cdot 10^{-2}$	$4.40 \cdot 10^{-1}$
	Number in 5118 h	32	69	2.2	10	6.0	88
100	Intensity $m^{-4} s^{-1} sr^{-1}$	$9.06 \cdot 10^{-2}$	$1.73 \cdot 10^{-1}$	$7.67 \cdot 10^{-3}$	$3.27 \cdot 10^{-2}$	$2.06 \cdot 10^{-2}$	$2.95 \cdot 10^{-1}$
	Number in 5118 h	18	35	1.5	7	4.1	59

TABLE 5.10

THE PREDICTED RATE OF MUON PAIRS USING THE CKP AND SCALING MODELS

THRESHOLD MOMENTUM FOR MUON PAIR GeV/c		MODEL A CKP		MODEL B SCALING		MODEL C SCALING	
		Protons Only	Mixed Composition	Protons Only	Mixed Composition	Protons Only	Mixed Composition
60	Intensity $m^{-4} s^{-1} sr^{-1}$	$1.16 \cdot 10^{-1}$	$1.98 \cdot 10^{-1}$	$1.15 \cdot 10^{-2}$	$1.06 \cdot 10^{-2}$	$3.03 \cdot 10^{-2}$	$2.95 \cdot 10^{-1}$
	Number in 3066 h	208	353	21	73	54	528
	Adjusted Number	28	47	2.9	9.6	7.2	70
100	Intensity $m^{-4} s^{-1} sr^{-1}$	$6.30 \cdot 10^{-2}$	$1.13 \cdot 10^{-1}$	$7.29 \cdot 10^{-3}$	$2.61 \cdot 10^{-2}$	$1.97 \cdot 10^{-2}$	$2.03 \cdot 10^{-1}$
	Number in 3066 h	113	201	13	47	35	363
	Adjusted Number	15	27	1.7	6.2	4.7	48

TABLE 5.11

however Marciano, (1975) has suggested that the neutral form may have a lower limit of only,

$$M_z > 6 \text{ GeV}/c^2$$

The recent detection of neutral current events in the large heavy liquid bubble chamber Gargamelle at CERN (Hasert, et al., 1973, see also Lee, et al., (1976) for a later view) lends weight to the hypothesis of both charged and neutral states of an intermediate vector boson. In this way a neutral current event may be represented by a neutrino (which only acts via the weak force) interacting with a proton and remaining as a (neutrally charged) neutrino and not converting (as it more usually does) to a negatively charged lepton. An interpretation is that a neutral particle,  $Z^0$ , passes between the neutrino and the proton communicating the weak force from one to the other. Thus the leptons involved have not changed the sign of their electric charge. With the more common charged currents, the communicator would be the  $W^\pm$ . Further experimental observations include directly produced muon pairs in neutrino and hadron collisions with protons. (See for example Benvenuti, et al., (1975) Branson, et al., (1977)). These 'dimuons' have raised much current interest centred around the possibility of confirming the existence of the quantum number charm or of the production of a heavy neutral lepton or even of a weak intermediate vector boson. (See Adler, et al., 1975, Chang et al., (1975) Brandt, et al., (1974)).

Kanofsky and Colter, (1973) have used a magnetic cosmic ray muon spectrograph to determine the rate of showerless penetrating particle-pairs of energy above 3.6 GeV. These authors suggest that the flux of pairs may be due in part to the decay of intermediate vector bosons or of two massive non-interacting quarks which could be produced in high energy cosmic ray interactions. The theoretical process they put forward is the peripheral production of a neutral vector boson whilst the other particles produced

carry very little energy, and hence no air shower will be produced. Their spectrograph is similar in general outlay to the MARS spectrograph consisting of two iron absorbers placed between counter arrays, and is designed to be sensitive to muon pairs separated by up to 60 inches. However, they report a rate of muon pairs of energy above 3.6 GeV and unaccompanied by an air shower that is consistent with zero. This is in agreement with Bingham and Kellerman (1965) who in over 2000 hours of recording with a neon tube hodoscope detected 19 muon pair events all associated with a shower of size at least  $5 \cdot 10^5$  particles. These workers could detect a muon pair separated by up to 30 cm.

The present experimental data as described in Section 5.3.2 contains 47 muon pair events, apparently unassociated with an air shower. Out of these, 26 are a combination of a positive and negative muon. Nieto (1968) has suggested that if a vector boson is produced in collisions of primary particles with nucleons of air nuclei its existence might be determined by detecting muon pairs produced. His model of neutral boson ( $Z^0$ ) production by a peripheral proton-proton collision leads to a  $Z^0$  that is a resonance of the muon pair system in which the  $Z^0$  muon - muon coupling is large. The  $Z^0$  mass is in the range

$$21 \text{ GeV}/c^2 \leq M_{Z^0} \leq 42 \text{ GeV}/c^2$$

and might be determined by transforming to the centre of mass of the pair of oppositely charged muons that are detected as a coincident pair. The present experiment is sensitive to muon momenta in the range of 10 to 1000 GeV/c and separations of the order of 1 metre for the detection of a muon pair. Thus even with a lower limit of about 6 km. (Wdowczyk, 1975) for the production of muons of this energy the upper limit of mass of any particle decaying to two muons for which this experiment is sensitive is below that predicted for the boson, unless it decays directly in the line of flight. Following Nieto,



1968, for a particle (boson) of total energy 1000 GeV (the sum of two muons) decaying transversely 6 km above an experiment detecting two muons separated by 1 m., the mass M is

$$M \sim \frac{1 \times 10^3}{6 \times 10^3 \times 2} \text{ GeV}/c^2$$
$$= .08 \text{ GeV}/c^2$$

Kinematically the two muons detected with four-momenta  $P_1$  and  $P_2$  are equivalent to one single particle with four-momentum  $P$  and invariant mass  $M$  such that

$$P^2 = (P_1 + P_2)^2 = M^2$$
$$M^2 = (E_1 + E_2)^2 - (\bar{P}_1 + \bar{P}_2)^2$$

where  $E$  and  $\bar{P}$  are the energy and momentum of the two muons.

The invariant mass of the oppositely charged showerless muon pairs determined in this way is shown in Table 5.12 and Figure 5.14 shows the histogram of the invariant mass of the shower accompanied muon pairs as well as the unassociated muon pairs. For small lateral separations of the pair of muons the energy difference will be greater than for widely separated pairs. The geometry of the spectrograph makes it sensitive to muon pairs where the muons are of approximately the same energy and hence in the view of the author no unique shape will be discernible with so few events.

Benvenuti, et al., (1975) have reported events in which high energy ( $\sim 100$  GeV) neutrinos and anti-neutrinos scatter off hadrons and produce muon pairs of opposite charge ( $\mu^+ \mu^-$ ). The authors conclude that the results are consistent with a new particle of mass less than or near 4 GeV but as the invariant dimuon mass extends to  $\sim 4$  GeV with no significant structure there

THE ENERGY OF THE MUONS AND THE INVARIANT MASS FOR SHOWER

UNASSOCIATED MUON PAIRS

Muon 1 Charge Energy, GeV	Muon 2 Charge Energy, GeV	Invariant Mass GeV/c <sup>2</sup>
- 10.6	+ 143.0	0.416771
+ 80.2	- 9.5	0.343297
+ 40.3	- 376.9	0.357611
- 23.8	+ 92.5	0.261850
- 22.8	+ 21.1	0.211440
+ 27.3	- 17.0	0.217235
- 41.6	+ 77.7	0.221674
- 15.7	+ 22.9	0.215056
- 14.2	+ 27.6	0.223053
+ 31.0	- 101.7	0.249667
+ 37.2	- 181.8	0.281324
+ 15.3	- 6.6	0.230226
+189.0	- 271.0	0.214728
+ 21.6	- 37.6	0.219449
- 52.7	+ 230.4	0.271410
-511.2	+ 23.6	0.514365
-129.6	+ 43.3	0.243826
+ 11.3	- 27.6	0.232695
+ 85.0	- 18.1	0.277678
+106.2	- 87.1	0.212321
- 11.8	+ 11.4	0.211313
+ 63.6	- 18.3	0.253607
+ 36.6	- 12.4	0.242983
+153.6	- 93.8	0.217738
-245.7	+ 125.8	0.223228
+ 59.5	- 20.3	0.242565

TABLE 5.12

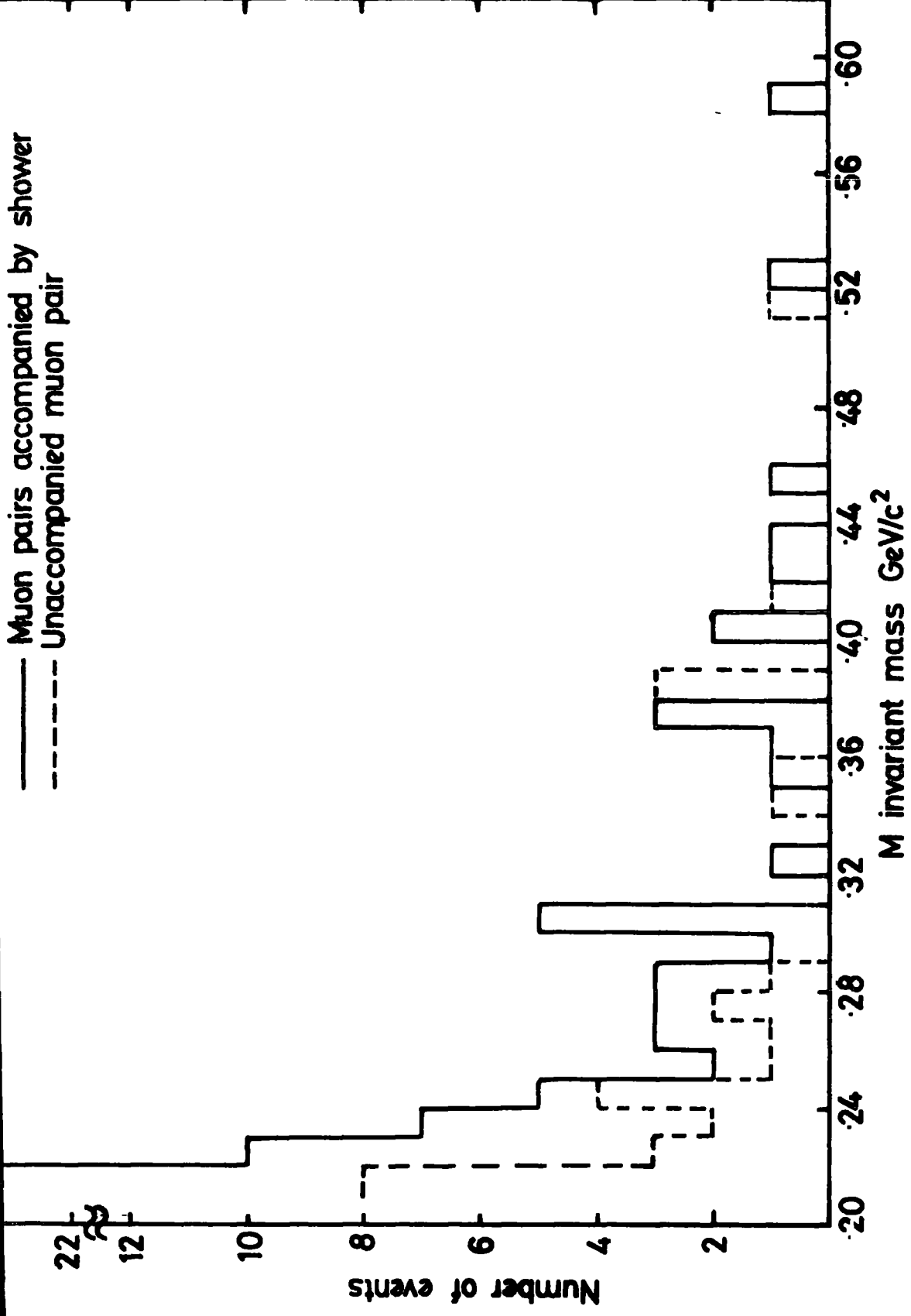


Figure 5-14 Invariant mass of muon pairs.

is no evidence of weak boson production. In considering this data further, Benvenuti, et al., 1975a, (and other publications referred to therein), point out a pronounced asymmetry in the energy distribution of the  $\mu^-$  and  $\mu^+$  such that the ratio of the mean energy of the positive muons,  $\bar{E}_{\mu^+}$ , to the mean energy of the negative muons,  $\bar{E}_{\mu^-}$ , is

$$\frac{\bar{E}_{\mu^-}}{\bar{E}_{\mu^+}} \approx 3$$

Dividing the muon pair data of the present experiment into the unaccompanied events, and the shower accompanied pairs (in this case more than 30 columns of data on both sides of the spectrograph) the following ratios occur

$$\frac{\bar{E}_{\mu^-}}{\bar{E}_{\mu^+}} \text{ (shower accompanied) } = 0.77 \text{ for 77 events}$$

whilst

$$\frac{\bar{E}_{\mu^-}}{\bar{E}_{\mu^+}} \text{ (unaccompanied) } = 1.20 \text{ for 26 events}$$

where any event in which a muon with a momentum of over 1000 GeV/c has been excluded. However, for the individual events the mean and standard deviation of the ratio of the energy of the negative muon to the energy of the positive muon are about 2.23 and 4.44 respectively for the 26 shower unaccompanied pairs.

It cannot be concluded that a significant difference is seen in the properties of the muon pairs unassociated with air showers compared to the shower accompanied pairs. Correlations between two muons are likely to be much stronger if they are from the same interaction, or carry away a substantial part of the energy of one interaction, than if they are from interactions or particle decays well separated in point of generation.

CHAPTER 6

THE INTERPRETATION OF THE RESULTS

6.1 INTRODUCTION

The measurements reported in this thesis do not lend themselves to direct comparison with other experimental results. The particular nature of the experiments described requires any interpretation of the results to rely heavily upon previously measured quantities, if comparisons are to be made with predictions. In this chapter the assumptions made, and methods used to interpret the results in the preceding chapters are discussed and alternative possibilities and sources of uncertainty in the calculations are considered.

A single measurement of ionizing particle density over a region of about one square metre has been assumed to imply the impact of an extensive air shower. Given that the recorded events are due to a range of shower sizes falling at a range of distances a summation has been used to extrapolate from this one measurement to infer properties of the whole shower, ie. a unique structure function has been assumed. In this context systematic variations in any of the assumed quantities (age, lateral distribution, muon content of the shower, and so on) will have a cumulative effect. No account has been taken of a possible variation of age over the lateral extent of the shower, (Khristiansen, et al., 1975) and a single fixed age parameter has been assumed for all showers at sea level. The same lateral structure has been assumed for all shower sizes which may be a reasonable approximation even for very small showers (Fukui et al., 1960). However, considerable variations have been seen in, for example, the steepness of the core of small showers (Fukui, et al., 1960, and as reported by Greisen, 1956). Taking into account variations in behaviour of an assumed initiating photon only, Greisen (1956), gives as an example a possible increase, due to fluctuations,

in the number of electrons by a factor of over 1.5 above the average value given by cascade theory for a shower of age  $S = 1.4$ . Thus even using an empirical expression for shower particle density as a function of radial distance (which has been derived from more conventional shower measurements by arrays of many detectors) systematic and fluctuation effects may play a significant part in the predictions reported here.

A further consideration is the role played by the muon component of showers. As the form of the radial distribution of muons above a threshold momentum must be known in order to interpret the present results another possible source of systematic error may be introduced into any predictions. Here a distinction can be made between the empirical muon structure function used and the radial distributions predicted by the interaction models. The exact shape of the lateral distribution near the axis becomes difficult to determine for increasing shower sizes, thus an empirical expression is likely to be less reliable near the axis than far from the axis, whereas interaction models will tend to give specific predictions for the density at each radial distance.

The energy threshold at which air shower particles are detected by the top flash tube trays is considered in Section 6.3. Once again a disparity is likely to occur in the present experiment. The empirical expressions used for the radial density of air shower particles may have been determined for different thresholds for particle detection, to the effective threshold of the present experiments.

As a further comparison of the CKP and scaling interaction models the same primary spectrum has been applied to both models and the rate of events for the present experiment predicted. This acts as a more direct contrast of the two processes but may lead to difficulties if comparison is then made on an absolute scale with the experimental results.

## 6.2 THE LATERAL STRUCTURE OF ELECTRONS

The lateral structure function of the electron component of air

showers that was used in the preceding chapters is essentially the empirical Nishimura-Kamata-Greisen (NKG) distribution

$$f\left\{s, \frac{r}{r_m}\right\} = C(s) \left\{\frac{r}{r_m}\right\}^{s-2} \left\{\frac{r}{r_m} + 1\right\}^{s-4.5} \quad (6.1)$$

as introduced by Greisen, (1956). The age of the shower is represented by  $s$  and  $r_m$  is the Moliere unit defined as

$$r_m = \frac{E_s}{\epsilon_0} X_0$$

where  $X_0$  is the radiation length,  $\epsilon_0$  is the critical energy,  $E_s$  is the scattering constant, and  $C(s)$  is a normalization factor. Following Greisen, (1960) the expression used for the present work (equation 4.5) follows from equation 6.1 with the age parameter fixed at 1.25 and the Moliere unit at 79 m. This is to represent sea level air showers. The local density of electrons can then be expressed as

$$\rho(r, N_e) = \left\{\frac{N_e}{r_m^2}\right\} f\left\{s, \frac{r}{r_m}\right\} \quad (6.2)$$

As the present experiment is possibly sensitive to very small showers a fixed age parameter of  $s = 1.4$  may be more appropriate and has been used to contrast with the earlier predictions made. This larger age parameter has been suggested for smaller showers, especially for measurements near the axis. (Campbell and Prescott, (1952) Greisen, (1960)). Thus the following expression has been determined to represent a shower of age  $s = 1.4$ ,

$$\rho(N_e, r) = \frac{0.434}{r_m^2} N_e \left\{\frac{r_m}{r}\right\}^{0.6} \left\{\frac{r_m}{r+r_m}\right\}^{3.1} \quad (6.3)$$

(this is similar to equation 4.5 with the last term removed as this only has effect at very large radial distances).

This structure function has been used in a calculation as described in Section 4.6, where  $P_T$ ,  $P_M$ , and  $F(N_e)$  are defined in the same way and have the same numerical values. Two different lower limits for the integral over shower size have been used,  $N_e = 1.0 \cdot 10^3$ , and  $N_e = 1.0 \cdot 10^4$ , and the rates of events predicted as a function of muon threshold momentum is shown in Figure 6.1 for both these lower limits. Thus from this consideration if the overall age of the showers contributing to the experimental rate is greater, the expected rate of events is lowered. However, the smallness of change of overall rate due to excluding showers of less than about  $10^4$  particles may indicate that the contribution is from showers with  $S$  not much larger than about 1.25.

A further consideration is the theoretical variation of age of the shower with radial distance, such that  $S$  decreases with distance from the shower axis. The theoretical maximum of a shower, and hence age, is reached earlier for the high energy particles near the axis than for the low energy particles far from the axis. The radial dependence of  $S$  is weak for distances of greater than about 30 m at sea level but can vary considerably at closer distances to the axis. As an example of this Greisen, (1956) points out that if a shower of  $10^5$  electrons is detected 16 radiation lengths below the point of origin and is initiated by ten identical collinear photons,  $S$  has the value 1.6 at one metre; 1.3 at 10 metres, and about 1.2 at 50 metres. However, Fukini et al., (1960) found that an age parameter of  $S < 1.0$  was needed to fit an N-K-G type function to the radial distribution of particle densities near the axis of some measured air showers.

Recently, Allen, et al., (1975) have made some extensive Monte Carlo simulations of electron-photon cascade development and have compared the results with other authors calculations including the Nishimura-Kamata, (N-K) functions. Allen et al., suggest that N-K functions over-estimate

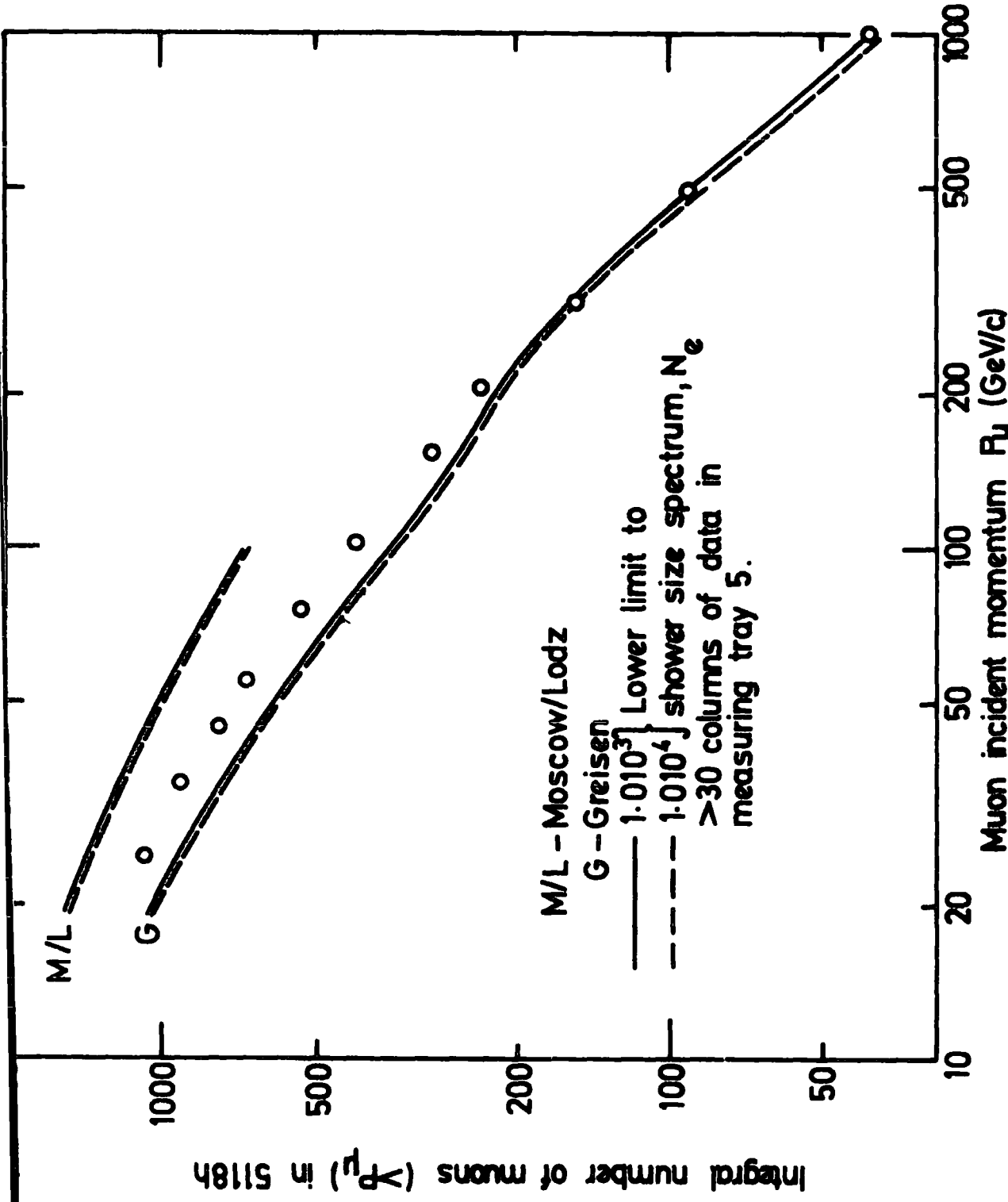


Figure 6.1. The rate of events predicted by the shower size spectrum and electron structure function with  $s=1.4$ .

the width of the electromagnetic cascade such that at shower maximum ( $S = 1.0$ ) the median width is 0.12 Moliere units (0.25 radiation lengths is about  $10 \text{ g cm}^{-2}$  in air) and not 0.27 as given by the N-K functions for a 10 GeV photon-initiated cascade. This will have implications not only for the actual radial electron structure of showers but if, as is usual, N-K type functions are used to determine the shower size from density measurements beyond several tenths of a Moliere unit, shower sizes will be under-estimated. This may have an effect on estimates made of the shower size spectrum by air shower arrays using N-K type functions.

### 6.3 THE ENERGY THRESHOLD FOR ELECTRON DETECTION

The expressions used this far for the density of electrons at different radial distances from the axis of air showers are appropriate to all electrons above zero energy (Greisen, 1956). However, a finite energy is required by an electron to penetrate the material above the measuring and momentum selector trays on the spectrograph. Thus in the present experiment fewer shower particles may be expected to be detected in measuring tray 5 but a certain amount of extra low energy electrons can be expected from the 'amplification' effect of this material. The amount of absorbing material vertically above measuring tray 5 is indicated in Table 6.1. However, all the material is not compacted immediately above the measuring tray and for a shower incident at an angle to the vertical different electrons will pass through different amounts of material. Thus although the  $24 \text{ gm cm}^{-2}$  of absorber represents a particle threshold of about 48 MeV this will only apply to vertically incident electrons and no unique energy threshold can be determined. The average energy of electrons over the whole shower is given by Hayakawa, (1969) as  $230 \pm 50$  MeV at sea level and Greisen, (1960) suggest an approximately constant average value of energy just below the critical energy for air,  $\epsilon_c = 84$  MeV, for the electrons well away from the axis (i.e. beyond  $r_m$ ). In Figure 6.2, is

THE ABSORBER THICKNESS OF THE DETECTOR ELEMENTS ABOVE MEASURING TRAY 5

Element	Material	Thickness		Density gm cm <sup>-3</sup>	Number of Elements	Thickness	
		cm				gm cm <sup>-2</sup>	
Scintillation Counter	NE 102a	5.0		1.032	1	5.160	
	Aluminium	0.7		2.7		1.89	
Momentum Tray	Aluminium	0.76		2.7	1	2.052	
	Glass	1.3		2.7		3.51	
Azimuth Tray	Aluminium	0.76		2.7	2	4.104	
	Glass	1.3		2.7		7.02	

Total Thickness 23.74

TABLE 6.1

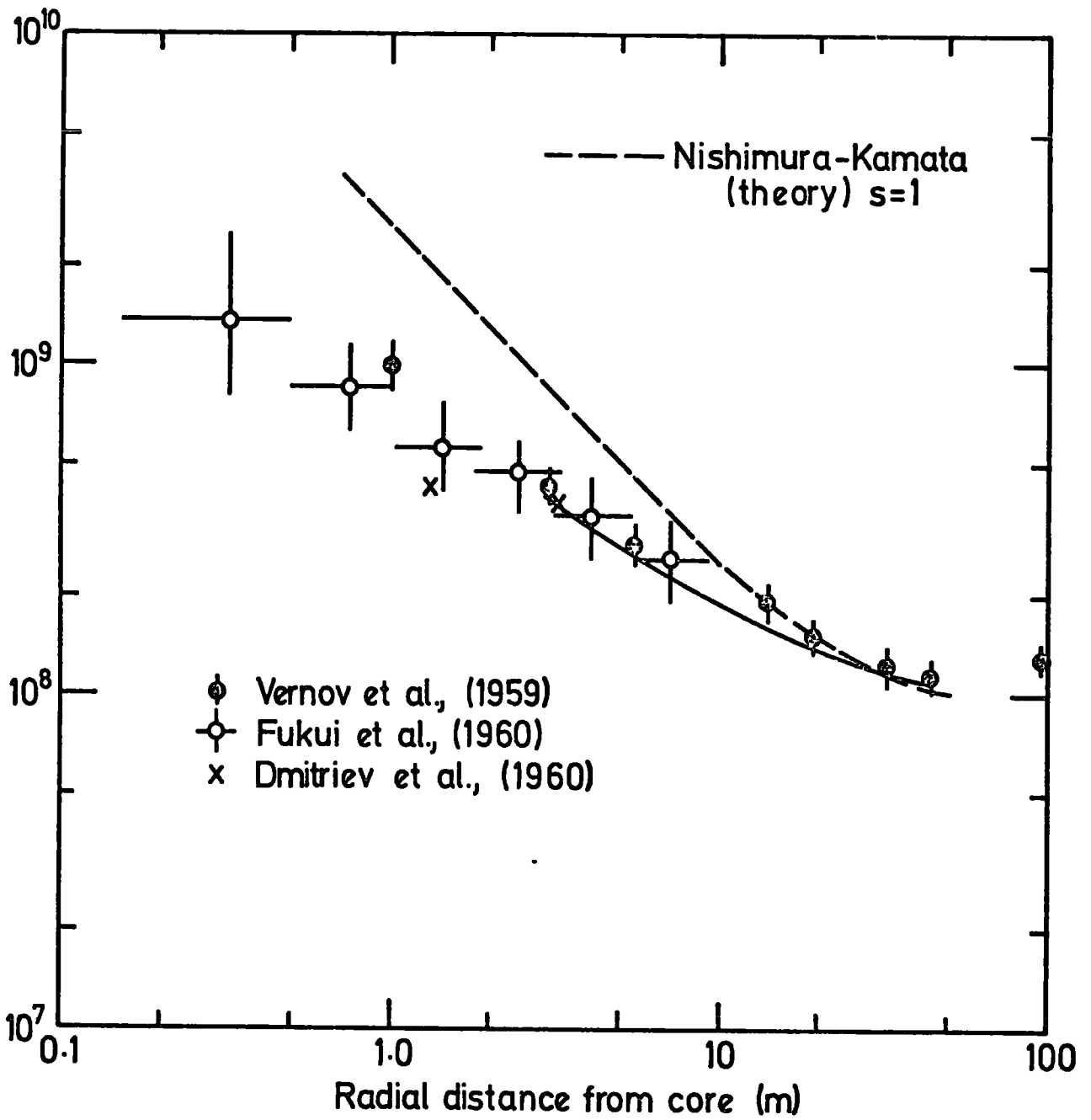


Figure 6-2.

shown the average energy per electron for radial distances less than 100 m, which is the region of interest for the present experiments. The data for the figure are taken from the work of Fukui, et al., (1960) and the references they quote. As these authors explain the average energy per electron has been determined by dividing the energy flux by the corrected particle density as the energy flow includes the energy carried by photons. Shown also is the theoretical curve they calculate using an N-K function for a shower with  $S = 1$  initiated by an infinite energy primary photon.

The approach adopted here to consider the effect of a threshold value below which the electrons will not be detected, involved the calculations of Dixon, et al., (1973). These workers have given two relations for the number of electrons expected at sea level which are both the result of simulations of air showers assuming a CKP type interaction model. These two predictions are shown in Figure 4.16 and differ only in the threshold energy of electron considered. There is a change of slope in both relations of shower size to primary energy at a primary energy of just over  $10^6$  GeV, and both relationships have been determined for proton initiated showers. The relation of shower size to primary proton energy for each energy region is given in Table 6.2. Here the conversion from the fixed energy primary case to the fixed shower size case is given by  $2.8 E_p^{-0.031}$  for all values of primary energy. The primary spectrum used with both of these relationships is shown in Table 6.3 and has been determined as described in Section 4.7.8 to be compatible with the sea level shower size spectrum. The rate of muons expected is then given by equation 4.32 where the parameters  $P_T$ ,  $P_M$ ,  $r$  are as before but the relation of shower size to primary proton energy and the primary spectrum are as given in Tables 6.2 and 6.3. However, the electron structure function equation 4.5 has been used and the cut off in electrons due to their energy falling below 10 MeV is governed by the relation of shower size to primary proton energy. This assumes that the

THE RELATION OF SEA LEVEL SHOWER SIZE TO PRIMARY PROTON ENERGY FOR THE

C.K.P. MODEL (FROM DIXON, ET AL., 1973)

Electron Threshold Energy	Shower Size Below Change of Slope	Shower Size at Change of Slope	Shower Size Above Change of Slope
0 MeV	Fixed $E_p$ $N_e = 6.08 \cdot 10^{-3} E_p^{1.233}$	$1.78 \cdot 10^5$	Fixed $E_p$ $N_e = 3.240 \cdot 10^{-2} E_p^{1.113}$
	Fixed $N_e$ $N_e = 1.702 \cdot 10^{-2} E_p^{1.202}$		Fixed $N_e$ $N_e = 9.075 \cdot 10^{-2} E_p^{1.082}$
10 MeV	Fixed $E_p$ $N_e = 9.41 \cdot 10^{-3} E_p^{1.177}$	$1.66 \cdot 10^5$	Fixed $E_p$ $N_e = 4.67 \cdot 10^{-2} E_p^{1.064}$
	Fixed $N_e$ $N_e = 2.635 \cdot 10^{-2} E_p^{1.146}$		Fixed $N_e$ $N_e = 1.31 \cdot 10^{-1} E_p^{1.033}$

TABLE 6.2

THE DIFFERENTIAL PRIMARY SPECTRUM USED WITH THE MODEL PREDICTIONS

OF DIXON, ET AL., 1973

Electron Threshold Energy		Differential Primary Spectrum
0 MeV	10 MeV	
Below 1.141 $10^6$ GeV	Below 1.457 $10^6$ GeV	$J(E_P) dE_P = 5.13 \cdot 10^4 E_P^{-2.80} dE_P$
Between 1.141 & 2.312 $10^6$ GeV	Between 1.457 & 2.312 $10^6$ GeV	$J(E_P) dE_P = 3.74 \cdot 10^3 E_P^{-2.62} dE_P$
Above $2.312 \cdot 10^6$ GeV	Above $2.312 \cdot 10^6$ GeV	$J(E_P) dE_P = 2.46 \cdot 10^7 E_P^{-3.2} dE_P$

TABLE 6.3

radial structure of electrons of all energies is the same. In fact the highest energy electrons will tend to be near the centre of the shower. In Figure 6.3 the predictions corresponding to this calculation are shown in comparison with the experimental points. The solid lines indicated as  $>10$  MeV and  $>0$  MeV correspond to the relevant electron energy thresholds. The dashed lines correspond to using the primary spectrum detailed in Section 6.5. Within the limits of the uncertainty about the radial structure of  $>10$  MeV electrons a significant reduction in the predicted rate occurs for higher detection thresholds of electron energy.

In the light of these considerations the remarkable closeness of agreement of predictions using Greisen's electron structure function with the experimental points in Figures 4.9 to 4.11, must be considered as largely fortuitous. However, given that a comparison has also been possible between the predictions of the CKP and scaling models the experimental situation can also be considered as a test of the relative success of the predictions as opposed to just an absolute measurement. As some of the uncertainties in the model predictions will be common to both, a contrast of the scaling and CKP models can be made by comparing the predictions of these models with the predictions of Greisen's empirical structure functions, assuming these latter functions to hold.

#### 6.4 THE LATERAL STRUCTURE OF MUONS

In Section 4.7.12 a comparison of the predictions was made between the empirical muon structure function suggested by Greisen, (1960) and a structure function fitted to the experimental values of Rozhdestvensky et al., (1975) by the present author. A direct comparison of the two expressions is shown in Figure 6.4 where the density of muons of momentum greater than 20 GeV/c is shown as a function of radial distance. Considering the discussion of Section 6.3 the absolute rate of events predicted by the 'fitted' structure function may not be as far in excess of the experimental

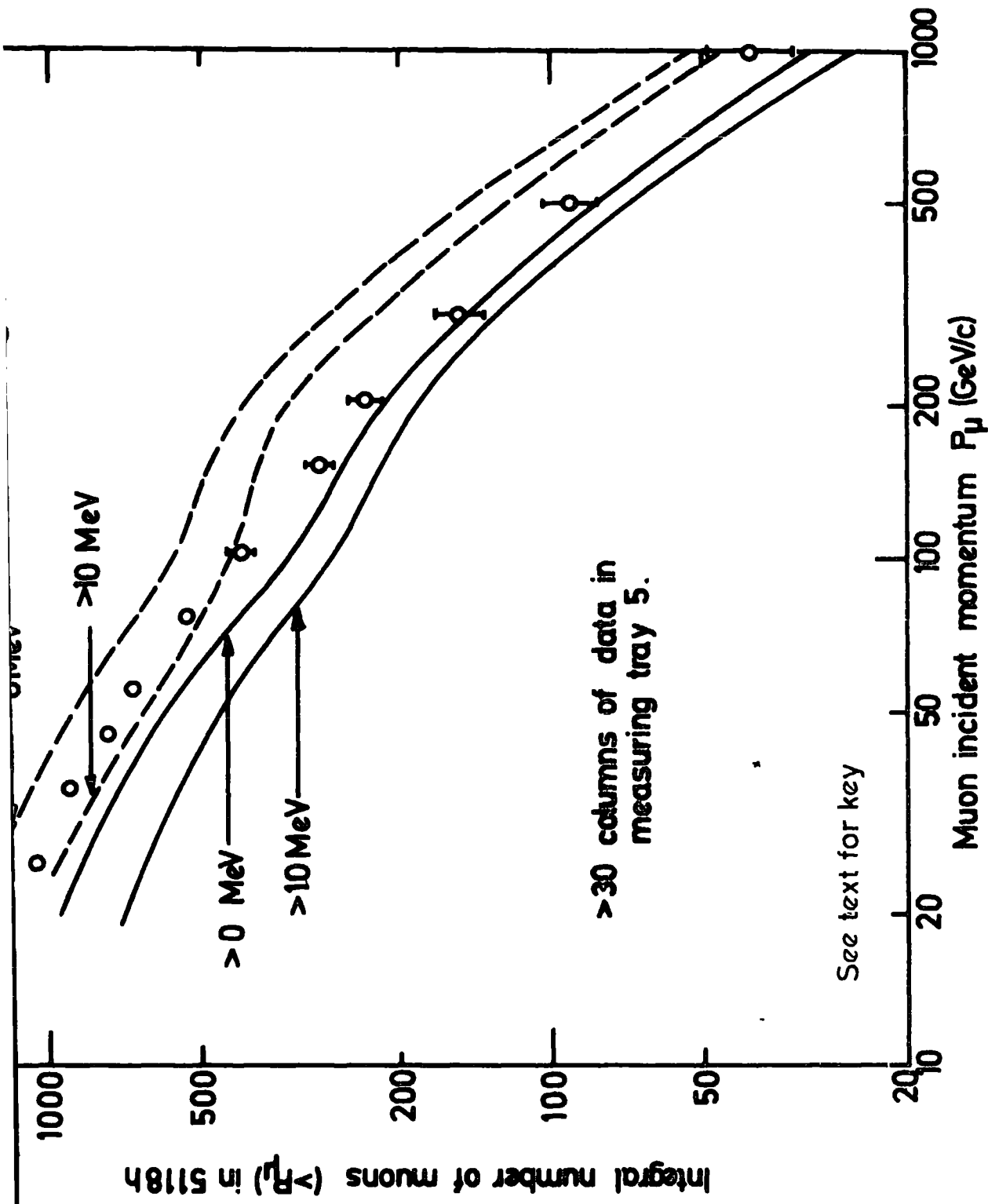
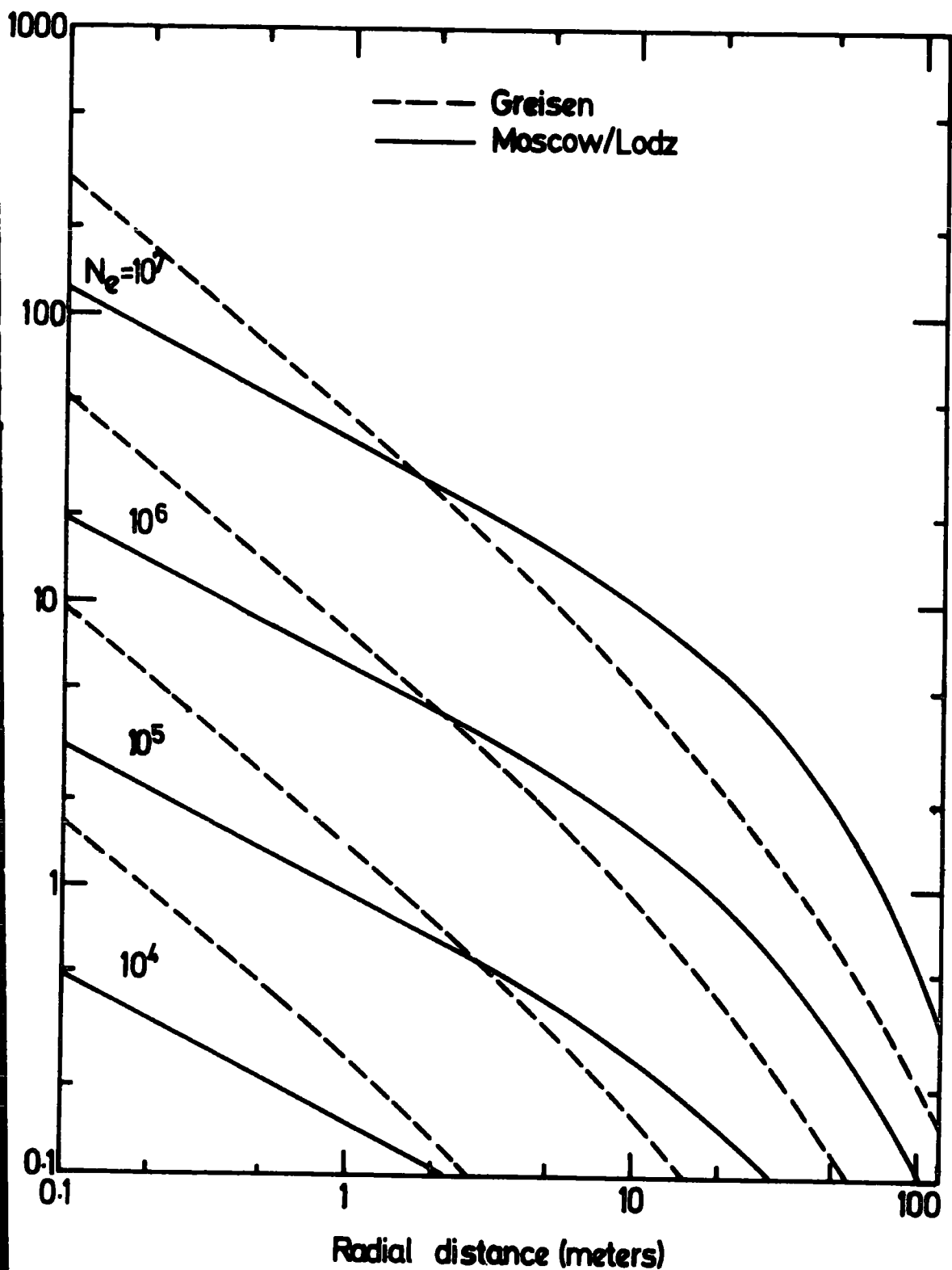


Figure 6.3. The predicted rate using the CKP model of Dixon et al., (1973) for two electron energy thresholds.



Comparison of muon structure functions due to Greisen (1960) and as fitted to Moscow/Lodz data points (Munich, 1975)

Figure 6.4

data as indicated in Figures 4.9 to 4.11. However, it can be seen from Figure 6.4 that this fitted structure function gives a density a factor of about 2 in excess of the Greisen function for the region of 5 to 50 metres from the axis. This corresponds to the region of greatest contribution to the rate of events as indicated by Figure 4.13. Iliyna, et al., (1971) found that the lateral distribution of muons of energy greater than 10 GeV fluctuates in the region near the axis of air showers. A correlation was found with the age parameter,  $s$ , such that the lateral distribution  $\rho_{\mu}(r)$  varied with radial distance  $r$  as

$$\rho_{\mu}(r) \sim r^{-0.2} \quad \text{for } s > 1.2$$

and as 
$$\rho_{\mu}(r) \sim r^{-1.0} \quad \text{for } s < 1.0$$

for distances  $r < 20$  m. Further measurements (Khristiansen, et al., 1975) confirm this correlation in showers of size  $2 \cdot 10^5$  to  $10^6$  particles such that

$$\rho_{\mu}(r) \sim r^{-n} \exp(-r/80)$$

where 
$$n = 0.7 \pm .07 \quad \text{for } s < 1.0$$

and 
$$n = 0.5 \pm .07 \quad \text{for } s > 1.3$$

From the work of these authors, it may be concluded that in younger showers the total number of muons is lower and the lateral distribution of muons is steeper than in older showers in this size range. A further confirmation that young showers have a high 'size to energy ratio' and consequently a lower muon to electron ratio comes from the work of Catz, et al., (1971) and (1973). These workers determined the shower age parameter (for showers whose axes had been determined independently of the electron lateral distribution) as a function of the muon content of the shower. The age was found to increase from about  $s = 1.1$  to about  $s = 1.3$  for a

change from 1 to 6% of muons in the shower. This was for showers of medium size  $3 \cdot 10^5$  and  $5 \cdot 10^5$  but these authors do not quote the threshold energy for muon detection. In relation to the present experiments, as the detection of at least one muon is an essential part of the trigger condition there may be a bias toward showers of large S.

The lateral structure of muons has been found to be wider than predicted by a standard model of the CKP type by several authors. Rozhdestvensky, et al., (1975) conclude from their studies of showers in the range of  $3 \cdot 10^4$  to  $10^6$  particles that the experimental lateral distributions are clearly wider than the predicted ones for muons, of threshold energies in the range 10 GeV to 90 GeV. A widening by a factor of about 1.6 is necessary to agree with predictions. A similar effect has been seen by Bonczak, et al., (1968) in studies of muons at a threshold momentum of 0.6 GeV/c in showers of about  $10^6$  particles. Here the experimental lateral distribution corresponds to a CKP type model of the transverse momentum ( $p_t$ ) distribution only if values of  $p_t$  below 0.1 GeV/c are suppressed. This is seen as a distinct 'flattening' of the lateral distribution at small distances from the shower axis.

The present experiments are sensitive to muons accompanied by a high density of electrons, and as the highest density of both muons and electrons will be in the centre of most showers the measurements are biased toward the central regions of air showers. However, given the uncertainty in threshold energy of detection of electrons, and possible correlations with the age of showers, no conclusive distinction can be made regarding the actual distribution of high energy muons. Although the absolute agreement of the rate of events predicted by the Greisen muon and electron structure functions cannot be concluded from the data the trend suggested at higher muon energies remains close to the data, whereas the combination of Greisen's electron structure function and the muon structure fitted to the Moscow-Lodz data points suggest a rate that diverges well above the data for values of high muon energy.

6.5 THE DEPENDENCE OF THE PREDICTIONS OF THE CKP AND SCALING MODELS  
ON THE PRIMARY SPECTRUM

In Chapters 4 and 5 three models, A, B and C, were used to compare the predictions of the CKP and scaling high energy particle interaction models. Use was made of separate primary spectra assumed appropriate for each situation such that the sea level shower size spectrum was predicted as a consequence of the combination of the interaction model and the primary spectrum. In this section a contrast is made more directly between the predictions of the interaction models by use of the same primary spectrum for both models.

Consideration is given first to the possibility of a primary spectrum composed entirely of protons. The differential intensity has been taken as

$$J(E_p) dE_p = 9.0 \cdot 10^3 E_p^{-2.6} dE_p \text{ m}^{-2} \text{ s}^{-1} \text{ sr}^{-1} \text{ GeV}^{-1} \quad (6.4)$$

following Adcock, et al., (1969) and Goned, et al., (1975) and a break is assumed to occur at a proton energy of  $2 \cdot 10^6$  GeV at which point the exponent changes to -3.3. A model, A2, can then be defined in the same way as Model A, as described in Section 4.7.11, with the single exception that the primary spectrum is taken to be as expressed in equation 6.4. Thus in Model A2, the CKP model has been used to predict the rate of events using equation 4.32 and the results are shown as a function of incident muon momentum in Figure 6.5. The corresponding predicted sea level shower size spectrum is shown in Figure 6.6. To contrast with the predictions of scaling, models B2 and C2 are defined in the same way as Model B and C respectively and again the primary proton spectrum, equation 6.4, has been used. The predictions of Models B2 and C2 and the corresponding shower size spectra are shown in Figures 6.5 and 6.6 also.

The primary spectrum suggested by Elbert, et al., (1973) has also

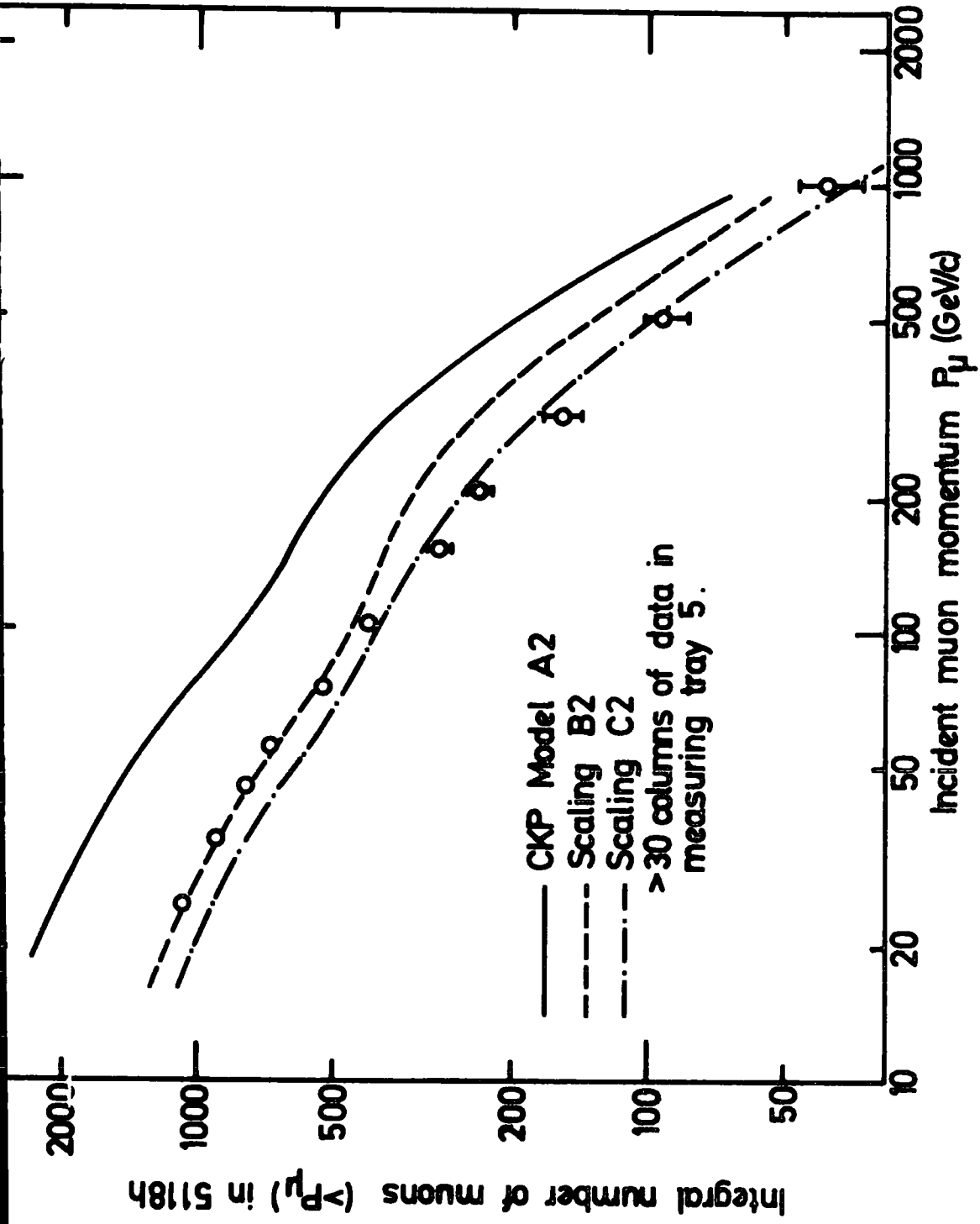


Figure 6.5. The rate of events determined from the primary proton spectrum.

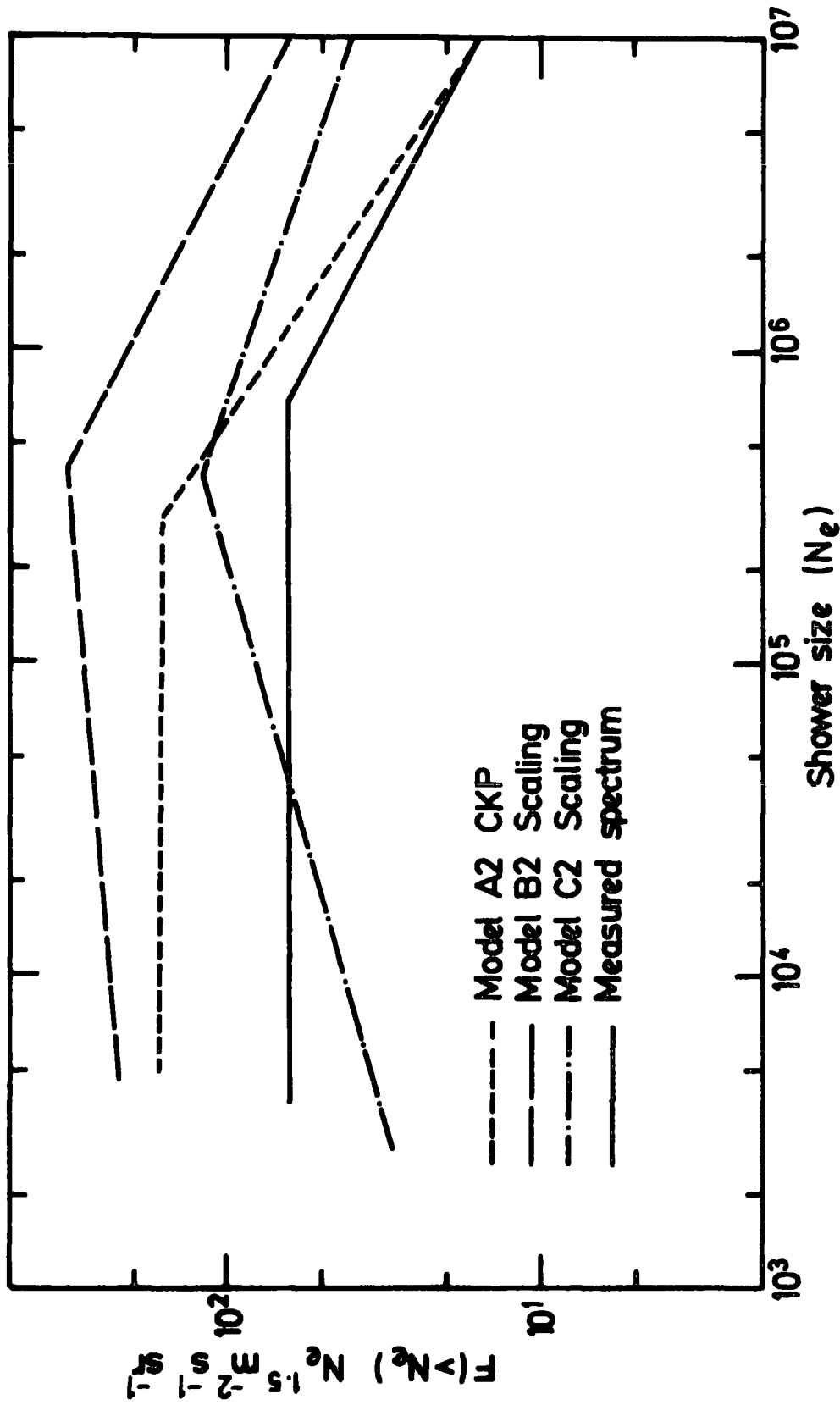


Figure 6.6. The sea level shower size spectra predicted by the proton primary spectrum and models A2, B2 and C2.

been used directly with the present versions of the CKP and scaling models used in air shower development. The spectrum has the form

$$J(E_p) dE_p = 5.54 \cdot 10^4 E_p^{-2.75} dE_p \text{ m}^{-2} \text{ s}^{-1} \text{ sr}^{-1} \text{ GeV}^{-1} \quad (6.5)$$

and the proportions of different nuclei are given in Table 4.5. Models A2, B2 and C2 are re-defined to incorporate 6.5 and the predicted rate of events is shown in each case as a function of muon incident momentum in Figure 6.7. The corresponding sea level shower size spectra predicted by each model is shown in Figure 6.8.

For a final comparison between the predictions of the CKP and scaling models the expected rate of coincident muon pairs was determined by using equation 5.5 and the primary spectra associated with models A2, B2 and C2 and the results are shown in Table 6.4.

#### 6.6 THE EFFECT OF THE RISING PROTON-AIR CROSS SECTION AND THE EFFECT OF A NUCLEAR PROJECTILE AND TARGET

One of the most recent successes of cosmic ray studies in the field of high energy particle interactions was the prediction of an energy dependent increase in the proton-proton total cross-section,  $\sigma_{p-p}(\text{TOT})$ , made by Yodh, et al., (1972). These workers determined the proton-air nucleus in elastic cross-section  $\sigma_{p\text{-air}}(\text{INEL})$  to be

$$\sigma_{p\text{-air}}(\text{INEL}) = 280 + 2.5 \ln^{1.8} (E/100) \text{ mb}$$

where E is in GeV and applies for E above about 100 GeV. By calculating the (theoretical) response of an air nucleus to a proton projectile, Yodh, et al., (1972) predicted that  $\sigma_{p-p}(\text{TOT})$  will rise for incident protons of energy above about 100 GeV up to at least  $2 \cdot 10^4$  GeV. This rise has now been confirmed to the extent that  $\sigma_{p-p}(\text{TOT})$  increases from about 39 mb to about 44 mb for a corresponding increase in energy of the incident proton

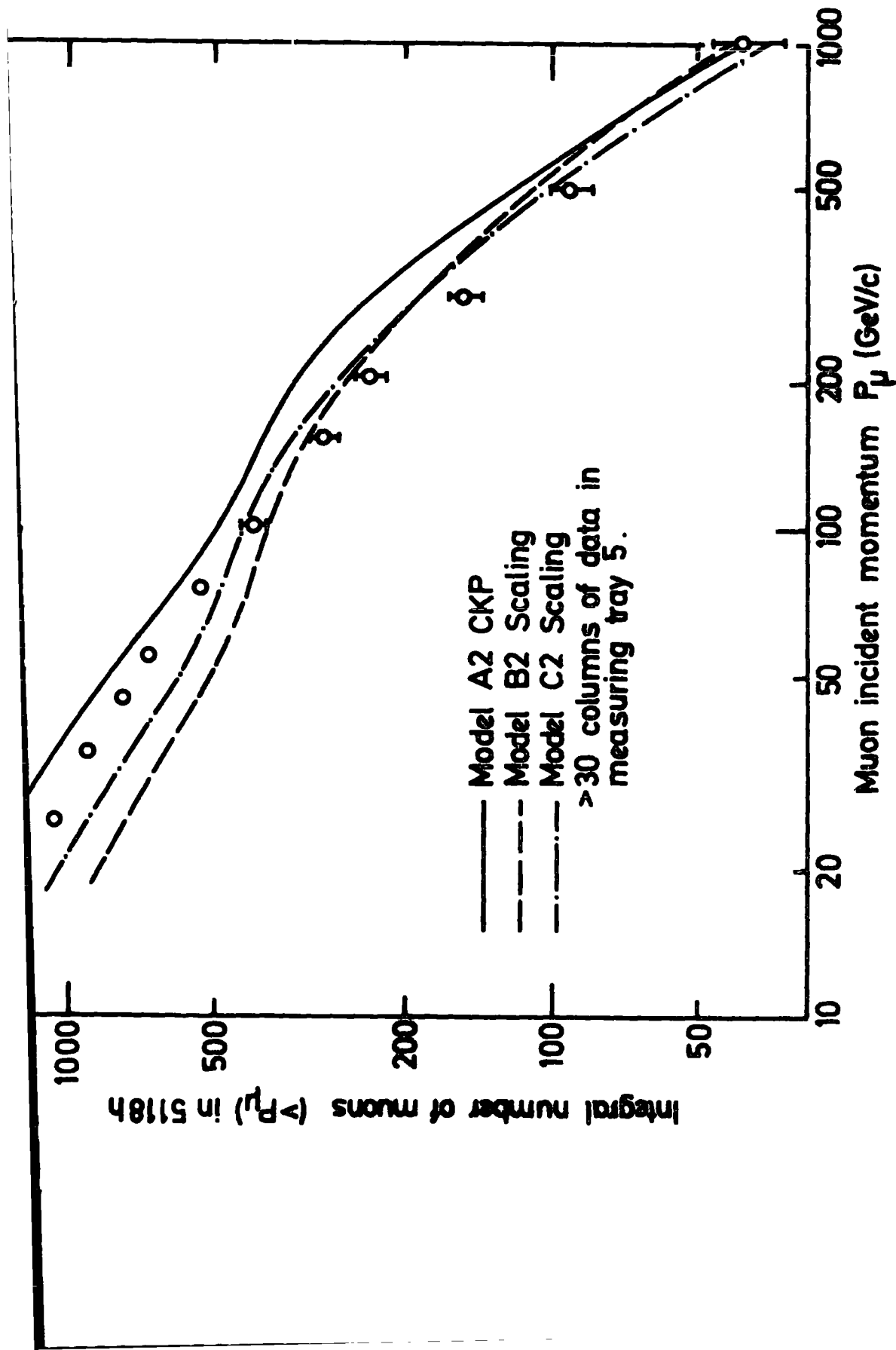


Figure 6-7. The rate of events determined from the primary composition spectrum.

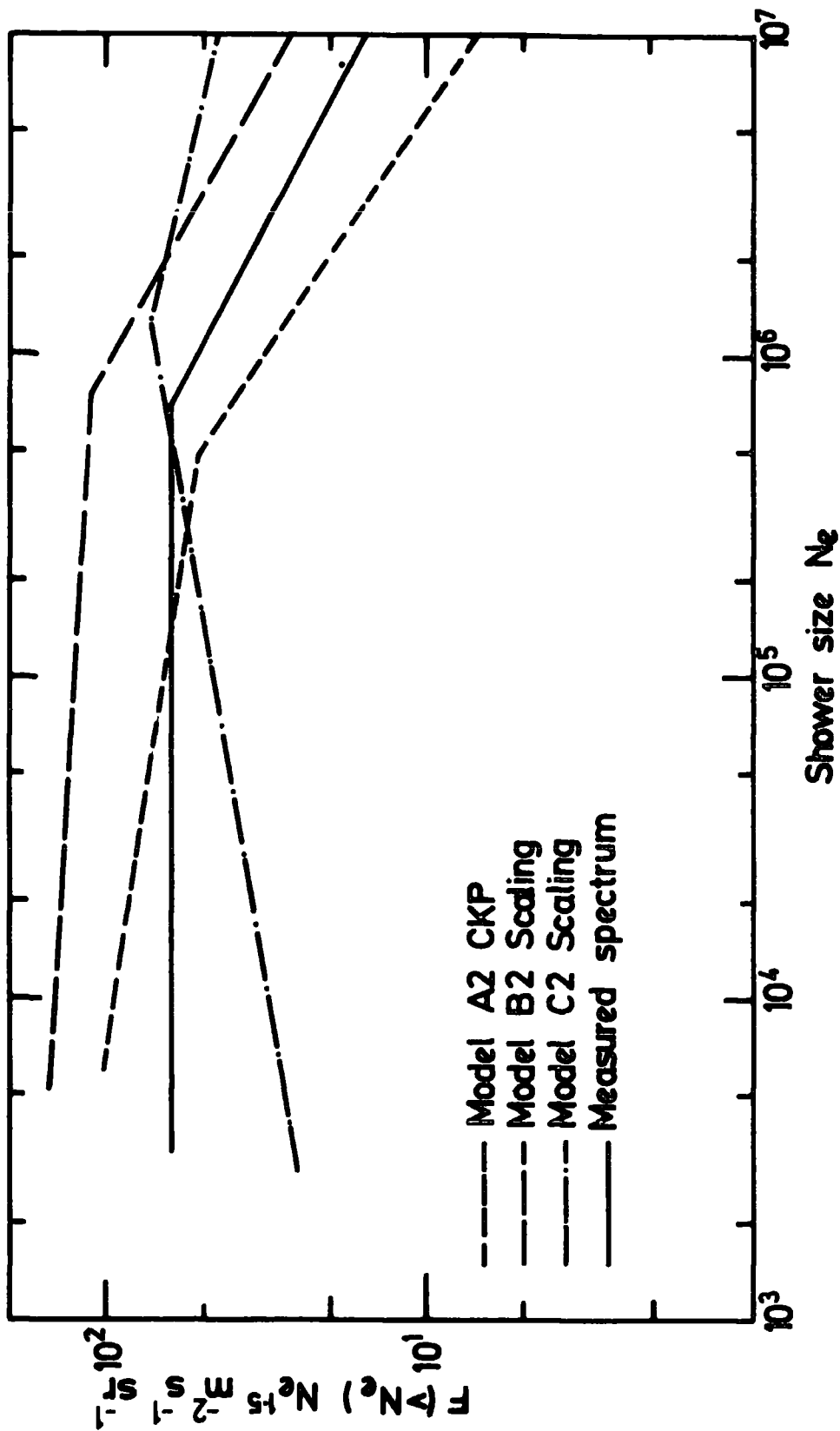


Figure 6.8. The sea level shower size spectra predicted by the primary composition spectrum and model A2, B2 and C2.

Muons Threshold Momentum, GeV/c	MODEL A2, CKP		MODEL B2, SCALING		MODEL C2, SCALING		
	Protons only	Composition	Protons only	Composition	Protons only	Composition	
60	Intensity $10^{-4} \text{ s}^{-1} \text{ sr}^{-1}$	$2.70 \cdot 10^{-1}$	$1.89 \cdot 10^{-1}$	$5.07 \cdot 10^{-2}$	$7.18 \cdot 10^{-2}$	$2.52 \cdot 10^{-1}$	$2.05 \cdot 10^{-1}$
	Number in 30 h	483	336	93	128	451	366
	Adjusted Number	64	45	13	17	60	49
100	Intensity $10^{-4} \text{ s}^{-1} \text{ sr}^{-1}$	$1.46 \cdot 10^{-1}$	$1.07 \cdot 10^{-1}$	$3.21 \cdot 10^{-2}$	$4.61 \cdot 10^{-2}$	$1.74 \cdot 10^{-1}$	$1.41 \cdot 10^{-1}$
	Number in 30 h	262	191	57	83	310	251
	Adjusted Number	35	25	75	11	41	33

TABLE 6.4

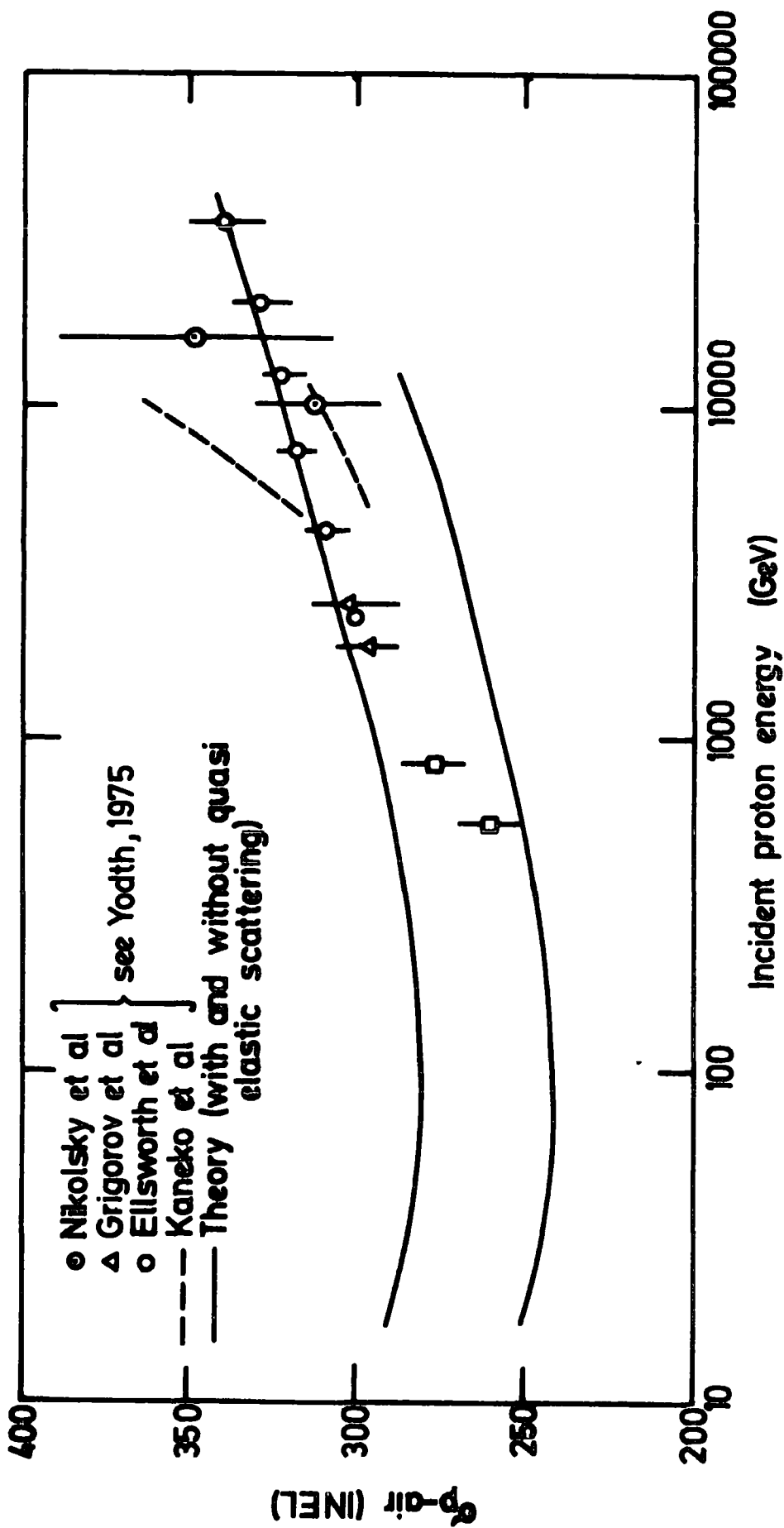


Figure 6.9 The variation of the inelastic proton-air nucleus cross section with proton energy (after Yodh, 1975).

from 100 GeV to about 2000 GeV. The charged pion and kaon cross sections for interactions with protons have been shown to rise also up to incident energies of 200 GeV. (see A.S. Carroll, et al., 1974). The importance for secondary cosmic rays of this change in hadron-hadron cross section with energy will be due to the corresponding decrease in interaction length for proton air nucleus collisions, and the pion air nucleus absorption length. Figure 6.9 shows the variation with energy of  $\sigma_{p\text{-air}}(\text{INEL})$  as compiled by Yodh,(1975) and Yodh (as reported by Olejniczak, et al., 1977) suggests that the interaction length for proton air nucleus collisions falls from  $80 \text{ g cm}^{-2}$  at incident proton energies of  $10^{12} \text{ eV}$  to  $40 \text{ g cm}^{-2}$  at energies of  $10^{15} \text{ eV}$ . The consequence of this for the present work is that the calculations that assume a constant  $\sigma_{p\text{-air}}(\text{INEL})$  will tend to predict a lower rate of events than measured.

Tests of hadron-hadron interaction models using primary and secondary cosmic rays suffer from the disadvantage that the interactions are in fact of hadrons with nuclei, or in the case of heavier primaries, the interactions will be of the nucleus-nucleus type. Indeed for primary nuclei, if complete initial fragmentation into the constituent nucleons of the incident nucleus does not take place some subsequent interactions may also be of the nucleus-nucleus type. Any masking of the hadron-hadron collision will be crucial in attempts to distinguish between different interaction models. This applies especially to the first few interactions where the energy is highest and the differences in the predictions of the models are greatest. Proton-proton collisions in the ISR have led to 3 'regions' being identified as containing the produced particles. Short-lived ( $\sim 10^{-23} \text{ s}$ ) fireballs or clusters appear to be produced and subsequently split up into several directly observed particles. Two dominant mechanisms of cluster formation occur. Fragmentation of the projectiles results in particles (mainly pions) with low

velocity in the projectiles rest frames, whilst production of particles (again mainly pions) from the central region (centre of momentum) is called pionization and the particles are emitted isotropically. Events of small total multiplicity are mainly due to fragmentation whilst pionization is responsible for high multiplicity events. The importance of these processes in determining air shower parameters is the response of a nucleus through which a projectile hadron passes. If the observed cosmic ray secondaries, such as the electron and muon component at sea level, are produced by particles which stem from the fragmentation region of the projectile then any intranuclear cascade would seem to be unimportant. For instance Jain, et al., (1975) have studied 200-300 GeV proton interactions with several different target nuclei and have found that the average number of relativistic charged particles (with  $\beta > 0.7$ ) increases slowly with atomic weight  $A$  of the target and is due to the target fragmentation region. These authors find that in the projectile fragmentation region the multiplicity is the same for heavy nuclei targets as for hydrogen. Elliot, et al., (1975) find that for 200 GeV pions incident on neon nuclei the increase in multiplicity of all secondaries is only  $25 \pm 7\%$  compared with pion proton collisions. Busza, et al., (1975) studied the development of hadronic showers inside nuclear matter in negative pion-nucleus collisions for 100 GeV and 175 GeV incident pions. These authors measured the multiplicity of charged relativistic particles as a function of angle of emission and target nuclear size and conclude that there is no increase in the number of particles produced at less than about  $3.5^\circ$  to the incident pion direction with atomic weight,  $A$ .

Yodh, (1975) in a survey has drawn the following conclusions for the dependence of the number of secondary particles  $n_s$  ( $\beta > 0.7$ ) on atomic weight  $A$  and incident energy  $E$ , in hadron-nucleus collisions,

1.  $n_s$  varies as  $\ln E$

2.  $n_s$  is a weak function of atomic weight, such that at E about 200 GeV

$$n_s \propto A^{0.129}$$

3. Shower particle multiplicity in the forward core ( $\sim 0.5^\circ$  in the laboratory) is the same as that in proton-proton collisions.

Thus it may be concluded that there is very little intranuclear cascading and that a hadron projectile traverses the nucleus in an excited state and interacts with the constituent nucleons with a hadron-nucleon cross section, for projectile energies below about 400 GeV. If extrapolation to higher energies is valid then it may be concluded that intranuclear cascading is not important for proton nucleus interactions to the extent that the parameters governing proton-proton interactions will dominate in air shower production.

A further complication in predicting the parameters of air showers which are initiated by primary nuclei is the lack of experimental evidence of the extent of fragmentation of the incident nucleus in the first collision high in the atmosphere. It seems that from studies of nucleus-nucleus collisions in the energy range up to about 2 GeV per nucleon the modes of fragmentation of projectile nuclei are independent of the target nucleus (Heckman, 1975), and there is evidence that an average iron nucleus undergoes about six interactions before it is totally reduced to nucleons (Waddington, et al., 1973). However, Tomaszewski and Wdowczyk, (1975) have concluded that about 75% of the nucleons of a nitrogen nucleus that emerge as free particles have interacted and produced pions in collisions with target nuclei in an emulsion stack. Dixon, et al., (1974) extrapolated a partial fragmentation model based on the data of Waddington, et al., (1973) and compared the predicted longitudinal development of air showers using this model and the superposition model (assuming complete fragmentation in the first interaction) for iron nuclei initiated showers. However, for an iron nucleus of energy

$10^{15}$  eV they find that the predicted electron cascade is the same for the two models but some effect is seen in the muon component. As the present experiments are sensitive to the muon component of showers the predicted rate of events will depend upon not only the content of heavy nuclei in the primary spectrum but also on the fragmentation process that is assumed to hold. Heavy nuclei showers will not only contain more muons than proton or light nuclei showers but the energy spectrum will have a larger slope as the energy degradation proceeds faster.

6.7 THE EFFECT OF REPRESENTING A DISTRIBUTION OF SHOWER SIZES BY A MEAN SHOWER SIZE

To allow for the effect of fluctuations in the shower size for a given primary energy in the calculations involving both the CKP and scaling models, the relationship of mean shower size to primary energy at fixed shower size was assumed to be appropriate. However, the use of a mean shower size, even adjusted in this way, may not be a good representation of the predicted distribution of shower sizes (de Beer, et al., 1966) and may not be justified in the case of the present experiment. The frequency histogram of shower sizes expected at sea level for a vertically incident proton primary of energy  $4 \cdot 10^5$  GeV as given by de Beer, et al., (1966) and Holyoak, 1967, is shown in Figure 6.10 Popowa, (1969) (as reported by Bell, 1974) suggests that in general the distribution of shower sizes is well represented by a gamma function. Bell, (1974) finds that the following combination of two gamma functions best fits the distribution of shower sizes as reported by de Beer, et al., (1966) who use the CKP particle interaction model for an assumed proton primary.

$$\int (N_e, \bar{N}_e) dN_e = \left\{ \frac{19}{\bar{N}_{e_c}} \left( \frac{N_e}{\bar{N}_{e_c}} \right)^{2.3} \exp \left\{ -3.3 \frac{N_e}{\bar{N}_{e_c}} \right\} + \frac{1.3 \cdot 10^3}{\bar{N}_{e_m}} \left( \frac{N_e}{\bar{N}_{e_m}} \right)^{6.12} \exp \left\{ -7.1 \frac{N_e}{\bar{N}_{e_m}} \right\} \right\} dN_e \quad (6.6)$$

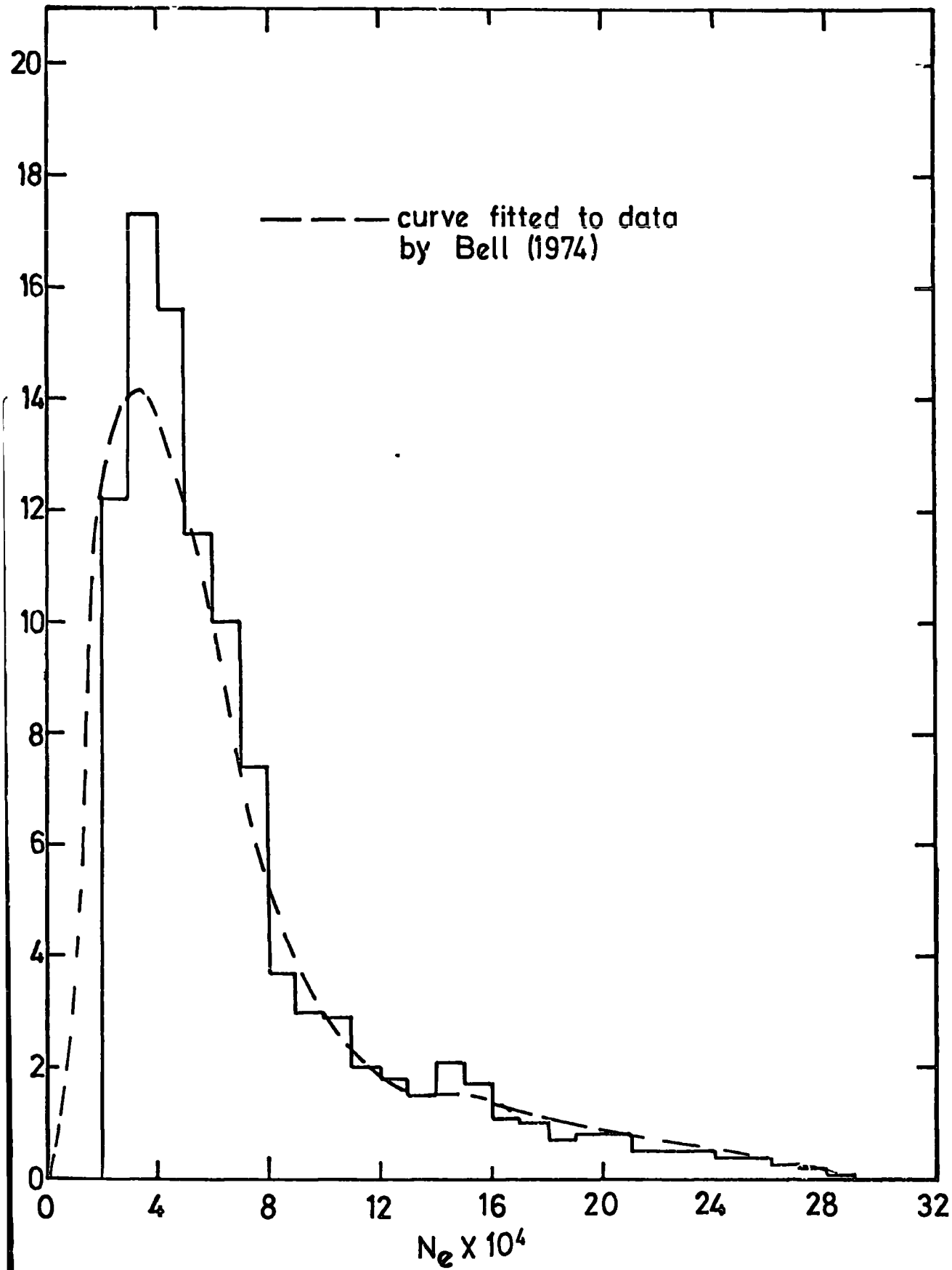


Figure 6.10 The electron size distribution expected at sea level for a primary proton of  $4 \cdot 10^5$  GeV as established by de Beer et al (1966)

where  $N_e$  is the shower size and  $\bar{N}_{e_c}$  and  $\bar{N}_{e_m}$  are the 'principle' and 'minor' mean shower sizes for the two gamma functions respectively such that

$$\bar{N}_{e_m} = 7.34 \cdot 10^{-2} E_p^{1.099} \tag{6.7}$$

and  $\bar{N}_{e_c} = 2.31 \cdot 10^{-2} E_p^{1.099}$  (6.8)

and  $E_p$  is the primary particle energy in GeV. The combination of expressions 6.7 and 6.8 gives

$$\bar{N}_e = 3.39 \cdot 10^{-2} E_p^{1.099} \tag{6.9}$$

This expression, equation 6.9, is close to the expression, see Table 4.3, used by the present author for the mean shower size for a given primary energy at fixed primary energy, as it must be and any discrepancy is due to inaccuracies in deducing relationships from the published work of de Beer, et al., (1966) and Holyoak, 1967

Allowing for the distribution of shower sizes at sea level for each primary energy, equation 4.32 can be modified to the following form,

$$R(>P_\mu) = \int_{\text{All Primary Energies}} J(E_p) \int_{\text{All Shower Sizes}} f(N_e, \bar{N}_e) \int_{\text{All Radial Distances}} P_M P_T 2\pi r dr dN_e dE_p \text{ s}^{-1} \text{ sr}^{-1} \tag{6.10}$$


---


$$\int_{\text{All Shower Sizes}} f(N_e, \bar{N}_e) dN_e$$

where  $P_M, P_T, r$  and  $R(>P_\mu)$  are as defined in Section 4.7.13. All the steeps

used to evaluate equation 4.32 were used in evaluating equation 6.10 with the addition of 25 steps over the shower size distribution,  $f(N_e, \bar{N}_e)$ .

A comparison of the result of evaluating equation 4.32 with the result of evaluating equation 6.10 is shown in Table 6.5. The values in Table 6.5 correspond to the proton only spectrum, equation 6.4, which has been used because the distribution shown in Figure 6.9 is for a proton initiated showers. de Beer, et al., (1968) find that heavy primaries produce narrower distributions and that there is almost a unique number of muons for each energy of primary. For all values of muon threshold momentum the rate predicted by using the distribution of shower sizes is lower than by using the expression adjusted to fixed shower size. The implication is that if the shower size distribution is assumed to apply in approximately the same form for both the CKP and scaling models the predicted rates will all be lower than the values calculated so far.

#### 6.8 COMPARISON OF THE MEASURED AND PREDICTED RATES

The limitations imposed by the considerations of this chapter may still allow a distinction between the predictions of the CKP model (representative of a high multiplicity model) and the predictions of the scaling model. However, any distinction will be qualified by the validity of the expressions used to represent the predictions of each model. For instance, and in particular, the relationship of shower size to primary energy corresponding to the scaling model calculations of Fishbane, et al., (1974) has been extrapolated to energies lower than the region covered by the original calculations.

Allowance has been made in the comparison of the measured and theoretical rates of events for the scintillation counter efficiencies as described in Appendix H. The predictions displayed must be regarded as indicating the central part of fairly extensive regions. The errors on the

MUON THRESHOLD MOMENTUM GeV/c		20	50	100	200	500	1000
Predicted Integral Number in 5118 h.	Fixed Shower Size Approximation Equation 4.32	2260	1418	815	536	183	62
	Distribution, Equation 6.10	2020	1290	722	461	163	55

TABLE 6.5

experimental points are statistical and as the plots are of the integral rate of events the errors are not independent. However, within the context of the various expressions actually used for the muon and electron components of air showers as predicted by the different models, the CKP model (Model A) predictions are significantly closer to the data than the straight forward scaling model calculations, (Model B). The interpretation of the success of scaling Model C must be seen with respect to the fact that although the although the rising  $\sigma_{p\text{-air}}(\text{INEL})$  with energy will indeed increase the predicted rate of events the effect of any intranuclear cascade may not be as extensive as suggested by Fishbane, et al., (1974), (Whose results for the cascade result in a mean elasticity of about 0.3 for nucleon-nuclear targets). The calculations of Section 6.3 which take into account the effect of a higher threshold energy for electron detection implies a reduction in the predicted rate which will tend to be the same for both interaction models. However, the actual, and variable, threshold for the present experiment remains uncertain.

Similar conclusions may be drawn about the relation between the measured rates of coincident muon pairs in showers and the predictions of the models. However, the form of decoherence of muon pairs over the measured range of separation, and the range of muon momentum and shower size, may not be flat, but unless the variation is very rapid indeed, the broad conclusion is unlikely to change.

The combination of the measured primary spectrum, extrapolated to the region of interest, and the mean shower size to primary energy relationships as used in section 6.5 predict too high an intensity of air showers at sea level. Thus either the spectrum or models, or both, are incorrect, and if adjustment is made the predicted rate of events will decrease. Again this favours the CKP as opposed to the scaling model.

CHAPTER 7

CONCLUSION AND FUTURE WORK

There is considerable contemporary interest in establishing the energy dependence of the multiplicity of particles produced in high energy particle collisions. The experimental data reported in this thesis has been considered in terms of the predictions of two different models of the fundamental interactions involved, viz, the empirically based CKP model, and the theoretically based scaling model. Interpretation of the collected data is complicated by not only experimental biases but by the fact that the properties of the extensive air showers measured, are a consequence of a cascade involving many hadronic interactions as well as the (uncertain) nature of the primary spectrum.

The broad conclusion of the present work is that agreement is found with the suggestion of a high multiplicity ( $\propto E_p^{1/4}$ ) of secondaries in particle interactions despite the failing of the actual model used (CKP) at lower incident energies.

The calculations performed to compare the measured rate of events with the rate of events predicted by the interaction models have necessarily involved approximations. However, both the effect of a higher energy threshold for electron detection and using a distribution of shower sizes instead of a fixed mean shower size for each primary energy, tends to predict a lower rate of events for both the models considered. Thus the higher multiplicity model is still favoured. This may be explained by a mechanism whereby more energy goes into the electromagnetic component of the air shower at an earlier stage of the development of the cascade. (Fishbane, et al., 1974). Indeed, with the observation of heavy lepton pairs produced in electron positron collisions at a c.m. energy of only

about 4 GeV, Perl et al., 1976, and of the observation of directly produced muons (not from pion or kaon decay) by both hadron-hadron (see Anderson, et al., 1976) and neutrino hadron collisions (see Barish, 1976) less justification exists for extrapolations of observations at lower interaction energies up to the energies involved in producing air showers. Gaisser, (1974a) points out that if the CKP model is modified to include a leading pion (an effect seen at machine energies) the predicted ratio of the number of muons to electrons in a shower produced by a primary of energy  $10^6$  GeV is reduced by a factor of two compared to the unmodified model.

Some of the predictions of the present work stem from calculations which neglect the effect of nucleon-antinucleon ( $N\bar{N}$ ) and kaon production in high energy particle interactions. At ISR energies the ratio of antinucleon to pion production is only about 5% and the ratio of kaon to pion production is about 10%. Grieder, (1973) suggest that if  $N\bar{N}$  production becomes significant at an energy of about  $10^6$  GeV an increase in the muon to electron ratio occurs that is most noticeable at low muon energies ( $< 10^2$  GeV). It may be justified to ignore kaon production, and assume pion production instead, as kaon hadron interactions are similar to pion hadron interactions and 2/3 of the charged kaons decay in the same way as charged pions. However, the transverse momentum distribution of produced kaons is wider than for pions and this may be important as the present experiment is sensitive to the actual location of muons in the air shower. Ng and Wolfendale, (1974) examined the variation of charge ratio of muons with zenith angle and conclude that there is no large scale change in the ratio of pions to kaons produced over the energy range  $5 \cdot 10^2$  GeV to  $10^4$  GeV.

The spectrograph and array are now being used for further studies of muons in air showers. It is planned to trigger the spectrograph on the advent of an air shower striking the array. In this way the converse of

the experimental arrangement described in this thesis will be employed, and a greater degree of calibration of the number of discharged flash tubes to particle density, and shower size, may be achieved. Certainly firmer conclusions could be drawn about the success of different models in predicting the number of high energy muons in small air showers at sea level. If a number of high energy muons are detected for which the corresponding shower size and core location are known, further weight may be added to the suggestion that a muon lateral structure function of the type introduced by Greisen, can be extrapolated up to muon energies of about 1000 GeV.

APPENDIX A

THE MONTE CARLO TECHNIQUE

For both the acceptance calculations and for determining the probability of triggering the spectrograph, a Monte Carlo technique has been used. The term Monte Carlo is used here to describe the selection and use of a pseudorandom number in a computer technique. The two processes in which this has been used are described below. The first used pseudorandom numbers to sample from a distribution, and the second is a simulation process. Simulation is essentially a technique that involves setting up a model of a real situation and then performing experiments on the model.

To sample randomly from a distribution successfully, the selections from the distribution must give rise to a frequency distribution of sampled values that matches the original distribution. Each selection must also be independent of the previous selections. The method chosen to select an arrival direction for air shower particles is used as an example of this "selection" and the determination of acceptance is used to demonstrate a "model".

In the case of an isotropic flux of incoming particles the probability that a particle incident on a plane surface will lie between zenith angle  $\theta$  and  $\theta + d\theta$  is given by

$$P(\theta)d\theta = \cos\theta\sin\theta d\theta \quad (A1.1)$$

and for a non-isotropic flux which has an intensity distribution in zenith angle of  $\cos^n\theta$ , n integer

$$P(\theta)d\theta = \cos^{n+1}\theta \sin\theta d\theta \quad (A1.2)$$

The cumulative distribution function  $F(x)$ , of  $x$  denotes the probability,  $P$ , that a random variable  $R$  takes on the value  $x$  or less. (Naylor et al., 1968)

$$\text{Thus } F(\theta) = P(R \leq \theta) \tag{A1.3}$$

where  $F(\theta)$  is defined over the range  $0 < F(\theta) < 1$

and  $f(\theta)$  is the probability density function,

$$\text{such that } f(\theta) = \frac{dF(\theta)}{d\theta} \tag{A1.4}$$

$$\text{so } f(\theta) = \int_{-\infty}^{\theta} f(t) dt \tag{A1.5}$$

and  $f(t)$  represents the value of the probability density function of the random variable  $R$  when  $R = t$ .

Since  $F(\theta)$  is defined over the range 0 to 1, we can generate uniformly distributed random numbers,  $r$ , and set  $F(\theta) = r$ .

$$\begin{aligned} \text{so } r &= \int_{-\infty}^{\theta} f(t) dt \\ &= \int_{-\infty}^{\theta} \cos^{n+1} t \sin t dt \end{aligned} \tag{A1.6}$$

$$\therefore r = \frac{1}{n+2} \left[ 1 - \cos^{n+2} \theta \right] \tag{A1.7}$$

$$\text{OR } \theta = \cos^{-1} \left\{ \left( 1 - (n+2)r \right)^{\frac{1}{n+2}} \right\} \tag{A1.8}$$

Thus by generating values of  $r$  from 0 to 1, the corresponding value of  $\theta$  can be determined by the "mapping" expression A1.8. The problem of making  $r$  random is considered as the last part of this appendix.

The determination of the acceptance of the spectrograph acts as an

example of using the above techniques where a selection must be made for all the initial parameters of the simulated situation. Here a model of the spectrograph was used which resembled the experiment closely. In the case of the acceptance of the blueside of the spectrograph for single unassociated muons, the arrival zenith angle  $\theta$ , azimuth angle  $\phi$ , and initial co-ordinates on the top detector,  $x$  and  $y$ , must be selected. Then, given this unique position and direction the subsequent passage of a muon of momentum  $P_{\mu}$  can be determined by incorporating magnetic deflection and energy loss in the model. This is explained in detail in Appendix B.

In order to produce an "acceptable" sequence of random numbers a digital computer can be made to produce a series of numbers, that is cyclic, (in more than about  $10^6$  numbers) that will satisfy the criterion of randomness that is appropriate here. This series of pseudorandom numbers, generated between 0 and 1, was checked for uniformity of distribution and statistical independence. In a selection from the full interval of 0 to 1, upon the advent of a number selected between 0 and 0.1 the very next number selected was stored. In  $10^6$  selections the distribution of these conditionally selected numbers was uniform and 'flat' between the limits of 0 and 1. Additional factors governing the use of this pseudorandom number generator in the work reported in this thesis were :

1. No conditions of secondary selection were applied to the numbers returned by the pseudorandom number generator. That is to say, all the numbers that were generated were used.
2. Two different forms of pseudorandom number generator were used in parallel, one being used to 'seed' or commence (or re-commence) the cyclic process in the other.

APPENDIX B

MONTE CARLO DETERMINATION OF ACCEPTANCE

In order to determine the intensity of muons incident on the spectrograph from the measured rate of events, the acceptance or geometrical factor of the instrument must be determined. Although an analytic solution for the acceptance of the blue side of the spectrograph has been determined for single muons, Whalley, 1974, Hume, 1974, a Monte Carlo technique to determine the acceptance has been used for the experimental situations described in this thesis. As the muons studied are accompanied by a shower of particles or a second muon the acceptance is a function of several variables. In the case of shower accompanied muons traversing the lower 4 measuring trays of the blue side, as was explained in Chapter 4, the muons trajectory must project back into the momentum selector tray 5 as an essential part of the trigger condition. Hence the acceptance will be '5 tray' in the bending plane and '4 tray' in the side plane. For the muon pair experiment (the 6-fold scintillation counter trigger) the acceptance will vary very rapidly at low muon momentum for different combinations of charge and distance of separation of the two muons. In this appendix the Monte Carlo technique that has been applied to determine the acceptance is explained. In Appendix C and E the application to the present situations is discussed.

Generally the counting rate in a detector is related to the incident flux of particles by an integral over the surface area and angular acceptance of the detector ;

$$\text{Counting Rate} = \iint J \cdot dA \cdot d\Omega I(\theta, \phi) \quad (\text{B1.1})$$

Geometrical  
Constraints of the  
Detector

where  $I(\theta, \phi)$  is the differential flux intensity and is a function of zenith angle  $\theta$  and azimuth angle  $\phi$ , and  $J$  is a unit vector in the direction of the flux, and  $dA$  and  $d\Omega$  are the area and solid angle elements.

Writing

$$I(\theta, \phi) = I_1(\theta, \phi)$$

where  $\iint_{\text{All Solid Angles}} d\Omega I(\theta, \phi) = 4\pi$

so the counting rate =  $I \times \text{Acceptance}$

where 
$$\text{Acceptance} = \iint_{\text{Detector}} J \, dA \, d\Omega_1(\theta, \phi) \tag{B1.2}$$

considering a computer model of the spectrograph for which the extremes of the blue side are the scintillation counters at levels 1 and 5, (Figure 2.1) each of area  $A = 1.32 \text{ m}^2$ . (0.75 m by 1.76 m) and separated by a distance of 6.49 m. Using this situation as an example the acceptance can be determined by the Monte Carlo technique via the use of computer simulation. For a flux of  $T$  simulated particles of any one value of momentum incident on the model of one side of the spectrograph

$$\text{Acceptance} = \int_{x,y} dA \int_0^{2\pi} d\phi \int_0^\pi P(\theta) d\theta \times \frac{S}{T} \tag{B1.3}$$

where  $\phi =$  azimuth angle,  $\frac{S}{T} = \frac{\text{Number of particles successfully through the model}}{\text{Total number of particles incident}}$

and  $P(\theta) d\theta = \cos^{n+1} \theta \sin \theta \, d\theta$  for a zenith angle intensity variation of  $\cos^n \theta$ , and  $x, y$  are the dimensions of the top scintillation counter. The initial co-ordinates on the top scintillation counter and the azimuth angle

of each simulated particle are selected linearly between limits of their minimum and maximum values, whilst the zenith angle is selected from a distribution as described in Appendix A. For a muon of momentum  $P_\mu$ , magnetic deflection and energy loss are applied during the traversal, and to successfully pass through, the muon must remain within the acceptance volume defined by the magnet blocks and all detecting levels. The values of energy loss for thickness of steel traversed have been taken from Whalley (1975, private communication). These values have been calculated from the work of Sternheimer, 1956, for ionization loss, and Heyman et al., 1963, for bremsstrahlung, pair production, and nuclear losses. The magnetic deflection and energy loss are applied at 50 intervals in each magnet block at which point the muon is considered to have a constant momentum, and the appropriate energy lost is subtracted and circular deflection applied. As  $P_\mu$  tends to infinity, the limiting value of acceptance is determined by considering straight line passages of muons through the spectrograph, deflection and energy loss being ignored.

A direct comparison of the results of this technique and the calculations due to Whalley (1974) are shown in Figure B1.1. The error bars shown are the square roots of the number of successful simulated events. The 'infinite' momentum acceptance is found to be  $407 \pm 3 \text{ cm}^2 \text{ sr}$  in comparison to  $408 \pm 2 \text{ cm}^2 \text{ sr}$  as determined by Whalley for an assumed isotropic arrival direction distribution.

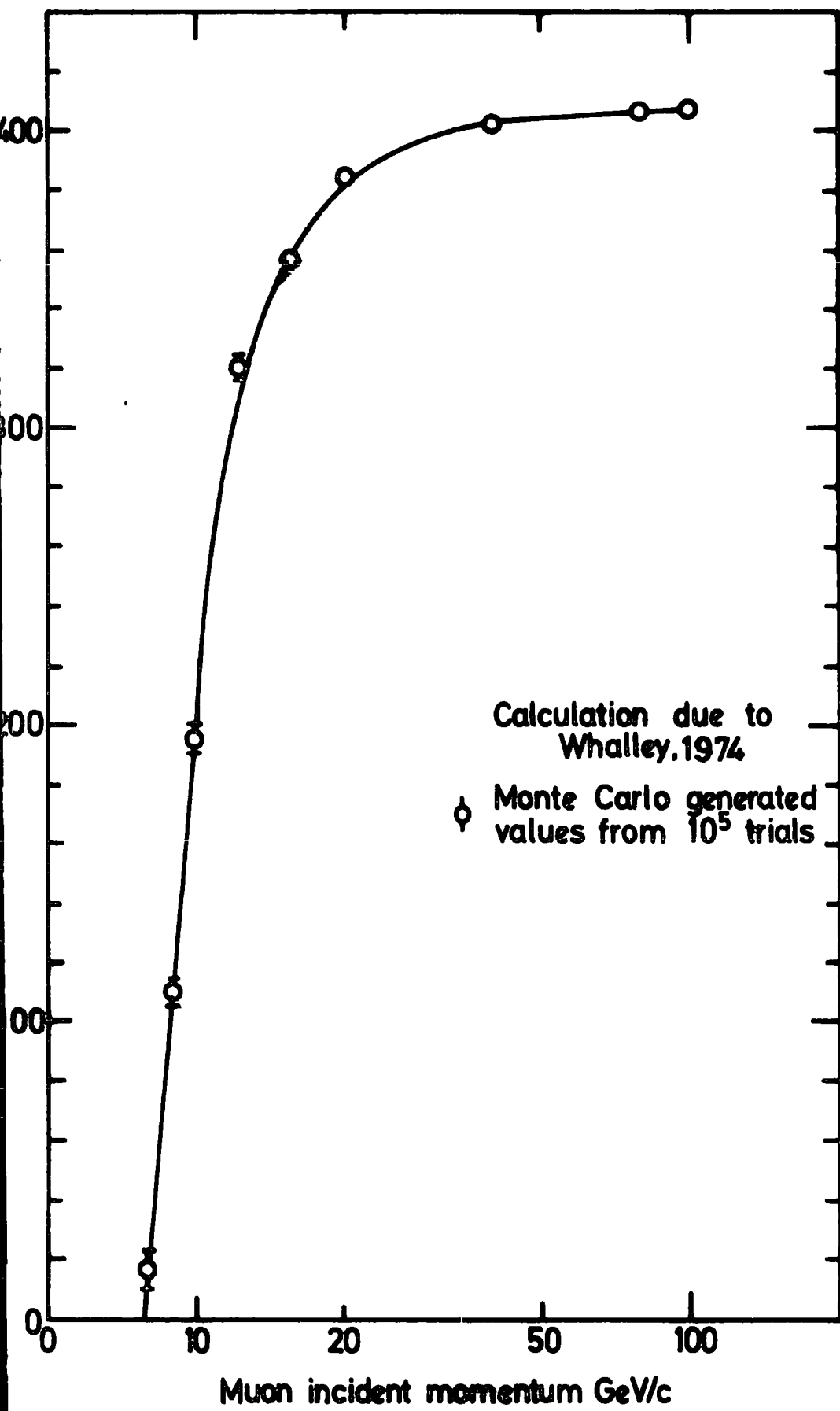


Figure B 1.1

APPENDIX C

THE SPECTROGRAPH ACCEPTANCE FOR SHOWER ASSOCIATED MUONS

For the spectrograph trigger conditions to be fulfilled as described in Chapter 4, when accompanied by a shower of particles the muon must pass through all 5 detecting levels in the bending plane but can pass into the spectrograph below the top detecting level in the side plane. Figure 4.7 shows the situation schematically. The Monte Carlo technique was applied to a computer model of the spectrograph and allowance was made for this increased acceptance by initializing particles over an increased area in the plane of the top momentum selector tray. The width of the top (in the bending plane) remained as 0.75 m but the effective length of the tray from back to front in the side plane was increased to 2.96 m. This dimension represents the extreme limit over which a muon could just pass from one top corner of measuring tray four to the bottom far corner of scintillation counter level 1. This applies to muons of all momenta as no bending takes place in this plane. Figure C1.1 is the variation of acceptance with momentum for this situation for a zenith angle ( $\theta$ ) intensity varying as  $\cos^8 \theta$  and Table C1.1 gives the values of acceptance vs  $n$ , the power of intensity variation.

n	Total Success in $10^6$ Trials	Acceptance $\text{cm}^2 \text{ sr}$
0	32547	540 $\pm$ 3
2	36291	527 $\pm$ 3
4	40114	513 $\pm$ 3
6	43840	497 $\pm$ 3
8	48137	487 $\pm$ 3

TABLE C1.1

THE VARIATION OF ACCEPTANCE FOR ONE SHOWER ACCOMPANIED MUON AS A FUNCTION OF THE DEGREE OF ZENITH ANGLE INTENSITY ANISOTROPY.

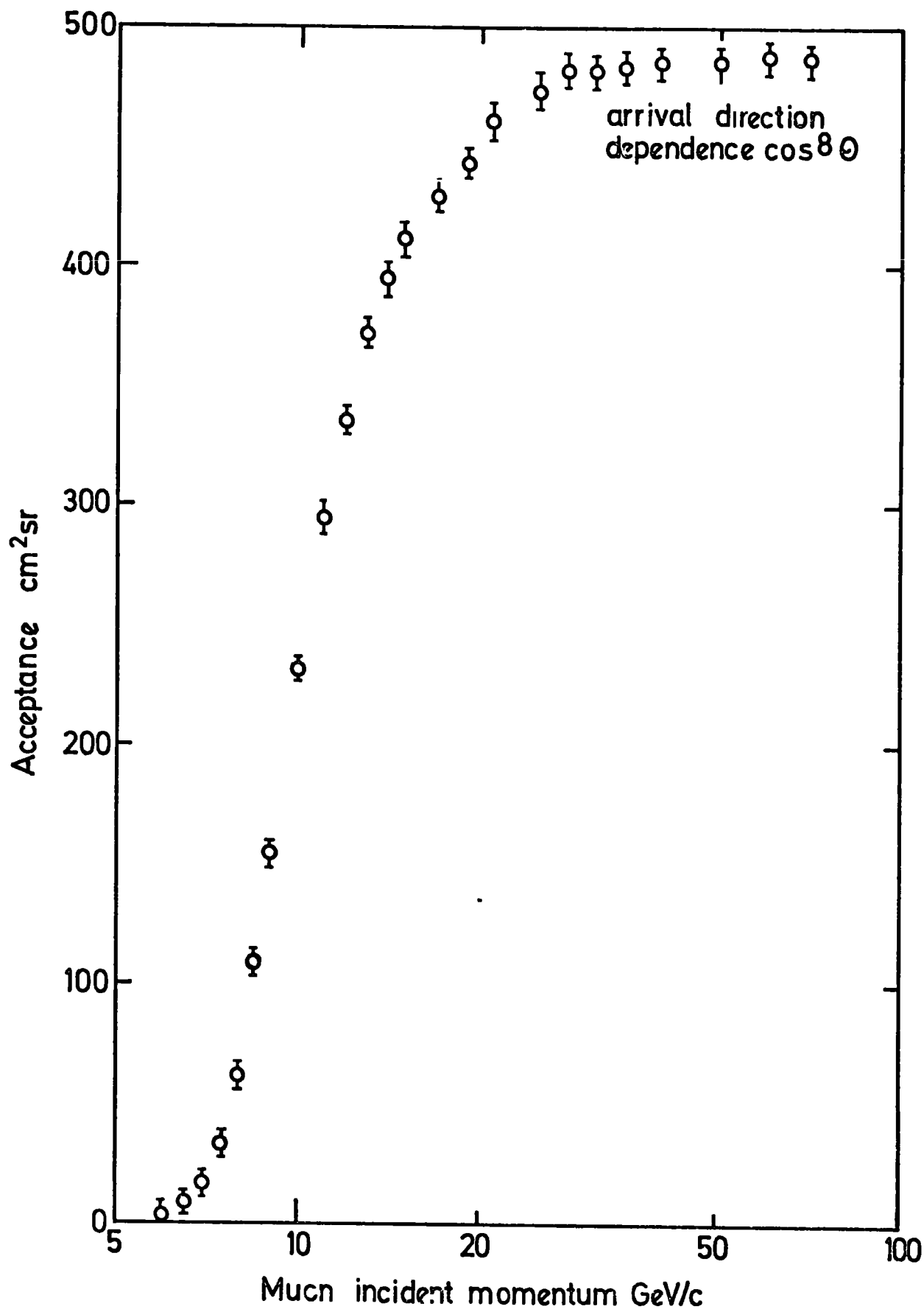


Figure C1.1 The acceptance for 5 trays in the bending plane and 4 in the side plane.

APPENDIX D

THE EFFECTIVE AREA AND SOLID ANGLE OF THE BLUE SIDE OF THE SPECTROGRAPH

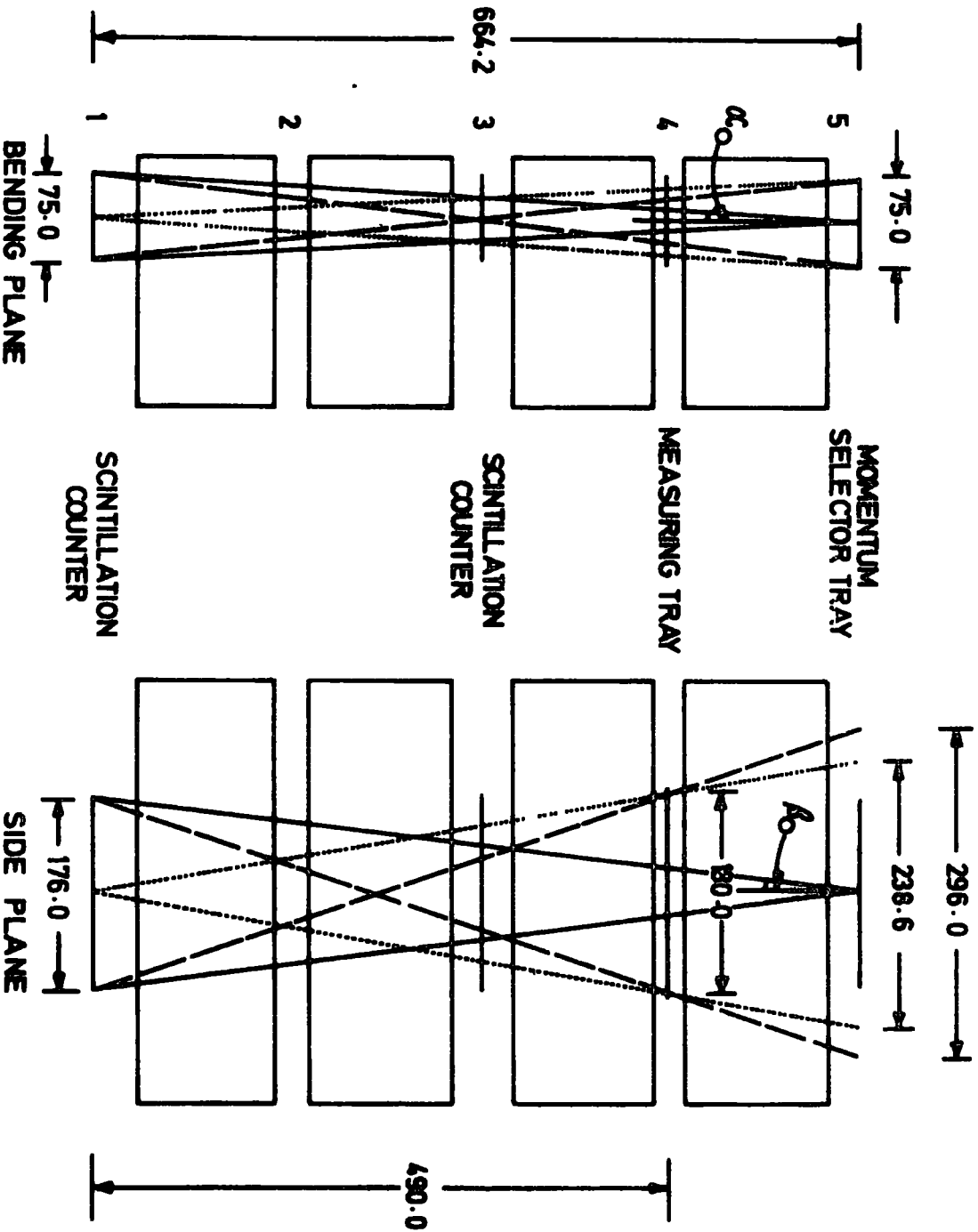
FOR AIR SHOWER ACCOMPANIED MUONS

For the calculation of expected rates of shower accompanied muons the Poisson probability of a particle counter being struck was used. Here the probability that  $n$  muons cross an area  $S \text{ m}^2$  when the mean density of muons in the shower is  $\rho \text{ m}^{-2}$  is

$$P_n = (\rho s)^n \frac{e^{-\rho s}}{n!} \quad (\text{D1.1})$$

This requires the representation of the spectrograph by an 'area' in the plane of the top detecting element. A value for the rate of events will likewise depend on the 'solid angle' that the bottom detector subtends when viewed from the top detector.

The area ( $s$ ) taken corresponds to the dimensions shown in Figure D1.1 (75.0 cm x 238.6 cm) in the plane of the top momentum selector tray. The constraints on a muon (of infinite momentum in the limiting case) are that it must pass through both the bottom scintillation counter and the top momentum selector tray in the bending plane. However, in the side plane the muon can come down into the spectrograph beneath the top detecting elements (the electrons in the shower strike these) but must still pass through the lower scintillation counters at levels 3 and 1. An extra condition applied to the data during analysis is that a track must be visible in measuring tray 4. Thus in this representation the area of the top will correspond to the area subtended from the centre of the bottom scintillation counter, constrained in the side plane by the length of measuring tray 4. This length has been taken as the length of flash tube covered by the electrode in that tray. The solid angle thus defined can be determined approximately by the following analytic solution.



$\alpha_0 = 3.23^\circ$        $\beta_0 = 7.54^\circ$

Figure D1.2 THE CO-ORDINATE REFERENCE FRAME USED TO CALCULATE THE EFFECTIVE SOLID ANGLE OF THE SPECTROGRAPH

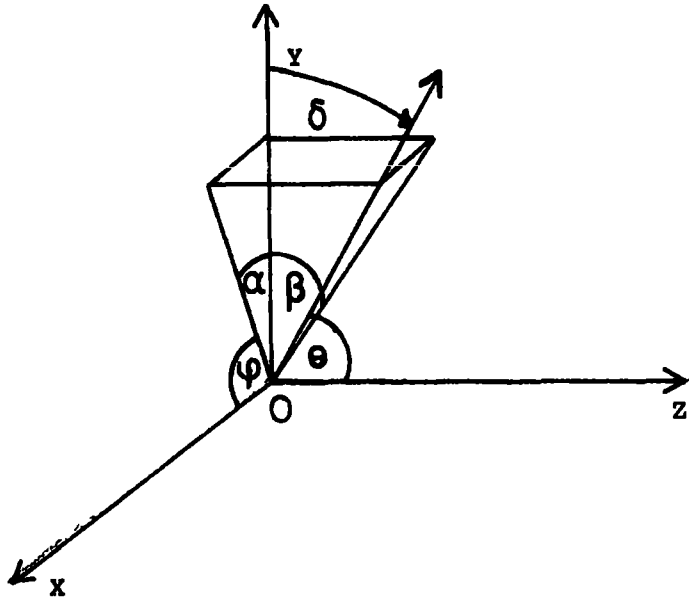


Figure D1.2 represents a general case of angles  $\alpha$  and  $\beta$  expressing a direction in space from origin O, and  $\theta$  and  $\phi$  are the spherical co-ordinate angles with axes x, y and z chosen arbitrarily. So the solid angle element subtended by an area ds at O is

$$d\Sigma = \sin\theta \, d\theta \, d\phi \quad (D1.2)$$

now  $\tan \theta = \cos\alpha \tan \beta \quad (D1.3)$

and  $\phi = \pi/2 - \alpha \quad (D1.4)$

hence  $\sec^2 \theta \partial\theta = \cos\alpha \sec^2 \beta \partial\beta \quad (D1.5)$

$$\begin{aligned} \partial\theta &= \frac{\cos\alpha \sec^2 \beta}{1 + \cos^2 \alpha \tan^2 \beta} \partial\beta \\ &= \frac{\cos \alpha}{1 - \sin^2 \alpha \sin^2 \beta} \partial\beta \end{aligned}$$

and  $\sin\theta = \frac{\cos \beta}{(1 - \sin^2 \alpha \sin^2 \beta)^{1/2}}$

while  $\partial\phi = -\partial\alpha$

so  $d\Sigma = \frac{\cos\alpha \cos\beta}{[1 - \sin^2 \alpha \sin^2 \beta]^{3/2}} d\alpha d\beta$  (D1.6)

Hence the solid angle is given by

$$\Sigma = \int_0^{\alpha_{\max}} \int_0^{\beta_{\max}} \frac{\cos\alpha \cos\beta}{[1 - \sin^2 \alpha \sin^2 \beta]^{3/2}} d\alpha d\beta \text{ sr,} \quad \text{(D1.7)}$$

Now considering the spectrograph with : y vertical, origin O as the centre of the top momentum selector tray and air showers arriving at an angle  $\delta$  to y with a distribution of  $\cos^m \delta$  (non-isotropic) where

$$\cos \delta = \frac{\cos\alpha \cos\beta}{(1 - \sin^2 \alpha \sin^2 \beta)^{1/2}}, \quad \text{(D1.8)}$$

Muons falling on a small area  $dA_{top}$  will pass through an area  $dA_{bottom}$  provided they fall within the solid angle  $d\Sigma$  which is the solid angle seen at  $dA_{bottom}$  when looking from  $dA_{top}$ .

Then the solid angle is given by

$$\Sigma = 4 \int_0^{\alpha_0} \int_0^{\beta_0} \frac{\cos^{m+1} \alpha \cos^{m+1} \beta}{(1 - \sin^2 \alpha \sin^2 \beta)^{(m+4)/2}} d\alpha d\beta$$

where the factor 4 arises because  $\alpha_0$  and  $\beta_0$  are the maximum angles in one quadrant only.

In Table D1.1 is the variation of  $\Sigma$  with  $m$ .

m	$\Sigma$ (Solid Angle) sr
0	.02893
2	.02873
4	.02854
6	.02834
8	.02815
10	.0278

THE VARIATION OF SOLID ANGLE WITH m

TABLE D1.1

Manno, et al., (1970) have shown with detailed calculations that when the separation of two unequal area circular detecting planes is much larger than the radius of either area (Radius about 10% of separation) then

the approximation

ACCEPTANCE = (AREA OF SECOND DETECTOR) X (SOLID ANGLE SUBTENDED  
BY FIRST DETECTOR WHEN VIEWED FROM CENTRE POINT OF  
SECOND DETECTOR)

is accurate to within 5% - so for the spectrograph, using the above determined  
values of solid angle and area,

$$\begin{aligned} \text{ACCEPTANCE } \pi &= .02815 \times 1.7895 \times 10^4 \text{ cm}^2 \text{ sr} \\ &= 504 \text{ cm}^2 \text{ sr for } m = 8 \end{aligned}$$

which is a close approximation to  $487 \text{ cm}^2 \text{ sr}$ , the more accurately determined  
value, as given in Appendix C.

APPENDIX E

THE ACCEPTANCE OF THE SPECTROGRAPH FOR TWO

COINCIDENT MUONS

The acceptance of the spectrograph for two experimental situations will be described in this appendix.

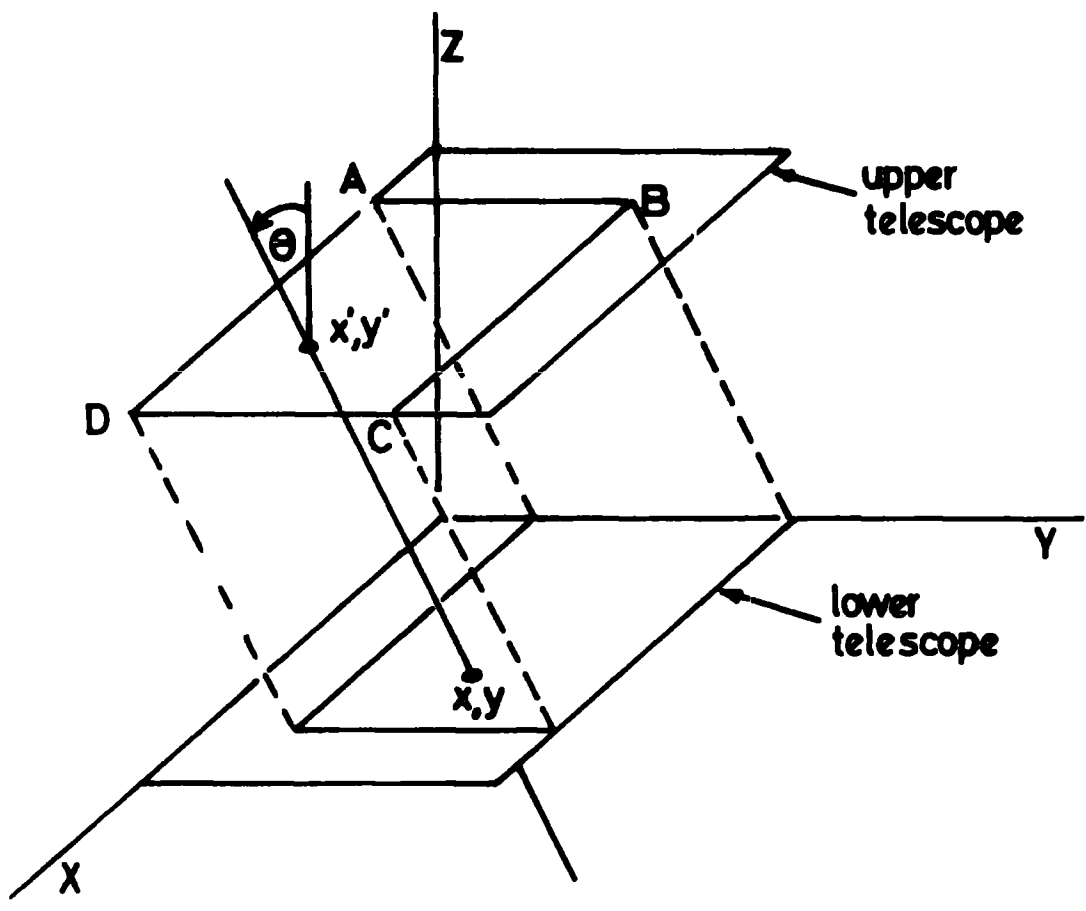
1. Two muons traversing the blue side accompanied by a shower detected in the top trays, with both the muons incident parallel.
2. One muon traversing the blue side and one traversing the red side. This will be considered for both shower accompanied and un-associated pairs of muons, again with parallel trajectories.

For both these situations the relationship of effective aperture to geometrical dimensions of a telescope due to Barton,(1971) as well as a Monte Carlo approach, have been used.

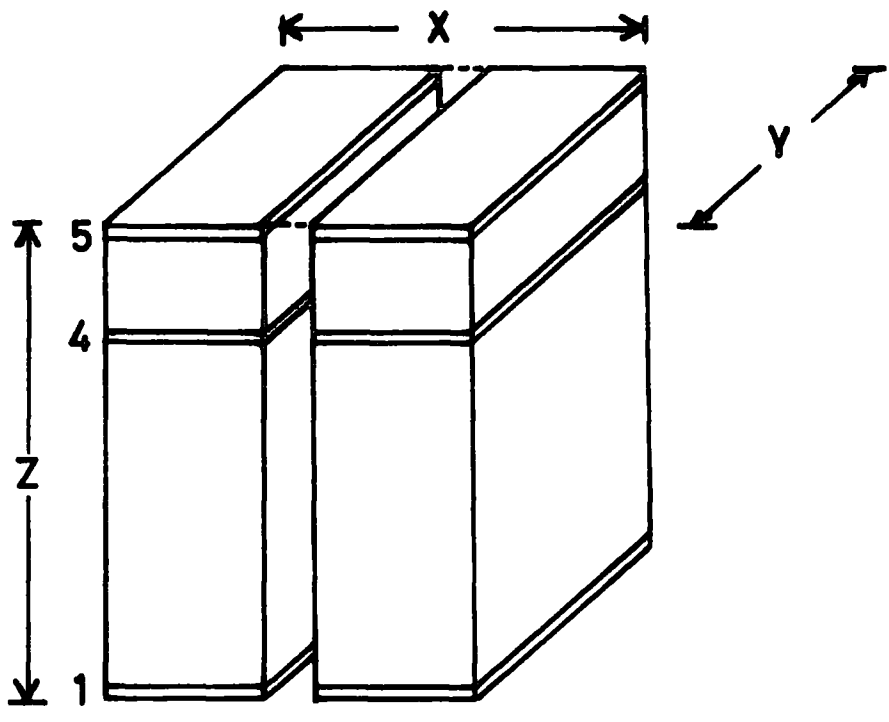
Considering first the blue side of the spectrograph as represented in Figure E1.1a where 'upper-telescope' represents the scintillation counter at level 5 and 'lower telescope' represents the scintillation counter at level 1. Barton,(1971) uses the representation of Stern,(1960) to define an aperture for single particles  $A_1(n)$  so that the counting rate,  $CR_1$ , for a particle intensity of  $I = I_0 \cos^n \theta$ ,  $\theta$  = zenith angle,  $I_0$  = vertical intensity, is

$$CR_1 = A_1(n) I_0 \quad (E1.1)$$

Thus for two rectangular counters of dimensions X and Y at a separation Z, Figure E1.1a, again from Stern,(1960)



(a)



(b)

Figure E1.1. Schematic view of the spectrograph, considered as a 'counter telescope.'

$$A_1(n) = \frac{1}{z^2} \int_0^x \int_0^y \int_0^x \int_0^y \cos^{n+4} \theta \, dx' dy' dx dy \, M^2 \text{ sr} \quad (\text{E1.2})$$

where  $\theta = \frac{z}{\{z^2 + (x-x')^2 + (y-y')^2\}^{1/2}}$  and the dimensions are in metres.

Now, following Barton,(1971) and defining the pair counting rate  $CR_2$  as

$$CR_2 = A_2(n) I_p \quad (\text{E1.3})$$

where the aperture for a pair  $A_2(n)$  and the intensity of pairs  $I_p$  are defined consistently. Thus  $I_p$  is the number of pairs per steradian crossing a horizontal area of one square metre in a vertical direction per unit time. So, if the first particle traverses the instrument as shown in Figure E1.1a, the second must fall within the area ABCD as shown. The area in a direction perpendicular to the direction of the muons is Area (ABCD) x cos  $\theta$  ; so

$$A_2(n) = \frac{1}{z^2} \int_0^x \int_0^y \int_0^x \int_0^y \cos^{n+5} \theta (X-x-x') (Y-y-y') dx' dy' dx dy \, m^4 \text{ sr} \quad (\text{E1.4})$$

Barton points out that provided the dimensions of the apparatus are small compared with the average separation between the particles this formula will apply.

The analysis given above can be applied to pairs of muons when both traverse the blue side of the spectrograph. However, for one muon passing each side account must be taken of the 'gap' between the two sides. Here the Monte Carlo approach allows the following interpretation.

Following directly the consideration of Appendix A and B and applying the result to two muons, the aperture for pairs incident on an area such as the top telescope of Figure E1.1a is

$$A_p = \int_{x,y} dA \int_{x,y} dA \int_0^{2\pi} d\phi \int_0^{\pi} P(\theta) d\theta \times \frac{S}{T} \text{ m}^4 \text{ sr} \quad (\text{E1.5})$$

where  $S, T, A, \theta, \phi, X, Y$  are as given in Appendix B. Following Barton, 'aperture' has been used as opposed to 'acceptance' in an attempt to distinguish the situation for pairs from the situation for single muons. The second term involving integration of area is to allow for the second muon in analogy with the approach of Barton. In the simulation of pairs of muons striking the top of the spectrograph the entire area is used for initializing the events following directly the process as described in Appendix B.

The aperture for one muon traversing each side has not been determined. However, selecting the co-ordinates of both muons from the whole area of the top,  $X$  times  $Y$ , as depicted in Figure E1.1b, a simulation of the acceptance for the experimental situation has been made. In this case the simulated event is successful only if one muon passes down each side of the instrument.

APPENDIX F

THE EFFECT OF DETECTOR AREA ON THE DENSITY OF PARTICLES  
DETERMINED FROM THE LATERAL DISTRIBUTION

To determine the density of shower particles over the whole area of the top of the spectrograph the radial distance of the core from the spectrograph must be considered. If the core is far away in relation to the area of the detector the variation of density over the area will be small and the density can be approximated by the density at the centre of the detector. For cores falling near or on the detector the density must be determined more precisely.

Consider a shower with core at X, a distance  $r$  from the centre of a circular detector of radius  $R$  and area  $S$ . Here the rectangular area of the top of the spectrograph has been approximated by a circle of equal area. See Figure Fl.1

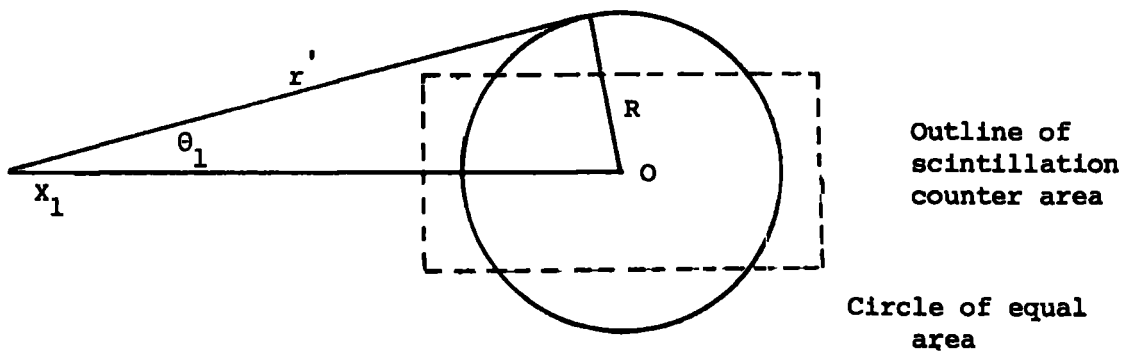


Figure Fl.1

The effective density  $\rho_{\text{eff}}$  will be

$$\rho_{\text{eff}}(r) = \frac{1}{S} \int_{r'} \int_{\theta} r' \rho(r') d\theta dr' \quad (\text{F1.1})$$

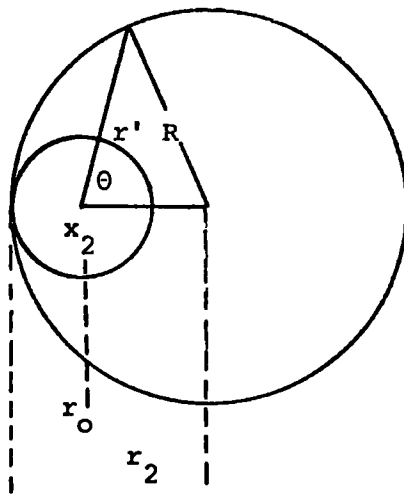
for any value  $r_1'$ ,

$$\theta = \cos^{-1} \left\{ \frac{r_1'^2 + r'^2 - R^2}{2r_1'r'} \right\} \quad (\text{F1.2})$$

so for  $r_1' > R$ , that is the core outside the detector,

$$\rho_{\text{eff}}(r) = \frac{1}{S} \int_{r_1'-R}^{r_1'+R} 2\theta(r,r') r' \rho(r') dr' \quad (\text{F1.3})$$

Figure F1.2



and for the axis inside the detector, (see Figure F1.2)  $r_0 = R - r_2$

$$\theta = \pi \quad \text{for} \quad r_2' \leq r_0$$

and 
$$\theta = \cos^{-1} \left\{ \frac{r_2^2 + r'^2 - R^2}{2r_2 r'} \right\} \quad (\text{F1.4})$$

and so 
$$\rho_{\text{eff}}(r) = \frac{1}{S} \left\{ 2\pi \int_0^{R-r_2} r' \rho(r') dr' + \int_{R-r_2}^{R+r_2} 2\theta(r_2 r') r' \rho(r') dr' \right\} \quad (\text{F1.5})$$

Values of  $\rho_{\text{eff}}$  determined in this way, and the corresponding density at the centre of the detector are shown as a function of radial distance in Figure F1.3. The N-K-G (see Section 6.2) electron structure function was used to determine the values shown in this figure.

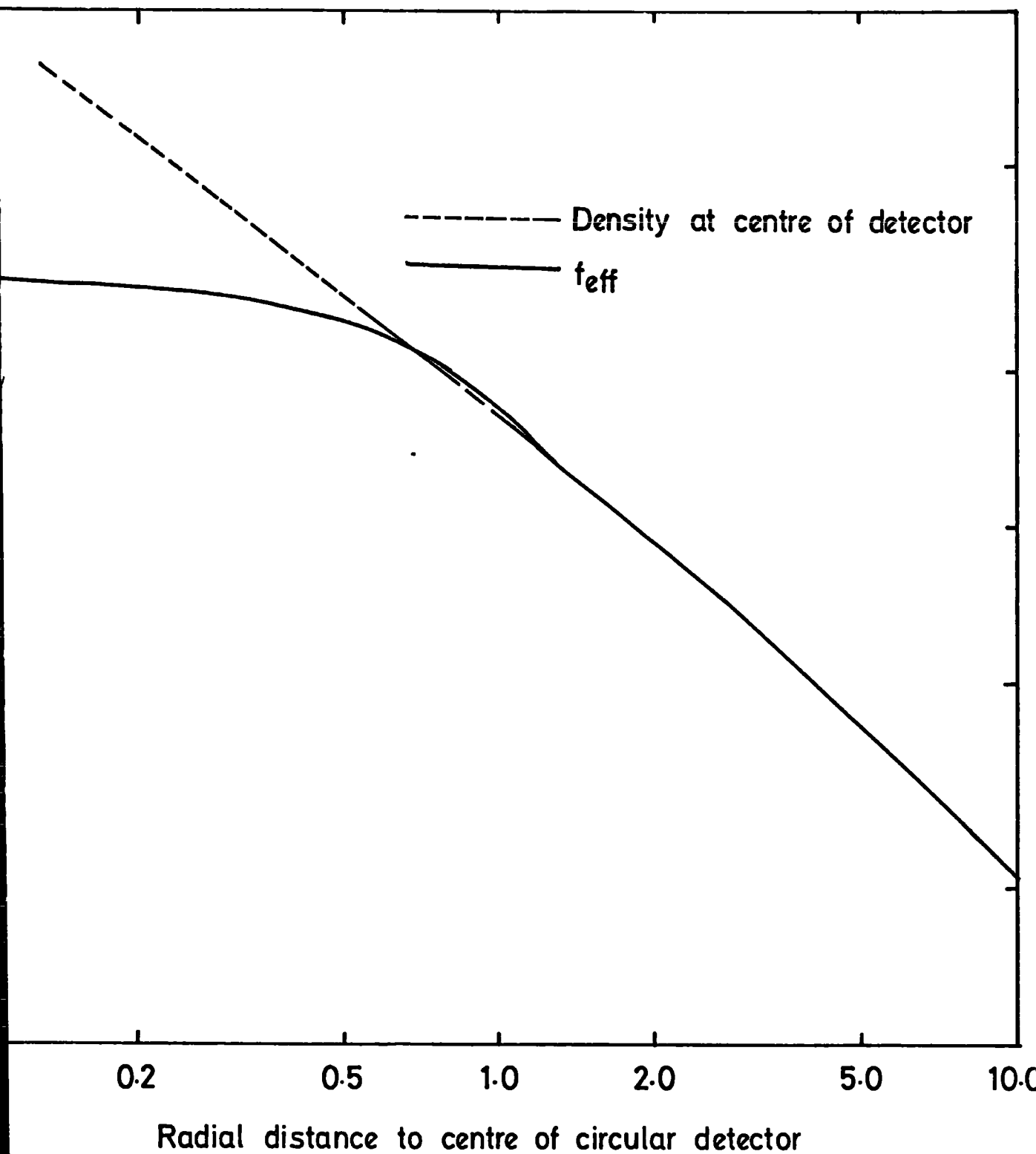


Figure F1-3. Density of particles as a function of radial distance.

APPENDIX G

THE RELATION OF THE SEA LEVEL SHOWER SIZE SPECTRUM TO THE

PRIMARY SPECTRUM FOR DIFFERENT MODEL PREDICTIONS

The differential intensity of showers of a given size at sea level will be related to the differential intensity of each component of the primary spectrum. For any assumed model of the atmospheric cascade if the mean shower size ( $N_e$ ) to primary particle energy ( $E$ ) and mass ( $A$ ) relation is known, then the following correspondence will hold,

$$F(N_e) dN_e = J(E_1) dE_1 + J(E_2) dE_2 + \dots + J(E_N) dE_N \quad (G1.1)$$

where  $F(N_e) dN_e$  is the differential shower size spectrum and  $J(E_i) dE_i$  is the differential primary spectrum of primary component  $i$ . The total primary spectrum can be considered as the sum of the fraction due to each component, and if all the components have the same spectral slope,  $\gamma$ , then

$$F(N_e) dN_e = \sum_i \text{FRACTION } (A) J_0 E^{-\gamma} dE \quad (G1.2)$$

where  $E$  is the primary nucleus energy, and  $J_0$  is a constant corresponding to the total intensity.

Now the mean shower size,  $N_e$ , is related to a primary nucleus of energy  $E$ , mass  $A$ , by

$$E = C N_e^\beta A^\alpha \quad (G1.3)$$

for fixed shower size conditions, where C,  $\beta$  and  $\alpha$  are constants.

$$\text{so } dE = C\beta N_e^{\beta-1} A^\alpha dN_e \quad (\text{Gl.4})$$

$$\begin{aligned} \text{thus } F(N_e) dN_e &= I_0 N_e^{-K} dN_e \\ &= \sum_i \text{FRACTION } (A)_i J_0 \left[ C N_e^\beta A_i^\alpha \right]^{-\gamma} C \beta A_i^\alpha N_e^{\beta-1} dN_e \end{aligned} \quad (\text{Gl.5})$$

so equating exponents in equation Gl.5,

$$- K = \beta(1-\gamma) - 1$$

$$\text{and } I_0 = J_0 C^{1-\gamma} \beta \left[ \sum_i \text{FRACTION } (A)_i A_i^{\alpha(1-\gamma)} \right]$$

APPENDIX H

THE SCINTILLATION COUNTER EFFICIENCIES

The rate at which events are detected by the spectrograph will depend on the scintillation counter efficiencies as these counters provided the basic trigger for all the experiments reported in this thesis. To determine the efficiencies a small scintillation counter (telescope) of dimensions 55 x 68 cm was placed under each of the 3 scintillation counters on one side of the spectrograph in turn to test them. For any particular position of the telescope, provided it is completely covered by the scintillation counter immediately above it that is on test, any muon passing through the telescope and the scintillation counters not on test must also have passed through the counter under test. In this way the 3 fold rate (the coincidences between the telescope and counters not under test) can be compared to the 4 fold rate (the coincidences between the telescope and all three counters), and the efficiency is defined as the ratio of 3 fold to 4 fold. To test the entire area of the scintillation counter the telescope had to be placed in 3 positions underneath, and the overall efficiency of each counter was taken as the mean of the 3 values, for the purpose of the present work. As described in Chapter 2, each scintillation counter (as well as the telescope) has its own discriminator. The efficiency of all six counters in the spectrograph was determined in this way for the same discriminator setting as used in the experiments reported here. The efficiency of each counter was assumed to be the mean of efficiency as measured before and after the course of the experiments. For the comparisons of the measured rate of events with the predicted rates the efficiency of the overall scintillation counter system was determined according to which counters were involved in the trigger system. For instance, the detection of shower accompanied muons on the blue side requires

a coincident signal from the 3 blue side counters. However, the uppermost counter, level 5, will be struck by many shower particles and hence have an efficiency of unity. Thus the overall efficiency was taken to be the product of the efficiencies of the two lower counters, which is about 0.91. The experimental values quoted in this thesis have not been corrected for the scintillation counter efficiencies but the appropriate adjustment has been applied to the predicted rate of events for each comparison of measured and predicted rate of events.

REFERENCES

- Adcock, C., Wolfendale, A.W., and Wdowczyk, J., 1969, *J. Phys. A. (Gen.Phys.)*, 2,2,574.
- Adler, S.L., Healy, J.B., Karlner, I., Lieberman, J., Ng., Y.J., Tsao, H.S., 1975, *Phys. Rev. D.* 12, 9, 2639.
- Albrow, M.G., Bagchus, A., Barber, D.P., Bogaerts, A., Bosnjakovic, B., Brooks, J.R., Clegg, A.B., Erne, F.C., Gee, G.N.F., Locke, D.H., Loebinger, F.K., Murphy, P.G., Rudge, A., and Sens, J.C., 1974, *Nucl. Phys.*, B73, 40.
- Allen, H.R., Crannell, C.J., Hough, J.H., Shutie, P.F., and Sun, M.P., 1975, *P.I.C.C.R.\**, Munich, 8, 3077.
- Allkofer, O.C., Carstensen, K., Dan, W.D., 1971, *P.I.C.C.R.*, Hobart, 4, 1314.
- Altarelli, G., 1974, *Riv. Del. Nuovo, Cim.* 4, 3, 335.
- Anderson, C.D., 1932, *Science*, 76, 238.
- Anderson, K.J., et al., 1976, *Phys. Rev. Lett.*, 37, 13, 799.
- Antinucci, M., et al., 1973, *Lett. Nuovo. Cim.*, 6, 2, 4, 121.
- Aseikin, V.S., et al., 1971, *P.I.C.C.R.*, Hobart, 6, 2152.
- Ashton, F., and Saleh, A.J., 1975, *P.I.C.C.R.*, Munich, 7, 2467.
- Ayre, C.A., 1971, Ph.D. Thesis, University of Durham.
- Ayre, C.A., Baxendale, J.M., Daniel, B.J., Goned, A., Piggott, J.L., Thompson, M.G., 1975, *Nucl. Inst. and Meth*, 124, 335.
- Ayre, C.A., Baxendale, J.M., Hume, C.J., Nandi, B.C., Thompson, M.G., and Whalley, M.R., 1975, *J. Phys. G. Nuc.*, 5, 584.
- Ayre, C.A., Hamdan, M.A., Hume, C.J., Stubbs, F.W., Thompson, M.G., Wells, S.C., and Whalley, M.R., 1972 (a), *Nucl. Inst. and Meth.*, 102, 19.
- Ayre, C.A., Hamdan, M.A., Hume, C.J., Stubbs, F.W., Thompson, M.G., Wells, S.C., and Whalley, M.R., 1972 (b), *Nucl. Inst. and Meth.*, 102, 29.
- Ayre, C.A., Hamdan, M.A., Hume, C.J., Thompson, M.G., Wells, S.C., Whalley, M.R., and Wolfendale, A.W., 1971 (a), *P.I.C.C.R.*, Hobart, 4, 1458.
- Ayre, C.A., and Thompson, M.G., 1969, *Nucl. Inst. and Meth*, 69, 106.
- Balasubrahmanyan, V.K., and Ormes, J.F., 1972, *Goddard Space Flight Centre Preprint x-661-72-447.*

- Barish, B.C., Bartlett, J.F., Buchholz, D., Humphrey, T., Merritt, F.S., Nagashima, Y., Sciulli, F.J., Shields, D., Suter, H., Krafczyk, T., and Maschke, A., 1973, Phys. Rev. Lett., 31,6,410.
- Barrett, P.H., Bollinger, L.M., Cocconi, G., Eisenberg, Y., and Greisen, K., 1952, Rev. Mod. Phys. 24, 2, 133.
- Barton, J.C., 1968, J. Phys. A. (Proc. Phys. Soc.) 2, 1, 43.
- Barton, J.C., 1971, J. Phys. A: Gen. Phys., 4, L18
- Baxendale, J.M., Daniel, B.J., Hawkes, R.C., Piggott, J.L., Thompson, M.G., and Thornley, R., 1975, P.I.C.C.R., Munich, 3, 2011.
- Baxendale, J.M., Hume, C.J., and Thompson, M.G., 1975, J. Phys. G. Nuc. Phys., 7, 781.
- de Beer, J.F., Holyoak, B., Wdowczyk, J., and Wolfendale, A.W., 1966, Proc. Phys. Soc., 89, 567.
- de Beer, J.F., Holyoak, B., Odd, H., Wdowczyk, J., and Wolfendale, A.W., 1968, J. Phys. A. (Proc. Phys. Soc.), 2,1,72.
- Bell, C.J., Bray, A.D., Denehy, B.V., Goorevich, L., Horton, L., Loy, J.G., McCusker, C.B.A., Nielsen, P., Outhred, A.K., Peak, L.S., Ulrichs, J., Wilson, L.S., and Winn, M.M., 1974, J. Phys. A, 7, 990.
- Bell, C.J., 1976, J. Phys. G., 2, 11, 867.
- Bell, M.C., 1974, Ph.D. Thesis, University of Durham.
- Benecke, J., Chou, T.T., Yang, N.N., and Yen, E., 1969, Phys. Rev., 188, 5, 2159.
- Bennett, M.M., and Greisen, K., 1961, Phys. Rev., 124, 1982.
- Benvenut, A., Cline, D., Ford, W.T., Imlay, R., Ling, T.Y., Mann, A.K., Orr, R., Reeder, D.D., Rubbia, C., Stefanski, R., Sulak, L., and Wanderer, P., 1975, Phys. Rev. Lett., 35, 18, 1119.
- Benvenuti, A., et al., 1975 (a), Phys. Rev. Lett., 34, 7, 419.
- Bergeson, H.E., Boone, J.C., Elbert, J.W., Lowe, G.H., Larson, M.O., and Morrison, J.L., 1975, P.I.C.C.R., Munich, 6, 2055.
- Bingham, R.G., and Kellermann, E.W., 1965, Nuovo, Cim., 38, 1.
- Blake, P.R., Nash, W.F., and Strutt, R.B., 1975, P.I.C.C.R., Munich, 8, 2778.
- Bradt, H., Clark, G., La Pointe, M., Domingo, V., Escobar, I., Kamata, K., Murakami, K., Suga, K., and Toyoda, Y., 1965, P.I.C.C.R., London, 2, 715.
- Brandt., R.A., Kaufman, A., and Preparata, G., 1974, Phys. Rev. D., 10, 1, 146.

Branson, J.G., Sanders, G.H., Smith, A.J.S., Thaler, J.J., Anderson, K.J. Henry, G.G., McDonald, K.T., Pilcher, J.E., and Rosenberg, E.I., 1977, Phys. Rev. Lett, 38, 9, 457.

Breake, J.M., 1973, Cosmic Rays at Ground Level, The Institute of Physics, London, p. 229.

Brooke, G., Hayman, P.J., Kamiya, Y., and Wolfendale, A.W., 1964, Proc. Phys. Soc. 83, 853.

Bonczak, B., Firkowski, R., Gawin, J., Hibrier, J., Maze, R., Wdowczyk, J., and Zawadzki, A., 1968, Can. J. Phys., 46, S102.

Busza, W., Elias, J.E., Jacobs, D.f., Swartz, P.A., Young, C.C., and Sogard, M.R., 1975, Phys. Rev. Lett., 34, 13, 836.

Carroll, A.S., Chiang, I.H., Kycia, T.F., Li, K.K., Mazur, P.O., Mockett, P., Ralm, D.C., and Rubinstein, R., 1974, Phys. Rev. Lett. 33, 15, 928.

Cartwright, B.G., Garcia-Munoz, M., and Simpson, J.A., 1971, P.I.C.C.R., Hobart, 1, 215.

Castagnoli, C., Picchi, P., and Verri, G., 1969, Nuovo Cim., 61B, 290.

Catz, Ph., Gawin, J., Grochalska, B., Hibner, J., Hochart, J.P., Milleret, G., Stanizuk, J., and Wdowczyk, J., 1975, P.I.C.C.R., Munich, 12, 4329.

Catz., P.L., Hochart, J.P., Maze, R., Zawadski, A., Gawin, J., and Wdowczyk, J., 1973, P.I.C.C.R., Denver, 4, 2495, and, 1971, P.I.C.C.R., Hobart, 3, 1035.

Chang, L.N., Derman, E., and Ng, J.P., 1975, Phys. Rev. Lett., 35, 1, 6.

Clay, J., 1927, Proc. Amsterdam, 30, 1115.

Cocconi, G., Koester, L.J., and Perkins, D.H., 1961, Lawrence Radiation Lab. High Energy Physics Study Seminars, No. 28, 2.

Cocconi, G., 1971, Nucl. Phys. B28, 341.

Colgate, S.A., and White, R.H., 1966, Astrophys. J., 143, 626.

Conversi, M., 1973, Riv. Nuo. Cim. 2,3,233.

Conversi, M., and Gozzini, A., 1955, Nuovo. Cim, 2, 189.

Coxell, H., Meyer, M.A., Scull, P.S., and Wolfendale, A.W., 1961, supp. Nuovo. Cim, 21, 7.

Dixon, H.E., Earnshaw, J.C., Hook, J.R., Smith, G.J., and Turver, K.E., 1973, P.I.C.C.R., Denver, 4, 2473.

Dixon, H.E., Turver, K.E., and Waddington, C.J., 1974, Proc. Roy. Soc. Lond. A. 339, i57.

Dodd, P., Jobs, M., Kinson, J., Tallini, B., French, B.R., Sherman, H.J., Skillicorn, I.O., Davies, W.T., Derrick, M., and Radojicic, D., 1961, Int. Conf. Elementary Particles, Aix-en-Provence, 1, 433, (Saclay: C.E.N.)

Earnshaw, J.C., Orford, K.J., Rochester, G.D. Somogyi, A.J., Turver, K.E., and Walton, A.B., 1967, Proc. Phys. Soc., 90, 91.

Edge, D.M., Evans, A.C., Garmston, H.J., Reid, R.J.O., Watson, A.A., Wilson, J.G., and Wray, A.M., 1973, J. Phys. A6, 1612.

Elbert, J.W., Larson, M.O., Lowe, G.H., Morrison, J.L., Mason, G.W., and Spencer, R.L., 1975, J. Phys. A. Math. Gen., 8, 1, L13.

Elliott, J.R., Fortney, L.R., Goshaw, A.T., Lamsa, J.W., Loos, J.S., Robertson, W.J., Walker, W.D., and Yeager, W.M., 1975, Phys. Rev. Lett., 34, 10, 607.

Elster, J., 1900, Phys. Zeit., 2, 560.

Feynman, R.P., 1969, Phys. Rev. Lett., 23, 1415.

Feynman, R.P., 1969 (a), High Energy Collisions (Gordon and Breach, N.Y.), 237.

Feynman, R.P., and Gell-Mann, M., 1958, Phys. Rev., 109, 193

Fishbane, P.M., Gaisser, T.K., Maurer, R.H., and Trefil, J.S., 1974, Phys. Rev. D. 9, 11, 3083.

Fowler, P.H., 1973, P.I.C.C.R., Denver, 5, 3627.

Fukui, S., 1961, J. Phys. Soc, Japan, 16,4,604.

Fukui, S., Hasegawa, H., Matano, T., Miura, I., Oda, M., Suga, K., Tanahashi, G., and Tanaka, Y., 1960, supp. Prog. Theo. Phys., 16, 1.

Gaisser, T.K., 1974, Nature, 248, 122.

Gaisser, T.K., 1974 a, J. Frank. Inst. 293, 4, 271.

Gaisser, T.K., and Maurer, R.H., 1972, Phys. Lett, 42B, 4, 444.

Geitel, H., 1900, Physik, Z., 2, 116.

Gell-Mann, M., 1962, Phys. Rev. 125, 1667.

- Gell-Mann, M., 1964, Phys. Lett, 8,214.
- George, E.P., MacAnuff, J.W., and Sturgess, J.W., 1953, Proc. Phys. Soc., A, LXVI, 345.
- Goned, A.,1975, Il. Nuovo, Cim., 29A, 3, 301.
- Goned, A., Stewart, T.R., Wolfendale, A.W., and Wdowczyk, J., 1975, Nuovo. Cim. 29A, 317.
- Greisen, K., 1966, Phys. Rev. Lett., 16,748.
- Greisen, K., 1960, Ann. Rev. Nucl. Sci., 10, 63.
- Greider, P.K.F., 1973, P.I.C.C.R., Denver, 4, 2467.
- Greider, P.K.F., 1976, University of Bera, Switzerland, Preprint, July 1976, To be published in Rivista del Nuovo Cimento.
- Grigorov, N.L., Nesterov, V.E., Rapoport, I.D., Savenko, I.A., and Skuridin, G.D., 1970, Yad. Fiz. 11, 1058: Sov. J. Nucl. Phys. 11, 588
- Grupen, C., Hamdan, M.A., Hansen, S., Thompson, M.G., Wolfendale, A.W., and Young, E.C.M., 1972, J. Phys. A: Gen. Phys., 5, 1913.
- Hamdan, M.A., 1972, Ph.D. Thesis, University of Durham.
- Hansen, S., 1975, Ph.D. Thesis, University of Durham.
- Hansen, S., and Thompson, M.G., 1975 (a), J. Phys. G: Nuc. Phys. 9, 995.
- Hansen, S., and Thompson, M.G., 1976, J. Phys.G: Nucl. Phys., 2, 523.
- Hasert, F.J., et al., 1973, Phys. Lett. B., 46B, 1, 138.
- Hasegawa, H., Naranan, S., Matano, T., Miura, I., Oda, M., Shibata, S., Tanahashi, G., and Tanak, Y., 1962, Journ. Phys. Soc. Japan, 17, Suppl. A-111, 189.
- Hawkes, R.C., et al., 1977, To appear in P.I.C.C R., Plovdiv.
- Hayakawa, S., 1969, Cosmic Ray Physics, J. Wiley & Sons, New York.
- Hayman, P.J., Palmer, N.S., and Wolfendale, A.W., 1963, Proc. Roy. Soc., 275A, 391.
- Heckman, H.H. Greiner, D.E., Lindstrom, P.J., and Shure, H., 1975, P.I.C.C.R., Munich, 7, 2319.
- Hess, V.F., 1912, Phys. Zeitschr., 13, 1084.
- Hillas, A.M., 1975, Phys. Rep.,(Phys. Lett. C.) 20C, 61.
- Higashi, S., et al., 1962, J. Phys. Japan 17: Suppl. AIII, 89.
- Holyoak, B. 1967, Ph.D. Thesis, University of Durham.
- Hunter, H.W., and Trent, P.T., 1962, Proc. Phys. Soc., 79, 487.

- Iliyna, N.P., Kalmykov, N.N., Khrenov, B.A., Khristiansen, G.B., and Jarochkina, Z.V., 1971, P.I.C.C.R., Hobart, 6, 2109.
- Jain, P.L., Girard, B., Kazuno, M., and Thomas, G., 1975, Phys. Rev. Lett., 34, 15, 972.
- James, F., and Roos, M., 1975, Comp. Phys. Comn., 10, 343.
- Johnson, T.H., and Street, J.C., 1933, Phys. Rev., 43, 381.
- Kalmykov, N.N., and Khristiansen, G.B., 1974, P.I.C.C.R., Munich, 8, 2861.
- Kamata, K., and Nishimura, J., 1950, Prog. Theo. Phys., 5, 899, *ibid.* 1951, 6, 628 and *ibid.* 1952, 7, 185.
- Kamata, K., and Nishimura, J., 1958, Prog. Theor. Phys. Suppl., 6, 93.
- Kanofsky, A.S., and Colter, D.C., 1973, Il. Nuovo, Cim., 17B, 1, 219.
- Karakula, S. Osborne, J.L., and Wdowczyk, J., 1974, J. Phys. A. Math., Nucl. Gen., 7, 437.
- Kempa, J., Wdowczyk, J., and Wolfendale, A.W., 1974, J. Phys. A. Math., Nucl. Gen., 7, 1213.
- Khristiansen, G.B., Kulikov, G.V., Sirodjev, N., and Solov'eva, V.I., 1975, P.I.C.C.R., Munich, 8, 2801.
- Khristiansen, G.B., Vedoneev, O.V., Kulukov, G.V., Nazarov, V.I., and Solovjeva, V.I., 1971, P.I.C.C.R., Hobart, 6, 2097.
- Kulikov, G.V., Solovjeva, V.I., and Khristiansen, G.B., 1974, IZV, Akad. Nauk. SSSR, Ser. fiz. 38, 1020.
- Lattes, C.M.G., Muirhead, H., Occhialini, G.P.S., and Powell, C.F., 1947, Nature, London, 159, 694.
- La Pointe, M., Kamata, K., Gaebler, J., Escobar, I., Domingo, V., Suga, K., Murakami, K., Toyoda, Y., and Shibita, S., 1968, Can. J. Phys., 46, 868.
- Lee, W., Maclady, E., Sippach, W., Sokolsky, P., Teig, L., Bross, A., Chapin, T., Nodulman, L., O'Halloran, T., Pang, C.Y., Goulianos, K., and Litt., L., 1976, Phys. Rev. Lett., 37, 4, 186.
- Lee, T.D., and Yang, C.N., 1957, Phys. Rev., 108, 1611.
- Lipkin, H.J., 1973, Phys. Rept., 8, 3, 174.
- Llewellyn-Smith, C.H., 1972, Phys. Rep. 3, 5, 261.
- Lowe, G.H., Bergeson, H.E., and Layson, M.O., 1975, P.I.C.C.R., Munich, 6, 2061.

- Machin, A.C., Orford, K.J., Pickersgill, D.R., and Turver, K.E., 1969, P.I.C.C.R., Budapest, EAS 44/1.
- Manno, V., Page, D.E., and Shaw, M.L., 1970, E.L.D.O.-S.E.C.E.S./E.S.R.O.-C.E.R.S., *Scienc. Tech. Rev.*, 2, 363.
- Marciano, W.J., 1975, *Phys. Rev. D.*, 11, 11, 3334.
- Mayer, P., Ramaty, R., and Webber, W.R., 1974, *Phys. Today*, 27, 23.
- Morrison, D.R.O., 1973, C.E.R.N. report, C.E.R.N./ D.Ph. II/ Phys. 43, 73.
- Naylor, T.H., et al., 1966, *Computer Simulation Techniques*; New York, Wiley.
- Ne'eman, Y., 1961, *Nucl. Phys.*, 26, 222.
- Neito, M.M., (Nieto) 1968, *Phys. Rev. Lett.*, 21,7, 488.
- Ng, L.K., Wdowczyk, J., and Wolfendale, A.W., 1973, P.I.C.C.R., Denver, 3, 1781.
- Olejniczak, J., Wdowczyk, J., and Wolfendale, A.W., 1977, University of Durham preprint. To be published in *J. Phys. A*.
- Orford, K.J., Turver, K.E., and Walton, A.B., 1968, *Can. J. Phys.*, 46, S119.
- Ostriker, J.P., and Gunn, J.E., 1969, *Astrophysics. J.*, 157, 1395.
- Pearl, M.L., et al., 1976, *Phys. Lett.* 63B, 4, 466.
- Piggott, J.L., 1976, Ph.D. Thesis, University of Durham.
- Porter, L.G., and Stenerson, R.O., 1969, *J. Phys. A. Gen. Phys.* 1, 2, 374.
- Protheroe, R.J., and Turver, K.E., 1976, Fifth European Cosmic Ray Symposium, Leeds. Unpublished.
- Rada, W.S. Shaat, E.A.M., Smith, A.C., Stewart, T.R., Thompson, M.G., and Treasure, *Nucl. Inst. Meth.* (Accepted for publication).
- Rochester, C.D., and Butler, C.C., 1947, *Nature*, (London), 160, 855.
- Rodgers, I.W., Thompson, M.G., Turner, M.J.L., and Wolfendale, A.W., 1969, *J. Phys. A. (Gen.Phys.)*, 2,2, 001.
- Roll, P.G., and Wilkinson, D.T., 1966, *Phys. Rev. Lett.* 16,405.
- Rozhdestvensky, S.M., Khrenov, B.A., Khristiansen, G.B., Yarochkina, Z.V., Ilyina, N.P., and Bezradin, S.N., 1973, P.I.C.C.R., Munich, 8, 2790.

- Ryan, M.J., Ormes, J.F., and Balasubrahmanydu, V.K., 1972, Phys. Rev. Lett., ZB, 195, 985.
- Salam, A., Elementary Particle Physics - in Nobel Symposium No.8, edited by N. Svartholm, Almquist and Wiksell, Stockholm, 1978, p.367.
- Samorski, M., 1973, Nucl. Inst. and Meth., 108, 285.
- Shapiro, M., and Silberberg, R., 1970, Ann. Rev. Nucl. Sci. 20, 323.
- Smith, A.C., 1976, Ph.D. Thesis, University of Durham
- Smith, A.C., and Thompson, M.G., 1977, Nucl. Inst. Meth. (Accepted for publication).
- Stern, D., 1960, Nuovo, Cim. Suppl., 16, 153.
- Sternheimer, R.M., 1956, Phys. Rev., 103, 511.
- Tomaszewski, A., and Wdowczyk, J., 1975, P.I.C.C.R., Munich, 8, 2899.
- Turner, M.J.L., 1969, Ph.D. Thesis, University of Durham.
- Turver, K.E., 1973, Survey of Computer Simulations of Air Showers, University of Durham internal report.
- Turver, K.E., 1975, J. Phys. G: Nucl. Phys., 1,1,134.
- Vernov, S.N., et al., 1967, P.I.C.C.R., Calgary, EAS-53, Can. J. Phys., 46, S197, 1968.
- Waddington, C.J. and Freier, P.S., 1973, P.I.C.C.R., Denver, 4, 2449.
- Wdowczyk, J., 1975, P.I.C.C.R., Munich, 11, 4002.
- Wdowczyk, J., and Wolfendale, A.W., 1972, Nat. Phys. Sci. 236, 29.
- Wdowczyk, J., and Wolfendale, A.W., 1973, J. Phys. A: Math. Gen. 6, 1594.
- Weinberg, S., 1967, Phys. Rev. Lett., 19, 1264.
- Wells, S.C., 1972, Ph.D. Thesis, University of Durham.
- Whalley, M.R., 1974, Ph.D. Thesis, University of Durham.
- Wilson, C.T.R., 1901, Proc. Roy. Soc. (London), A68, 151; A69, 277.
- Wilson, C.T.R., 1900, Proc. Camb. Phil. Soc., 11, 52.
- Yodh, G.B., 1975, P.I.C.C.R., Munich, 11, 3936.

Yodh, G.B., Pal, Y., and Trefil, J.S., 1972, Phys. Rev. Lett.,  
28, 1005 and 1973, Phys. Rev. D, 8, 3233.

Yukawa, H., 1935, Proc. Phys. Math. Soc. Japan, 17, 48.

\* Proc. Int. Conf. on Cosmic Rays

